INFORMATION TO USERS

This manuscript has been reproduced from the microfilm master. UMI films the text directly from the original or copy submitted. Thus, some thesis and dissertation copies are in typewriter face, while others may be from any type of computer printer.

The quality of this reproduction is dependent upon the quality of the copy submitted. Broken or indistinct print, colored or poor quality illustrations and photographs, print bleedthrough, substandard margins, and improper alignment can adversely affect reproduction.

In the unlikely event that the author did not send UMI a complete manuscript and there are missing pages, these will be noted. Also, if unauthorized copyright material had to be removed, a note will indicate the deletion.

Oversize materials (e.g., maps, drawings, charts) are reproduced by sectioning the original, beginning at the upper left-hand corner and continuing from left to right in equal sections with small overlaps.

Photographs included in the original manuscript have been reproduced xerographically in this copy. Higher quality 6" x 9" black and white photographic prints are available for any photographs or illustrations appearing in this copy for an additional charge. Contact UMI directly to order.

Bell & Howell Information and Learning
300 North Zeeb Road, Ann Arbor, MI 48106-1346 USA

UMI®
800-521-0600

ON THE PARALLEL COMPUTATION OF TURBULENT ROTATING STRATIFIED FLOWS

A DISSERTATION
SUBMITTED TO THE DEPARTMENT OF MECHANICAL ENGINEERING
AND THE COMMITTEE ON GRADUATE STUDIES
OF STANFORD UNIVERSITY
IN PARTIAL FULFILLMENT OF THE REQUIREMENTS
FOR THE DEGREE OF
DOCTOR OF PHILOSOPHY

Anqing Cui

August 1999

UMI Number: 9958084

Bell & Howell Information and Learning Company
300 North Zeeb Road
P.O. Box 1346
Ann Arbor, MI 48106-1346

I certify that I have read this dissertation and that in my opinion it is fully adequate, in scope and in quality, as a dissertation for the degree of Doctor of Philosophy.

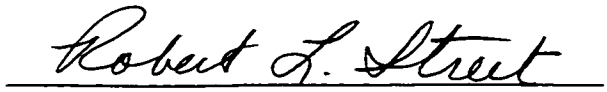

Robert L. Street
(Principal Adviser)

I certify that I have read this dissertation and that in my opinion it is fully adequate, in scope and in quality, as a dissertation for the degree of Doctor of Philosophy.

Joel H. Ferziger

I certify that I have read this dissertation and that in my opinion it is fully adequate, in scope and in quality, as a dissertation for the degree of Doctor of Philosophy.

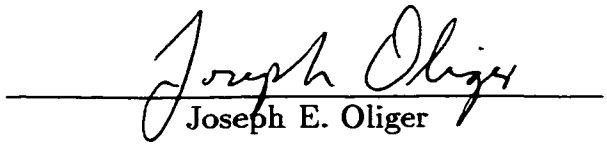

Joseph E. Oliger

Approved for the University Committee on Graduate Studies:

Abstract

The objectives of this study were to implement a high-performance numerical code for three-dimensional, unsteady, incompressible flow governed by the Navier-Stokes equations and to carry out large-eddy simulations of several laboratory-scale realizations of geophysical flows in complex geometries. The code was implemented on a distributed memory massively parallel computer, *viz.*, the IBM SP2.

The governing equations are the continuity, Navier-Stokes, and the scalar transport equations under the Boussinesq approximation, and they are solved in a rotating reference frame. A finite-volume method is used to discretize the governing equations in general curvilinear coordinates on a single non-staggered grid. A fractional-step projection method is used to solve the incompressible Navier-Stokes equations. A pressure Poisson equation is solved by the multigrid method. Three different dynamic subgrid-scale turbulence models were implemented in the code. An accurate and efficient parallel code was developed on the IBM SP2 using the message passing interface (MPI). A code performance of 38 MFlops per node was achieved, which was the reported peak rate on NASA's IBM SP2. The use of MPI enables good portability of the code among a broad class of parallel computers. This simulation tool was then used to study three rather different laboratory-scale realizations of geophysical flows.

First, large-eddy simulations of a laboratory model of rotating convective flows were carried out. The turbulent convection processes in a rotating tank driven by the energetic heating at the tank bottom have been studied for the purpose of modeling the convective flow caused by intense cooling at the ocean surface. The simulations showed Rayleigh-Bénard instability in the form of the circular concentric convective rolls, which were not seen in a related physical experiment due to the visualization technique used. New insights were gained into the evolution process of the convection and baroclinic wave formation via detailed three-dimensional simulation results. The

simulation results also were in reasonable agreement with the experimental data.

Second, large-eddy simulations of motion in an annular tank with a sloping bottom were carried out to simulate laboratory-scale coastal upwelling. The simulation results were compared with experimental data both qualitatively and quantitatively. Baroclinic waves, meanders and pinched-off eddies near the upwelled-surface front in the form of jets and cyclone/anticyclone pairs, as reported in the related experiments, were observed in the simulation results. A data assimilation algorithm, *i.e.*, the nudging method, was incorporated into the code. Hindcast data assimilation was successfully performed for the laboratory-scale coastal upwelling flow, demonstrating that nudging is applicable to baroclinically-unstable flows.

Third, numerical simulations of flows induced by source-sink pairs in a rotating stratified fluid were performed under the same conditions as in an on-going experiment. The purpose of the experiments was to examine the formation of essentially two-dimensional eddies in a stratified fluid. The effects of different rotation rates were evaluated with the jet-forcing internal Froude number being held constant. It is found that the size of the formed vortices decreases, while the expansion rate of the jet increases with increasing rotation rate.

Acknowledgments

I will always be grateful to my advisor, Professor Robert Street, for giving me the opportunity to pursue a Ph.D. at Stanford University and for his advice and guidance throughout the study. Professor Street always has the best interest of his students at heart, and I cannot imagine a better advisor. I would like to thank my reading committee members, Professors Joel Ferziger and Joseph Oliger, for their many useful suggestions, and Professors Brian Cantwell and Brad Osgood for serving on my oral examination committee. I would also like to thank Professors Jeffrey Koseff and Stephen Monismith for providing me with a good working environment at the EFML and for giving me their constant support.

I owe thanks to many of my fellow graduate students in the EFML for their friendship and support over the years. In particular, I would like to thank Dr. Yan Zang for helping me to get started with the project; Dr. Rajat Garg for his invaluable advice on parallel computing; Nancy Monsen, Gerard Ketefian, Oliver Fringer and Lucinda Shih for their excellent service as system administrators; Alex Horner for his help with his expertise in the experiment; Dr. Ron Calhoun and Dr. Lester Yuan for many helpful discussions; Dr. Lisa Lucas for her support and friendship; and my officemates Emily Zedler and Li Ding for making our office a pleasant place to stay.

I thank my parents for their inspiration, support and encouragement. I hope this work brings them joy. My thoughts also go to my late grandmother to whom I am indebted for life. The completion of this work would not have been possible without the understanding and support from my husband, Ganyu. Also, I would like to thank our unborn child for bringing great joy to my life and motivating me to finish writing.

This research was sponsored by NSF HPCC Grant ASC 9318166. The computations were performed on the NAS facility at NASA-Ames Research Center. These sponsors made this work possible and are gratefully acknowledged.

Dedicated To My Parents

Nomenclature

Roman Symbols

A	coefficient in the mapping function
a	coefficient in the mapping function
B	buoyancy flux
b	coefficient in the mapping function
B_i	operator for the pressure gradient term in the momentum equation
C	SGS model coefficient
C	coefficient in the mapping function
C_i	convective term in the momentum equation
C_{ij}	SGS cross term
C_{ij}^m	modified SGS cross term
C_M	coefficient for the modified Leonard term in subgrid-scale stress
C_p	specific heat at constant pressure
C_S	coefficient for the resolved term in subgrid-scale flux
c	coefficient in the mapping function
D_E	operator for the off-diagonal viscous term
D_I	operator for the diagonal viscous term
E	Ekman number

E_S	convective term in the scalar equation
f	Coriolis parameter
F_E	operator for the off-diagonal diffusion term
F_I	operator for the diagonal diffusion term
F_{ij}	flux tensor in the momentum equation
G_{mn}	mesh skewness tensor
g	gravitational acceleration constant
g'	reduced gravity
H	height of tank
J	Jacobian
k	thermal diffusivity or molecular diffusivity
L_{ij}	Leonard term
L_{ij}^m	modified Leonard term
N	number of grid points
P	pressure
P_i	resolved term in the SGS scalar flux
Pr	Prandtl number
Pr_t	turbulent Prandtl number
p	reduced dynamic pressure

Q	heat flux
R	radius of tank
Ra	Rayleigh number
R_D	Rossby deformation radius
Re	Reynolds number
R_i	flux in the scalar equation
R_{ij}	SGS Reynolds stress
R_{ij}^m	modified SGS Reynolds stress
r	radial coordinate
Sc	Schmidt number
S_i	source term in the momentum equation
S_{ij}	strain rate tensor
S_S	source term in the scalar equation
T	friction torque
T	temperature
Ta	Taylor number
T_0	reference temperature
t	time
U_m	volume flux

U_m^* intermediate volume flux

u, v, w Cartesian velocities x, y and $z$directions

u_i Cartesian velocity

u_* disk friction velocity

u_i^* intermediate Cartesian velocity

u_r, u_θ radial and azimuthal velocities

u_w wave speed of the frontal waves

x_i Cartesian coordinate

x, y, z Cartesian coordinates

Greek Symbols

α ratio of the test scale to the grid scale

α angle of the sloping bottom

β thermal or salt expansion coefficient

$\bar{\Delta}$ length scale of the grid filter

Δt time step

δ conductive layer thickness

δ_E Ekman layer thickness

δ_{ij} Kronecker delta

ϵ Rossby number

ζ	curvilinear coordinate
η	curvilinear coordinate
Θ	circumferential coordinate in mapped computation space
θ	circumferential coordinate
θ_*	non-dimensional parameter for the upwelling flow
κ	thermal diffusivity or molecular diffusivity
κ_T	eddy diffusivity
λ	wavelength
μ	dynamic viscosity
ν	kinematic viscosity
ν_T	eddy viscosity
ξ	curvilinear coordinate
ξ_m	curvilinear coordinate
π	pi, 3.14159265...
ρ	density
ρ_0	reference density
ρ_b	background relative density
ρ_*	relative density
τ_{ij}	subgrid-scale stress tensor

τ_w surface stress tensor

ϕ scalar

χ_i subgrid-scale flux vector

Ω rotation rate

Calligraphic Letters

$\mathcal{R}$ radial coordinate in mapped computation space

$\mathcal{Y}$ axial coordinate in mapped computation space

Other Symbols

∂ partial derivative operator

$\int$ integration

$\sum$ summation

$\prod$ product

$\overline{()}$ grid filtering operator

Superscripts

n nth time step

$'$ a subgrid-scale or spatial perturbation quantity

$''$ a temporal perturbation quantity

Subscripts

i, j, k indices for the Cartesian coordinates or vector quantities

m, n indices for the curvilinear coordinates or vector quantities

Abbreviations

ADI alternating direction implicit

CFL Courant-Friedrichs-Lewy

CPU central processing unit

DMM dynamic mixed model

DNS direct numerical simulation

DSM dynamic subgrid-scale model

DTM dynamic two-parameter model

EFML Environmental Fluid Mechanics Laboratory

LDA Laser-Doppler Anemometer

LES large-eddy simulation

MIMD multiple-instruction multiple-data

MPI message passing interface

NASA National Aeronautics and Space Administration

NCAR National Center for Atmospheric Research

NM Narimousa and Maxworthy

OTIS Optimum Thermal Interpolation Scheme

QUICK quadratic upstream interpolation for convective kinematics

RANS Reynolds-averaged Navier-Stokes

RHS right-hand side

SGS subgrid scale

SHARP simple high accuracy resolution program

SIMD single-instruction multiple-data

SPMD single-program multiple-data

SYNOP Synoptic Ocean Prediction

TGL Taylor-Görtler-like

Table of Contents

List of Tables

List of Figures

Chapter 1

Introduction

1.1 Motivation and Objectives

Atmospheric and oceanic flows may be thought of as turbulent motions under the constraints of geometry, stratification and rotation. Different kinds of geophysical flows hold both fascination and great physical importance in many areas, such as weather prediction, environmental protection and marine ecology. Field observation, analytical research and experimental study all are promising problem-solving approaches. With the rapid advancement of vector and parallel supercomputers, numerical simulation is becoming an increasing effective tool. The numerical simulation of laboratory-scale flows can provide complete and detailed information about the flow fields under completely controlled conditions. It is the purpose of this study to develop an efficient numerical simulation tool and to collaborate with experimental studies to obtain physical insight into different laboratory-scale realizations of geophysical flows relevant to our atmosphere and oceans.

Due to the wide range of spatial scales in the real flows, direct numerical simulation (DNS), which requires a fine computational grid to resolve all the scales of the flow motion, is limited to low Reynolds number flows and flows with relatively simple geometry. With recent improvement in the modeling of the subgrid-scale motions, the large-eddy simulation (LES) is now emerging as a most practical and powerful tool for the simulations of real engineering and geophysical flows. In LES, the large scale motions are computed explicitly, and the effect of sub-grid scales is modeled by

the use of large scale quantities. Unfortunately, for some flows of practical importance, the computational and memory requirements of LES render such simulation infeasible on a single-processor computer system, such as the Cray Y-MP. In recent years, distributed memory parallel computers have been widely recognized as a likely means of achieving scalable high performance computing. The typical design of a parallel computer exploits many small processors, working simultaneously, each accompanied by a small memory of its own. In such a design, which is called parallel processing, memory capacity and processing capacity can both be utilized with high efficiency. A novel aspect of this study is the development of a high-performance parallel code on a distributed memory architecture parallel machine, namely, the IBM SP2, using the standard portable message-passing library definition - Message Passing Interface (MPI). This simulation tool is then used to study three rather different laboratory-scale geophysical flows. Since three-dimensional numerical simulations reproduce many important characteristics of turbulent flows and allow one to extract information which cannot be easily obtained from laboratory experiments or field observations, the objectives of the present study are to generate simulation results to both guide and compare with experiments and to gain better understanding of the flow physics.

The first problem: Turbulent, rotating, convective flow arises when intense cooling at the ocean surface occurs in places, such as the Gulf of Lions in the Mediterranean and some areas of the polar seas, namely, the Greenland Sea, the Labrador Sea and the Weddell Sea. There are very few observations of convective events which allow an identification of the structure and scales of the flow. Nevertheless, turbulent convection in the open ocean is important due to its role in the transport of surface water to deep locations and ultimately in the large scale thermohaline circulations, which in turn play a central part in determining global climate. A series of laboratory experiments of isolated buoyant-convection in unstratified water with shelf and slope topography was carried out by Jacobs and Ivey (1998) at the University of Western

Australia to model the turbulent downflow-convection processes in an ocean driven by the energetic cooling at the ocean surface. In their study, the effects of different heat fluxes and rotating rates are investigated. A time scale characterizing the convective overturning stage is proposed. Both baroclinic instability and baroclinic eddies have been observed in their experiments. The wavelength of the baroclinic eddies is found to be a function of the Rossby deformation radius. In the present study, large-eddy simulations are carried out under the same conditions as the experiment to study the flow in detail.

The second problem: The fluid flow in this study is a laboratory-scale model of coastal upwelling in the ocean. Upwelling occurs mostly from spring to summer near the eastern boundary of oceans (along the western coasts of continents) where prevailing winds carry the surface water away from the coast because of the Coriolis effect. Because upwelling brings cold and nutrient-rich deep water into the surface layer, it affects fishery productivity, ecology and climatology in the coastal regions. A series of laboratory-scale experiments of shear-driven coastal upwelling was conducted by Narimousa and Maxworthy (hereafter referred to as NM) at the University of Southern California. In NM's experiments (1985 and 1987), they used a rotating cylindrical tank with a sloping bottom, which was filled with a two-layer stratified fluid; the upwelling was generated by the relative rotation of a solid top lid. They found that most of the characteristics of the flow field can be described by a single non-dimensional parameter, which combines the effects of stratification, rotation and surface stress. In their experiments, waves, meanders and pinched-off eddies were observed near the ocean surface front in the form of jets and cyclone/anticyclone pairs. Similar experiments are being carried out at the Environmental Fluid Mechanics Laboratory (hereafter referred to as EFML) at Stanford University. A wider and taller annular tank is used at the EFML. Zang and Street (1995) were the first to carry out a large-eddy simulation of coastal upwelling flows which solved the full set of Navier-Stokes and scalar transport equations, and they compared their results with

the experimental results of Narimousa and Maxworthy (1985 and 1987). Zang and Street made two approximations in their simulations: they employed a fluid viscosity that is 12.5 times larger than that of the water and they simulated upwelling flow in a section (one quadrant) of the tank used in the corresponding laboratory study due to the CPU time and memory limitations of the CRAY Y-MP. In the present study, large-eddy simulations are carried out under the same conditions as the experiments conducted by NM and EFML and simulation results are compared with experimental data obtained by NM's experiments. The purpose of the combined numerical and experimental study at the EFML is to develop and test methodologies for prediction systems using numerical methods in conjunction with observing systems. The numerical simulation code is used to generate a forecast of the upwelling flow in the rotating tank. Measurements will then be taken in the rotating tank using computer controlled data gathering, directed by the results of the simulation; data assimilation is performed to utilize these measured data and the old numerical forecast to produce a new forecast and the process is repeated as required. In this study, a data assimilation algorithm, *i.e.*, the nudging method, is incorporated into the simulation code to test the feasibility of using accurate numerical simulations to both predict physical behavior and to direct the measurement program needed to enhance predictions.

The third problem: This study investigates the flow dynamics generated by source-sink pairs in a rotating stratified fluid. The on-going experiments of Hacker and Linden at Cambridge University consist of forcing a linearly stratified fluid in an annular tank with eight source-sink pairs around the inner perimeter of the tank. These sources and sinks induce motion in a single horizontal plane; thus, their experiments are capable of producing horizontal eddies directly without there first being a decay of three-dimensional motion. It is one of the most striking features of our weather that it is dominated by the passage of high and low pressure systems that are essentially two-dimensional and horizontal. Similar features, called mesoscale eddies, occur in the ocean. Thus, the laboratory system has the capability of studying flows

with direct application to the atmosphere and oceans under controlled conditions and enables accurate measurements of the flow to be made. The insight drawn from the numerical experiments in this study is being used in the experimental design and planning. Ultimately, the numerical simulations and the experimental results will then be examined together so that underlying dynamics can be investigated.

1.2 Outline

The remainder of the dissertation is organized as follows. The mathematical formulation and numerical algorithm are presented in Chapter 2. The test of different dynamic subgrid-scale models and the code validation are performed in Chapter 3. Chapter 4 describes procedures adopted in this study for the code development and code optimization. The large-eddy simulations of rotating convective flows are presented in Chapter 5. The large-eddy simulations of the coastal upwelling flows and the data assimilation in the upwelling flow are presented in the consecutive chapters, Chapters 6 and 7. The numerical investigation of rotating stratified flows is presented Chapter 8. Concluding remarks are given in Chapter 9.

Chapter 2

Mathematical Formulation and Numerical Algorithm

2.1 Introduction

The governing equations for unsteady, three-dimensional, rotating, non-hydrostatic, and variable-density fluid flows are the continuity, Navier-Stokes, and the scalar transport equations in a rotating frame of reference. The Boussinesq approximation is used to simplify the governing equations. The filtered governing equations are obtained by applying grid-filtering to the governing equations to handle large-eddy simulation of flow turbulence. In order to deal with complex flows associated with irregular domain boundaries, the filtered governing equations are transformed from physical space to a regular computational space, and the final set of the governing equations in general body-fitted curvilinear coordinates are obtained. A finite-volume method is used to discretize the governing equations in general curvilinear coordinates on a single non-staggered grid.

In Section 2.2, the original set of governing equations based on the conservation principles are presented. The Boussinesq approximation is used to simplify the governing equations in Section 2.3. The filtered governing equations for large-eddy simulation are described in Section 2.4. Coordinate transformations are performed in Section 2.5 to give the governing equations in general curvilinear coordinates. The numerical scheme, including the time and space discretization, the solution method and the solution procedures are given in Section 2.6.

2.2 Governing Equations

The motions of a three-dimensional, unsteady, variable density and rotation-influenced incompressible fluid are governed by the equations for the conservation of mass, the conservation of momentum and the transport of a scalar quantity,

$$\frac{\partial \rho}{\partial t} + \frac{\partial \rho u_j}{\partial x_j} = 0 \tag{2.1}$$

$$\frac{\partial \rho u_i}{\partial t} + \frac{\partial F_{ij}}{\partial x_j} = S_i \tag{2.2}$$

$$\frac{\partial \rho \phi}{\partial t} + \frac{\partial R_j}{\partial x_j} = 0, \tag{2.3}$$

where the flux term F_{ij}, the source term S_i for the momentum and the flux term R_j for the scalar are given by

$$F_{ij} = \rho u_i u_j + P\delta_{ij} - \mu\left(\frac{\partial u_i}{\partial x_j} + \frac{\partial u_j}{\partial x_i}\right) \tag{2.4}$$

$$S_i = -\rho g \delta_{i2} + \rho\Omega^2(x_i - \delta_{i2}x_2) + 2\rho\Omega(-u_3\delta_{i1} + u_1\delta_{i3}) \tag{2.5}$$

$$R_j = \rho u_j \phi - k\frac{\partial \phi}{\partial x_j}. \tag{2.6}$$

In the above equations, t is the time, x_i the Cartesian coordinate, ρ the density, u_i the velocity, P the pressure, g the gravitational constant, Ω the system rotation rate, ϕ a scalar (*e.g.*, density or temperature), and μ and k represent, respectively, the dynamic viscosity and molecular diffusivity. The Einstein summation rule applies to all the terms. The axis of rotation is in the positive x_2 direction, and the direction of the gravity is in the negative x_2 direction (see Figure 2.1). The set of governing equations is closed with an equation of state which relates the density ρ to the scalar ϕ via

$$\rho = \rho(\phi). \tag{2.7}$$

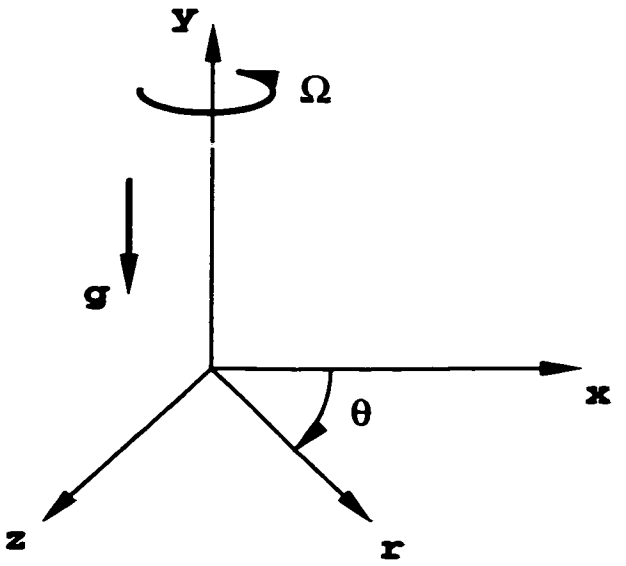

Figure 2.1: Coordinate diagram.

2.3 Boussinesq Approximation

To make the Boussinesq approximation, one assumes that the effect of variable density is negligible except in the buoyancy term of the momentum equations. The fluid density can be represented by a reference density ρ_0 and the relative deviation from the reference state ρ_* as

$$\rho = \rho_0(1 + \rho_*). \tag{2.8}$$

Based on the fact that the density variations are very small compared to the reference density, *i.e.*, $\rho_* \ll 1$, in all the cases that have been studied in the present work, we can use the Boussinesq approximation to simplify the governing equations. The density ρ may be replaced by the reference density ρ_0 in all the terms except the buoyancy term in the momentum equation, and the values of μ and k are taken as constants. The relative density ρ_* can be further decomposed into a background relative density ρ_b and a perturbation relative density ρ' as

$$\rho_* = \rho_b(x_2) + \rho'. \tag{2.9}$$

The momentum equation (2.2) can be further simplified if we eliminate the effects of the background stratification and the centrifugal force by defining a dynamic pressure p as proposed by Zang (1993)

$$p = P/\rho_0 + g\left[x_2 + \int_0^{x_2} \rho_b(x_2')d(x_2')\right] - \frac{1}{2}\Omega^2(x_1^2 + x_3^2), \tag{2.10}$$

where P is the total pressure.

If the working fluid is salt-stratified, the resulting simplified governing equations are

$$\frac{\partial u_j}{\partial x_j} = 0 \tag{2.11}$$

$$\frac{\partial u_i}{\partial t} + \frac{\partial F_{ij}}{\partial x_j} = S_i \tag{2.12}$$

$$\frac{\partial \rho_*}{\partial t} + \frac{\partial R_j}{\partial x_j} = 0, \tag{2.13}$$

where

$$F_{ij} = u_i u_j + p\delta_{ij} - \nu\frac{\partial u_i}{\partial x_j} \tag{2.14}$$

$$S_i = -g(\rho_* - \rho_b)\delta_{i2} + 2\Omega(-u_3\delta_{i1} + u_1\delta_{i3}) \tag{2.15}$$

$$R_j = u_j\rho_* - \kappa\frac{\partial \rho_*}{\partial x_j} \tag{2.16}$$

and $\nu = \mu/\rho_0$ is the kinematic viscosity and κ equals to k/ρ_0. The ratio ν/κ is the Schmidt number Sc, which is equal to 722 in this work.

If the working fluid is thermally stratified, the scalar for which we are solving is the temperature T. The equation of the state, Eqn. (2.7), which relates the temperature to the density, can be linearized with respect to the reference state as

$$\rho_* = \frac{\rho - \rho_0}{\rho_0} = \frac{1}{\rho_0}\frac{\partial \rho}{\partial T}(T - T_0) = \beta(T - T_0), \tag{2.17}$$

where T_0 is a reference temperature and β is the thermal expansion coefficient.

The simplified governing equations are

$$\frac{\partial u_j}{\partial x_j} = 0 \tag{2.18}$$

$$\frac{\partial u_i}{\partial t} + \frac{\partial F_{ij}}{\partial x_j} = S_i \tag{2.19}$$

$$\frac{\partial T}{\partial t} + \frac{\partial R_j}{\partial x_j} = 0, \tag{2.20}$$

where

$$F_{ij} = u_i u_j + p\delta_{ij} - \nu \frac{\partial u_i}{\partial x_j} \tag{2.21}$$

$$S_i = -g\beta(T - T_0)\delta_{i2} + 2\Omega(-u_3\delta_{i1} + u_1\delta_{i3}) \tag{2.22}$$

$$R_j = u_j T - \kappa \frac{\partial T}{\partial x_j} \tag{2.23}$$

and $\nu = \mu/\rho_0$ is the kinematic viscosity and κ equals to k/ρ_0. The ratio ν/κ is the Prandtl number Pr, which is equal to 7 in this work where water is the working fluid.

Two sets of governing equations, *i.e.*, the governing equations for the salt-stratified fluid and for the thermally stratified fluid, have been used in this study. In the text after this, only the set of the governing equations for salt-stratified fluid will be presented to avoid any redundancy.

2.4 Filtered Governing Equations

In large-eddy simulation (LES), each flow variable f is decomposed into a large-scale (or resolved) component $\overline{f}$ and a subgrid-scale (or unresolved) component f'

$$f = \overline{f} + f'. \tag{2.24}$$

A filtered quantity $\overline{f}$ is defined as:

$$\overline{f}(x_1, x_2, x_3) = \int_D \prod_{i=1}^{3} G_i(x_i, x_i') f(x_1', x_2', x_3') dx_1' dx_2' dx_3', \tag{2.25}$$

where G_i is the filter function and D is the entire domain. In the present work, a box filter is used for the finite volume method as proposed by Zang (1993), in which $G_i = 1$ and D spans a region equal to the local size of the grid. The governing equations for the LES are space-filtered by applying the filtering operation, Eqn. (2.25), to the instantaneous equations of motion, *i.e.*, Eqns. (2.1) to (2.3). The resulting filtered equations are:

$$\frac{\partial \overline{u}_j}{\partial x_j} = 0 \tag{2.26}$$

$$\frac{\partial \overline{u}_i}{\partial t} + \frac{\partial \overline{F}_{ij}}{\partial x_j} = \overline{S}_i \tag{2.27}$$

$$\frac{\partial \overline{\rho}_*}{\partial t} + \frac{\partial \overline{R}_j}{\partial x_j} = 0, \tag{2.28}$$

where

$$\overline{F}_{ij} = \overline{u}_i \overline{u}_j + \overline{p}\delta_{ij} - \nu \frac{\partial \overline{u}_i}{\partial \overline{x}_j} + \tau_{ij} \tag{2.29}$$

$$\overline{S}_i = -g(\overline{\rho}_* - \rho_b)\delta_{i2} + 2\Omega(-\overline{u}_3\delta_{i1} + \overline{u}_1\delta_{i3}) \tag{2.30}$$

$$\overline{R}_j = \overline{u}_j \overline{\rho}_* - \kappa \frac{\partial \overline{\rho}_*}{\partial x_j} + \chi_j. \tag{2.31}$$

The filtered equations govern the evolution of the large, energy-carrying, scales of motions. Two extra terms which represent the effect of the unresolved, or subgrid-scale, on the resolved part of turbulence also appear in the above equations. The two terms are the subgrid-scale (SGS) stress tensor τ_{ij} and the subgrid-scale flux vector χ_j, which are defined as

$$\tau_{ij} = \overline{u_i u_j} - \overline{u}_i \overline{u}_j \tag{2.32}$$

$$\chi_j = \overline{u_j \rho_*} - \overline{u}_j \overline{\rho}_*. \tag{2.33}$$

The large-scale momentum and scalar transport equations are closed by modeling τ_{ij} and χ_j using the filtered quantities. Discussion of different SGS models and comparison of results obtained by using different SGS models will be presented in Chapter 3. In the present study, the models for τ_{ij} and χ_j take the following form (Zang *et al.* 1993, and Salvetti and Banerjee 1995):

$$\tau_{ij} - \frac{1}{3}\delta_{ij}\tau_{kk} = -2\nu_T \overline{S}_{ij} + C_M \left(L^m_{ij} - \frac{\delta_{ij}}{3} L^m_{kk} \right) \tag{2.34}$$

$$\chi_j = -\kappa_T \frac{\partial \overline{\rho}_*}{\partial x_i} + C_S P_j, \tag{2.35}$$

where ν_T and κ_T are called the "eddy viscosity" and the "eddy diffusivity", respectively, and $\overline{S}_{ij}$ is the resolved strain rate tensor

$$\overline{S}_{ij} = \frac{1}{2} \left(\frac{\partial \overline{u}_i}{\partial x_j} + \frac{\partial \overline{u}_j}{\partial x_i} \right). \tag{2.36}$$

L^m_{ij}, the "modified Leonard term" (Germano 1986), and P_j are defined as

$$L^m_{ij} = \overline{\overline{u}_i \overline{u}_j} - \overline{\overline{u}}_i \overline{\overline{u}}_j \tag{2.37}$$

$$P_j = \overline{\overline{u}_j \overline{\rho}_*} - \overline{\overline{u}}_j \overline{\overline{\rho}}_*. \tag{2.38}$$

Rewriting τ_{ij} as

$$\tau_{ij} - \frac{1}{3}\delta_{ij}\tau_{kk} = -\nu_T \frac{\partial \overline{u}_i}{\partial x_j} - \nu_T \frac{\partial \overline{u}_j}{\partial x_i} + C_M \left(L^m_{ij} - \frac{\delta_{ij}}{3} L^m_{kk} \right), \tag{2.39}$$

then substituting Eqns. (2.35) and (2.39) into Eqns. (2.27)-(2.28) and finally rearranging the equations yield

$$\frac{\partial \overline{u}_j}{\partial x_j} = 0 \tag{2.40}$$

$$\frac{\partial \overline{u}_i}{\partial t} + \frac{\partial \overline{F}_{ij}}{\partial x_j} = \overline{S}_i \tag{2.41}$$

$$\frac{\partial \overline{\rho}_*}{\partial t} + \frac{\partial \overline{R}_j}{\partial x_j} = \overline{S}_S, \tag{2.42}$$

where

$$\overline{F}_{ij} = \overline{u}_i\overline{u}_j + \overline{p}\delta_{ij} - (\nu + \nu_T)\frac{\partial \overline{u}_i}{\partial x_j} \tag{2.43}$$

$$\begin{aligned}\overline{S}_i &= -g(\overline{\rho}_* - \rho_b)\delta_{i2} + 2\Omega(-\overline{u}_3\delta_{i1} + \overline{u}_1\delta_{i3}) \\ &+ \frac{\partial \nu_T}{\partial x_j}\frac{\partial \overline{u}_j}{\partial x_i} - C_M\frac{\partial L_{ij}^m}{\partial x_j} - L_{ij}^m\frac{\partial C_M}{\partial x_j}\end{aligned} \tag{2.44}$$

$$\overline{R}_j = \overline{u}_j\overline{\rho}_* - (\kappa + \kappa_T)\frac{\partial \overline{\rho}_*}{\partial x_j} \tag{2.45}$$

$$\overline{S}_S = -C_S\frac{\partial P_j}{\partial x_j} - P_j\frac{\partial C_S}{\partial x_j}. \tag{2.46}$$

Note that the isotropic parts involving τ_{kk} and L_{kk} have been lumped into the pressure term.

2.5 Governing Equations in Curvilinear Coordinates

In order to deal with complex flows associated with irregular boundaries, the governing equations are transformed into the governing equations in boundary-fitted curvilinear coordinates by performing coordinate transformation. In the present study, only independent variables (x_1, x_2, x_3) are transformed to reduce the extent of the complexity. By applying the chain rule of derivatives

$$\frac{\partial}{\partial x_j} = \frac{\partial \xi_m}{\partial x_j}\frac{\partial}{\partial \xi_m}, \tag{2.47}$$

the governing equations in the physical space (x_1, x_2, x_3) are transformed to the corresponding computational space (ξ_1, ξ_2, ξ_3) as

$$\frac{\partial \xi_m}{\partial x_j}\frac{\partial \overline{u}_j}{\partial \xi_m} = 0 \tag{2.48}$$

$$\frac{\partial \overline{u}_i}{\partial t} + \frac{\partial \xi_m}{\partial x_j}\frac{\partial \overline{F}_{ij}}{\partial \xi_m} = \overline{S}_i \tag{2.49}$$

$$\frac{\partial \overline{\rho}_*}{\partial t} + \frac{\partial \xi_m}{\partial x_j}\frac{\partial \overline{R}_j}{\partial \xi_m} = \overline{S}_S, \tag{2.50}$$

where

$$\overline{F}_{ij} = \overline{u}_i\overline{u}_j + \overline{p}\delta_{ij} - (\nu + \nu_T)\frac{\partial \xi_m}{\partial x_j}\frac{\partial \overline{u}_i}{\partial \xi_m} \tag{2.51}$$

$$\begin{aligned}\overline{S}_i &= -g(\overline{\rho}_* - \rho_b)\delta_{i2} + 2\Omega(-\overline{u}_3\delta_{i1} + \overline{u}_1\delta_{i3}) \\ &+ \frac{\partial \xi_m}{\partial x_j}\frac{\partial \nu_T}{\partial \xi_m}\frac{\partial \xi_n}{\partial x_i}\frac{\partial \overline{u}_j}{\partial \xi_n} - C_M\frac{\partial \xi_m}{\partial x_j}\frac{\partial L^m_{ij}}{\partial \xi_m} - L^m_{ij}\frac{\partial \xi_m}{\partial x_j}\frac{\partial C_M}{\partial \xi_m}\end{aligned} \tag{2.52}$$

$$\overline{R}_j = \overline{\rho}_*\overline{u}_j - (\kappa + \kappa_T)\frac{\partial \xi_m}{\partial x_j}\frac{\partial \overline{\rho}_*}{\partial \xi_m} \tag{2.53}$$

$$\overline{S}_S = -C_S\frac{\partial \xi_m}{\partial x_j}\frac{\partial P_j}{\partial \xi_m} - P_j\frac{\partial \xi_m}{\partial x_j}\frac{\partial C_S}{\partial \xi_m}. \tag{2.54}$$

Multiplying the above equations by the inverse of the Jacobian defined as

$$J^{-1} = \det\left(\frac{\partial x_i}{\partial \xi_m}\right), \tag{2.55}$$

and utilizing the metric identity

$$\frac{\partial}{\partial \xi_m}\left(J^{-1}\frac{\partial \xi_m}{\partial x_i}\right) \equiv 0, \tag{2.56}$$

we obtain the final set of governing equations in the "Strong-Conservation-Law Form" (Hindman 1982),

$$\frac{\partial \overline{U}_m}{\partial \xi_m} = 0 \tag{2.57}$$

$$\frac{\partial J^{-1}\overline{u}_i}{\partial t} + \frac{\partial \overline{F}_{im}}{\partial \xi_m} = \overline{S}_i \tag{2.58}$$

$$\frac{\partial J^{-1}\overline{\rho}_*}{\partial t} + \frac{\partial \overline{R}_m}{\partial \xi_m} = \overline{S}_S, \tag{2.59}$$

where

$$\overline{F}_{im} = \overline{U}_m \overline{u}_i + J^{-1}\frac{\partial \xi_m}{\partial x_i}\overline{p} - (\nu + \nu_T)G_{mn}\frac{\partial \overline{u}_i}{\partial \xi_n} \tag{2.60}$$

$$\begin{aligned}\overline{S}_i &= -J^{-1}g(\overline{\rho}_* - \rho_b)\delta_{i2} + 2J^{-1}\Omega(-\overline{u}_3\delta_{i1} + \overline{u}_1\delta_{i3}) \\ &+ J^{-1}\frac{\partial \xi_m}{\partial x_j}\frac{\partial \xi_n}{\partial x_i}\frac{\partial \nu_T}{\partial \xi_m}\frac{\partial \overline{u}_j}{\partial \xi_n} \\ &- C_M\frac{\partial}{\partial \xi_m}\left(J^{-1}\frac{\partial \xi_m}{\partial x_j}L^m_{ij}\right) - L^m_{ij}\frac{\partial}{\partial \xi_m}\left(J^{-1}\frac{\partial \xi_m}{\partial x_j}C_M\right)\end{aligned} \tag{2.61}$$

$$\overline{R}_m = \overline{U}_m\overline{\rho}_* - (\kappa + \kappa_T)G_{mn}\frac{\partial \overline{\rho}_*}{\partial \xi_n} \tag{2.62}$$

$$\overline{S}_S = -C_S\frac{\partial}{\partial \xi_m}\left(J^{-1}\frac{\partial \xi_m}{\partial x_j}P_j\right) - P_j\frac{\partial}{\partial \xi_m}\left(J^{-1}\frac{\partial \xi_m}{\partial x_j}C_S\right). \tag{2.63}$$

The relevant curvilinear quantities are defined as:

$$\text{resolved volume flux : } \overline{U}_m = J^{-1}\frac{\partial \xi_m}{\partial x_j}\overline{u}_j \tag{2.64}$$

$$\text{mesh skewness tensor : } G_{mn} = J^{-1}\frac{\partial \xi_m}{\partial x_j}\frac{\partial \xi_n}{\partial x_j}. \tag{2.65}$$

2.6 Numerical Scheme

2.6.1 Discretization

Following Zang (1993), a finite volume method is used to discretize the governing equations in general curvilinear coordinates on a single non-staggered grid. The pressure and the Cartesian velocities are defined at the control volume centers and the volume fluxes are defined at the mid-point of their corresponding faces of the control volume in the computational space. The viscous term $\partial\left[(\nu + \nu_T)G_{mn}\partial\overline{u}_i/\partial\xi_n\right]/\partial\xi_m$

and the diffusive term $\partial\left[(\kappa+\kappa_T)G_{mn}\partial\overline{\rho}_*/\partial\xi_n\right]/\partial\xi_m$ are split into diagonal (when $m=n$) parts and off-diagonal (when $m\neq n$) parts. The governing equations (2.57) to (2.59) can be re-written schematically as:

$$\frac{\partial\overline{U}_m}{\partial\xi_m} = 0 \tag{2.66}$$

$$\frac{\partial J^{-1}\overline{u}_i}{\partial t} = C_i + B_i(\overline{p}) + D_I(\overline{u}_i) + D_E(\overline{u}_i) + S_i \tag{2.67}$$

$$\frac{\partial J^{-1}\overline{\rho}_*}{\partial t} = E_S + F_I(\overline{\rho}_*) + F_E(\overline{\rho}_*) + S_S, \tag{2.68}$$

where C_i and E_S represent the convective terms for the momentum and scalar transport equations, respectively; $B_i(\overline{p})$ represents the pressure gradient terms; and $D_I(\overline{u}_i)$ and $D_E(\overline{u}_i)$ ($F_I(\overline{\rho}^*)$ and $F_E(\overline{\rho}^*)$) represent, respectively, the diagonal and off-diagonal viscous (diffusive) terms. These terms are:

$$C_i = -\frac{\partial\overline{U}_m\overline{u}_i}{\partial\xi_m} \tag{2.69}$$

$$B_i(\overline{p}) = -J^{-1}\frac{\partial\xi_m}{\partial x_i}\frac{\partial\overline{p}}{\partial\xi_m} \tag{2.70}$$

$$D_I(\overline{u}_i) = \frac{\partial}{\partial\xi_m}\left[(\nu+\nu_T)G_{mn}\frac{\partial\overline{u}_i}{\partial\xi_n}\right] \quad \text{for} \quad m=n \tag{2.71}$$

$$D_E(\overline{u}_i) = \frac{\partial}{\partial\xi_m}\left[(\nu+\nu_T)G_{mn}\frac{\partial\overline{u}_i}{\partial\xi_n}\right] \quad \text{for} \quad m\neq n \tag{2.72}$$

$$\begin{aligned} S_i &= -J^{-1}g(\overline{\rho}_*-\rho_b)\delta_{i2} + 2J^{-1}\Omega(-\overline{u}_3\delta_{i1}+\overline{u}_1\delta_{i3}) \\ &+ J^{-1}\frac{\partial\xi_m}{\partial x_j}\frac{\partial\xi_n}{\partial x_i}\frac{\partial\nu_T}{\partial\xi_m}\frac{\partial\overline{u}_j}{\partial\xi_n} \\ &- C_M\frac{\partial}{\partial\xi_m}\left(J^{-1}\frac{\partial\xi_m}{\partial x_j}L^m_{ij}\right) - L^m_{ij}\frac{\partial}{\partial\xi_m}\left(J^{-1}\frac{\partial\xi_m}{\partial x_j}C_M\right) \end{aligned} \tag{2.73}$$

$$E_S = -\frac{\partial\overline{U}_m\overline{\rho}_*}{\partial\xi_m} \tag{2.74}$$

$$F_I(\overline{\rho}_*) = \frac{\partial}{\partial\xi_m}\left[(\kappa+\kappa_T)G_{mn}\frac{\partial\overline{\rho}_*}{\partial\xi_n}\right] \quad \text{for} \quad m=n \tag{2.75}$$

$$F_E(\overline{\rho}_*) = \frac{\partial}{\partial\xi_m}\left[(\kappa+\kappa_T)G_{mn}\frac{\partial\overline{\rho}_*}{\partial\xi_n}\right] \quad \text{for} \quad m\neq n \tag{2.76}$$

$$\overline{S}_S = -C_S \frac{\partial}{\partial \xi_m}\left(J^{-1}\frac{\partial \xi_m}{\partial x_j}P_j\right) - P_j\frac{\partial}{\partial \xi_m}\left(J^{-1}\frac{\partial \xi_m}{\partial x_j}C_S\right). \qquad (2.77)$$

Following Kim and Moin (1985), a semi-implicit time-advancement scheme, with the second-order implicit Crank-Nicolson scheme for the diagonal viscous term $D_I(\overline{u}_i)$ and diffusive term $F_I(\overline{\rho}_*)$ and the second-order Adams-Bashforth method for all the other terms, has been used. The diagonal viscous and diffusive terms are treated implicitly in order to remove the viscous stability limit. The off-diagonal viscous and diffusive terms usually have less significant contributions, unless the grid is severely skewed. They are treated explicitly here in order to yield easily-inverted left-hand-side matrices of the momentum and scalar transport equations. In the present study, highly skewed grids are avoided in order to preserve the accuracy of the numerical method. Equations (2.66) to (2.68) are discretized in time as the following:

$$\frac{\partial \overline{U}_m^{n+1}}{\partial \xi_m} = 0 \qquad (2.78)$$

$$\begin{aligned}\frac{J^{-1}}{\Delta t}(\overline{u}_i^{n+1} - \overline{u}_i^n) &= \frac{3}{2}\left[C_i^n + D_E(\overline{u}_i^n) + S_i^n\right] \\ &- \frac{1}{2}\left[C_i^{n-1} + D_E(\overline{u}_i^{n-1}) + S_i^{n-1}\right] \\ &+ \frac{1}{2}\left[D_I(\overline{u}_i^{n+1}) + D_I(\overline{u}_i^n)\right] + B_i(\overline{p}^{n+1}) \qquad (2.79)\end{aligned}$$

$$\begin{aligned}\frac{J^{-1}}{\Delta t}(\overline{\rho}_*^{n+1} - \overline{\rho}_*^n) &= \frac{3}{2}\left[E_S^n + F_E(\overline{u}_i^n) + S_S^n\right] \qquad (2.80) \\ &- \frac{1}{2}\left[E_S^{n-1} + F_E(\overline{u}_i^{n-1}) + S_S^{n-1}\right] \\ &+ \frac{1}{2}\left[F_I(\overline{\rho}_*^{n+1}) + F_I(\overline{\rho}_*^n)\right], \qquad (2.81)\end{aligned}$$

where superscript n represents the time step.

All the spatial derivatives are approximated with second-order central differences with the exception of the convective terms, which are handled with special upwind-difference schemes. The convective terms in the momentum equation are discretized

using a variation of QUICK (Quadratic Upstream Interpolation for Convective Kinematics) (Leonard 1979, Perng and Street 1989). The convective term in the scalar transport equation is discretized using SHARP (Simple High Accuracy Resolution Program) (Leonard 1988). The preference of SHARP to QUICK is because QUICK may produce spurious oscillations in regions where the dependent variables change very rapidly (Perng 1990). However, SHARP is only used in solving the scalar field since it is more expensive than QUICK.

2.6.2 Solution Procedure

A two-step time-advancement method developed by Kim and Moin (1985) based on the fractional-step method used by Chorin (1967) is employed for time-advancement of the governing equations in the present study. The two-step time-advancement method for Eqns. (2.78) and (2.79) can be written as the predictor and the corrector steps as the following:

$$\begin{aligned}\frac{J^{-1}}{\Delta t}(\overline{u}_i^* - \overline{u}_i^n) &= \frac{3}{2}[C_i^n + D_E(\overline{u}_i^n) + S_i^n] \\ &- \frac{1}{2}\left[C_i^{n-1} + D_E(\overline{u}_i^{n-1}) + S_i^{n-1}\right] \\ &+ \frac{1}{2}D_I(\overline{u}_i^*) + \frac{1}{2}D_I(\overline{u}_i^n) \qquad (2.82)\\ \frac{J^{-1}}{\Delta t}(\overline{u}_i^{n+1} - \overline{u}_i^*) &= -J^{-1}\frac{\partial \xi_m}{\partial x_i}\frac{\partial \phi^{n+1}}{\partial \xi_m} = B_i(\phi^{n+1}) \qquad (2.83)\end{aligned}$$

with

$$\frac{\partial \overline{U}_m^{n+1}}{\partial \xi_m} = 0, \qquad (2.84)$$

where ϕ is a scalar to be determined and it is related to pressure $\overline{p}$ by

$$B_i(\overline{p}) = B_i(\phi) - \frac{\Delta t}{2}D_I\left[\frac{1}{J^{-1}}B_i(\phi)\right]. \qquad (2.85)$$

Multiplying Eqn. (2.83) by $\partial\xi_m/\partial x_i$ yields

$$\frac{1}{\Delta t}(\overline{U}_m^{n+1} - \overline{U}_m^*) = -G_{mn}\frac{\partial\phi^{n+1}}{\partial\xi_n} \tag{2.86}$$

and taking $\partial/\partial\xi_m$ on the above equation yields the Poisson equation for ϕ^{n+1}

$$\frac{\partial}{\partial\xi_m}\left(G_{mn}\frac{\partial\phi^{n+1}}{\partial\xi_n}\right) = \frac{1}{\Delta t}\frac{\partial\overline{U}_m^*}{\partial\xi_m}, \tag{2.87}$$

where $\overline{U}_m^* = J^{-1}(\partial\xi_m/\partial x_j)u_j^*$ is called the "intermediate volume flux".

The solution procedures are as the following. First, an intermediate velocity field (u_i^*) is obtained by solving Eqn. (2.82) using the approximate factorization technique of Beam and Warming (1976). The approximate factorization scheme only requires inversions of tridiagonal matrices rather than inversion of a large sparse matrix. This results in a significant reduction in computing time and memory. Then, the Poisson equation [Eqn. (2.87)] is solved by a V-cycle multi-grid method (Brandt 1975, 1981) with the *alternating direction implicit* or ADI method (Hageman and Young 1981) as the smoother. The velocity field at the next time step is obtained by solving Eqn. (2.83) using the information of the intermediate velocity field u_i^* and the scalar field ϕ. Finally, the scalar transport equation [Eqn. (2.83)] is solved by the same approximate factorization technique as the predictor equation [Eqn. (2.82)]. Initial and boundary conditions are required to complete the solution procedure. The typical conditions are described as part of the set-up description for each application in their respective chapters. Two special conditions are noted here. First, a pressure boundary condition is required for a non-orthogonal coordinate system. Second, a pressure correction must be made at boundaries by employing Eqn. (2.86) when one is computing the intermediate velocity u_i^*. In Eqn. (2.86), $\overline{U}_m^{n+1}$ is the imposed boundary volume flux and the intermediate volume flux $\overline{U}_m^*$ is computed from u_i^*. A detailed discussion of the pressure boundary condition can be found in Zang (1993).

Since the viscous stability limit is removed by advancing the diagonal viscous terms implicitly, the time step Δt is then determined by the Courant-Friedrichs-Lewy (CFL) number

$$\text{CFL} = \left(\frac{|u_1|}{\Delta x} + \frac{|u_2|}{\Delta y} + \frac{|u_3|}{\Delta z}\right)\Delta t = \frac{\Delta t}{J^{-1}}(|U_1| + |U_2| + |U_3|), \tag{2.88}$$

where $\Delta x, \Delta y, \Delta z$ are the grid spacings in the three Cartesian coordinates in the physical domain. The stability condition of the present method requires the maximum value of the CFL number obtained from Eqn. (2.88) over the entire computational domain to be less than one.

2.7 Numerically-Induced Physics

In the course of this study, we encountered situations where certain flow phenomena were caused by numerical errors or the numerical scheme used rather than by the physics. We call such flow phenomena "numerically-induced physics". Two examples of the numerically-induced physics are given below:

Case I:

The scalar $\rho*$ transport equation in curvilinear coordinates can be written as

$$\frac{\partial J^{-1}\rho_*}{\partial t} + \frac{\partial U_m \rho_*}{\partial \xi_m} = \kappa \frac{\partial}{\partial \xi_m}\left(G_{mn}\frac{\partial \rho_*}{\partial \xi_n}\right). \tag{2.89}$$

The convective term in the above equation can be split into two parts as

$$\frac{\partial U_m \rho_*}{\partial \xi_m} = \rho_* \frac{\partial U_m}{\partial \xi_m} + U_m \frac{\partial \rho_*}{\partial \xi_m}. \tag{2.90}$$

For an incompressible fluid, mass conservation $\partial U_m/\partial \xi_m = 0$ holds. For a stably-stratified two-layer system, such as the one described in Chapter 6 for the coastal upwelling flow, the density ρ_* remains uniform, *i.e.*, $\partial \rho_*/\partial \xi_m = 0$, in the lower layer of the fluid far away from the two layer interface. Therefore, Eqn. (2.89) can be

simplified to

$$\frac{\partial J^{-1}\rho_*}{\partial t} = 0, \tag{2.91}$$

which means that the density ρ_* does not change with time if it does not change in space. However, mass conservation can not be satisfied exactly since the pressure Poisson equation is not converged to machine accuracy in the actual simulation. In other words, mass conservation can only be satisfied to a certain degree, *e.g.*,

$$\partial U_m/\partial \xi_m = \epsilon, \tag{2.92}$$

where ϵ is a small number which depends on the convergence error for the pressure Poisson equation. Thus, Eqn. (2.89) can only be simplified to

$$\frac{\partial J^{-1}\rho_*}{\partial t} + \rho_* \frac{\partial U_m}{\partial \xi_m} = 0. \tag{2.93}$$

With $\partial U_m/\partial \xi_m$ acting as a source/sink term, the density ρ_* will change with time. The density may not change much during one time step, but it will change significantly after hundreds to thousands time steps. The density change will cause changes in the velocity field via the buoyancy term in the momentum equation. The observed flow phenomenon caused by the change in the density field with time is induced by numerical errors. A simple fix for the problem is to replace Eqn. (2.89) with the following equation

$$\frac{\partial J^{-1}\rho_*}{\partial t} + \frac{\partial U_m \rho_*}{\partial \xi_m} - \rho_* \frac{\partial U_m}{\partial \xi_m} = \kappa \frac{\partial}{\partial \xi_m}\left(G_{mn}\frac{\partial \rho_*}{\partial \xi_n}\right) \tag{2.94}$$

to enforce the mass conservation.

Case II:

The multigrid method has been demonstrated as one of the most efficient iterative schemes for solving elliptic problems, such as the pressure Poisson equation

encountered in this study. A four-color ZEBRA scheme proposed by Rosenfeld *et al.* (1991) was picked first to serve as the smoother on each level of the V-cycle grid of the multigrid method. The three-dimensional ZEBRA scheme is an iterative solution which solves implicitly all the equations along one coordinate line. However, the order in which the lines are processed is not the usual lexicographic order (by rows or columns), but a "colored" order, devised so that the implicit solution of a line is decoupled from the solution of the other lines that belong to the same order.

The ZEBRA scheme gives good parallelization and vectorization possibilities with no sacrifice in convergence properties. However, the ZEBRA scheme will produce two-delta[1] waves whose amplitude are comparable to the convergent error at each grid level. A periodicity in the ZEBRA scheme was reported by Brandt (1981). The two-delta waves at the coarse level of the V-cycle grid will become four-delta waves at the grid level that is one level finer during the coarse to fine inter-grid transfer process, which is also known as the prolongation process. At the end of the prolongation process, there are 2^n-delta waves existing on the finest level of the V-cycle grid, where n varies from 1 to the maximum number of levels used in the V-cycle grid. Those waves caused by the ZEBRA and the multigrid schemes co-exist with the waves resulting from the baroclinic instability. The numerically-generated waves with wave numbers close to the unstable wave numbers will grow in amplitude. Therefore, the waves observed in the flow field might be generated by the numerical schemes used instead being those waves associated with the most unstable wave mode. We observed that our simulations with four multigrid levels tended to produce waves containing 16 grid points without regard to the the fineness of the grid. Thus, precautions should be taken when the ZEBRA scheme is used as the smoother for the multigrid method in periodic and unstable flows. In this work, an ADI smoother has been used in lieu of the four-color ZEBRA scheme (See section 2.6.2).

[1]delta refers to the grid space at each corresponding grid level.

Chapter 3

Test of Different Subgrid-Scale Turbulence Models

3.1 Introduction

There are many different approaches in the numerical simulation of turbulent flows. The most straight forward approach is the direct numerical simulation (DNS) of turbulence. In DNS, the Navier-Stokes equations are solved without recourse to any turbulence model. A fine computational grid is required to resolve all the scales of the flow motions and higher-order numerical schemes are desirable to limit dispersion and dissipation errors. Therefore, DNS is limited to low Reynolds number and simple geometry turbulent flows.

If Reynolds time averaging is applied to the Navier-Stokes equations, one obtains the Reynolds-averaged Navier-Stokes (RANS) equations, which describe the evolution of the mean quantities. The Reynolds stress term appearing in the RANS equations must be modeled. There are a variety of models for the Reynolds stress and all of them have the same shortcoming, that is the model must represent a wide range of scales.

Large-eddy simulation (LES) is the approach between DNS and the solution of the RANS equations. In LES, the large scale motions are computed explicitly, and the effect of sub-grid scales is modeled by the use of large-scale quantities. Since the small scales are believed to be more isotropic and universal than large scales, and only carry a small fraction of the total turbulent energy, they can be modeled using

simpler parameterizations than those used for the Reynolds stress term in the RANS equations. In LES, the effect of the unresolved, small scales on the resolved, large scales of turbulence appears in the subgrid-scale (SGS) stress. The key to the success of LES is to accurately represent this term. A review of the present state of the LES technique can be found in Piomelli (1999).

In this chapter, three different dynamic SGS models, *i.e.,* the dynamic subgrid-scale eddy-viscosity model of Germano *et al.* (1991), the dynamic mixed subgrid-scale model of Zang *et al.* (1993) and the dynamic two-parameter model of Salvetti and Banerjee (1995), are briefly described. The models are then applied to three-dimensional isothermal lid-driven cavity flows. The LES results are compared to previous experimental results of Prasad and Koseff (1989) to test the different SGS models and to validate the code.

3.2 Subgrid-Scale Turbulence Models

In Chapter 2, the filtered equations [Eqns. (2.26) to (2.28)] for LES are obtained by applying the space filtering operation to the governing equations [Eqns. (2.11) to (2.13)]. Two extra terms, which are the subgrid-scale (SGS) stress τ_{ij}

$$\tau_{ij} = \overline{u_i u_j} - \overline{u}_i \overline{u}_j \tag{3.1}$$

and the subgrid-scale flux vector χ_j

$$\chi_j = \overline{u_j \rho_*} - \overline{u}_j \overline{\rho}_* \tag{3.2}$$

are introduced. The SGS stress τ_{ij} and the subgrid-scale scalar flux χ_j have to be modeled by the use of the resolved quantities.

The simplest and most widely used SGS model in LES is the eddy-viscosity model

proposed by Smagorinsky (1963), which assumes that the SGS stress τ_{ij} is proportional to the local strain rate tensor $\overline{S}_{ij}$, so that

$$\tau_{ij} - \frac{\delta_{ij}}{3}\tau_{ij} = -2C\overline{\Delta}^2|\overline{S}|\overline{S}_{ij} = -2\nu_T\overline{S}_{ij}, \tag{3.3}$$

where ν_T is the eddy viscosity, C is a dimensionless model coefficient, $\overline{\Delta}$ is the filter width, which is usually defined as

$$\overline{\Delta} = (\Delta x_1 \Delta x_2 \Delta x_3)^{1/3} \tag{3.4}$$

and $|\overline{S}| = (2\overline{S}_{ij}\overline{S}_{ij})^{1/2}$ is the magnitude of the resolved strain rate tensor

$$\overline{S}_{ij} = \frac{1}{2}\left(\frac{\partial \overline{u}_i}{\partial x_j} + \frac{\partial \overline{u}_j}{\partial x_i}\right). \tag{3.5}$$

The main advantage of eddy-viscosity models is that they are dissipative. The Smagorinsky model, however, has some notable drawbacks, which include the requirement of an input model coefficient C which is flow dependent, the incorrect prediction of asymptotic behavior near a wall or in a laminar flow, and the inability to account for energy backscatter from small scales to large scales.

Unlike the standard Smagorinsky model (Smagorinsky 1963), in which the model coefficient is a constant given *a priori*, the model coefficient(s) of the dynamic models are determined as the calculation proceeds, based on the energy content of the smallest resolved scales. In the dynamic SGS model (DSM) developed by Germano *et al.* (1991), the Smagorinsky model is employed as the base model, in which τ_{ij} is of the form

$$\tau_{ij} - \frac{\delta_{ij}}{3}\tau_{ij} = -2C\overline{\Delta}^2|\overline{S}|\overline{S}_{ij}. \tag{3.6}$$

The model coefficient C is now a function of time and space. Lilly (1992) proposed a least square technique, which allows the coefficient C to be computed locally. The

DSM exhibits correct asymptotic behavior near a wall and in a laminar flow and permits energy backscatter from small scales to large scales. However, the model still required that the principal axes of the SGS stress tensor to be aligned with the resolved strain rate tensor since the Smagorinsky model is employed as the base model.

Zang *et al.* (1993) modified the dynamic eddy-viscosity model by employing the mixed model of Bardina *et al.* (1983) as the base model, which is a linear combination of the scale similarity model and the Smagorinsky model. If the subgrid-scale velocity is defined as $u_i' = u_i - \overline{u}_i$, Germano (1986) suggested that the SGS stress can be decomposed into three parts:

$$\tau_{ij} = L_{ij}^m + C_{ij}^m + R_{ij}^m \tag{3.7}$$

where

$$L_{ij}^m = \overline{\overline{u}_i\overline{u}_j} - \overline{\overline{u}}_i\overline{\overline{u}}_j \tag{3.8}$$

$$C_{ij}^m = \overline{\overline{u}_i u_j' + u_i'\overline{u}_j} - \overline{\overline{u}}_i\overline{u_j'} - \overline{u_i'}\overline{\overline{u}}_j \tag{3.9}$$

$$R_{ij}^m = \overline{u_i'u_j'} - \overline{u_i'}\,\overline{u_j'}. \tag{3.10}$$

The three terms are referred to, respectively, the "modified Leonard term", the "modified cross term" and the "modified SGS Reynolds term". From Germano's decomposition of the SGS stress, the dynamic mixed model (DMM) of Zang *et al.* explicitly computes the modified Leonard term, and only models the modified cross-term and the modified SGS Reynolds stress by a Smagorinsky-type model; thus

$$\tau_{ij} - \frac{1}{3}\delta_{ij}\tau_{kk} = -2C\overline{\Delta}^2|\overline{S}|\overline{S}_{ij} + \left(L_{ij}^m - \frac{1}{3}\delta_{ij}L_{kk}^m\right). \tag{3.11}$$

The least square technique proposed by Lilly (1992) can be used to compute the coefficient C locally. The DMM retains the favorable features of the DSM, but it

does not require the SGS stress tensor to be aligned with the strain rate tensor. This model has been used by Zang *et al.* to study the lid-driven cavity flow (Zang *et al.* 1993) and coastal up-welling (Zang and Street 1995).

Salvetti and Banerjee (1995) improved upon the DMM by assuming the modified cross-term to be proportional to the modified Leonard term. The modified SGS Reynolds stress is still modeled by a Smagorinsky-type model. The proposed dynamic two-parameter model (DTM) of Salvetti and Banerjee is thus characterized by two dynamic coefficients as

$$\tau_{ij} - \frac{1}{3}\delta_{ij}\tau_{kk} = -2C\overline{\Delta}^2|\overline{S}|\overline{S}_{ij} + C_M\left(L^m_{ij} - \frac{1}{3}\delta_{ij}L^m_{kk}\right). \tag{3.12}$$

They showed that dynamic coefficients (C and C_M) can be computed for each element of the model, *i.e.*, not only the coefficient C for the Smagorinsky term, but also the coefficient C_M for the modified Leonard term. The DTM retains all the positive features of the DMM, but it improves the modeling of the terms in the SGS stress tensor arising from the overlap between resolved and unresolved scales. This model was used in the code of Zang (1993) to study free surface flow (Salvetti *et al.* 1997).

Fluctuations of the dynamically computed model coefficient occur in all the three models. Numerical instability caused by too large negative values of the model coefficient has been reported by Cabot (1991) and Zang (1993). In many cases, the model coefficient values can be averaged over a homogeneous plane in the flow (Germano *et al.* 1991 and Moin *et al.* 1991). However, since there is usually no homogeneous direction for the wall-bounded flows in complex geometries, the model coefficient has to be averaged locally in space. However, at times the use of local averaging alone cannot prevent numerical instability. The cut-off criteria $\nu_T = \max(\nu_T, -\nu)$ and $\kappa_T = \max(\kappa_T, -\kappa)$ proposed by Zang *et al.* (1993) have been used in the present study.

3.3 Application to Lid-Driven Cavity Flow

In this section, large-eddy simulations are carried out using three different dynamic SGS models, *i.e.*, DSM, DMM and DTM, in isothermal three-dimensional lid driven cavity flows for different Reynolds numbers. Simulation results are compared to the data obtained from previous experiments by Prasad and Koseff (1989) to test the different SGS models and to validate the code.

Figure 3.1 is a schematic representation of the lid-driven cavity, in which the nomenclature for the lid-driven cavity flow is given. For our example, the cavity depth D and the cavity stream-wise width B are both 150mm, while the cavity length L is varied from 75mm to 150mm. The initial condition is that the entire system is at rest. A no-slip boundary condition is applied to all the solid walls. The experimental study of Koseff and Street (1984) found that at Reynolds numbers lower than 5000, the flow is essentially laminar although inherent unsteadiness may occur. At Reynolds numbers higher than about 6000, the flow becomes unstable near the downstream eddy. Flow becomes increasingly turbulent near walls as the Reynolds number further increases. The flow becomes fully turbulent at Reynolds number higher than 10,000. Two different Reynolds numbers, Re=3200 and 10,000, are examined here. The Reynolds number Re is based on the lid velocity (U_B) and the cavity width (B). A computational grid, which is non-uniform in the stream-wise (x) and vertical (y) directions and is uniformly distributed in span-wise (z) direction, is used to simulate the whole cubic cavity. The parameters and the grid resolutions for the simulations are summarized in Table 3.1. The grid resolutions in Table 3.1 are chosen to ensure that there are at least five grid points inside each boundary layer for each simulation. The number of grid points for each case shown in Table 3.1 is for interior points. Two fictitious points outside the physical domain are added in each dimension in the simulations to facilitate implementing boundary conditions.

Simulation results of instantaneous streamlines at Re=3200 (Fig. 3.2), taken at

the symmetry plane, at 10, 30, 60 and 90 seconds after the start-up, have been compared to experimental flow visualization (Fig. 3.3) of Prasad (1989). Qualitatively, good agreement was found between the computation results and experimental flow visualizations.

At 90 seconds after the start-up, the vertical motion has already reached the lower boundary of the cavity, and the flow has begun to enter the fully-developed state. Previous experiments by Koseff and Street (1984) have shown that three-dimensional cavity flow at high Reynolds number (above 3000) is characterized by a number of inherently unstable flow phenomena, such as the Taylor-Görtler-Like (TGL) vortices, which prevent the flow from ever reaching a truly steady state. Therefore, "fully-developed" here means the mean flow characteristics have become unchanging with time.

In Figure 3.4, the instantaneous streamlines at Re=3200 at a plane, which is parallel to and 0.25B away from the downstream side wall, show the existence of two pairs of TGL vortices in the cavity flow. The computed span-wise wavelength of the TGL vortices is $0.33B$ (B=150mm), which matches the preferred wavelength of 50mm suggested by Prasad (1989) for the given flow conditions.

The time-averaged quantities at the centerlines at the symmetry plane, *i.e.*, the mean velocities ($< u > /U_B$ and $< v > /U_B$), the root-mean-square (r.m.s.) velocities ($\sqrt{< u''^2 >}/U_B$ and $\sqrt{< v''^2 >}/U_B$) and the Reynolds stress ($< u''v'' > /U_B^2$), have been compared quantitatively with those obtained from the LDA measurements by Prasad and Koseff (1989) at two different Reynolds numbers (Re=3200 and 10,000). Time averaging is denoted by <> and u_i'' equals $u_i - < u_i >$. In the figures presented below, the computed r.m.s. velocities and the Reynolds stress are multiplied by a factor of 10 and 500, respectively. The experimental data were 5-minute averages at the fully-developed state, while the computed statistics were 4.5-minute averages from 9 to 13.5 minutes after the start-up.

Figures 3.5 to 3.7 display the mean velocity profiles ($< u > /U_B$ and $< v > /U_B$),

the root-mean-square (r.m.s.) velocity profiles ($\sqrt{< u''^2 >}/U_B$ and $\sqrt{< v''^2 >}/U_B$) and the Reynolds stress profiles ($< u''v'' > /U_B^2$) at the centerlines at the symmetry plane at Re=3200. In Figure 3.5, the mean u- and v-velocity profiles from LES agree well with those obtained from the experiments of Prasad and Koseff (1989). Figure 3.6 shows that all three models accurately predict the magnitude of the peaks of the r.m.s. velocities near the walls, except that the DSM over-predicts the r.m.s. velocity near the downstream wall. The computation also captures the two bumps near the upstream and the bottom walls in the experimental profiles with remarkable accuracy. The values of Reynolds stress computed respectively by the DSM, DMM and DTM compare reasonably well with the values obtained from the experiment (Prasad and Koseff 1989), with the exception that both the DMM and DTM slightly over-predict the magnitude of the negative Reynolds stress near the upstream wall and the DSM over-predicts the magnitude of the Reynolds stress near the downstream wall (Figure 3.7).

The same profiles as those shown in Figures 3.5 to 3.7 but at a higher Reynolds number (Re=10,000) are shown in Figures 3.8 to 3.10. Figure 3.8 shows that the mean velocity profiles predicted by DSM, DMM and DTM are close to each other. All the mean u-velocity profiles agree well with the experimental data, while all the mean v-velocity profiles slightly over-predict the maximum velocity near the upstream and downstream walls. The r.m.s. velocity profiles and the Reynolds stress profiles, shown in Figures 3.9 to 3.10, also agree with the experimental data except that the r.m.s. velocities are under-predicted inside the boundary layers of the top and downstream walls. Both DMM and DTM are found to give more accurate prediction along the vertical centerline than DSM.

3.4 Conclusion

The predictions of three dynamic SGS models, *i.e.,* DSM, DMM and DTM have been compared with experimental data of Prasad and Koseff (1989) in a three-dimensional isothermal lid-driven cavity flow at low (Re=3200) and moderately high (Re=10,000) Reynolds numbers. Both DMM and DTM results are found to show better agreement with experimental data than that of DSM. However, the CPU time required by different models is increased by model complexity. For the lid-driven cavity flow that we studied, the CPU time ratio for the three different models is $\mathrm{CPU_{DSM}} : \mathrm{CPU_{DMM}} : \mathrm{CPU_{DTM}} = 1.0 : 1.5 : 1.8$. DMM will be used in the cases studied in later chapters since DMM gives better results than DSM and essentially equivalent accuracy to DTM, yet it requires less CPU time than DTM.

Table 3.1: Grid resolutions and parameters of lid-driven cavity flow simulations

Case	SGS Model	Re $U_B B/\nu$	B:D:L	Grid $N_x \times N_y \times N_z$
Run1	DSM	3200	1:1:1	64 × 64 × 64
Run2	DMM	3200	1:1:1	64 × 64 × 64
Run3	DTM	3200	1:1:1	64 × 64 × 64
Run4	DSM	10,000	1:1:0.5	64 × 64 × 48
Run5	DMM	10,000	1:1:0.5	64 × 64 × 48
Run6	DTM	10,000	1:1:0.5	64 × 64 × 48

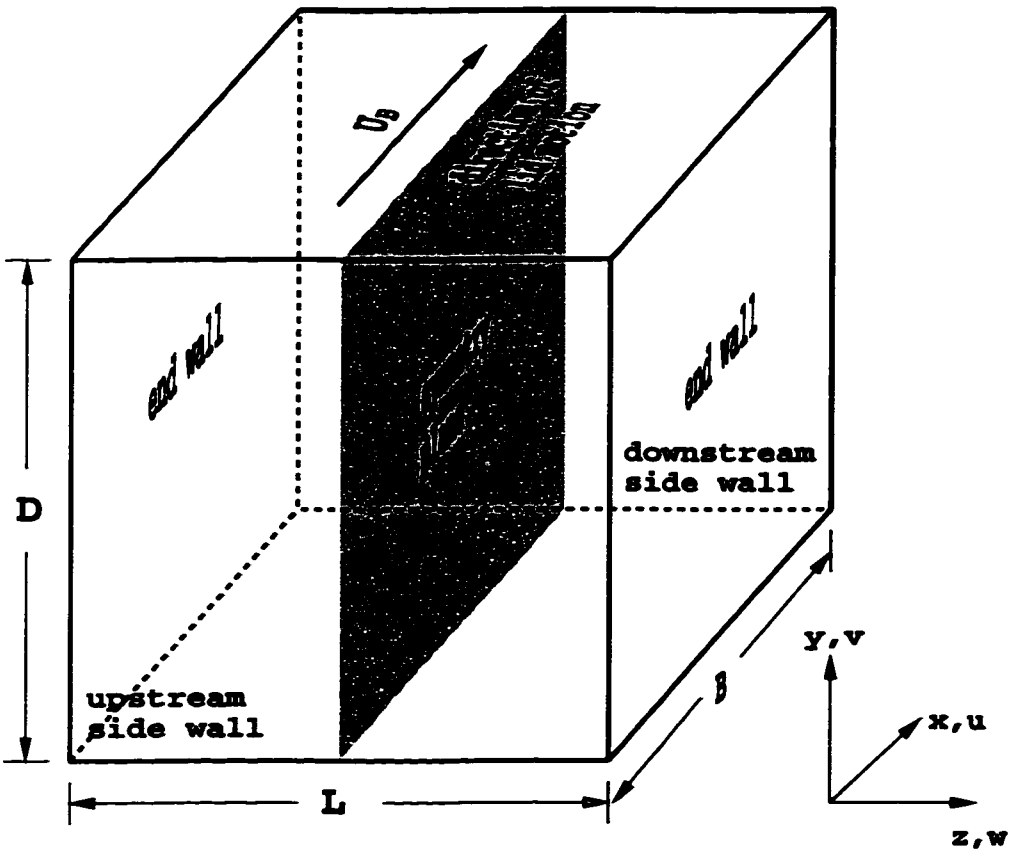

Figure 3.1: Definitions for the lid-driven cavity flows.

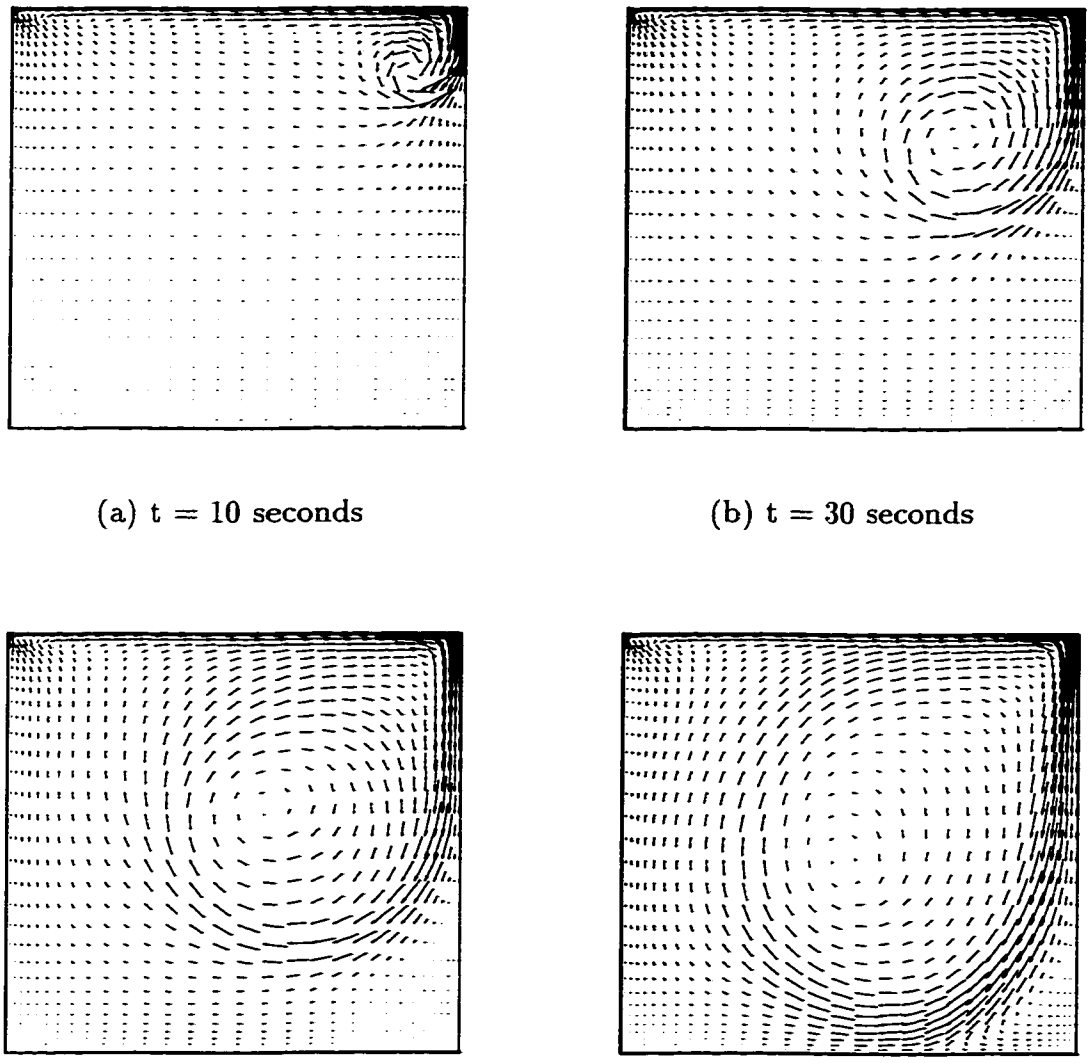

(a) t = 10 seconds

(b) t = 30 seconds

(c) t = 60 seconds

(d) t = 90 seconds

Figure 3.2: Developing flow fields at the symmetry plane of the isothermal cubic lid-driven cavity flow obtained from numerical simulation at Re=3200. (a) 10 seconds; (b) 30 seconds; (c) 60 seconds; (d) 90 seconds.

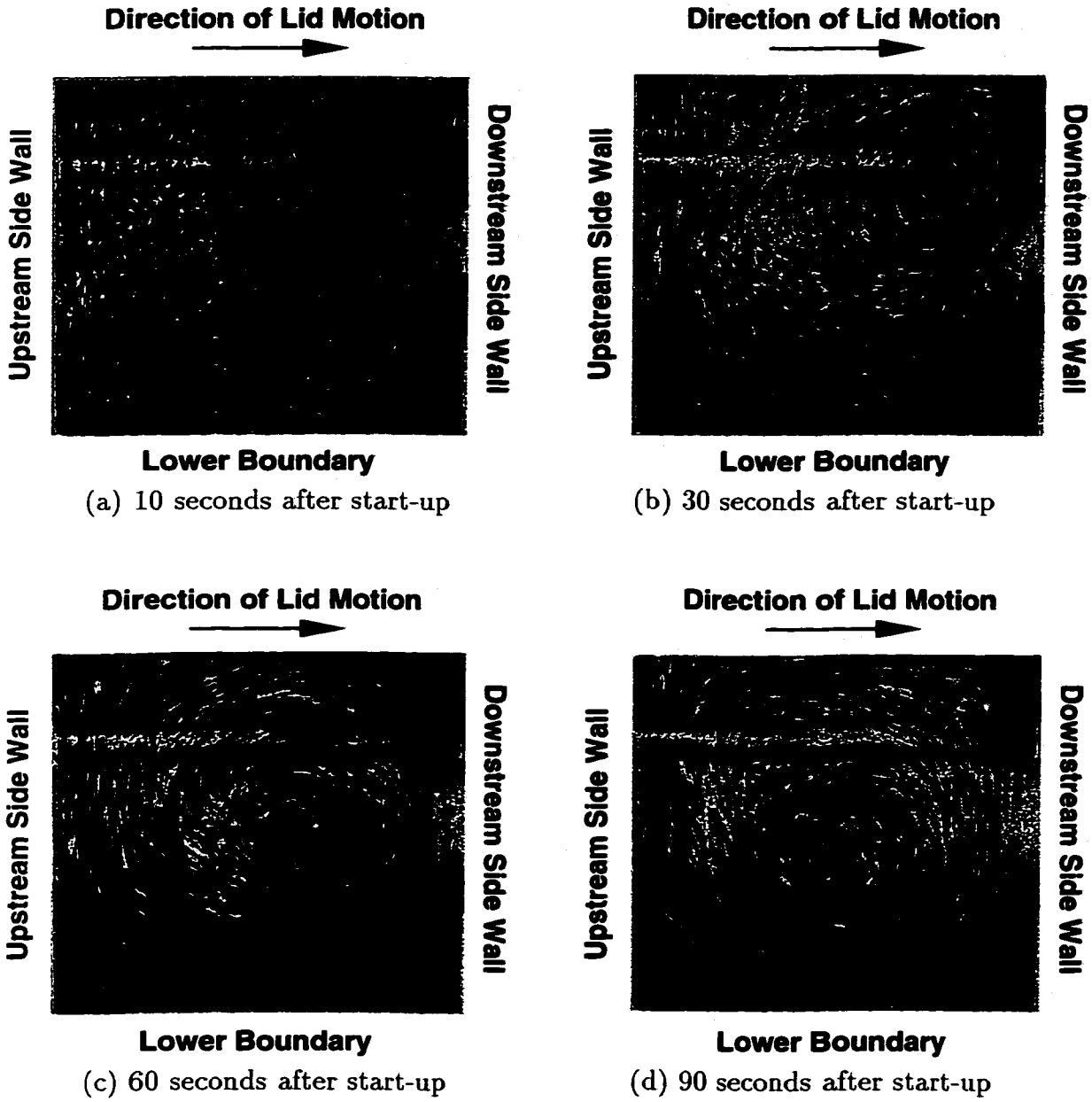

(a) 10 seconds after start-up

(b) 30 seconds after start-up

(c) 60 seconds after start-up

(d) 90 seconds after start-up

Figure 3.3: Visualizations of the start-up of the isothermal cubic lid-driven cavity flow at the symmetry plane at Re=3200 (Prasad 1989). (a) 10 seconds; (b) 30 seconds; (c) 60 seconds; (d) 90 seconds.

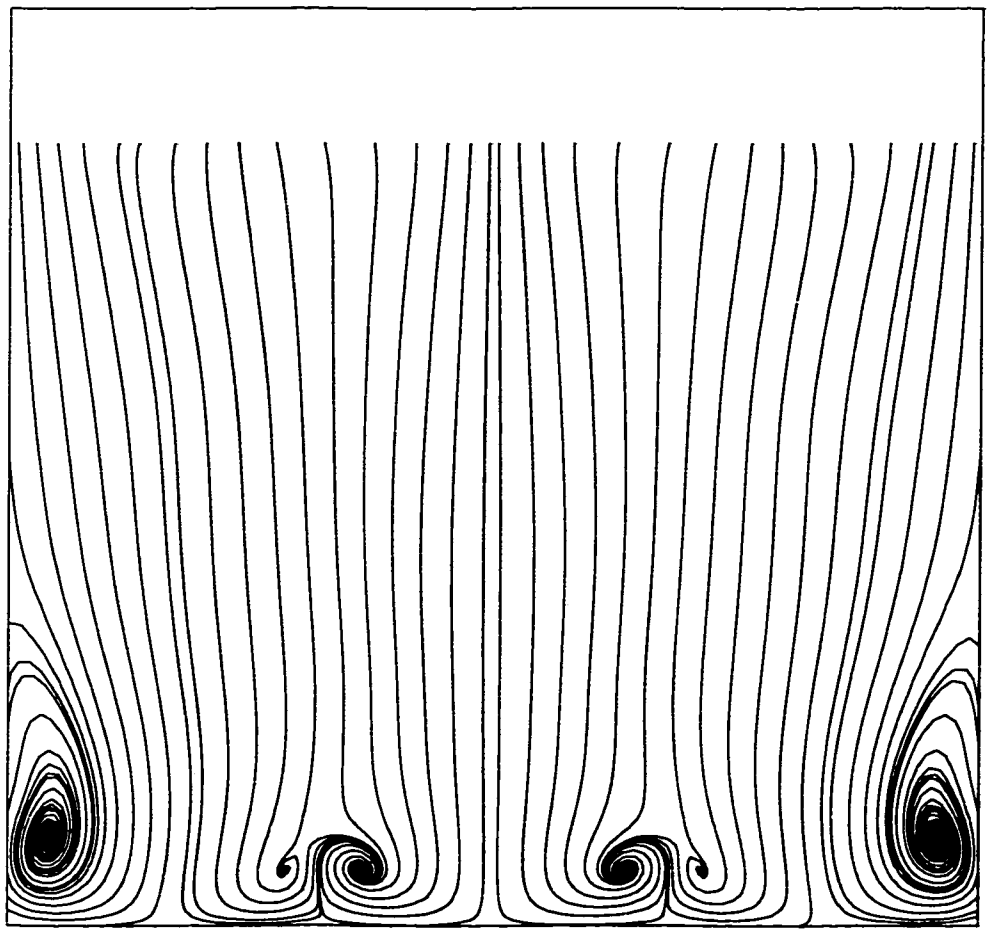

Figure 3.4: Instantaneous flow field of the isothermal cubic lid-driven cavity flow at the plane 0.25B from the downstream side-wall at t=540 seconds and Re=3200.

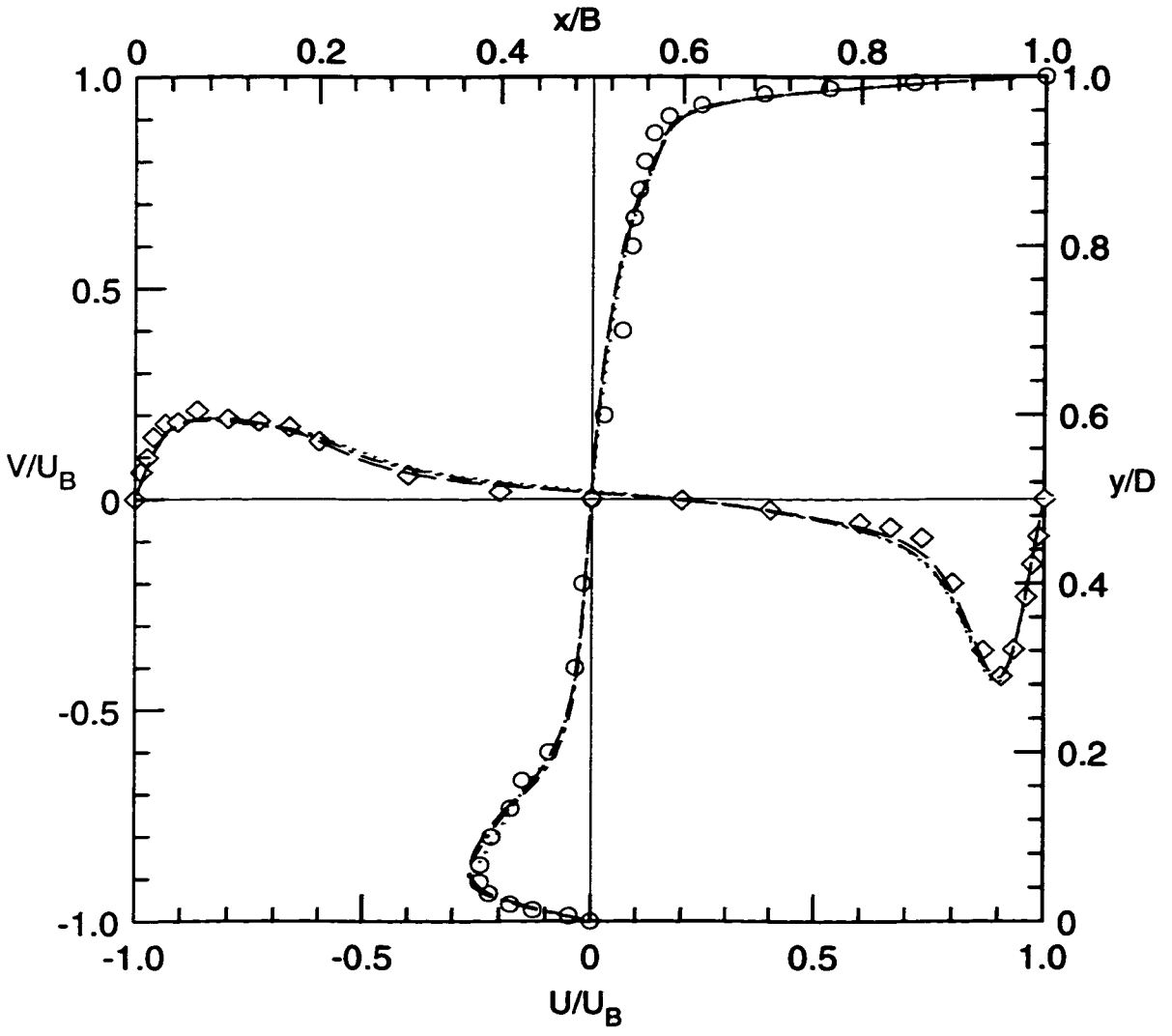

Figure 3.5: Mean velocity profiles along the centerlines at the symmetry plane at Re=3200. $U/U_B = < u > /U_B$ and $V/V_B = < v > /U_B$, $\circ$ and $\diamond$: Prasad and Koseff (1989); $\cdots$: DSM; $- - -$: DMM; $- \cdot -$: DTM.

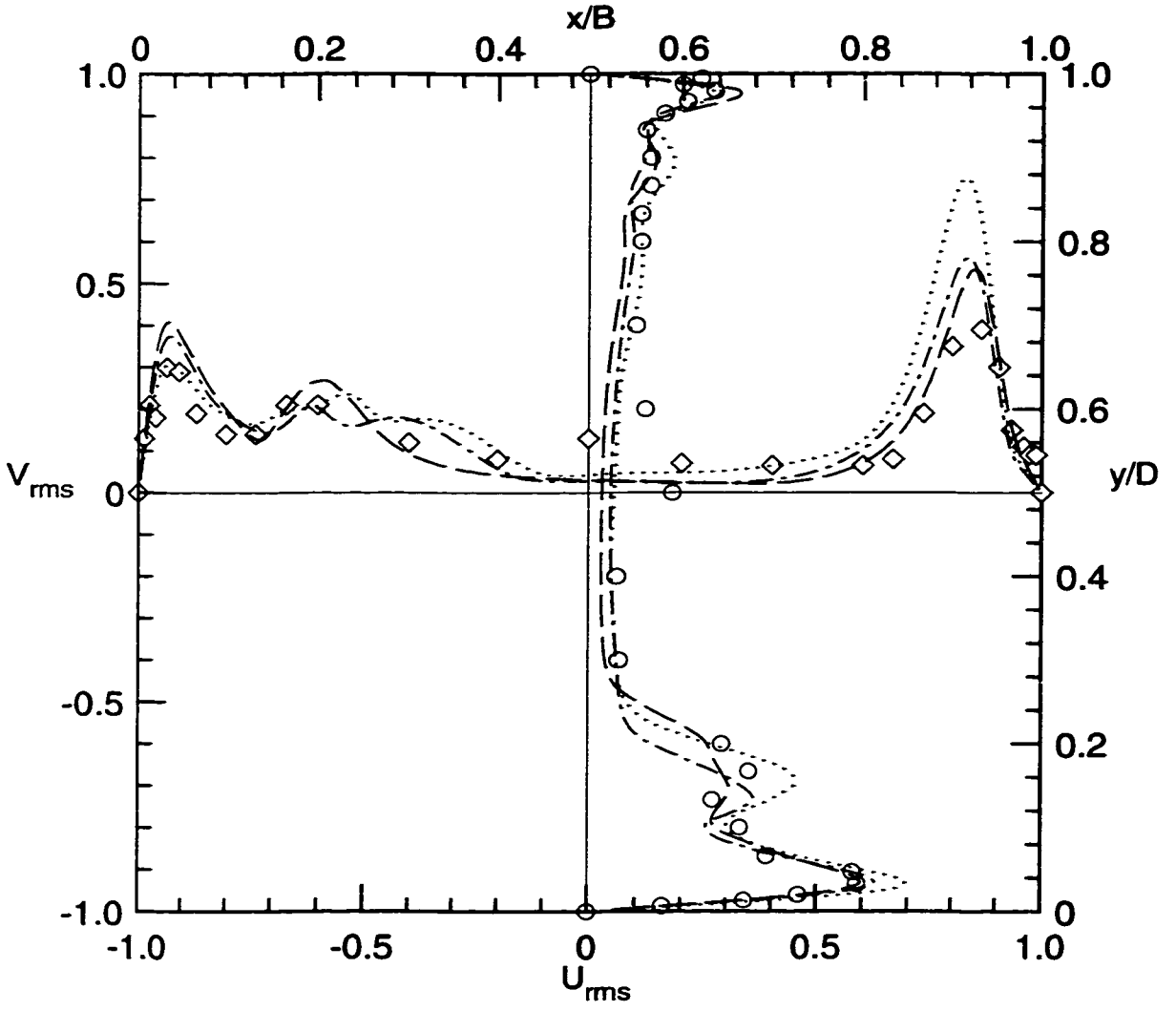

Figure 3.6: The r.m.s. velocity profiles along the centerlines at the symmetry plane at Re=3200. $U_{\rm rms} = 10(< u''^2 >)^{1/2}/U_B$ and $V_{\rm rms} = 10(< v''^2 >)^{1/2}/U_B$, $\circ$ and $\diamond$: Prasad and Koseff (1989); $\cdots$: DSM; $- - -$: DMM; $- \cdot -$: DTM.

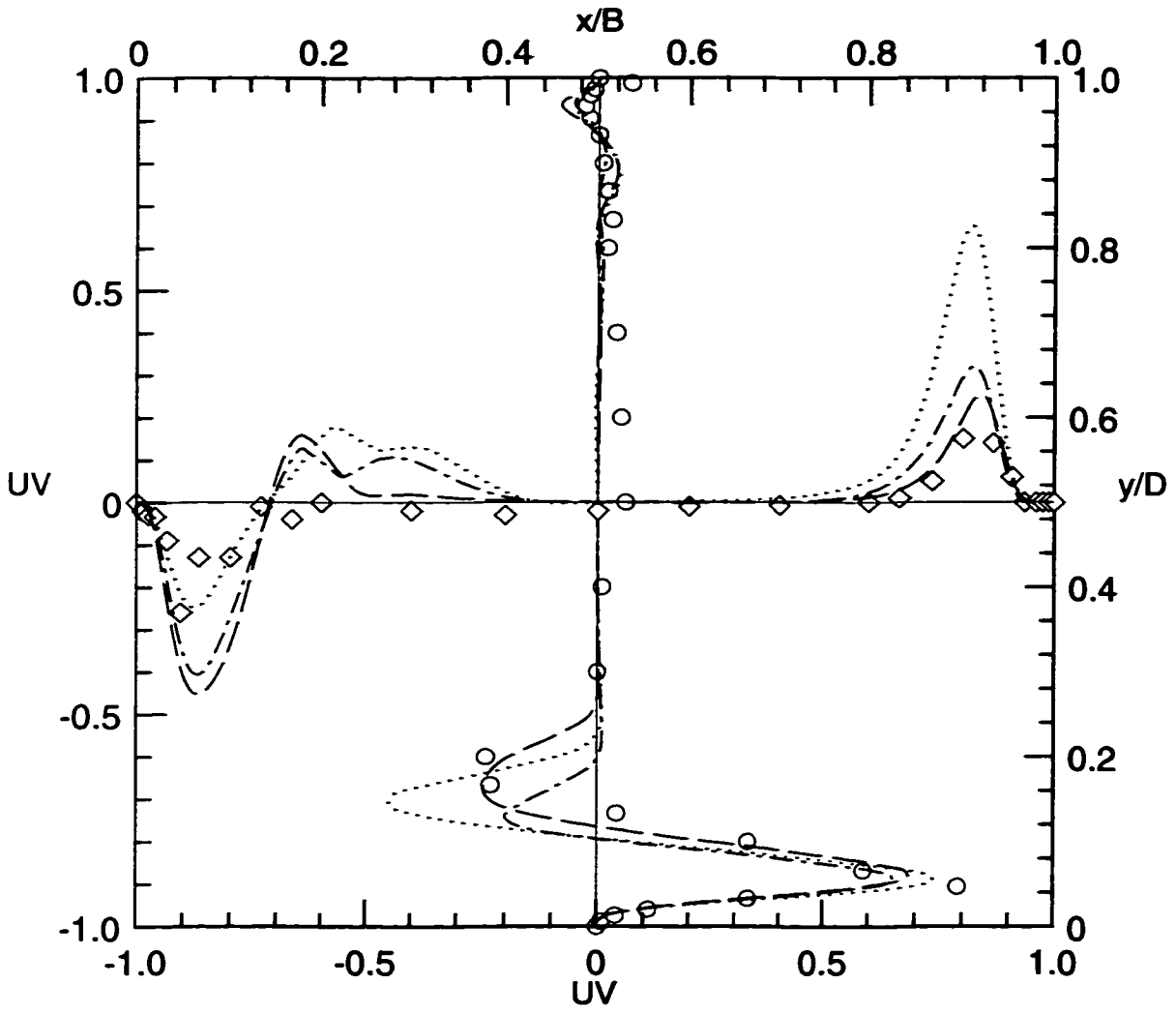

Figure 3.7: The Reynolds stress along the centerlines at the symmetry plane at Re=3200. $UV = 500 < u''v'' > /U_B^2$, ∘ and ◇ : Prasad and Koseff (1989); ··· : DSM; − − − : DMM; − · − : DTM.

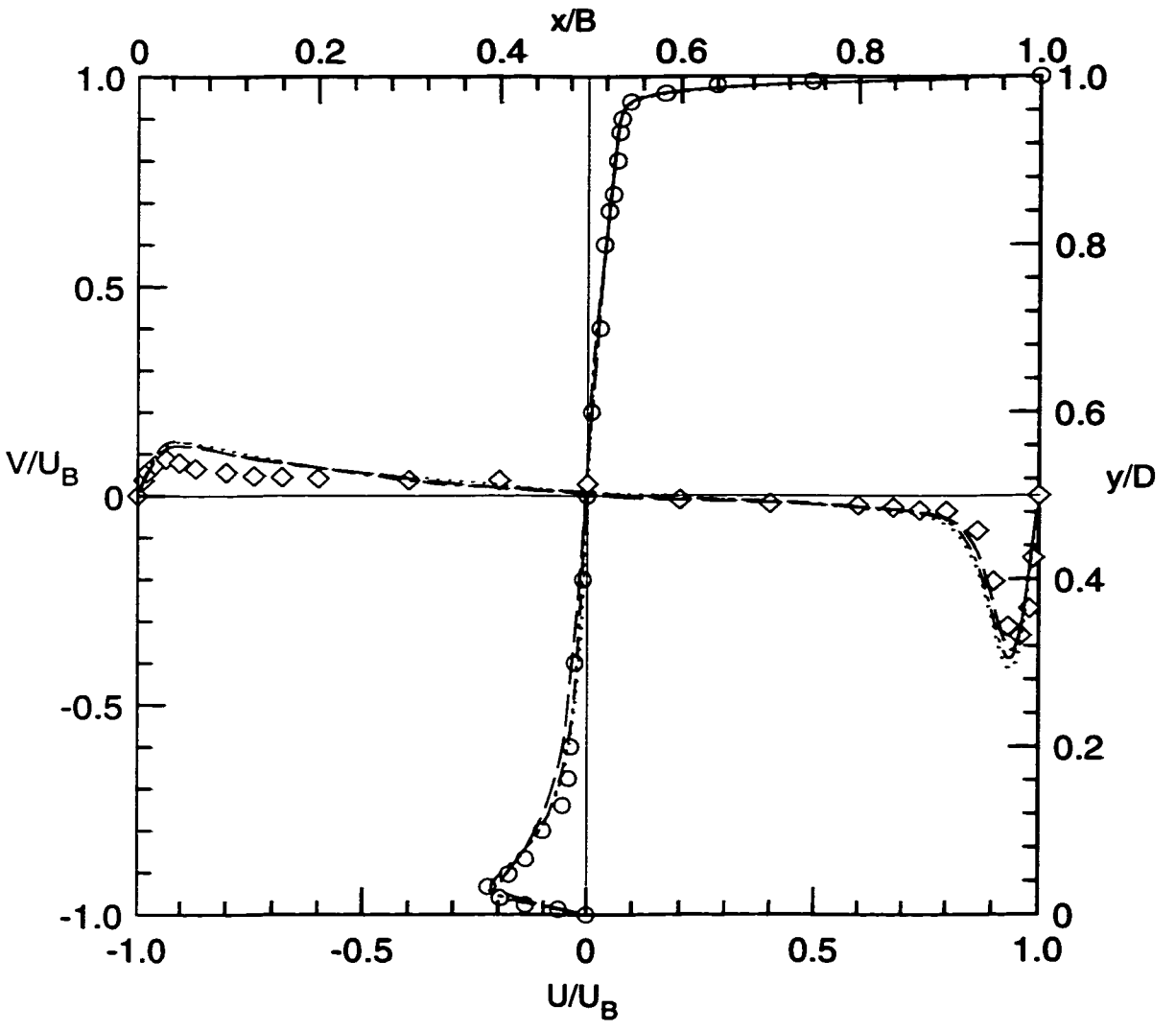

Figure 3.8: Mean velocity profiles along the centerlines at the symmetry plane at Re=10,000. $U/U_B =< u > /U_B$ and $V/V_B =< v > /U_B$, ∘ and ◇ : Prasad and Koseff (1989); ··· : DSM; − − − : DMM; − · − : DTM.

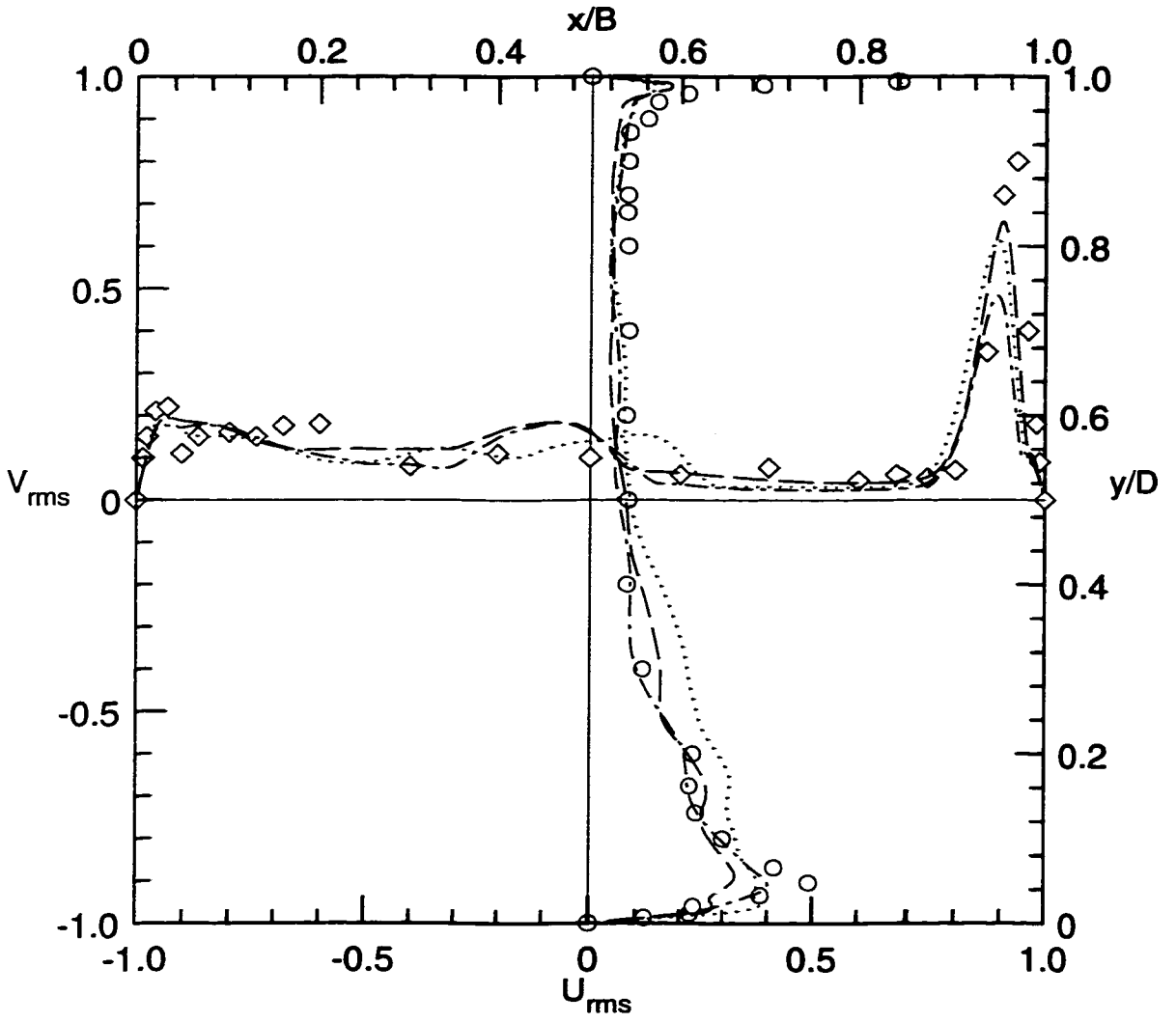

Figure 3.9: The r.m.s. velocity profiles along the centerlines at the symmetry plane at Re=10,000. $U_{\rm rms} = 10(< u'^2 >)^{1/2}/U_B$ and $V_{\rm rms} = 10(< v'^2 >)^{1/2}/U_B$, $\circ$ and $\diamond$: Prasad and Koseff (1989); $\cdots$: DSM; $- - -$: DMM; $- \cdot -$: DTM.

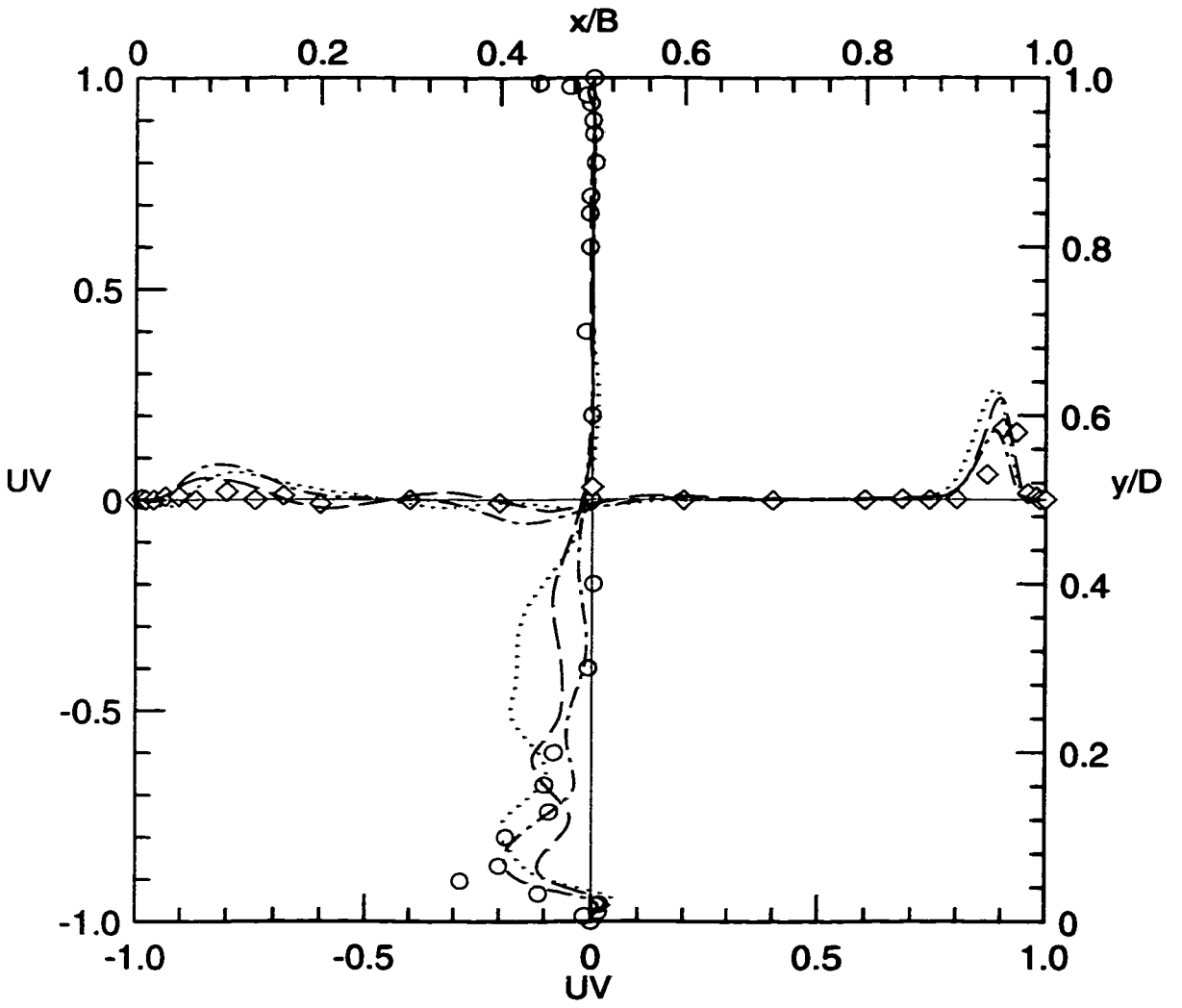

Figure 3.10: The Reynolds stress along the centerlines at the symmetry plane at Re=10,000. $UV = 500 < u''v'' > /U_B^2$, ∘ and ◇ : Prasad and Koseff (1989); ··· : DSM; – – – : DMM; – · – : DTM.

Chapter 4

Parallel Code Implementation

4.1 Introduction

In recent years, distributed memory parallel computers have been widely recognized as the most likely means of achieving scalable high performance computing. The typical design of a distributed memory parallel computer exploits many small processors, working simultaneously, each accompanied by a small memory of its own. In such a design, memory capacity and processing capacity can both be utilized with high efficiency. Each processor is much less powerful than the single processor in traditional sequential machine, but hundreds to thousands of less powerful processors together make the parallel computer one of the fastest computers ever constructed. The two most commonly used programming paradigms in parallel environments are the Single-Instruction Multiple-Data (SIMD) approach (also referred to as the data parallel mode) and the Multiple-Instruction Multiple-Data (MIMD) approach which is also referred to as the message passing mode. Since 1993, a broadly-based group of parallel computer vendors, software writers, and application scientists have collaborated on the development of a standard portable message-passing library definition called MPI, for Message Passing Interface. MPI, as an industry standard, enables good portability among a broad class of parallel computers. It is one of the objectives of the present study to develop an efficient parallel code to carry out large eddy simulations of different geophysical flows on distributed memory massively parallel computers. Due to the existence of different parallel computer architectures and consequently different programming paradigms, it was an interest of this study to

examine the code performance using different programming paradigms on different parallel machine architectures.

4.2 Programming Paradigms

As noted above the SIMD (the data parallel mode) and MIMD (the message passing mode) approaches are the two most commonly used programming paradigms in parallel environments. In the data parallel mode, data in each array is laid out across all the processors and a single instruction acts on all the data simultaneously. In this environment, the compiler generates the required communication directives between processing nodes. By using the Fortran 90/High Performance Fortran (HPF) array syntax, this method can be quite powerful in extracting the inherent parallelism in a solution algorithm. In the message passing mode, the programmer explicitly subdivides the work at the processor level. Each processor sees only the data in its local memory and must explicitly send and receive messages to coordinate work and exchange data with other processors. Each approach has its strengths and limitations. In particular, data parallel works best on problems with large amounts of data. Small data structures generally do not have enough inherent parallelism at the data level. The data parallel mode is very easy to use, but in general it does not have a high degree of versatility. Message Passing, which explicitly handles both communication and data partitioning among processors, leads to a high degree of versatility, but it is more difficult to implement. The Message Passing Interface (MPI), a standard portable message passing library definition, provides the portability necessary for the message passing parallel programming to have wide applicability. The most common form of MIMD approach is the Single-Program Multiple-Data (SPMD) mode, which avoids having to write numerous separate programs. In the present work, two Navier-Stokes solvers have been developed using the same numerical algorithm, one has been programmed in Fortran 77 with some Fortran 90 features and implemented on the

IBM SP2 and the SGI Origin2000 in the message passing mode; and the other one has been programmed in CM Fortran (Thinking Machine Corp. 1991) and implemented on the Connection Machine model CM-5 in the data parallel mode.

In the following sections of this chapter, the architectures of the parallel computers used in the this work are introduced. The different procedures adopted in this study to develop the two different parallel codes and some code optimization issues are discussed. The performances for the two parallel codes are also presented.

4.3 Parallel Implementation on the IBM SP2 Using MPI

The parallel code described in this section was developed on the IBM SP2 using the message passing interface (MPI), then ported to the SGI Origin2000. The use of MPI enables good portability of the code among a broad class of parallel computers. The code implementation issues and code performance are discussed below.

4.3.1 The Architectures of IBM SP2 and SGI Origin2000

The parallel code in this work was developed on the IBM SP2 and then ported to the SGI Origin2000. The IBM SP2 at NASA (The National Aeronautics and Space Administration) is a distributed memory 144-node RS6000/590 cluster connected by a high-performance proprietary IBM network. The network displays a bandwidth (the rate at which data can be transferred between processors) of 34 Mbytes/second and a latency (the time required to get a data transfer started) of approximately 45 micro-seconds. Each node has at least 128 Mbytes of main memory and 2 Gbytes of disk space. Each node operates at a clock rate of 66.7 MHz, and displays a peak performance of 267 MFlops. The SGI Origin2000 at NASA has 128 processors with 32 Gbytes of shared memory. Each processor is rated at 250 MHz with a theoretical

memory transfer rate of 1.6 Gbytes/second. The processors are arranged in pairs with a small amount of memory (512 Mbytes) on a single card.

4.3.2 Message Passing Interface

Message passing interface (MPI) is a standard portable message-passing library definition, which resulted from the efforts of numerous of computer vendors, software writers and application scientists. The book by Gropp *et al.* (1994) provides an easy to understand tutorial and guidance on the use of MPI. MPI is not a revolutionary new way of programming parallel computers. Rather, it is an attempt to collect the best features of many existing message-passing systems. MPI, as an industry standard, enables good portability among a broad class of parallel computers. The present code, which was originally developed on the IBM SP2, was directly ported to the SGI Origin2000 without making any changes to the code.

4.3.3 Data Structure

In the current code, a finite volume method is used to discretize the governing equations in general curvilinear coordinates on a single non-staggered grid. The Cartesian velocity components u, v and w, the scalar ρ or T, the pressure p and the inverse of the Jacobian J^{-1} (the volume of the control volume) are stored at the center of each control volume. On the face of the control volume, the vector surface area $J^{-1}\partial\xi_m/\partial x_i$ $(i = 1, 2, 3)$, three corresponding elements of the mesh skewness tensor G_{mn} $(n = 1, 2, 3)$ and the volume fluxes U_m $(m = 1, 2, 3)$ are stored. Only one set of metric quantities needs to be stored per control volume. More variables have to be stored if a large-eddy simulation is performed. The executable code for a large-eddy simulation with a grid size of $192 \times 160 \times 320$ running on forty processors of the IBM SP2 requires 8 Gbytes of core memory.

4.3.4 Domain Decomposition

In message passing parallel mode, the programmer has to explicitly partition the data at the grid level. The key issues in developing efficient message passing codes are to maintain load balance and minimize communication cost. Thus, a uniform domain decomposition is a natural way to maintain load balance among the processors. The three-dimensional computation grid ($N_x \times N_y \times N_z$) is subdivided evenly into N_p partitions, which equal the number of processors allocated for the computation, and one partition is assigned to each processor. According to the way the grid is partitioned, there can be 1-D, 2-D and 3-D partitioning, as illustrated in Figure 4.1. Assume that the number of processors in each dimension is N_{p1}, N_{p2} and N_{p3}, with $N_{p1} \times N_{p2} \times N_{p3} = N_p$, then each partition contains an equal number $N_x/N_{p1} \times N_y/N_{p2} \times N_3/N_{p3}$ of data items. Since communication occurs at the boundaries, the communication cost can be reduced by minimizing the surface to volume ratio for each partition. This criterion can be used as guidance for choosing specific partitioning. In the present implementation, the domain decomposition is done statically. Thus, the change from one partitioning to another can be done by simply changing the number of the processors in each dimension before compiling the code.

4.3.5 Algorithm Implementation

Based on the nature of the inter-grid data dependencies, there are two types of parallel calculations in the present work: *parallel-by-point* and *parallel-by-line*. The "parallel-by-point" calculations are the simplest because computations can be done at each grid point independently of the computations at the other grid points. Depending on the discretization stencil used, known values at one or more neighboring grid points in each dimension are needed in computations at any grid point. The "parallel-by-point" schemes were extensively analyzed for partitioning and minimizing the communication overhead by Reed *et al.* (1987). For "parallel-by-line" calculations,

the computation at each grid is coupled to other grid points in a fixed direction, but can be done independently of the computations at grid points on all other lines in that direction. Computations on different lines may proceed without any dependence or communication delays.

It is important to divide the numerical algorithm into its separate components and to identify the computation and communication requirements for the basic kernels. For the fractional step method employed in the present study, the solution algorithm naturally divides into three steps:

(i) calculating the intermediate velocity field [Eqn. (2.82)].

(ii) solving the Poisson equation [Eqn. (2.87)].

(iii) updating the velocity field [Eqn. (2.83)].

In step (i), the computation of the partial derivatives of the advective and diffusive terms using known velocity and scalar fields is "parallel-by-point". To invert the matrix on the left hand side of Eqn. (2.82), the approximate factorization technique (Beam and Warming 1976) is used. Solving the resulting three tridiagonal systems is "parallel-by-line". In step (ii), the Poisson equation is solved by the multi-grid method with ADI as the smoother. Except for solving of the tridiagonal systems in the ADI steps, the calculations are "parallel-by-point". Finally, step (iii) is completely "parallel-by-point". Examples of the two-different types of calculations are given in the following.

4.3.6 Point-to-Point Communication

The "parallel-by-point" calculation and the nearest neighbor point-to-point communication will be demonstrated by a simple example of computing the second-order x-component derivative $u''=\partial^2 u/\partial x^2$. At a point i, it is discretized as:

$$u_i'' = \frac{1}{\Delta x^2}(u_{i-1} - 2u_i + u_{i+1}). \tag{4.1}$$

The procedures of computing u_i'' are divided into the following two steps:

(i) domain decomposition

The first step of the calculation is to do a domain decomposition. In the example, the length of the global array u is N=12, and the number of processors used in the computation is *nprocs*=3. As illustrated in Figure 4.2, the global array u is divided evenly into *nprocs*=3 sub-arrays, one assigned to each processor, and "shadow" entries (or "ghost points") are added to each sub-arrays to hold data from other processors. The static domain decomposition can be done by the following code fragment:

```
c    Domain decomposition
     integer, parameter ::  N=12
     integer, parameter ::  nprocs=3
     integer, parameter ::  MyN=N/nprocs
     real, dimension(0:MyN+1) ::  u, d2udx2
```

(ii) break calculations into communication and computation

For the specific example, we use a "parallel-by-point" type of calculation. The computation is entirely local and the communication is point-to-point communication between the neighbors at the boundaries. There are different ways to perform this point-to-point communication in MPI. The most commonly used ones will be demonstrated by actual code fragments and each of them will be analyzed.

• *Communication Routine I : blocking communication*

The simplest approach is to use the basic blocking send and receive, as shown in the following code fragment:

```
c    Exchange data at the boundaries
     if ( n_left .ne.  MPI_PROC_NULL )
   < call MPI_SEND( u(1), 1, MPI_REAL, n_left, 0, comm1d, ierr )
     if ( n_right .ne.  MPI_PROC_NULL )
   < call MPI_RECV( u(MyN+1), 1, MPI_REAL, n_right, 0, comm1d, ierr )
     if ( n_right .ne.  MPI_PROC_NULL )
```

```
  < call MPI_SEND( u(MyN), 1, MPI_REAL, n_right, 1, comm1d, ierr )
      if ( n_left .ne.  MPI_PROC_NULL )
  < call MPI_RECV( u(0), 1, MPI_REAL, n_left, 1, comm1d, ierr )
c   Calculate d2udx2
    do i = 1, MyN
    d2udx2(i) = 1/dx**2*(u(i-1)-2*u(i)+u(i+1))
    enddo
```

The values of **n_left and n_right** are set elsewhere and are different on different processors. In the above code fragment, each processor sends data to the processors on the left and then receives data from the processor on the right. The order is then reversed and data is sent to the processor on the right and received from the processor on the left. The blocking sends do not complete until the matching receives are issued on the destination processor. Since processor P1 (the leftmost processor in Figure 4.3) does not send data to any processor in the first step, it can receive data [5] from the processor P2. Only after data [5] has been received by the processor P1, *i.e.*, the blocking send of P2 is completed, will the processor P2 begin to receive data [9] from the processor P3. This produces a staircase pattern of sends and receives. Thus, processor P3 has to wait longer than processor P2 for the blocking send to complete and the communication is entirely sequential. After the communication is over, computation can be done in parallel, as shown in Figure 4.3. Even though the above approach is simple, but it is not the best way to implement the exchange of ghost points.

- *Communication Routine II : buffered (non-blocking) communication*

Instead of requiring the programmer to determine a safe ordering of the send and receive operations, MPI allows the programmer to provide a buffer into which data can be placed until it is delivered. Note that the send and receive orders shown in the code fragment below will cause deadlock if a blocking send is used. The change from blocking send to buffered send is simple; one just replaces the **MPI_SEND** calls

with MPI_BSEND. The resulting code fragment is shown below:

```
c   Exchange data at the boundaries
    if ( n_left .ne. MPI_PROC_NULL )
  < call MPI_BSEND( u(1), 1, MPI_REAL, n_left, 0, comm1d, ierr )
    if ( n_right .ne. MPI_PROC_NULL )
  < call MPI_BSEND( u(MyN), 1, MPI_REAL, n_right, 1, comm1d, ierr )
    if ( n_right .ne. MPI_PROC_NULL )
  < call MPI_RECV( u(MyN+1), 1, MPI_REAL, n_right, 0, comm1d, ierr )
    if ( n_left .ne. MPI_PROC_NULL )
  < call MPI_RECV( u(0), 1, MPI_REAL, n_left, 1, comm1d, ierr )
```

In addition to the replace of MPI_SEND with MPI_BSEND, MPI requires that the programmer provide the storage into which the message may be placed with the routine MPI_BUFFER_ATTACH. This buffer should be large enough to hold all the messages that must be sent before the matching receives are called. Once a program no longer needs to use a buffer, the routine MPI_BUFFER_DETACH should be called. It is important to remember that buffering incurs a performance penalty, since the message must be copied an extra time when a message is buffered. From the code optimization point of view, the programmer should avoid using buffered communication.

• *Communication Routine III : asynchronous communication*

On most parallel computers, moving data from one processor to another takes more time than moving or manipulating data within a single processor. To keep a program from being slowed down (also described as "starved for data"), MPI allows programmers to start sending and receiving several messages and to proceed with other operations by providing nonblocking, asynchronous send and receive (MPI_ISEND and MPI_IRECV). The arguments for the routine MPI_ISEND are the same as for MPI_SEND with the addition of a handle as the next to last argument. The *handle* argument is used to determine whether a message has been delivered. The buffering can be avoided with the following code fragment:

```
c Exchange data at the boundaries
  if ( n_left .ne.  MPI_PROC_NULL )
  call MPI_IRECV(u(0), 1, MPI_REAL, n_left, 0, comm1d, req(1), ierr)
  call MPI_ISEND(u(1), 1, MPI_REAL, n_left, 1, comm1d, req(2), ierr)
  endif
  if ( n_right .ne.  MPI_PROC_NULL ) then
  call MPI_IRECV(u(MyN+1),1,MPI_REAL,n_right,1,comm1d,req(3),ierr)
  call MPI_ISEND(u(MyN),1,MPI_REAL,n_left,0,comm1d,req(4),ierr)
  endif
  call MPI_WAITALL( 4, req, status, ierr )
```

The above approach allows for both sends and receives to take place at the same time. In principle, the message passing in this approach can be almost twice as fast as the blocking sends and receives. However, the communication is still separated from the computation, as demonstrated in Figure 4.3. The best strategy is to overlap computation and communication, as demonstrated in Figure 4.4, and it can be achieved by the following code fragment:

```
c Start data exchange
  if ( n_left .ne.  MPI_PROC_NULL )
  call MPI_IRECV(u(0), 1, MPI_REAL, n_left, 0, comm1d, req(1), ierr)
  call MPI_ISEND(u(1), 1, MPI_REAL, n_left, 1, comm1d, req(2), ierr)
  endif
  if ( n_right .ne.  MPI_PROC_NULL ) then
  call MPI_IRECV(u(MyN+1),1,MPI_REAL,n_right,1,comm1d,req(3),ierr)
  call MPI_ISEND(u(MyN),1,MPI_REAL,n_left,0,comm1d,req(4),ierr)
  endif
c Calculate d2udx2 (interior)
  do i = 2, MyN-1
  d2udx2(i) = (1/dx**2)*(u(i-1)-2*u(i)+u(i+1))
```

```
  enddo
c Wait for boundary data
  call MPI_WAITALL( 4, req, status, ierr )
c Calculate d2udx2 (boundaries)
  do i = 1, MyN, MyN-1
  d2udx2(i) = (1/dx**2)*(u(i-1)-2*u(i)+u(i+1))
  enddo
```

The first part of the above code fragment begins with both the nonblocking sends and receives. While the messages are "in transit", the computations involving only interior points are in progress. Once data from other processors is received, the computations on the boundary points are performed. The above approach is effective but can be difficult to implement when the overlapping of the communication and computation is not as simple as in the given example.

4.3.7 Pipelined Thomas Algorithm

One major task of the present numerical algorithm includes solving many tri-diagonal systems. Sequentially, the most efficient algorithm for inverting a tri-diagonal system is the Thomas algorithm. To solve a system of size n, with coefficients A_i, B_i and C_i, and the right hand side f_i, given by,

$$A_i u_{i-1} + B_i u_i + C_i u_{i+1} = f_i \tag{4.2}$$

where u_1 and u_n are known, the Thomas algorithm performs two sweeps over the index i. In the forward sweep, coefficients P_{i+1} and $q_{i+1}, i = 2, ..., n-1$, are computed, where

$$P_{i+1} = (B_i - A_i P_i)^{-1} C_i \tag{4.3}$$

$$q_{i+1} = (B_i - A_i P_i)^{-1} (f_i - A_i q_i). \tag{4.4}$$

The unknowns $u_i, i = n-1, ..., 2$, are determined in the back sweep from

$$u_i = q_{i+1} - P_{i+1} u_{i+1}. \tag{4.5}$$

Note that the computation requires storage of all P_{i+1} and q_{i+1} from the forward sweep for computing unknowns u_i in the back sweep. Clearly, both phases of the Thomas algorithm have recursive data dependencies and hence the algorithm, when used for solving a single system, is inherently sequential. The single tridiagonal system can be solved in parallel by the cyclic reduction algorithm (Stone 1975). The cyclic reduction algorithm is highly parallelizable, but it is computationally expensive. Though the Thomas algorithm is sequential when solving a single tridiagonal system, a significant amount of parallelism can be extracted from the Thomas algorithm for 2-D and 3-D problems when several independent systems are to be solved. This is achieved by pipelining the computations of these systems so that the computation of several solves overlaps with each other, as in the pipelined version of the Thomas algorithm proposed by Naik *et al.* (1993). In the *pipelined Thomas algorithm*, if a processor is to compute unknowns u_i through u_k, $i \leq k$, for one of the systems, it receives the coefficients P_i and q_i from a preceding processor and then proceeds to compute the coefficients through P_{k+1} and q_{k+1}. On completion of these computations, it sends the final coefficients P_{k+1} and q_{k+1} to the succeeding processor. The same is repeated for all other systems assigned to it. After completing all the forward sweeps, the back sweep is completed by computing (in reverse order) the unknowns u_k through u_i. The computed value of u_i is sent to the preceding processor and the process is repeated for all the systems assigned to that processor. The pipelined Thomas algorithm is a typical "parallel-by-line" calculation.

The pipelined Thomas algorithm can be clearly demonstrated by a simple 2-D problem. Assume that a two-dimensional computation grid ($N_i \times N_j$) and $N_p = 3$ processors are given. Parallelism can be extracted from the Thomas algorithm for

the 2-D problem when $N_j = 3$ tri-diagonal systems of size $N_i = 9$ are to be solved. The grid is partitioned evenly in the i—direction into three sub-domains, with each partition containing $N_i/N_P \times N_j$ data items. Then, ghost points are added to each partition to hold data from other processors, as shown in Figure 4.5. At first (Figure 4.6a), when Processor P1 is beginning the forward sweep of the tri-diagonal system $j = 1$, processors P2 and P3 are idle. Once processor P1 finishes the forward sweep of the tri-diagonal system $j = 1$, it passes a message with updated data information at location $(i = 3, j = 1)$ to Processor P2 and then begins the forward sweep of the tri-diagonal system $j = 2$. Once processor P2 receives the message from processor P1, it begins the forward sweep of tri-diagonal system $j = 1$ while processor P3 is still idle (Figure 4.6b). The process continues in a similar manner. At the next moment (Figure 4.6c), all the three processors are working on the forward sweep of different tri-diagonal systems. Thus, the algorithm is called the pipelined Thomas algorithm.

4.3.8 Code Performance

All the computations in the present study were performed on the NASA's IBM SP2 and SGI Origin2000. At NASA, a performance measurement tool, RS2HPM, was used to record the performance of individual batch jobs on the IBM SP2. Users and system personnel examined and analyzed the hardware counter reported for these jobs. By examining the entire workload measured over a 9-month period during 1995 and 1996, Bergeron (1998) showed the performance per node of jobs as a function of the number of nodes requested in Figure 4.7. The code performance result is presented in terms of MFLOPS (Million FLoating point Operations per Second). A performance of about 40 MFLOPS per node on a 28-node job was achieved by the parallel code developed in this work. This was the peak rate (see Figure 4.7) on NASA's IBM SP2 - outdistancing the next best performance by 41%. Subsequently, the parallel code developed in this work was used by NASA for benchmark testing.

A CPU time per computation cell per time step, *i.e.*, the "normalized CPU", of $5\mu s$ was achieved for the large-eddy simulation of the laboratory-scale coastal upwelling flow (Narimousa and Maxworthy 1987), which is presented in Chapter 6, when forty IBM SP2 processors are used. The normalized CPU for the serial version of the code (Zang 1993) running on a single processor of the Cray Y-MP was about $45\mu s$. The serial version of the code carried out a large-eddy simulation of the same upwelling flow using the same geometric parameters but a viscosity 12.5 times larger than the viscosity used in this study. The numbers of grid points, resolution and flow domain were also all less in the serial computation.

4.4 Parallel Implementation on the CM-5 Using Data Parallel

In the early phases of this work, the parallel code was implemented in CM Fortran on the CM-5 in the data parallel mode. The code implementation and code performance issues are discussed below.

4.4.1 The Architecture of Connection Machine CM-5

The Connection Machine model CM-5 was a massively parallel processing computer with a "universal architecture" supporting both SIMD and MIMD models. The node in a CM-5 system, each with its own memory, can fetch from the same address in their respective memories to execute the same (SIMD-style) instruction, or from individually chosen addresses to execute an independent (MIMD-style) instruction. A CM-5 system may contain tens, hundreds or thousands of parallel processing nodes, one or more control processors and input/output units. All these components are integrated into a system by two internal communication networks, the control network and the data network. The CM-5 at NCAR (The National Center for Atmospheric

Research) contained 32 processing nodes. Each CM-5 processing node consisted of a Sun SPARC microprocessor, a memory subsystem of 32 Mbyte node memory and a CM-5 network interface. Each CM-5 processing node was accelerated by four vector units. Each vector unit had 32 MFlops peak 64-bit floating-point performance and a peak memory bandwidth of 128 MBytes/sec. Therefore, a single CM5 node had a total of 128 MFLops of peak 64-bit performance and four 64-bit paths to node memory.

4.4.2 CM Fortran

The CM-5 architecture can be used as either a SIMD or MIMD machine. In this study we only employed the SIMD approach on the CM-5. This is done by making use of the Fortran for the Connection Machine, *i.e.,* CM Fortran (Thinking Machine Corp. 1991). CM Fortran is an implementation of Fortran 77 supplemented with array processing extensions from Fortran 90 (Metcalf 1991). The most important difference is that it is not necessary to refer to array elements separately by means of subscripts with Fortran 90 constructions. Therefore, `DO` loop structures and other explicit indexing are not necessary. CM Fortran also offers several extensions beyond Fortran 90, such as the `FORALL` statement and some additional intrinsic functions. The use of CM Fortran array notations results in much more compact codes. The CM-5 Scientific Subroutine Library (CMSSL) provides a wide range of common mathematical operations, including dense vectors, dense matrices, LU factor and solve, tri-diagonal solvers, FFT, and eigenvalue analysis.

4.4.3 Data Structure and Array Layout

The data structure of data parallel implementation in the present study is the same as that used in the SPMD implementation using MPI (see Section 4.3). The number of data elements does not need to be equal to the number of processors requested in each

partition. If there are fewer processors required, the system temporarily switches off the processors that are not needed. If there are more data elements than the number of processors, the CM-5 hardware operates in virtual processor mode. Each physical processor simulates multiple processors, each with a smaller memory. The CM-5 operates automatically in the virtual processor mode. However, it is better to choose the number of data elements to be a multiple of four times the number of processors, since four vector units are used in a single CM5 node to pipeline all processing node computations.

While programming on the CM-5, the emphasis is on the use of a large uniform data structure, such as arrays whose elements can be processed at once. To take full advantage of the data parallel mode of computation, all the arrays have to be conformable, which means arrays with the same dimensions. The compiler directive `LAYOUT` allows the user to specify which dimension is parallel and which dimension is serial.

Consider, for example, the following compiler directive to layout data:

```
      double precision, array(ni,nj,nk) ::  rho, u, uxi
CMF$  layout rho(:news,:news,:news)
CMF$  layout u(:news,:news,:news)
CMF$  layout uxi(:news,:news,:news)
```

where `rho`, `u` and `uxi` are conformable arrays. The dimensions, denoted by "`:news`", are the parallel dimensions. **NEWS** indicates that processors along that axis are to be ordered in **NEWS** ordering. **NEWS**-ordered processors are physically connected on a dimension if their grid indices on that dimension differ by one. A statement like `rhou=rho*u` would proceed in parallel on all the data elements with array **rhou** having the same size as arrays **rho** and **u**. If a dimension is denoted by "`:serial`", that dimension is a serial dimension. **SERIAL** indicates that array elements along that axis are to be allocated up the memory of each processor. In the present study, all arrays have the layout of the axes in the **NEWS** configuration. Such mapping was found to be

optimal for the present study.

4.4.4 Algorithm Implementation

The Connection Machine CM-5 architecture allows a serial programming style, and similar programming environment, therefore programming on the CM-5 is very similar to that on the Cray Y-MP if data parallelism is used. The solution procedure in the data parallel implementation has the same three steps as used in the SPMD implementation using MPI (see Section 4.3). Efficient programming on the Connection Machine requires communication time to be minimized and utilization of all processors at the same time. In step (i) to (iii), there are three types of communication patterns used, which are regular communication, irregular or send/get type of communication and reduction. Communication comprises a major part of the numerical algorithm.

Regular communication, *i.e.*, the **NEWS** communication, is the most prevalent and the least expansive. **NEWS** communications allow communication between nearest neighbors. They are encountered in calculating finite volume stencils. All regular communications in this study are performed using the intrinsic CM Fortran functions CSHIFT and EOSHIFT. The command **CSHIFT(ARRAY, DIM, SHIFT)** performs a circular shift of the element **ARRAY** along the dimension **DIM** by the amount specified in SHIFT; while the command **EOSHIFT(ARRAY, DIM, SHIFT, BOUNDARY)** is appropriate when a boundary value **BOUNDARY** is to be imposed. For example, the second-oder x-component derivative at point i, u_i'' [Eqn. (4.1)], is computed as

```
c     Calculate d2udx2 (interior)
      d2udx2(i) = (1/dx**2)*(cshift(u,1,-1)-2*u+cshift(u,1,1))
```

The slowest form of communication is irregular communication, also known as the router, which allows each processor to communicate with any other processor.

There are two types of router communication, the "send" and the "get". Irregular or send/get operations are used in the restriction and prolongation of data between different levels of multigrid in step (ii). The pressure Poisson solver is the most computationally intensive algorithm in the fractional-step method. Therefore, send/get communication, which is the slowest form of communication on the CM-5, encountered in the multigrid method when solving the Poisson equation dominates the communication time and the total CPU time.

The reduction operations, such as the operation `cfl=maxval(cfl_local)`, which computes the maximum CFL number, do not contribute in a significant way to the total communication costs since they are not used extensively in present implementation.

The set of tridiagonal systems is solved simultaneously by the method of parallel cyclic reduction (Stone 1975) provided by CMSSL. The diagonals are setup in the preprocessing stage by calling `gen_banded_factor`. The solve stage is performed by calling `gen_banded_solve`.

To apply the boundary conditions, masks are pre-set which define the boundary of interest. The mask is a logical array of bits, each bit associated with a single processor, whose context (`true` or `false`) determines whether or not the result of the operation of the processor is actually used. For example, the following code fragment defines the mask for the boundaries of the physical domain.

```
logical mask(ni, nj, nk)
mask = .false.
mask(1:ni:ni-1, :, :)  = .true.
mask(:, 1:nj:nj-1, :)  = .true.
mask(:, :, 1:nk,nk-1) = .true.
```

where `ni`, `nj` and `nk` are the total number of grid points in each direction.

4.4.5 Code Performance

There is no facility on the CM-5 for measuring floating point operations. Therefore, computational performance in terms of MFLOPS is hard to measure precisely. A normalized CPU of $38\mu s$ was achieved for the numerical simulation of the laboratory-scale coastal upwelling flow (Narimousa and Maxworthy 1987) with a $80 \times 80 \times 256$ computation grid when thirty-two CM-5 processors were used. The normalized CPU for the serial version of the code (Zang 1993) running on a single processor of the Cray Y-MP was about $45\mu s$. In this context, the performance of the data parallel code on the CM-5 is unsatisfactory.

Several factors that can influence the performance are given below. The boundaries are a source of computational inefficiency on the CM-5 with SIMD implementation because many processors will be idle while a few processors perform the calculations associated with the boundary conditions. The cyclic reduction algorithm is computationally expensive, because it requires twice as many as floating point operations per grid point as the Thomas algorithm. The pressure Poisson solver is the most time-consuming part of the numerical algorithm. The slowest form of communication on the CM-5, send/get communication, which is required by the multigrid method when solving the Poisson equation, dominates the communication time and the total CPU time and contributes to the low overall performance. For the above reasons, we reached the conclusion that data parallel was not the best approach for the present study. The code performance of SPMD implementation using MPI (see Section 4.3) suggests that message passing was the correct approach for the present study.

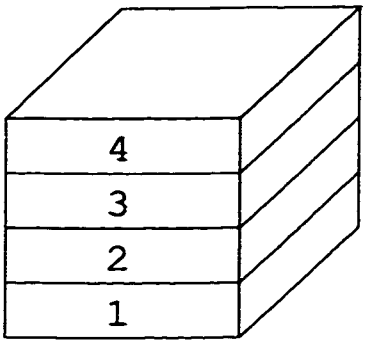

(a) 1-D partitioning

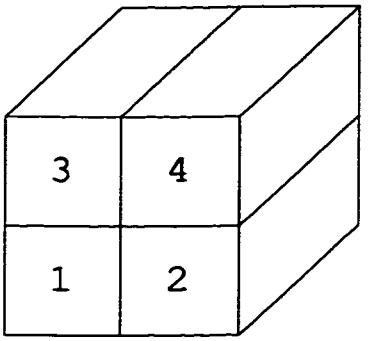

(b) 2-D partitioning

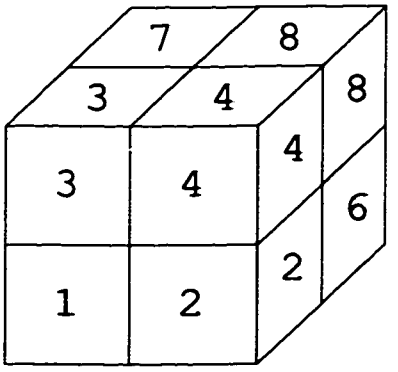

(c) 3-D partitioning

Figure 4.1: Grid partitioning alternatives

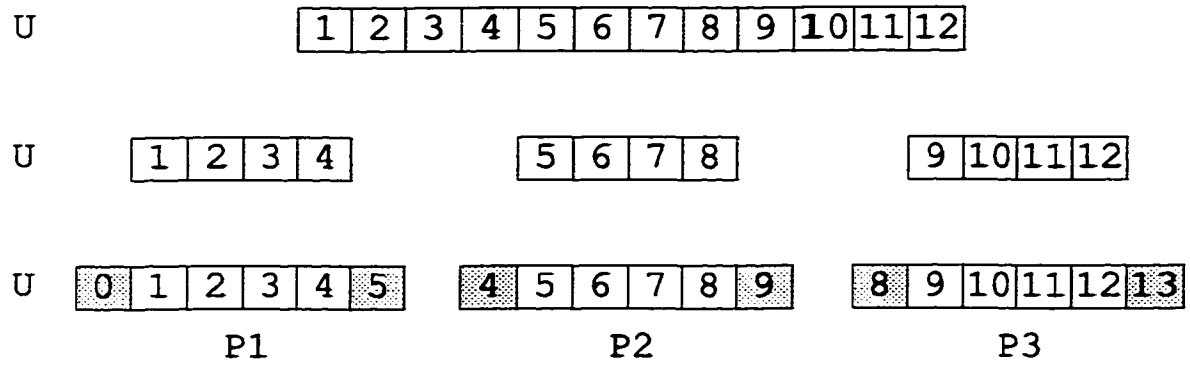

Figure 4.2: An illustration of the domain decomposition process.

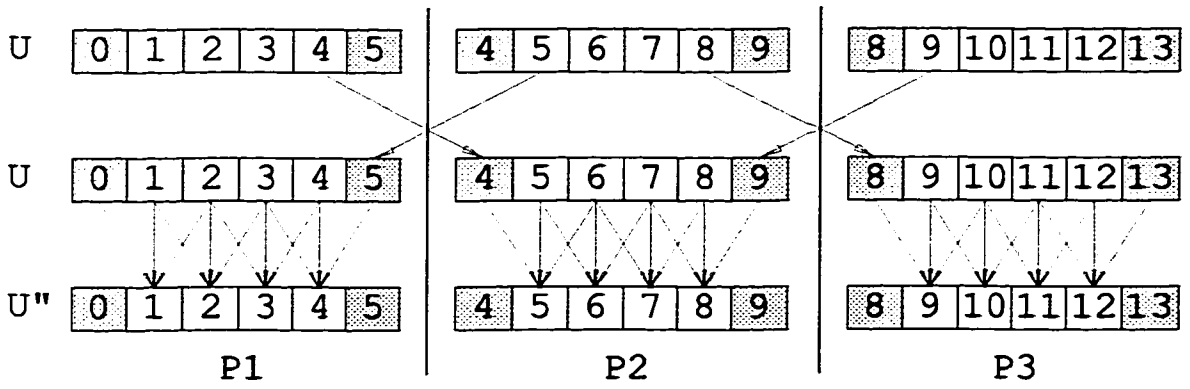

Figure 4.3: The separation of the communication and the computation.

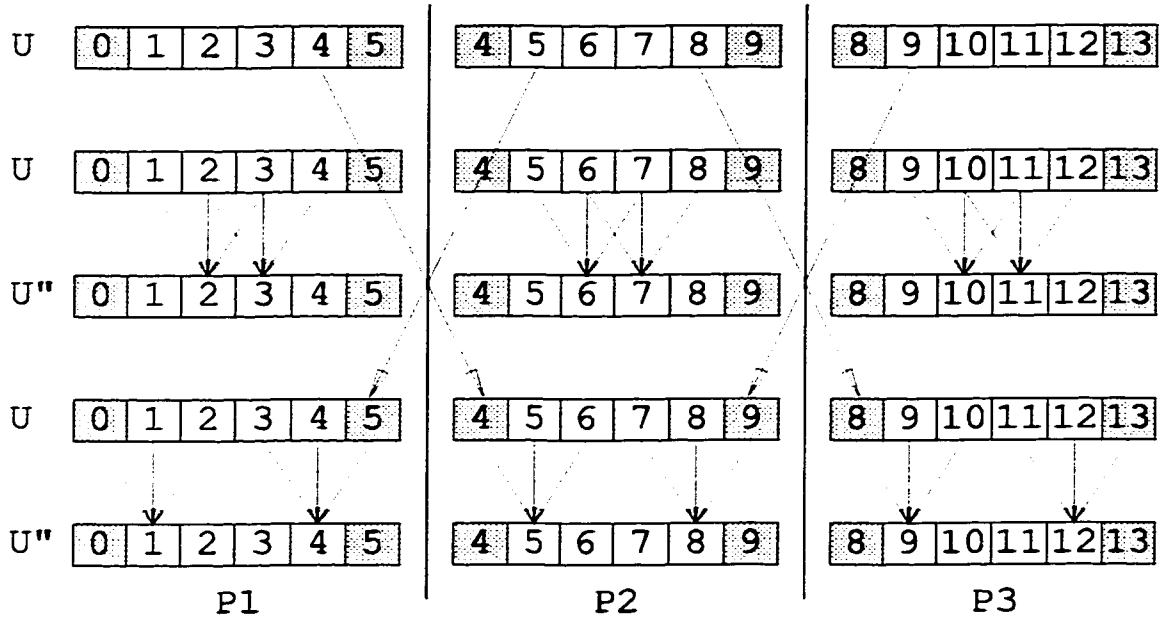

Figure 4.4: The overlap of the communication and the computation.

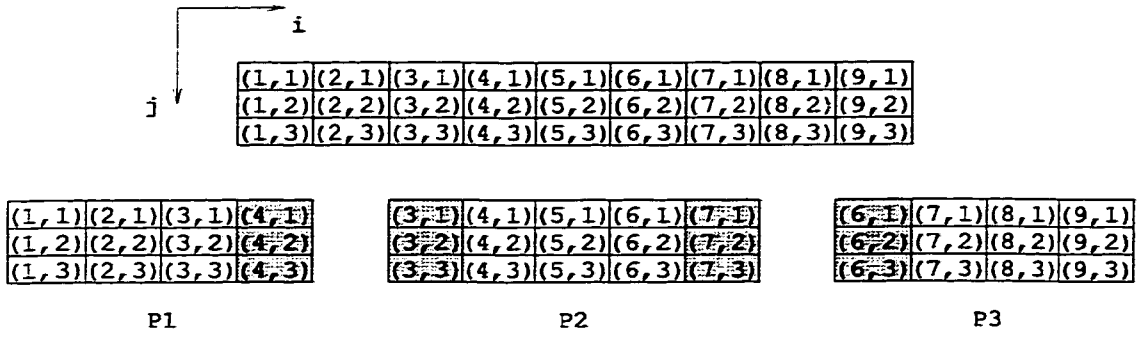

Figure 4.5: Domain decomposition of the 2-D problem.

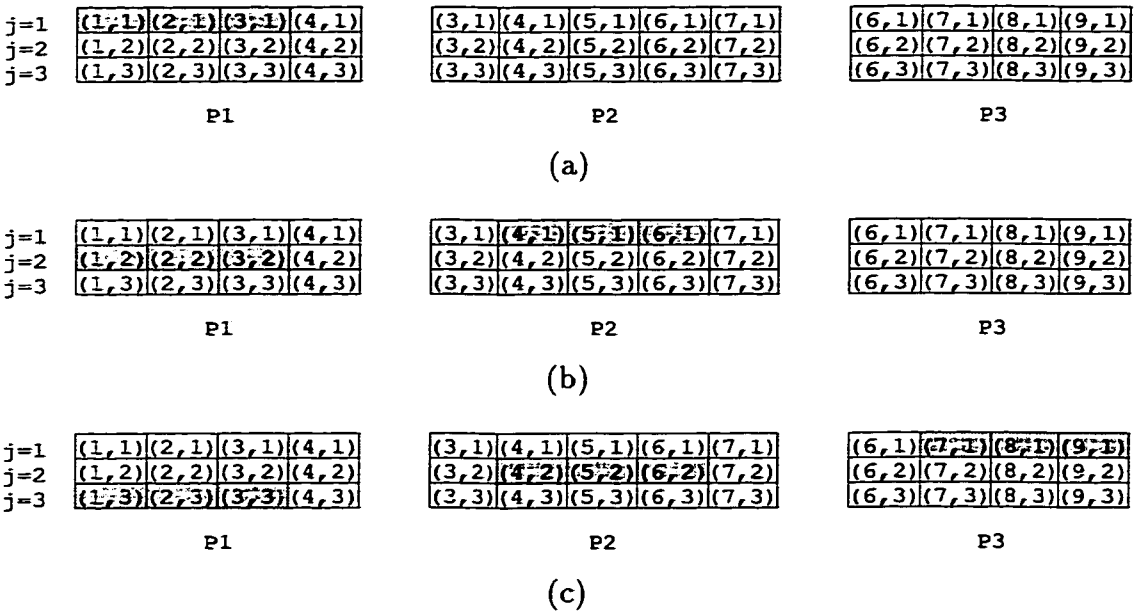

Figure 4.6: An illustration of the pipelined Thomas algorithm. The shaded area indicates the area that a processor is working on.

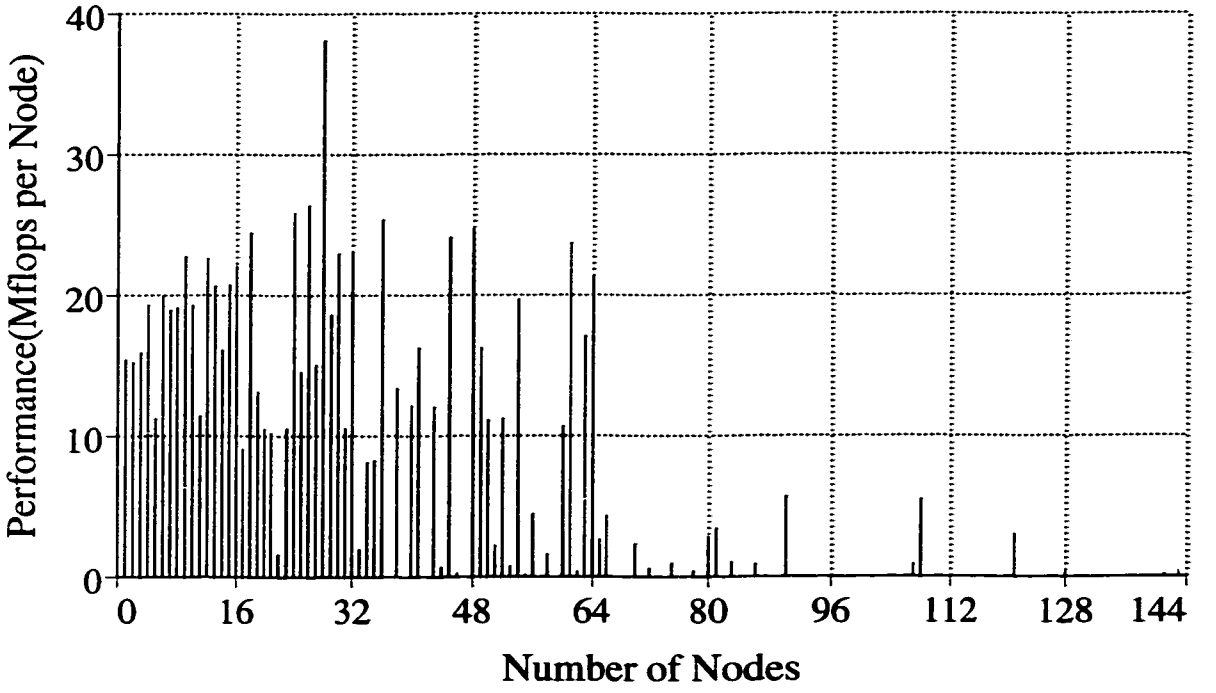

Figure 4.7: NASA SP2 batch job performance vs. nodes requested [Figure 3 of Bergeron (1998)].

Chapter 5

Large-Eddy Simulation of Turbulent Rotating Convective Flow

5.1 Introduction

Thermal convection in rotating fluids is important in many geophysical and engineering situations. Turbulent, rotating, convective flow arises when intense cooling at the ocean surface occurs in places, such as the Gulf of Lions in the Mediterranean and some areas of the polar seas, namely, the Greenland Sea, the Labrador Sea and the Weddell Sea. There are very few observations of convective events which allow an identification of the structure and scales of the flow. Nevertheless, turbulent convection in the open ocean is important due to its role in the transport of surface water to deep locations and ultimately in the large-scale thermohaline circulations, which in turn play a central part in determining global climate. During the past four decades, numerous analytical works, laboratory studies and numerical simulations have been performed on this subject.

The topic of the onset of thermal instability in horizontal layers of fluid heated from below without and with rotation about a vertical axis has been discussed in the second and third chapters of Chandrasekhar (1961). Analytical solutions of Rayleigh-Bénard convections with rigid-rigid, rigid-free and free-free horizontal boundaries are

also provided in Chandrasekhar (1961). Laboratory studies of rotating Rayleigh-Bénard convection have been done by Nakagawa and Frenzen (1955), Koschmieder (1966), Rossby (1969), and Buse and Heikes (1980). Three-dimensional numerical simulations of Bénard-like convections in a rotating frame have been performed by Somerville and Lipps (1973) and Hathaway and Somerville (1983).

The importance of rotation and its effect on the modeling of the relevant turbulent processes have been studied experimentally by Golitsyn (1981), Boubnov and Golitsyn (1986, 1990), Fernando *et al.* (1989, 1991), Maxworthy and Narimousa (1994), Coates and Ivey (1993, 1997), Coates *et al.* (1995), and Jacobs and Ivey (1998). The laboratory investigations were supported by numerical modeling efforts. Madec *et al.* (1991) parameterized the convective processes and used a hydrostatic model to focus on the dynamics of the large-scale flow driven by the vertical convection. Raasch and Etling (1991) applied a k-ϵ type of turbulent closure scheme to the case of turbulent convection subjected to strong background rotation. However, they did not take into account of the influence of background rotation in their sub-grid turbulence parameterization. Jones and Marshall (1993) studied the convection process in a homogeneous, rotating ocean using a non-hydrostatic model, but did not include all terms of the Coriolis force . In their study, the subgrid-scale transport process were parameterized by constant vertical and horizontal eddy diffusivities. Sander *et al.* (1995) developed a three-dimensional, non-hydrostatic model based on the primitive equations. The sub-grid turbulence in their study was taken into account through eddy viscosity and thermal diffusion, where the respective coefficients were taken as constant.

The two common problems with previous numerical simulations are insufficient grid resolution and poor turbulence models. The advent of massively parallel processing and the extensive efforts that have been put into the development of new large-eddy simulation models provide the possibility to perform large-scale computations of turbulent flows for complex geometries. The objective of this study is to

conduct a large-scale large-eddy simulation to complement an experimental study in investigating the fundamental mechanisms of a turbulent rotating convective flow.

5.2 Experiment of Jacobs and Ivey

Laboratory-scale experiments have been carried out by Ivey and Jacobs at the University of Western Australia to model the turbulent convection processes in an ocean driven by the energetic cooling at the ocean surface. In their experiment (Jacobs and Ivey 1998), the flow was inverted for experimental convenience so that heating at the bottom is used to drive the convective, rotating flow. All the experiments were conducted using water. Figure 5.1 is a schematic of the experimental apparatus. The experiments were conducted in a circular perspex tank of radius $R_o = 0.48$m. The circular tank was surrounded by a slightly larger outer tank, with the volume between the two tank walls filled with water at the same temperature as the water in the working section. The tank was fitted with a false bottom with built-in circular copper plate of radius $R_i = 0.2$m that acted as a heat exchanger. The copper plate formed the upper surface of a heat exchanger and could be heated uniformly by pumping hot fluid from a constant temperature bath through a circuit of pipes built into the copper plate. The plate was insulated on the sides and the bottom, so that heat could only escape through the top surface. The heat flux Q was determined by the measurements of the volume flow rates and temperature drop of the heated fluid passing through the heat exchanger. According to Jacobs and Ivey (1998), the heat flux Q could be determined with an accuracy of about 6%, and buoyancy flux with an accuracy up to 10%. The tank top was closed with a model of a shelf and slope with an angle $\alpha = 28°$ commencing at the same radius as the edge of the heated area. The top lid consists of a cellular perspex construction with air sealed in the interior, which is an adequate insulator. The distance H between the tank bottom and the shelf was 0.04 m. The entire assembly was mounted on a rotating table,

revolving counter-clockwise about the vertical axis at a constant rate Ω. Details of the experimental apparatus can be found in Jacobs and Ivey (1998).

5.3 Setup for the Numerical Simulations

Large-eddy simulations have been carried out under exactly the same conditions as the experiment except that a small cylinder of 0.02 m radius (R_h) was cut from the numerical domain to eliminate the coordinate singularity at the center for the numerical simulation. Figure 5.2 is a schematic of the setup for numerical simulation. In this simulation, the sub-grid dynamic mixed model (DMM) of Zang *et al.* (1993) was used.

5.3.1 Analytical Computation of the Grid Stretching and Mapping

When the coordinate transformation from physical space to computational space is performed, extra quantities, such as the inverse Jacobian J^{-1}, the mesh skewness tensor G_{mn} and $\partial\xi_m/\partial x_i$, will be introduced. Analytical stretching functions are used so that the above quantities are continuous in space. In order to have a smooth transition between the shelf and the slope, analytical mapping functions are also used in the present study.

The computational domain in the physical space (r, y, θ) can be mapped into a unit cube in the computational space $(\mathcal{R}, \mathcal{Y}, \Theta)$ by the following mapping functions:

$$\mathcal{R} = \frac{r - R_h}{R_b} \tag{5.1}$$

$$\mathcal{Y} = \frac{y}{H + \frac{\tan\alpha}{2A}\left[\log\frac{\cosh A(r-R_h-R_t)}{\cosh AR_t} - \log\frac{\cosh A(r-R_h-R_b+C)}{\cosh A(R_b-C)}\right]} \tag{5.2}$$

$$\Theta = \frac{\theta}{2\pi}, \tag{5.3}$$

where

$$R_t = R_i - R_h \tag{5.4}$$

$$R_b = R_o - R_h \tag{5.5}$$

$$C = 10\text{mm} \tag{5.6}$$

$$A = 0.4\text{mm}^{-1} \tag{5.7}$$

and

$$\mathcal{R} \in [0,1] \tag{5.8}$$

$$\mathcal{Y} \in [0,1] \tag{5.9}$$

$$\Theta \in [0,1]. \tag{5.10}$$

The grid points in the azimuthal direction of physical space (r, y, θ) are distributed uniformly due to the axisymmetric nature of the flow field. A uniform grid is also used in the vertical direction. In order to resolve the small scale flow structures inside the convected region, a non-uniform grid is used in the radial direction with grid points clustered in the constant-height shelf region and then stretching out radially. A section of the computational grid is illustrated in Figure 5.3. The grid points in the computational space (ξ, η, ζ) are distributed uniformly with grid size $\Delta\xi = \Delta\eta = \Delta\zeta = 1$. The following stretching functions are used,

$$\mathcal{R} = \left[\xi/N_\xi + \frac{c}{a}\log\frac{\cosh a(\xi/N_\xi - b)}{\cosh ab}\right] / \left[1 + \frac{c}{a}\log\frac{\cosh a(1-b)}{\cosh ab}\right] \tag{5.11}$$

$$\mathcal{Y} = \eta/N_\eta \tag{5.12}$$

$$\Theta = \zeta/N_\zeta, \tag{5.13}$$

where

$$\xi \in [0, N_\xi] \tag{5.14}$$

$$\eta \in [0, N_\eta] \tag{5.15}$$

$$\zeta \in [0, N_\zeta] \tag{5.16}$$

and N_ξ, N_η and N_ζ are the numbers of control volumes in the ξ-, η- and ζ-directions of the computational space. The values of the parameters used in the stretching function are

$$a = 6 \tag{5.17}$$

$$b = 1 \tag{5.18}$$

$$c = 0.8, \tag{5.19}$$

so that the stretching factor is less than 1.1 everywhere, which is consistent with the recommendation of Hodges (1997) regarding the maximum stretching factor.

In the physical space, the Cartesian coordinates (x, y, z) and cylindrical coordinates (r, y, θ) are related as follows (Figure 5.4):

$$x = r\cos\theta \tag{5.20}$$

$$y = y \tag{5.21}$$

$$z = r\sin\theta. \tag{5.22}$$

In summary, the relationship between the points in the physical space (x, y, z) and those in the computational space (ξ, η, ζ) are defined by Eqns. (5.11) to (5.13) and the following equations:

$$x = (R_h + R_b\mathcal{R})\cos(2\pi\Theta) \tag{5.23}$$

$$y = H\mathcal{Y} + \frac{\mathcal{Y}\tan\alpha}{2A}\left[\log\frac{\cosh A(R_b\mathcal{R}-R_t)}{\cosh AR_t} - \log\frac{\cosh A(R_b\mathcal{R}-R_b+C)}{\cosh A(R_b-C)}\right] \quad (5.24)$$

$$z = (R_h + R_b\mathcal{R})\sin(2\pi\Theta). \quad (5.25)$$

5.3.2 Initial and Boundary Conditions

The working fluid, *i.e.*, pure water, is initially at a uniform temperature T_i and is in solid body rotation with the tank. At time $t = 0$, a constant and uniform heat flux Q is applied to the bottom central disk. No-slip velocity boundary conditions are imposed at all solid walls. Except at the bottom central disk, where a constant and uniform heat flux Q is applied, the temperature boundary conditions for the inner vertical wall, the top lid and the bottom of the tank are obtained by assuming that those walls are adiabatic. A constant temperature, equal to the initial temperature T_i, is applied to the outer vertical wall. The buoyancy flux B can be related to the heat flux Q through $B = g\beta Q/(\rho C_p)$, with the thermal expansion coefficient $\beta = 2.5 \times 10^{-4}/°\mathrm{C}$, the gravitational acceleration constant $g = 9.81\mathrm{m/s}^2$, the density $\rho = 1000\mathrm{kg/m}^3$ and the specific heat at constant pressure $C_p = 4180$ J/(kg K).

5.4 Simulation Results

A number of simulation runs were performed covering three different angular velocities Ω and two different buoyancy fluxes B while the geometric parameters were fixed. A summary of the grid resolutions and physical parameters for the simulation runs is given in Table 5.1. The number of grid points for each case shown in Table 5.1 is for interior points. Two fictitious points outside the physical domain are added in each dimension in the simulations to facilitate implementing boundary conditions. Case Run1 to Case Run6 have the same physical parameters as the Experiment Run No. 14 of Jacobs and Ivey's experiment (Jacobs and Ivey 1998). An extensive grid resolution study has been conducted during the first six runs and led to the use of

up to twelve million grid points in the simulation. The difference between Case Run7 and Case Run6 is that the angular velocity Ω of Run7 is half of that of Run6. The difference between Case Run8 and Case Run6 is that the angular velocity Ω of Run8 is twice of that of Run6. The difference between Case Run9 and Case Run6 is that the buoyancy flux B of Run9 is twice of that of Run6. The following sections give a step-by-step description of the convection process.

5.4.1 Grid Resolution

Case Run1 to Case Run6 have the same physical parameters as the Experiment Run Number 14 of Jacobs and Ivey's experiment (Jacobs and Ivey 1998). A grid resolution study has been conducted during the first six runs. The temperature fields at t=46s obtained by using different number of vertical grid points have been compared in Figures 5.5 a, b and c. The temperature field with 128 vertical grid points shows little difference from the temperature field with 160 vertical grid points, suggesting that 128 grid points in the vertical direction are sufficient for the present study. The temperature fields at t=40s obtained by using different number of horizontal grid points have been compared in Figures 5.6 a, b and c. The results show that the number of rings remain unchanged when the horizontal grid points increases from 352 to 384, suggesting that 352 grid points in the horizontal direction have to be used. Jacobs and Ivey's experiment found less than ten azimuthal eddies for the present case. Two hundred and fifty-six grid points have been used in the azimuthal direction to resolve less than ten eddies.

5.4.2 Growth of the Conductive Layer

The working fluid is initially at uniform temperature T_i and is in solid body rotation with the tank. At time $t = 0$, a constant and uniform buoyancy flux B is applied to the bottom central disk. A thin thermal layer then forms immediately above the

heat source and grows diffusively with time. The thin thermal layer grows uniformly in the vertical direction except at the outer edge of the heated disk (Figure 5.7a). In response to the lateral temperature difference between the heated and ambient fluids at the outer edge of the heated disk, some radial exchanges take place with a thin layer of warm fluid just above the heat source moving radially out into the ambient fluid and the ambient fluid moving radially into heated region right above the thin layer of moving warm fluid (Figure 5.7b). As a direct result, a roll of warm water can be seen rising off the heated disk (Figure 5.7c).

The velocity profiles, shown in Figure 5.8, indicate that all the three velocity components are negligibly small within the thermal layer and, therefore, that a basic static state of heat conduction exists. Since molecular conduction dominates inside this thermal layer, we call it "the conductive layer". Temperature profiles in Figure 5.9 show that the angular velocity Ω has no effect on the growth of the conductive layer. In addition, temperature profiles for different buoyancy fluxes B at t=20s presented in Figure 5.10 show that the conductive layer thickness does not depend on the buoyancy flux B. A dimensionally correct scale for the conductive layer thickness $\delta(t)$ can be introduced as

$$\delta(t) \sim \sqrt{\kappa t}, \tag{5.26}$$

where κ is the molecular thermal diffusivity and t is the time. This scale is derived from the unsteady one-dimensional heat conduction equation.

The temperature profiles for Case Run6 at different times plotted against the non-dimensionalized vertical distance $y/\sqrt{\kappa t}$ are shown in Figure 5.11. All the curves approach the same non-dimensional thickness value, suggesting that $\sqrt{\kappa t}$ is the correct length scale for the conductive layer thickness.

5.4.3 Onset of the Rayleigh-Benard Convection

The temperature difference across the conductive layer increases as the layer thickness increases. When the temperature difference exceeds a critical value ΔT_c, the buoyancy of the fluid is able to overcome the dissipation caused by the viscosity and thermal diffusivity of the fluid, the basic static state becomes unstable and the convective instability, *i.e.*, the Rayleigh-Bénard convection, sets in. The Rayleigh number Ra is a non-dimensional measure of the vertical temperature difference across the layer that is necessary to overcome the dissipative influences of viscosity and heat conduction; Ra is given by

$$Ra = \beta g \Delta T \delta^3 / (\nu \kappa), \tag{5.27}$$

where ΔT is the temperature difference across the layer, δ the conductive layer thickness, β the thermal expansion coefficient, g the gravitational acceleration constant, ν the kinematic viscosity and κ the thermal diffusivity. The Taylor number Ta is a non-dimensional measure of the rotation rate of a fluid layer rotating with angular velocity Ω; Ta is defined as

$$Ta = 4\Omega^2 \delta^4 / \nu^2, \tag{5.28}$$

where ν is the kinematic viscosity and δ is the conductive layer thickness. The conductive layer thickness δ, instead of the distance H between the tank bottom and the shelf, is used here since a fluid particle has traveled only within the distance δ until Rayleigh-Bénard convection takes place. The onset of the Rayleigh-Bénard convection can be observed through the formation of circular concentric convective rolls (see Figure 5.12). An expanded side view of the velocity and temperature field (Figure 5.13) shows the warm water trapped in the convective rings rising from the bottom heat source and the cold water descending between them. Table 5.2 tabulates the values of the time t, the critical temperature difference ΔT_c, the corresponding critical Rayleigh number Ra_c, the layer thickness δ and Taylor number Ta when the onset of Rayleigh-Bénard convection occurs for different runs.

From Table 5.2, the following conclusions can be drawn :

(i) The time for the formation of the convective rings does not depend on the rotation rate Ω, but is determined by the supplied buoyancy flux B.

(ii) The critical Rayleigh number Ra_c dictates the onset Rayleigh-Bénard convection. For the current geometric configuration, the critical Rayleigh number Ra_c is found to be between 1.25×10^5 and 1.26×10^5 for all four simulation runs, *i.e.*, essentially constant.

The analytical solutions for three combinations of the horizontal boundary conditions, *i.e.*, the cases of two free boundaries, two rigid boundaries, and one rigid and one free boundary, are available for the thermal instability of a layer of fluid heated from below with or without rotation (Chandrasekhar 1961). Without rotation, the critical Rayleigh number Ra_c is found to be a different constant for different boundary conditions. Under the effect of rotation, Ra_c increases with the Taylor number Ta when Ta is greater than 10^3. When Ta is less than 10^3, the dependence of Ra_c on Ta is not significant. The present numerical study differs from the analytical work in the following respects:

(i) The horizontal boundary conditions of the present study do not fall into any of the three cases of the boundary conditions in the analytical work.

(ii) In the analytical work, a steady adverse temperature gradient is maintained within an infinite horizontal layer of fluid. The present numerical results (Figure 5.11) show clearly an unsteady, non-linear temperature distribution within the conductive layer.

Although the numerical result can not be compared to the analytical result quantitatively, the analytical result should serve as a guide to the numerical results. From Table 5.2, the Taylor numbers are less than 5×10^3 for all four simulation runs. The finding of that the critical Rayleigh number Ra_c is essentially constant for all four simulation runs is supported by the analytical solution.

5.4.4 Development of the Convective Rings

The convective ring development stage in this study refers to the process from the initial formation of the convective rings near the bottom of the tank to the arrival of the convective rings at the top shelf. At t=40s, the presence of radially uniform convective rings is apparent for Cases Run6 to Run8 (Figures 5.12 and 5.14a, b and c). By t=55s, the continuing penetration of the rings is evident, and some of the rings have already reached the top shelf (Figures 5.15a, b and c). The simulation results in Figure 5.15 show that the horizontal motions are directly affected by the rotation. As the angular velocity Ω decreases, the horizontal velocity components are less restrained, and some blobs of warm water are already detached from the rings (Figures 5.15a and b). The rings are also more deformed in the vertical direction with the decrease of the angular velocity Ω, resulting in a radially irregular ring pattern. Despite the non-uniform pattern in the vertical and radial directions, the rings are still axisymmetric in the azimuthal direction (Figure 5.16). A comparison of results at t=55s for different rotation rates (Figures 5.15a, b and c) shows that rotation has little effect on the time it takes for the rings to reach the top shelf, suggesting that the time scale for the ring development stage is independent of the angular velocity Ω.

The temperature fields of Case Run9 (Figures 5.17a and b) with twice the buoyancy flux of Cases Run6 to Run8 show that increasing the buoyancy flux reduces the time for the rings to reach the top shelf. As suggested by Jacobs and Ivey (1998), the time scale characterizing the convective ring development stage is given by the time it takes for a fluid particle with a typical vertical convective velocity $(BH)^{1/3}$ to travel over the vertical length scale H :

$$t_v \sim H/(BH)^{1/3} = (H^2/B)^{1/3}. \tag{5.29}$$

From the time of the onset of the convective instability for Cases Run6 and Run9

tabulated in Table 5.1 and by observation of the time near the end of the ring development stage for Cases Run6 and Run9 (Figures 5.15b and 5.17b), the ratio of the two time scales $t_{vRun6}/t_{vRun9}[= (55s-35s)/(40s-23s) = 1.2]$ is approximately equal to cube root of the ratio of the buoyancy flux $(B_{Run9}/B_{Run7})^{1/3}(= 1.3)$, suggesting that $t_v \sim (H^2/B)^{1/3}$ is the correct time scale for the ring development stage within the current angular velocity range.

The horizontal velocity components are more restrained with increasing rotation rate, and the lateral temperature difference increases near the edges of the heat source with increasing buoyancy flux, therefore the radial momentum and heat exchanges near the edges of the heated disk are different for the system under different rotation rates and subjected to different buoyancy fluxes. As a direct result, flow patterns and temperature distributions near the edges of the heated disk are different from early in the simulation (Figures 5.14a, b, c and 5.17a). In terms of the number of the rings observed for different rotation rates and buoyancy fluxes, it is only reasonable to make comparisons within a region that is away from the edges of the heated disk. From Figures 5.14a, b, c and Figure 5.17a, a uniform ring pattern can be seen for the radius range from 0.03m to 0.17m in all four simulations (Cases Run6 to Run9). Within that radius range, the number of observed rings is 17 for all the four runs for the current geometric configurations, suggesting that the number of rings formed (or the critical wavelength λ_c) depends only on the geometric parameters. The critical wavelength λ_c is the width of the layer divided by the number of rings when the critical Rayleigh number Ra_c occurs. As pointed out by Koschmieder (1993), little work has been devoted to the measurements of the critical wavelength λ_c (therefore the number of the rings) although λ_c is a fundamental feature of the Rayleigh-Bénard convection. There seem to be no reports in the literature about specific efforts to measure λ_c. Because the experiment carried out by Jacobs and Ivey (1998) did not study the early stages of the convection process, no comparison can be made at this point.

5.4.5 Generation of the Convective Cells

As the convective rings reach the top shelf, a chimney of the convected fluid, which is mainly confined to the volume defined by the heated disk, is formed. Once the convected fluids reach the top shelf, they begin to spread out along the top shelf. Figure 5.18 shows that the axisymmetric ring structure still holds at t=140s. Figures 5.19 to 5.22 show a sequences of the side views of the temperature and instantaneous velocity fields[1], and illustrate the development of the temperature and velocity fields with time. Due to the existence of the adjacent slope, and therefore the along-slope component of the gravitational acceleration constant, the convected fluid is transported away along the top slope within a thin layer. Some radial adjustments also occur at the bottom of the tank with colder ambient fluid moving radially in over the heated disk. An inclined front dividing the heated and ambient fluid is observed, and it evolves with time after the collapse of the chimney of the convected fluid. Successive top views of the temperature field at corresponding times are shown in Figures 5.23 to 5.26 to illustrate the evolution of the temperature field with time. At t=140s, small wavy perturbations are observed on some of the convective rings (Figure 5.23). The amplitude of the perturbations grows with time and some rings have broken into vortices by t=160s (Figure 5.24). By t=180s, the convective rings have completely broken down into vortices (Figure 5.25). The convective vortices already begin to merge at t=200s (Figure 5.26). Even though the temperature distribution at t=200s (Figure 5.22a) is more uniform than that at t=140s (Figure 5.19a) due to the horizontal mixing, individual convective cells are still being seen rising from the heated disk (Figure 5.26). The individual elements of the convective cell consist of an ascending core in the middle surrounded by a cylindrical surface on which descending motions are observed (Figure 5.22).

The horizontal characteristics of the convective cells (vortices) can be seen from

[1]The velocity vectors in the side view velocity field plots in this chapter are plotted at every third point in the radial direction, at every seventh point in the vertical direction.

the horizontal slices of velocity field[2] cut at three different vertical levels (5mm, 20mm and 35mm, in Figures 5.27 to 5.29, respectively). By t=180s, a number of small scale convective vortices is clearly visible at the lower level of the tank (5mm level) (Figure 5.27) above the heated disk . At this level, most of the cells are rotating cyclonically. Away from the heated disk, there is a quiescent region. Between the two regions, an azimuthal rim current which flows in a cyclonic direction is already developed. The rim current is perturbed by the individual vortices. As explained by Coates *et al.* (1995), the incoming ambient flow at the bottom of the tank must speed up in order to conserve angular momentum and hence acquires a cyclonic rotation. The opposite is true for the rim current at the upper level of the tank. Figure 5.29 shows that the rim current at the 35mm level indeed flows in the anti-cyclonic direction. Figure 5.29 also shows that the outlines of the individual convective cells at the 35mm level are not as clear as those at the 5mm level and the vortices now have no preferred direction of rotation. As pointed out by Nakagawa and Frenzen (1955), the direction of the horizontal circulation of each cell is that appropriate to the conservation of angular momentum in the divergent or convergent field. At the mid-height of the tank (20mm level), there is no distinguished rim current and only the general outline of the convective cells can be seen (Figure 5.28). Three horizontal slices of the velocity field, cut at the same three different vertical levels (5mm, 20mm and 35mm), are shown in Figures 5.30 to 5.32 for t=200s. The merging of convective cells is evident at the 5mm level. The rim currents both at the 5mm and 35 mm levels, are stronger, and the convective cells at all the three levels are more energetic. The along-front wave-like instability appears to grow with time. By t=200s, the horizontally axisymmetric flow pattern (Figure 5.18) has fully evolved into a quasi-2D vortex field (Figure 5.33). A similar evolution process was also observed in the experiments of Boubnov and Golitsyn (1986).

[2]The velocity vectors in the top view velocity field plots in this chapter are plotted at every sixth point in the radial direction and at every point in the azimuthal direction.

5.4.6 Development of the Baroclinic Instability

As mentioned before, the rim current is already perturbed by individual vortices by t=180s (Figure 5.27). The vertical temperature fields at later times (Figures 5.34a and 5.35a) show that the horizontal temperature difference between the convected and ambient fluid increases with time. The lateral temperature (density) difference increases with time, and so does the available potential energy. This available potential energy is the energy source for baroclinic instability (c.f., Jacobs and Ivey 1998). Therefore, the increasing lateral temperature gradient leads the rim current to undergo a baroclinic instability, which is forced by the individual vortices of the convective flow. The vertical velocity fields (Figures 5.34b and 5.35b) show that both the radial outflow at the top shelf and the inflow at the bottom have become stronger with time. As shown in both the velocity field (Figures 5.36 to 5.39) and the temperature field (Figures 5.40 and 5.41), the instability grows in amplitude with time, while the number of the baroclinic eddies formed around the edge of the heated disk decreases with time. A close examination of the horizontal velocity field at t=240s (Figure 5.36) reveals that each baroclinic eddy is made up of a number of individual convective vortices. The shape of the eddies are somewhat different at different vertical levels, *i.e.,* the eddies at the lower level have narrow heads (Figure 5.37) and the eddies at the higher level have full round heads (Figure 5.39).

Continuous temperature-time series were obtained at two fixed positions in the tank, *i.e.,* r/R_i=0.5, 0.75 and $y/H = 0.75$. Figure 5.42 shows that the fluid is well mixed horizontally within the convected region at y/H=0.75 level from early on and therefore there was little horizontal temperature difference between the two radial locations (r/R_i=0.5, 0.75 and $y/H = 0.75$) within the convected region. Figure 5.43 compares the temperature-time history obtained by numerical simulation at two radial locations with an angular separation of 90 degrees (r/R_i=0.75 and y/H=0.75) with the experimental data collected at the same radial location (r/R_i=0.75 and

y/H=0.75) by Jacobs and Ivey (1998). Except for the spike between 100s and 120s in the experimental data, which might be caused by uncertainty in the experiment or the ramp up of the plate heating, the simulation result follows the trend of the experimental data well. For time beyond 280s, the differences between the experimental data and simulation results are simply due to the fact that the experimental probes and the simulation probes were located at the different parts of the baroclinic eddies at a given time.

There are conflicting results regarding whether the density anomaly between the convected and ambient regions depends on the system rotation rate. Jones and Marshall (1993), Chapman and Gawarkiewicz (1997) and Jacobs and Ivey (1998) all found such a dependency. However, Brickman (1995) and Narimousa (1997) reached the conclusion that the final density anomaly is independent of the background rotation in a constant depth ocean. A comparison of the side view of the temperature and velocity field for two cases (Case Run6 and Case Run8) with different system rotation rates (Figures 5.35 and 5.44) shows that the lateral heat and momentum exchanges are more restrained for higher rotation rates. Figure 5.45 shows the continuous temperature-time history for Cases Run6 and Run8, in which exact the same conditions were maintained except for the different rotation rates. The temperature is consistently higher for the higher rotation rate case, indicating clearly that the temperature difference, and therefore the density anomaly, between the convected and ambient regions depends on the rotation rate.

By the comparison of the horizontal velocity fields at the same level for two different rotating rates (Cases Run6 and Run8), it is clear that the size of the baroclinic eddies depends on the rotation rate Ω of the system. The wavelength λ of the baroclinic eddies is found to be a function of the Rossby deformation radius R_D (Jacobs and Ivey 1998), which is given by

$$R_D = \frac{\sqrt{g'H}}{2\Omega} \tag{5.30}$$

where $g' = g\beta\Delta T$, β is the thermal expansion coefficient, ΔT is the average temperature increase within the convected region, Ω is the system rotation rate, and H is the distance between the tank bottom and the top shelf.

The number of baroclinic eddies observed by the Jacobs of Ivey (1998) was six at y=20mm level for Case Run6. In their experiment, the flow pattern was obtained by injecting fluorescent dye in the convective region. Their observed flow field resembled more or less the simulated temperature field. There appear to be six baroclinic eddies in the simulation result for the temperature field at t=280 (Figure 5.41) as well. However, a close look at the velocity fields at at the same time and the same vertical level reveals (Figure 5.38) that there may be as many as nine instead of six baroclinic eddies formed around the rim of the heated disk. The nine eddies can be seen more clearly at the lower vertical level (Figure 5.37), yielding a correlation of $\lambda = 4.3R_D$. For Case Run9, twelve baroclinic eddies were found at t=280s (Figure 5.46), which leads to a correlation of $\lambda = 5.8R_D$. Due to the difference in the number of eddies observed in the simulation and the experimental results, the correlation constants found in the two numerical simulation cases are lower than those found by Jacobs and Ivey (1998), who reported a constant of 5.9 ± 0.3. The correlation constant found by present study falls within the experimental range of Saunders (1973) who indicated a constant of 4.3 ± 0.8, the experimental range of Brickman (1995) who found a constant of 5.7 ± 0.9 and the numerical result of Gawarkiewicz and Chapman(1995) who found a constant of 5.

5.4.7 Transfer of the Kinetic Energy

The resolved kinetic energy is defined as

$$\frac{\overline{q}^2}{2} = \frac{\overline{u_i}\overline{u_i}}{2}. \tag{5.31}$$

The transport equation for $\overline{q}^2/2$ can be derived by multiplying the momentum equation [Eqn. (2.41)] by $\overline{u}_i$. Thus, we have

$$\frac{\partial}{\partial t}\left(\frac{1}{2}\overline{q}^2\right)+\frac{\partial}{\partial x_j}\left(\overline{u}_j\frac{\overline{q}^2}{2}\right) = -\frac{\partial}{\partial x_j}\left[\overline{p}\,\overline{u}_j-\overline{u}_i\tau_{ij}+\nu\frac{\partial}{\partial x_j}\left(\frac{\overline{q}^2}{2}\right)\right]-g\beta(T-T_0)\overline{u}_2 - \nu\frac{\partial\overline{u}_i}{\partial x_j}\frac{\partial\overline{u}_i}{\partial x_j}+\tau_{ij}\overline{S}_{ij}, \tag{5.32}$$

where $\overline{S}_{ij}$ is the resolved strain-rate tensor. The last two terms on the right hand side of Eqn. (5.32) represent the viscous dissipation (ϵ_v) and SGS dissipation (ϵ_{sgs}) terms. For the dynamic mixed model (Zang *et al.* 1993) introduced in Chapter 3 and used in this chapter, τ_{ij} is

$$\tau_{ij}=-2\nu_T\overline{S}_{ij}+L^m_{ij}, \tag{5.33}$$

and the resulting expression for ϵ_{sgs} is

$$\epsilon_{sgs}=-2\nu_T\overline{S}_{ij}\overline{S}_{ij}+L^m_{ij}\overline{S}_{ij}. \tag{5.34}$$

When ϵ_{sgs} is negative, energy is transferred from the resolved scales to the sub-grid scales; this is denoted as "forward scatter". On the contrary, when ϵ_{sgs} is positive, energy is fed into the resolved scales from the sub-grid scales, which is called "backscatter". Examination of the energy dissipation constituents and the energy transfer between the resolved and the sub-grid scales provides information about the effect of the SGS model.

The ratio of SGS to viscous dissipation at t=280s for case Run6 is shown in Figure 5.47. The area around the inclined front (Figure 5.35) which divides the heated and ambient fluid is the location where SGS dissipation is the the largest, being up to 40% of the total dissipation. Throughout other locations within the convected region, the SGS dissipation represents a minor fraction of the total dissipation. The SGS dissipation (ϵ_{sgs}) at t=280s for case Run6 is shown in figure 5.48. In Figure

5.48, in order to highlight the forward and backscatter regions, ϵ_{sgs} has been non-dimensionalized by the volume average of the molecular viscous dissipation, $\epsilon_v = < \nu \frac{\partial \overline{u}_i}{\partial x_j} \frac{\partial \overline{u}_i}{\partial x_j} >$, where $< \cdot >$ denotes the average over the whole domain. Figure 5.48 shows that interaction between the resolved and the sub-grid scales is again strong near the lower part of the inclined front (Figure 5.35), resulting in both forward and backward energy transfer. Forward scatter appears in the most of the other locations within the convected region.

5.5 Summary

This study provided a step-by-step precise description of the development of a turbulent rotating convective flow. The present simulations were able to show for the first time the detailed temporal evolution and spatial structure of the three-dimensional convective flow field. The simulation results also were in reasonable agreement with the experimental data from an experiment by Jacobs and Ivey (1998). The following are the findings for each stage of the convection process:

- The Growth of the Conductive Layer

  A basic static state of heat conduction exists within a thin thermal layer - the conductive layer. A correct length scale for the thickness of the conductive layer is $\delta(t) \sim \sqrt{\kappa t}$.

- The Onset of Rayleigh-Bénard Convection

  The time for the formation of the convective rings is determined only by the supplied buoyancy flux B. The critical Rayleigh number Ra_c dictates the onset Rayleigh-Bénard convection, and is found here to be essentially independent of rotation rate and buoyancy fluxes.

- The Development of the Convective Rings

The time scale characterizing the convective ring development stage is given by $t \sim (H^2/B)^{1/3}$.

- The Generation of the Convective Cells

  The horizontally axisymmetric ring pattern breaks down and evolves into a quasi-2D vortex field. A rim current develops around the rim of the heated disk as a result of the Coriolis force.

- The Development of the Baroclinic Instability

  The density anomaly depends on the system rotation rate Ω. The wavelength of the baroclinic eddies relates to the Rossby deformation radius as $\lambda = cR_D$. The correlation constant c for present study is between 4.3 and 5.8.

- The Transfer of the Kinetic Energy

  The SGS effect is significant around the inclined interface that divides the heated and ambient fluid.

Several questions remain unanswered. The precise nature of the mechanism that causes the breakdown of the convective rings and the formation of the individual convective cells is unclear. In the turbulent rotating convective flow, the density anomaly is thought to depend on the ratio R/H of the radius of the heated disk to the distance between the tank bottom and the shelf. However, it is difficult to create an aspect ratio R/H larger than 5-8 in the existing rotating convective flow laboratory setup. Thus, it would be desirable to explore the case for R/H $>$ 10 numerically and to determine the dependence of the density anomaly on the ratio R/H in the future work. The effect of changing the bottom slope on the size of the baroclinic eddies could also be investigated by numerical simulations.

Table 5.1: Grid resolutions and physical parameters of rotating convection flow simulations

Case	Grid $N_r \times N_y \times N_\theta$	Ω rad/s	$B \times 10^6$ m^2/s^3
Run1	128 × 96 × 256	0.2	1.57
Run2	128 × 128 × 256	0.2	1.57
Run3	128 × 160 × 256	0.2	1.57
Run4	320 × 128 × 256	0.2	1.57
Run5	384 × 128 × 256	0.2	1.57
Run6	352 × 128 × 256	0.2	1.57
Run7	352 × 128 × 256	0.1	1.57
Run8	352 × 128 × 256	0.4	1.57
Run9	352 × 128 × 256	0.2	3.14

Table 5.2: Values observed at the onset of Rayleigh-Bénard convection

Case	t (s)	$\Delta T_c(°C)$	δ(mm)	$Ra_c \times 10^5$	$Ta \times 10^3$
Run6	35	5.3	9.2	1.25	1.1
Run7	35	5.3	9.2	1.25	0.3
Run8	35	5.3	9.2	1.25	4.6
Run9	23	8.5	8.2	1.26	0.7

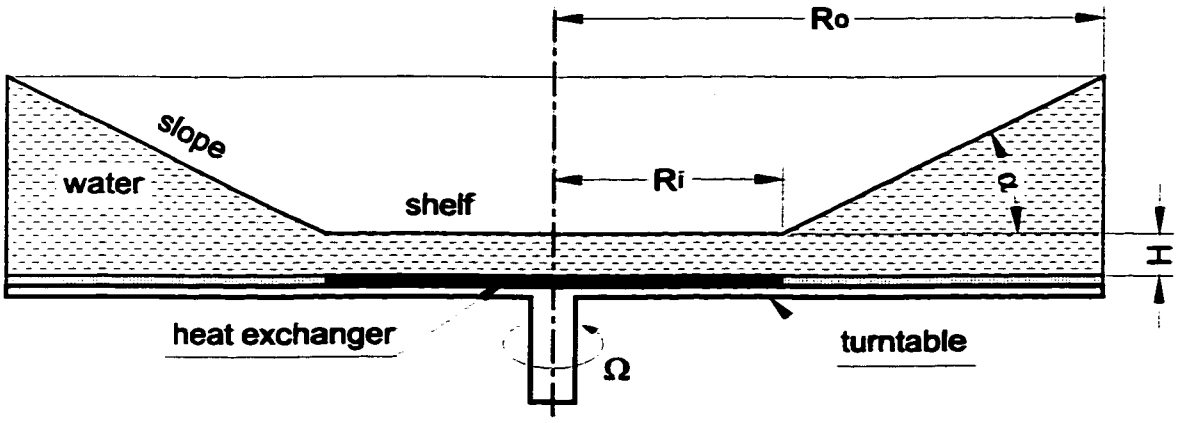

Figure 5.1: A schematic of the cross-section of the experimental apparatus.

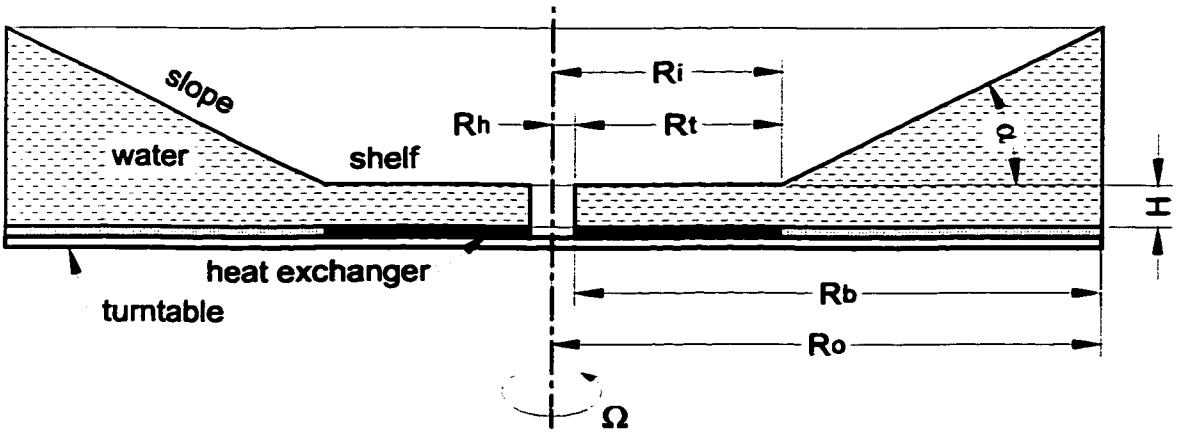

Figure 5.2: A schematic of the setup for numerical simulation.

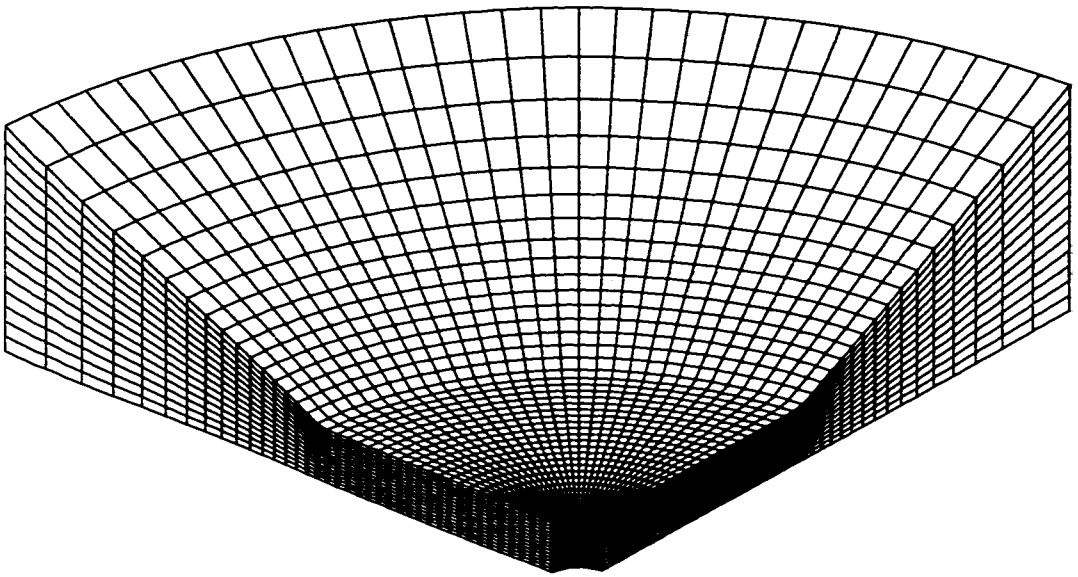

Figure 5.3: An illustration of a section of the computational grid.

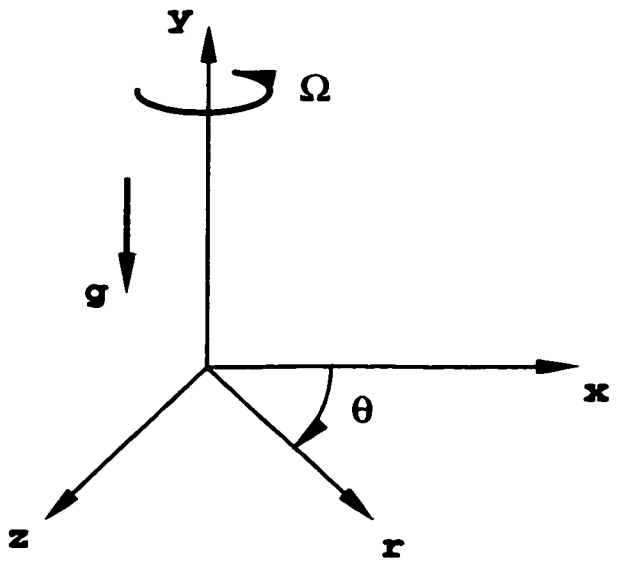

Figure 5.4: Coordinate diagram.

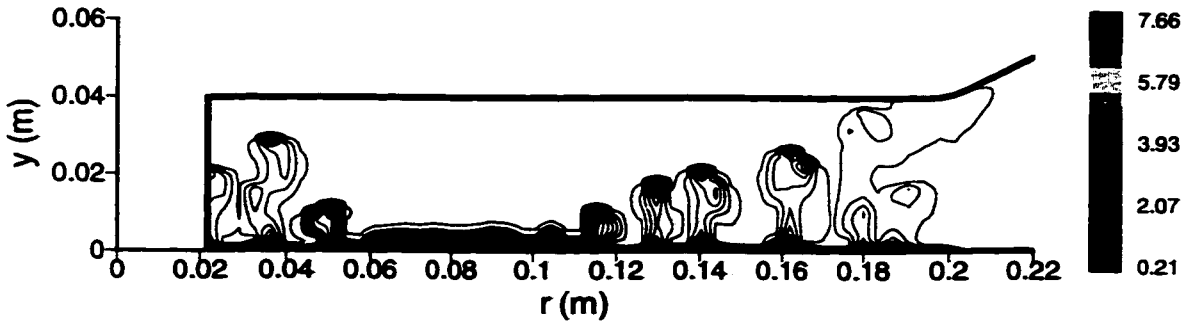

(a) Grid size $128 \times 96 \times 256$

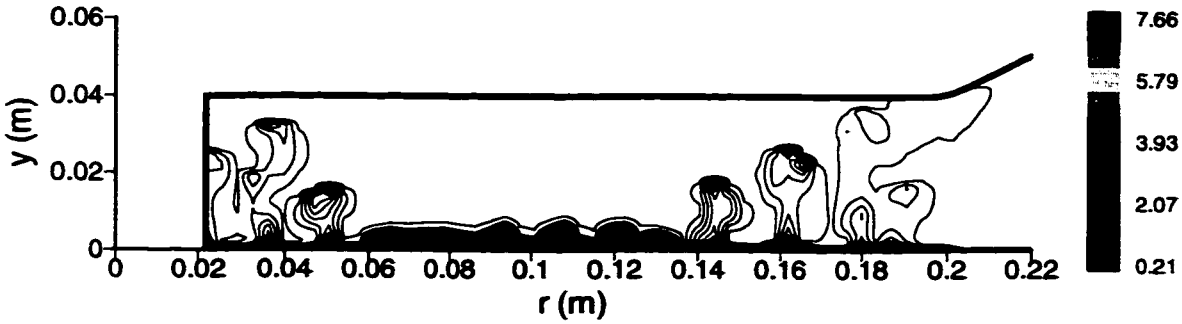

(b) Grid size $128 \times 128 \times 256$

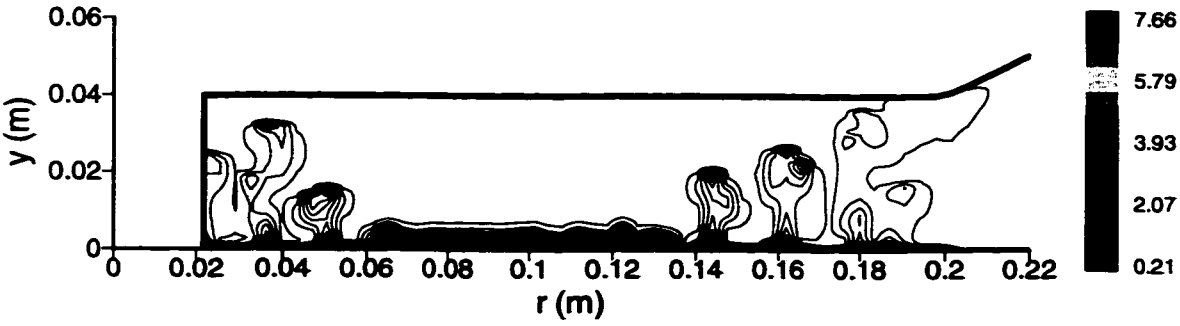

(c) Grid size $128 \times 160 \times 256$

Figure 5.5: Side view of the temperature field for $\Omega = 0.2$ rad/s, $B = 1.57 \times 10^{-6}$ m^2/s^3 at t=46s.

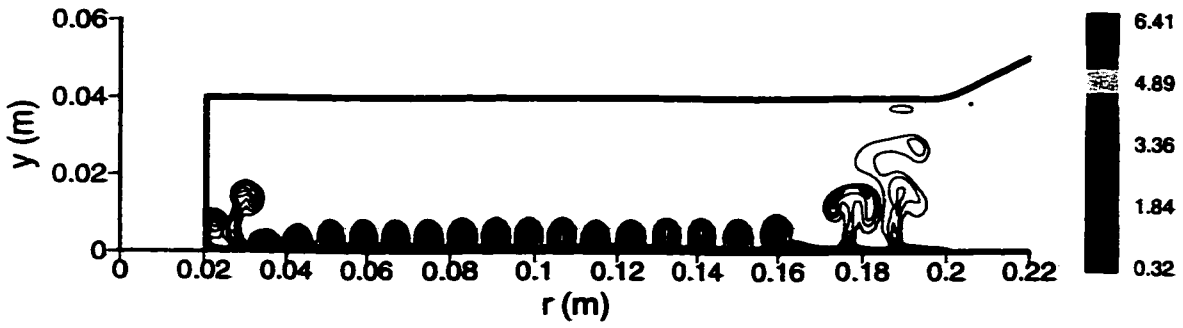

(a) Grid size 320 × 128 × 256

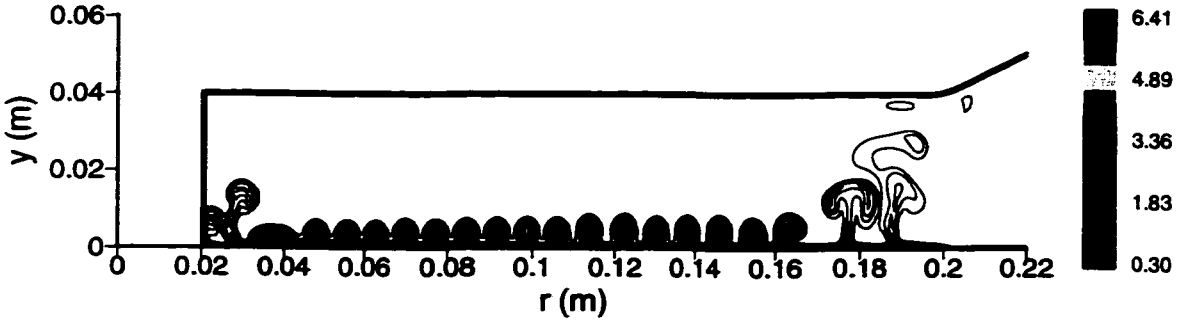

(b) Grid size 352 × 128 × 256

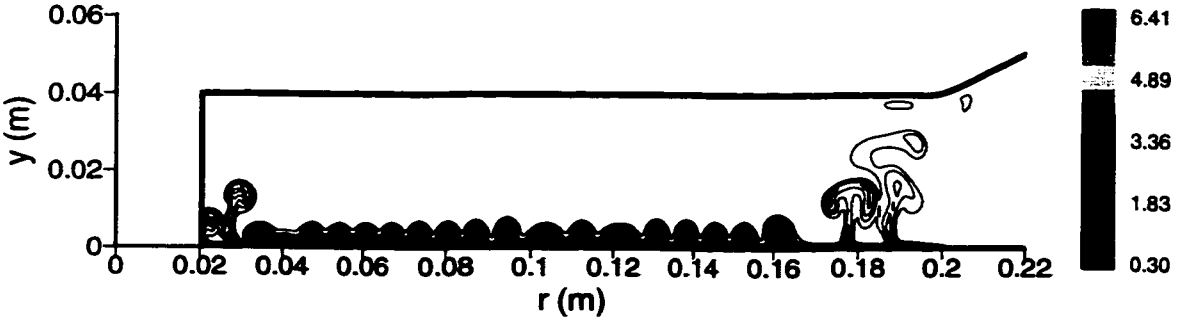

(c) Grid size 384 × 128 × 256

Figure 5.6: Side view of the temperature field for $\Omega = 0.2$ rad/s, $B = 1.57 \times 10^{-6}$ m^2/s^3 at t=40s.

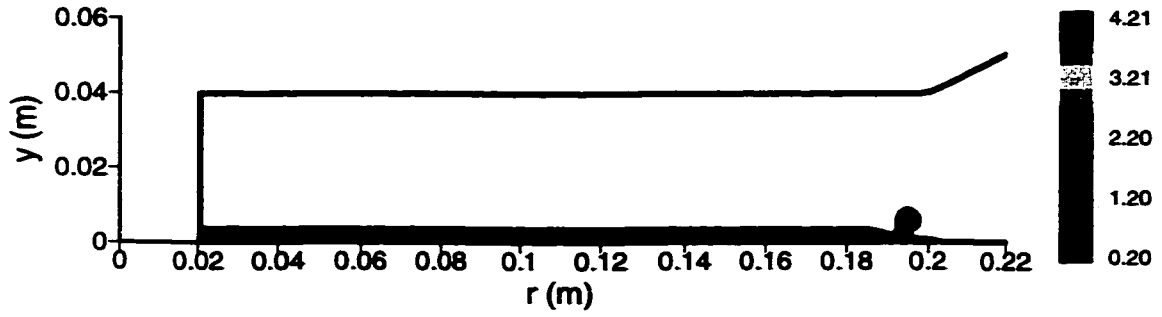

(a)

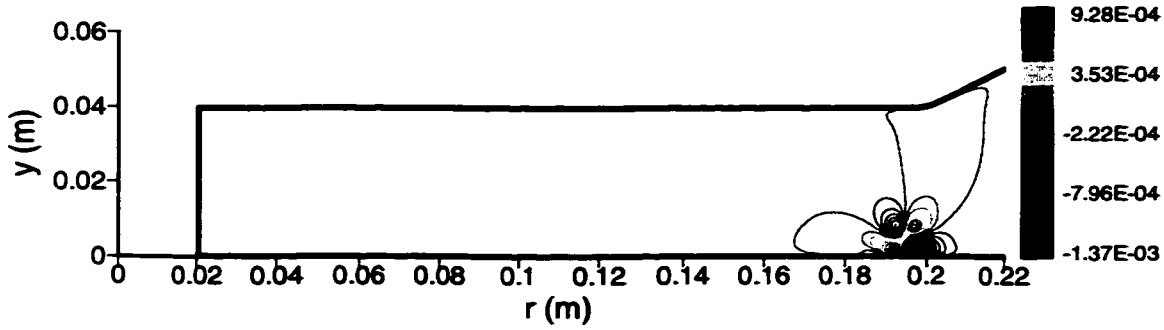

(b)

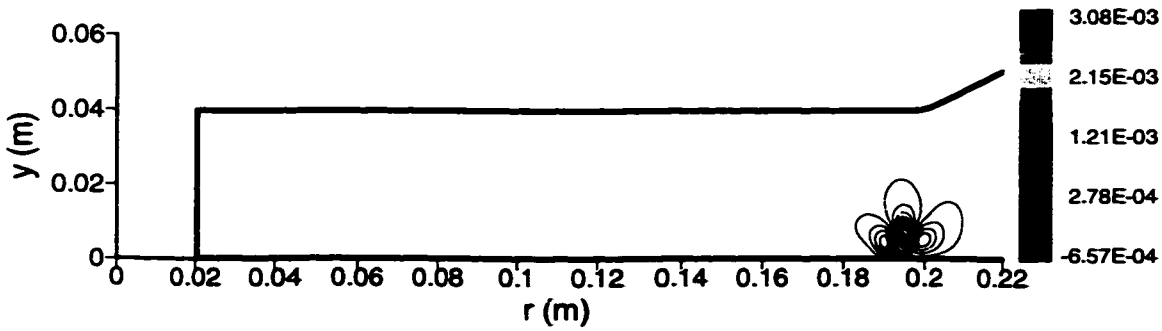

(c)

Figure 5.7: Side view of (a) temperature field, (b) radial velocity field and (c) vertical velocity field at t=20s for $\Omega = 0.2$ rad/s, $B = 1.57 \times 10^{-6}$ m^2/s^3 (Case Run6).

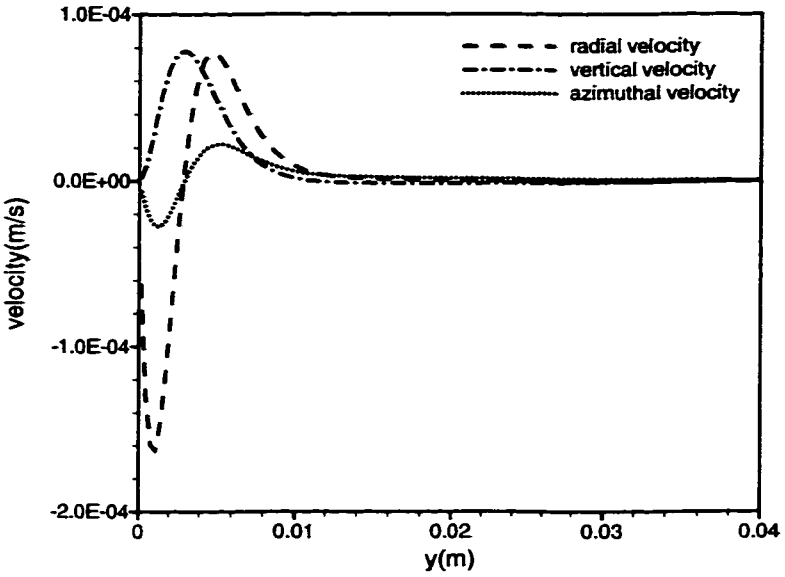

Figure 5.8: Velocity profiles at r/R_i = 0.5 and t=35s (Case Run6).

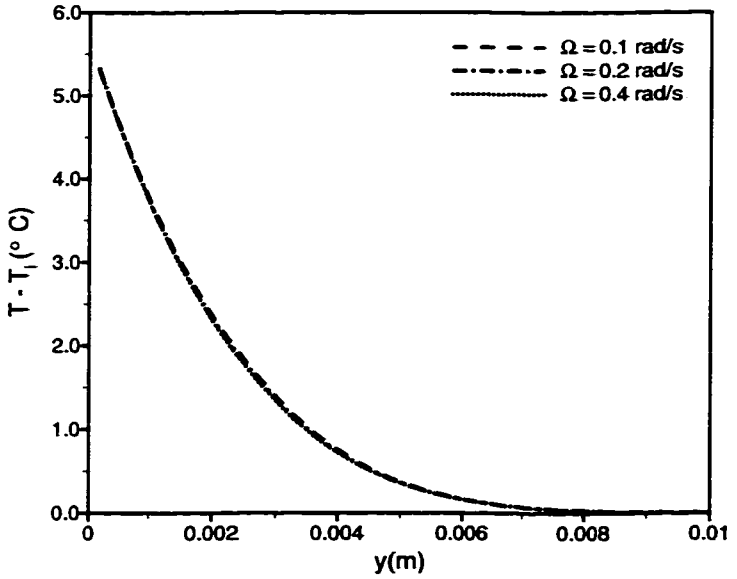

Figure 5.9: Temperature profiles at r/R_i = 0.5 and t=35s for different angular velocities Ω (Cases Run6, Run7 and Run8).

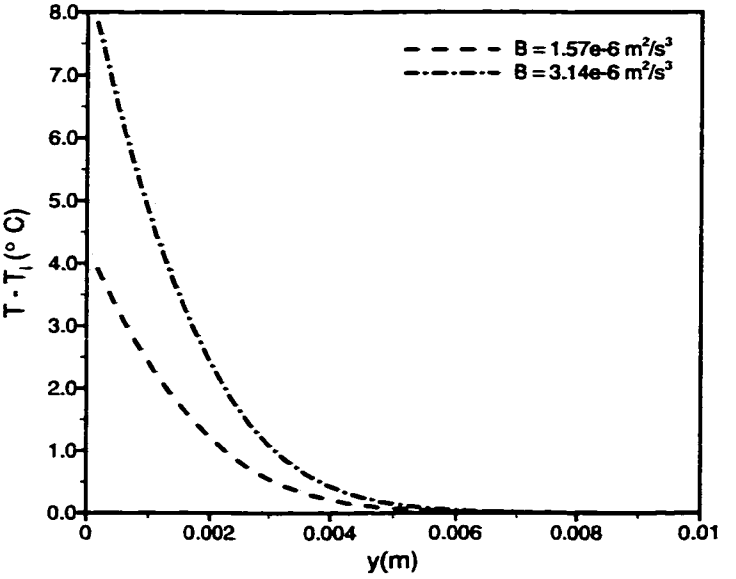

Figure 5.10: Temperature profiles at $r/R_i = 0.5$ and t=20s for different buoyancy fluxes B (Cases Run6 and Run9).

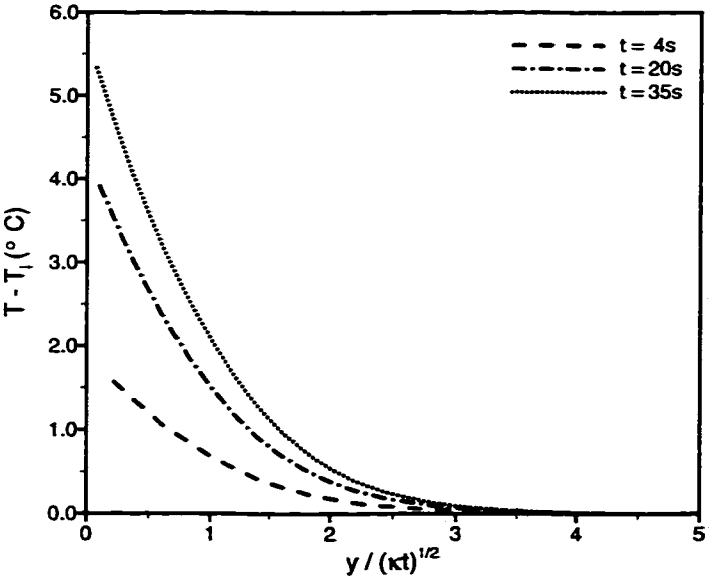

Figure 5.11: Temperature profiles at $r/R_i = 0.5$ and different times (Case Run6).

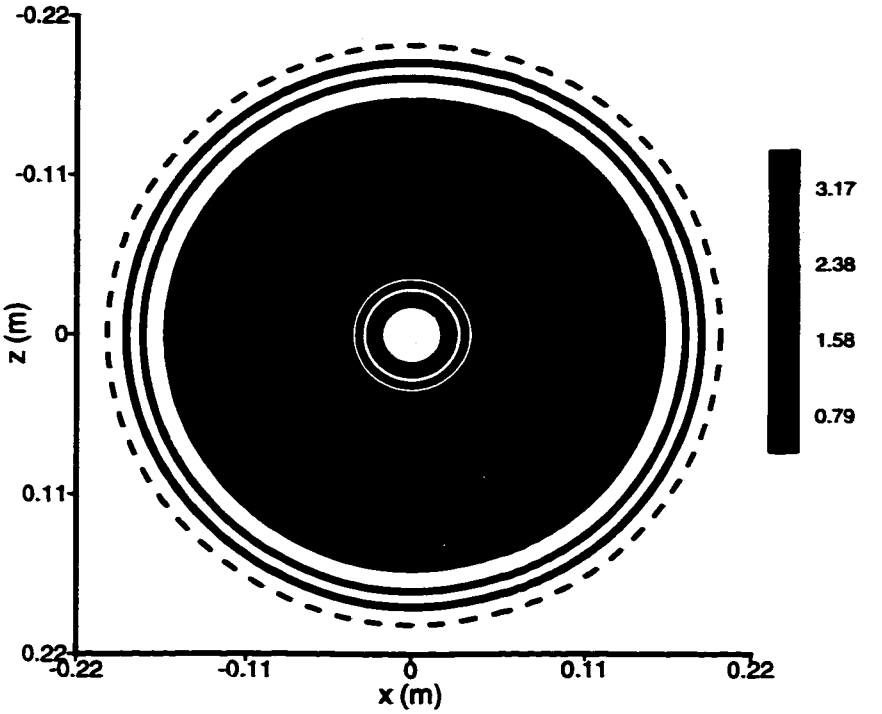

Figure 5.12: Top view of the temperature field at t=40s and y=20mm for $\Omega = 0.2$ rad/s, $B = 1.57 \times 10^{-6}$ m^2/s^3 (Case Run6). The rim of the heated disk is marked by the dashed line.

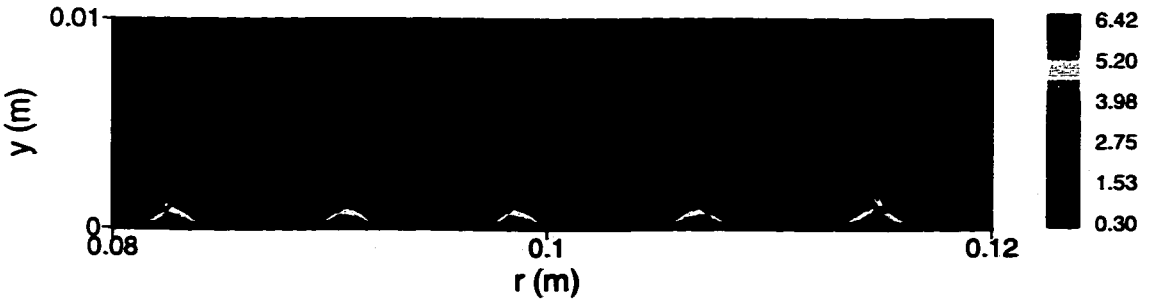

Figure 5.13: Expanded side view of the temperature and velocity fields at t=40s for $\Omega = 0.2$ rad/s, $B = 1.57 \times 10^{-6}$ m^2/s^3 (Case Run6).

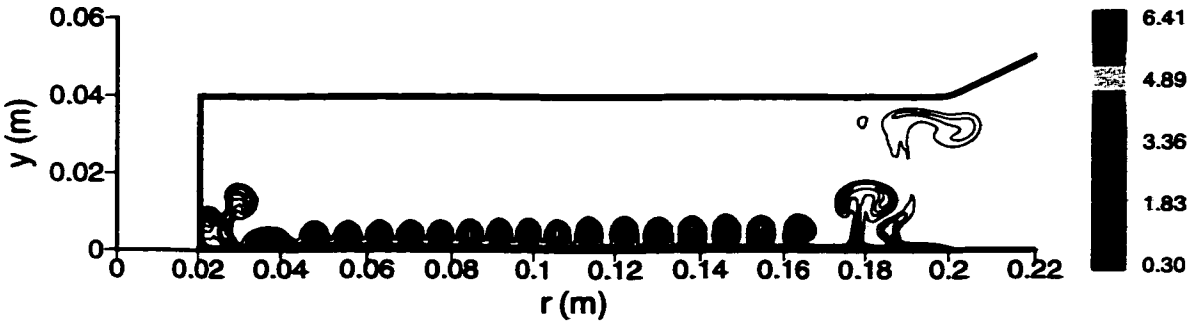

(a) $\Omega = 0.1$ rad/s, $B = 1.57 \times 10^{-6}$ m^2/s^3 (Case Run7)

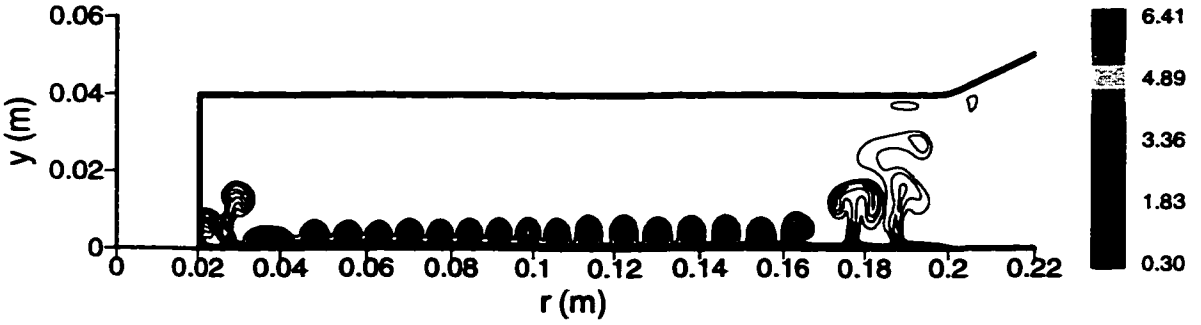

(b) $\Omega = 0.2$ rad/s, $B = 1.57 \times 10^{-6}$ m^2/s^3 (Case Run6)

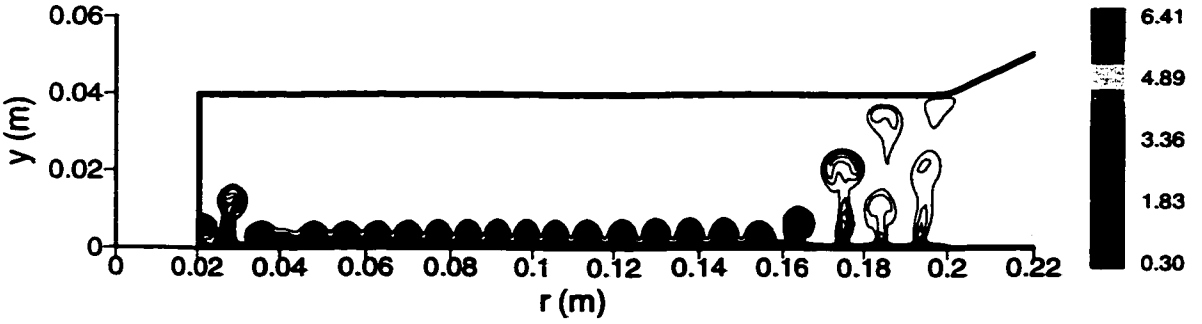

(c) $\Omega = 0.4$ rad/s, $B = 1.57 \times 10^{-6}$ m^2/s^3 (Case Run8)

Figure 5.14: Side view of the temperature field at t=40s.

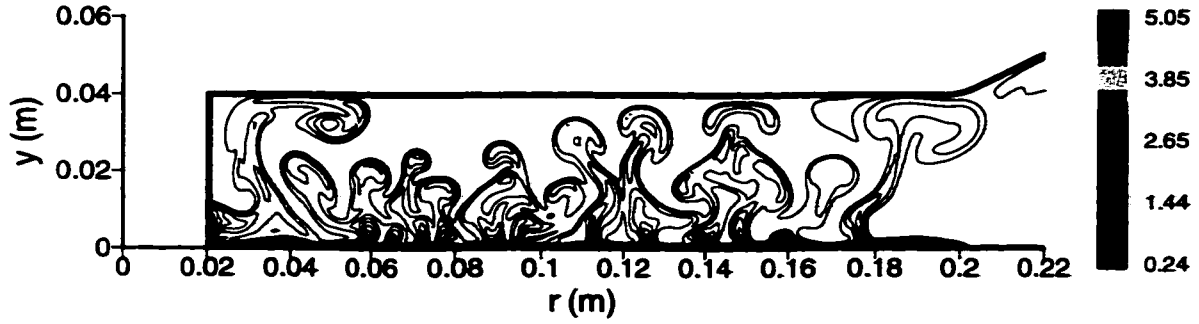

(a) $\Omega = 0.1$ rad/s, $B = 1.57 \times 10^{-6}$ m^2/s^3 (Case Run7)

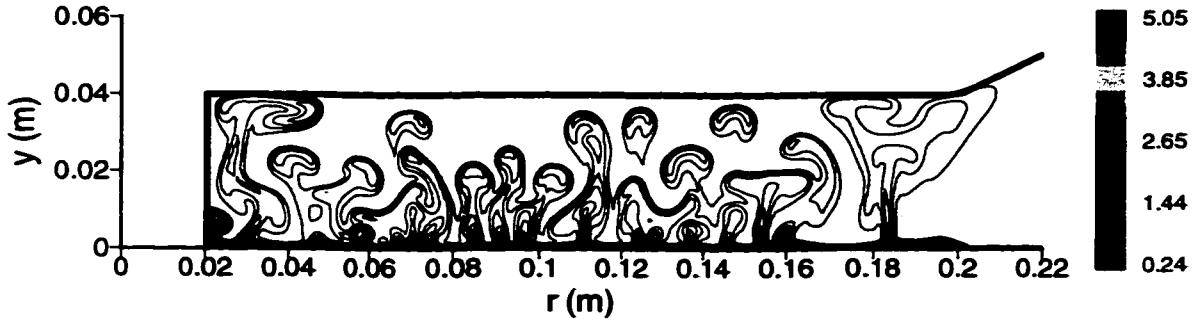

(b) $\Omega = 0.2$ rad/s, $B = 1.57 \times 10^{-6}$ m^2/s^3 (Case Run6)

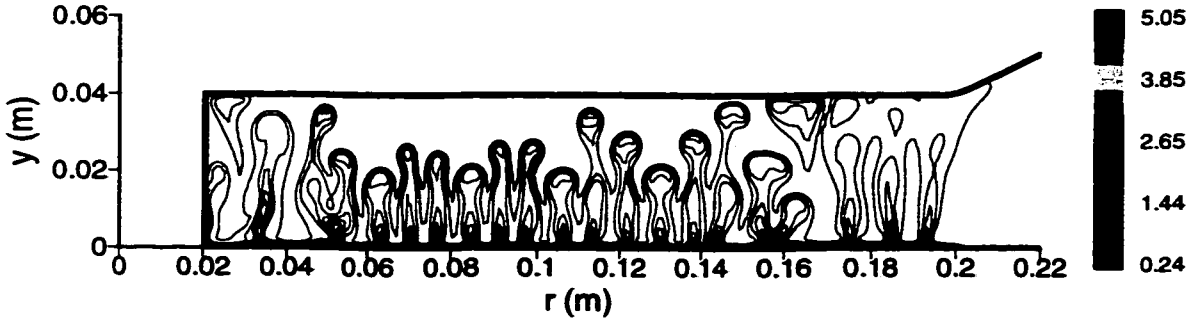

(c) $\Omega = 0.4$ rad/s, $B = 1.57 \times 10^{-6}$ m^2/s^3 (Case Run8)

Figure 5.15: Side view of the temperature field at t=55s.

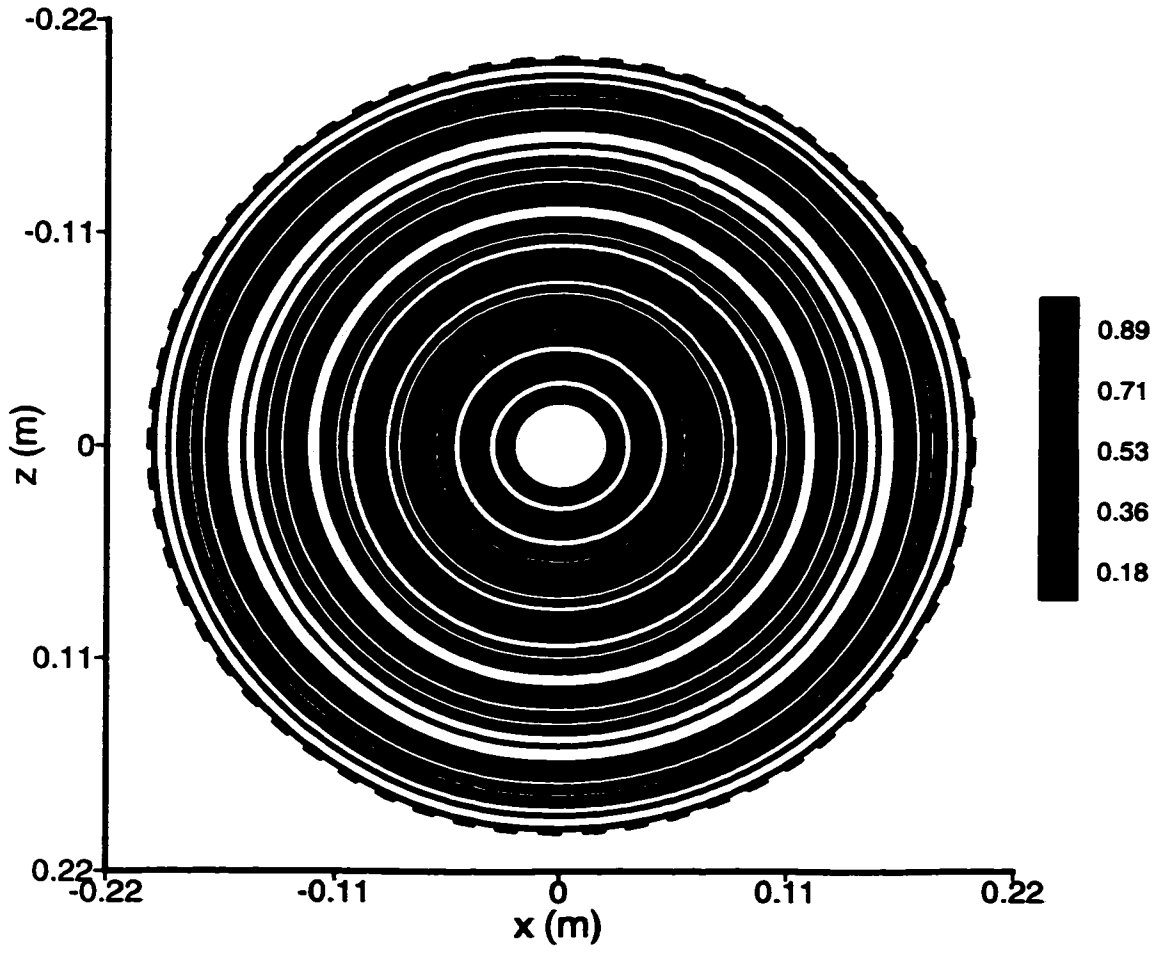

Figure 5.16: Top view of the temperature field at t=55s and y=20mm for $\Omega = 0.2$ rad/s, $B = 1.57 \times 10^{-6}$ m^2/s^3 (Case Run6). The rim of the heated disk is marked by the dashed line.

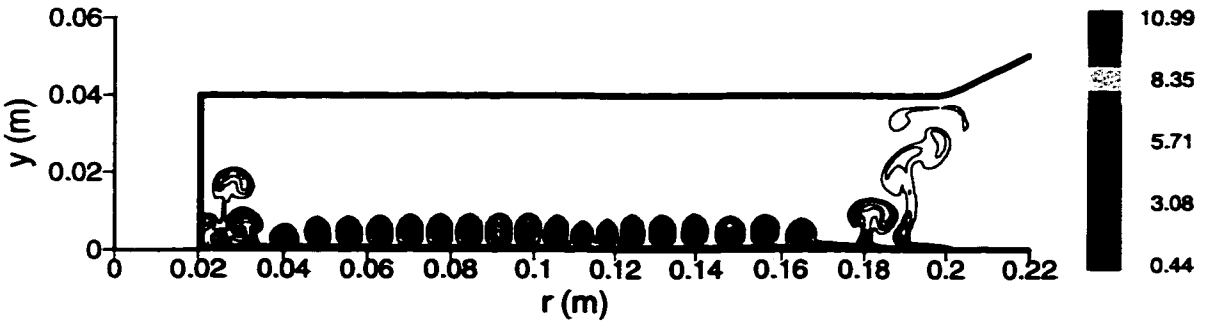

(a)

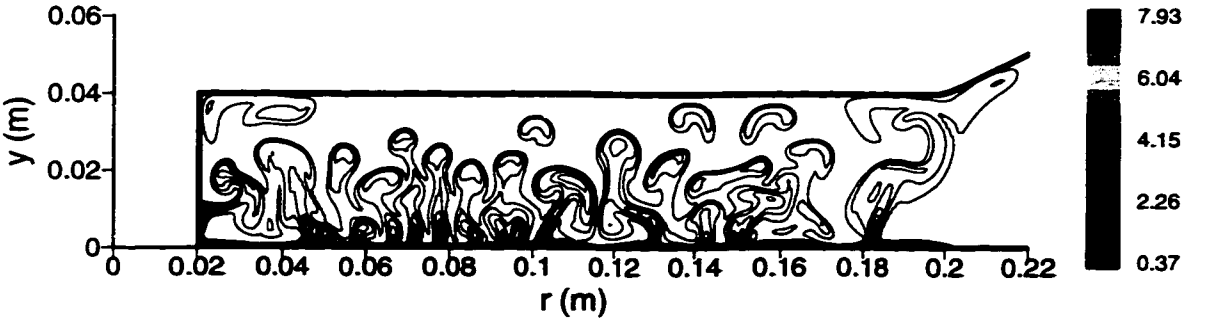

(b)

Figure 5.17: Side view of the temperature field for $\Omega = 0.2$ rad/s, $B = 3.14 \times 10^{-6}$ m^2/s^3 (Case Run9) at (a) t=30s and (b) t=40s.

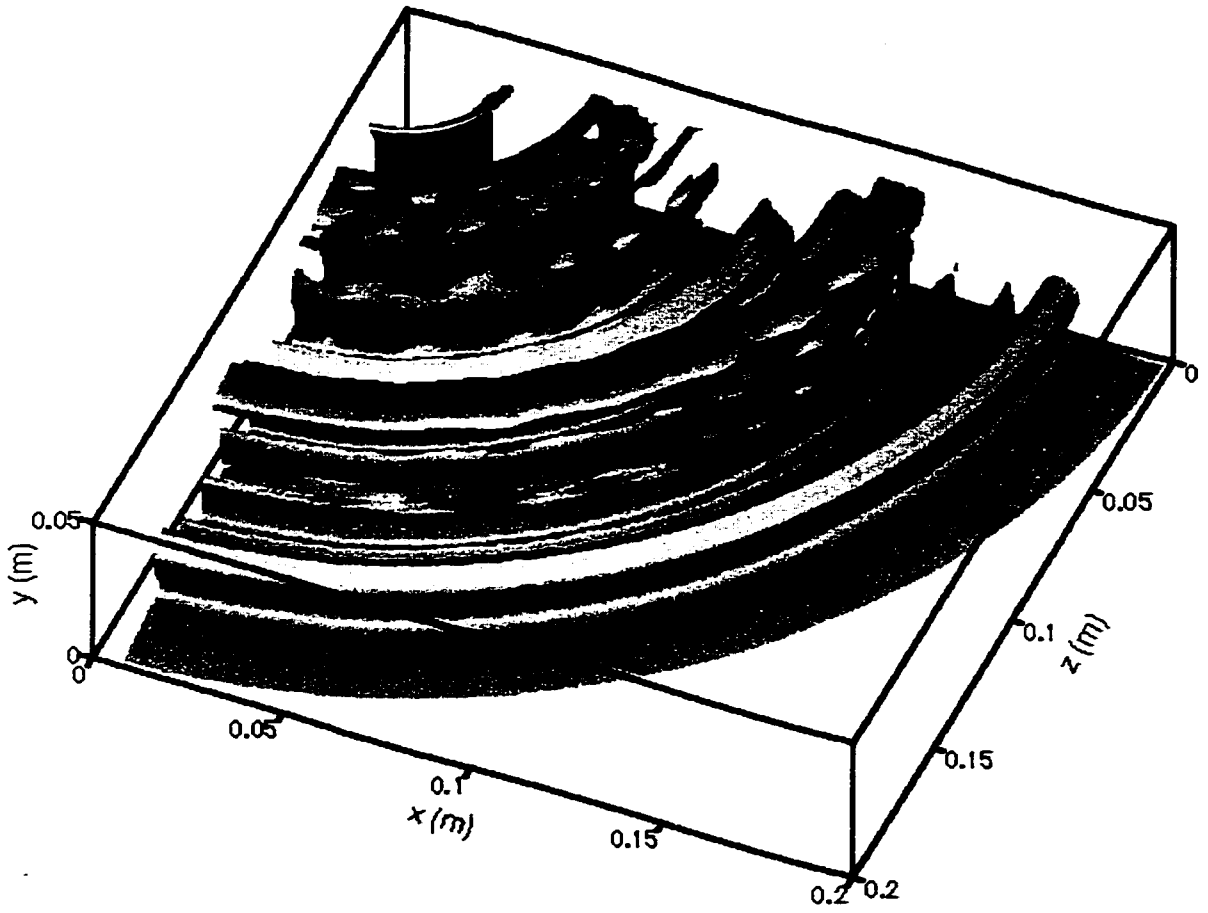

Figure 5.18: An iso-thermal surface at t=140s for $\Omega = 0.2$ rad/s, $B = 1.57 \times 10^{-6}$ m^2/s^3 (Case Run6).

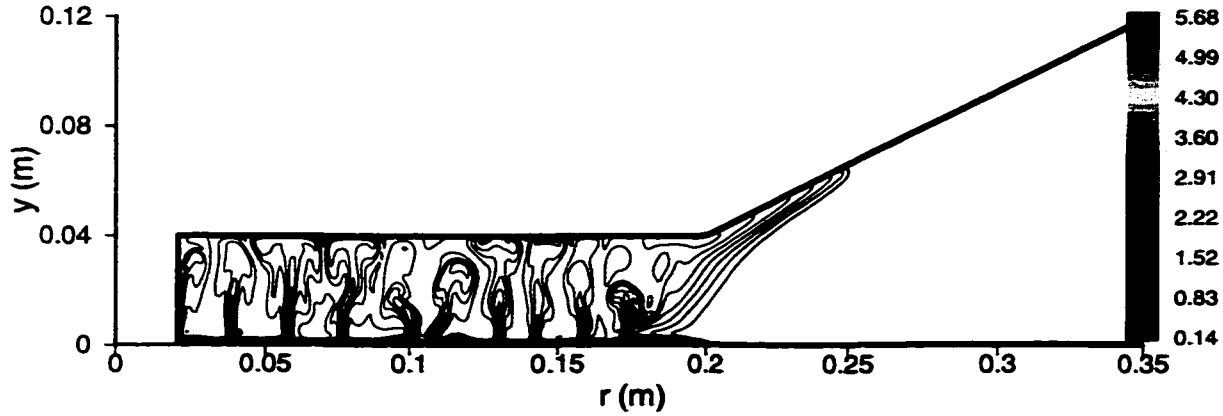

(a)

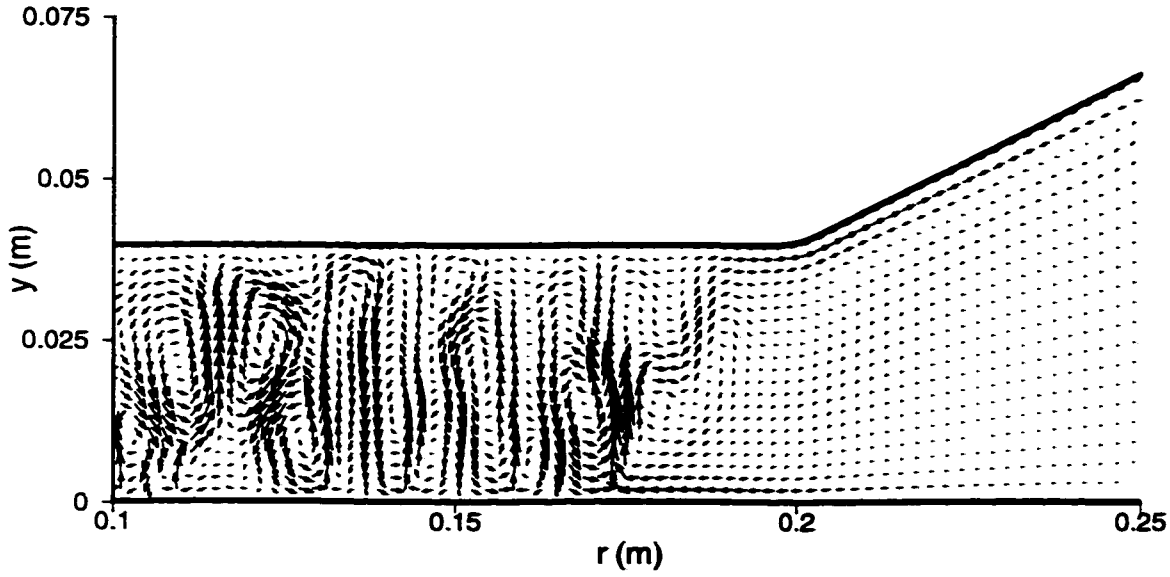

(b)

Figure 5.19: Side view of (a) temperature field (b) expanded velocity field at t=140s for $\Omega = 0.2$ rad/s, $B = 1.57 \times 10^{-6}$ m^2/s^3 (Case Run6).

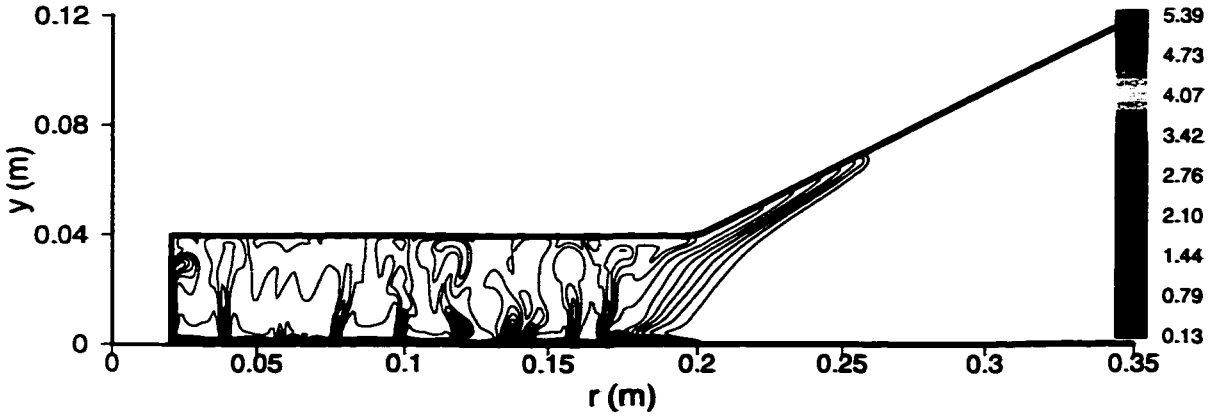

(a)

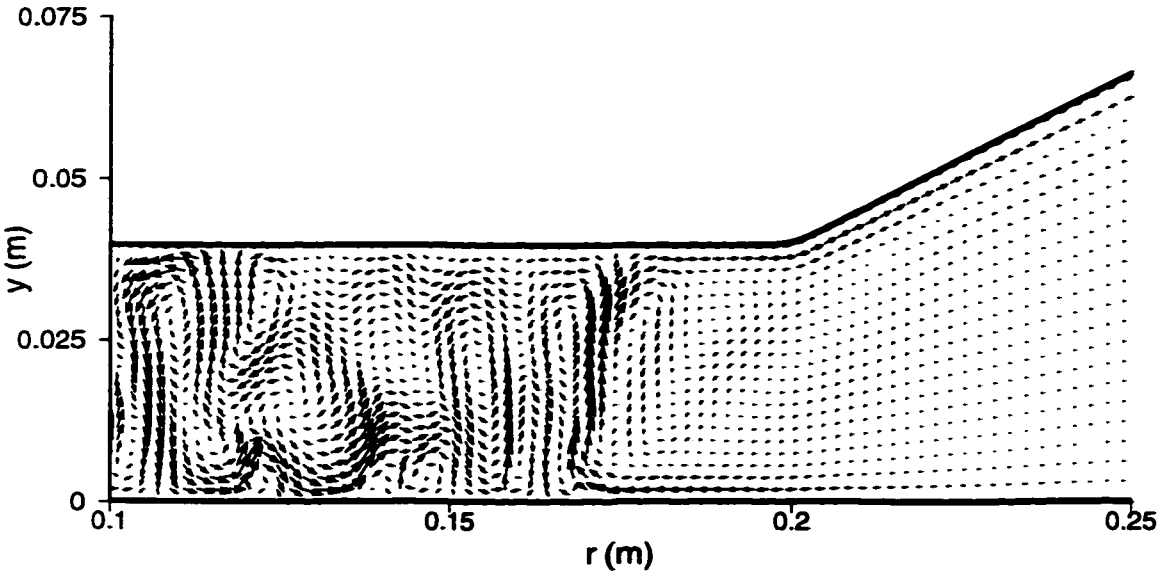

(b)

Figure 5.20: Side view of (a) temperature field (b) expanded velocity field at t=160s for $\Omega = 0.2$ rad/s, $B = 1.57 \times 10^{-6}$ m^2/s^3 (Case Run6).

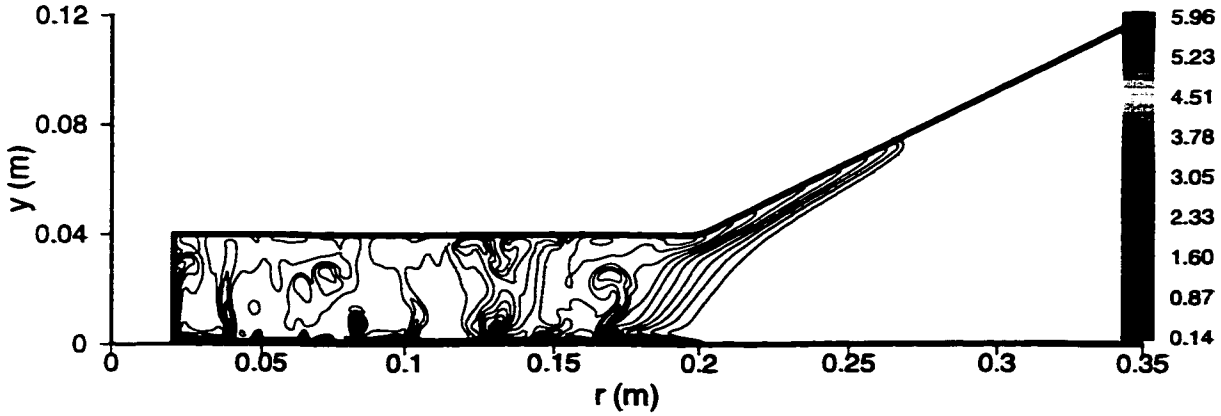

(a)

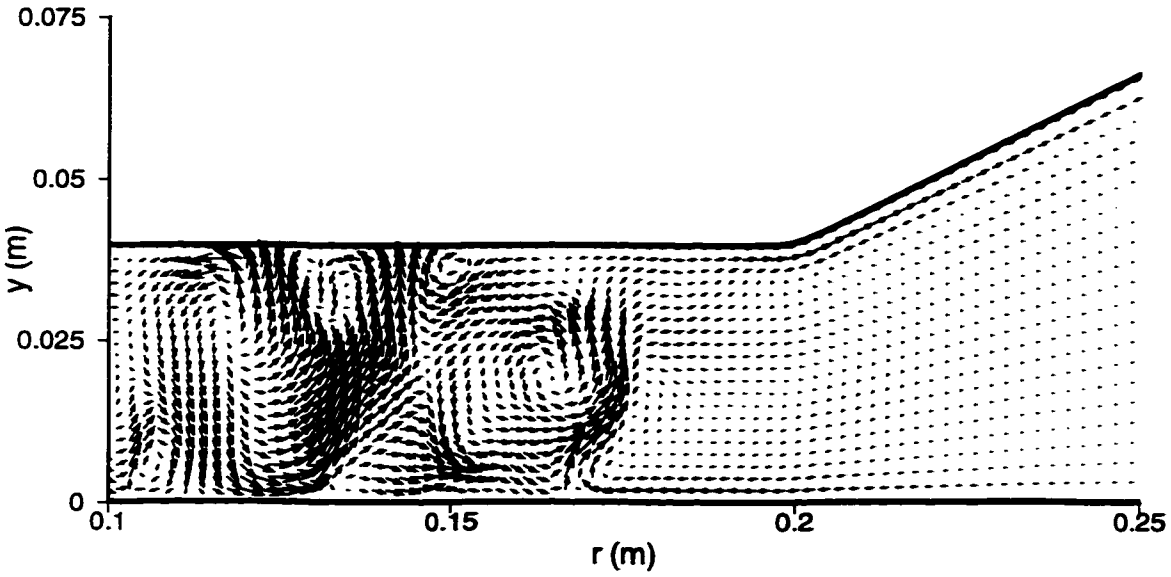

(b)

Figure 5.21: Side view of (a) temperature field (b) expanded velocity field at t=180s for $\Omega = 0.2$ rad/s, $B = 1.57 \times 10^{-6}$ m^2/s^3 (Case Run6).

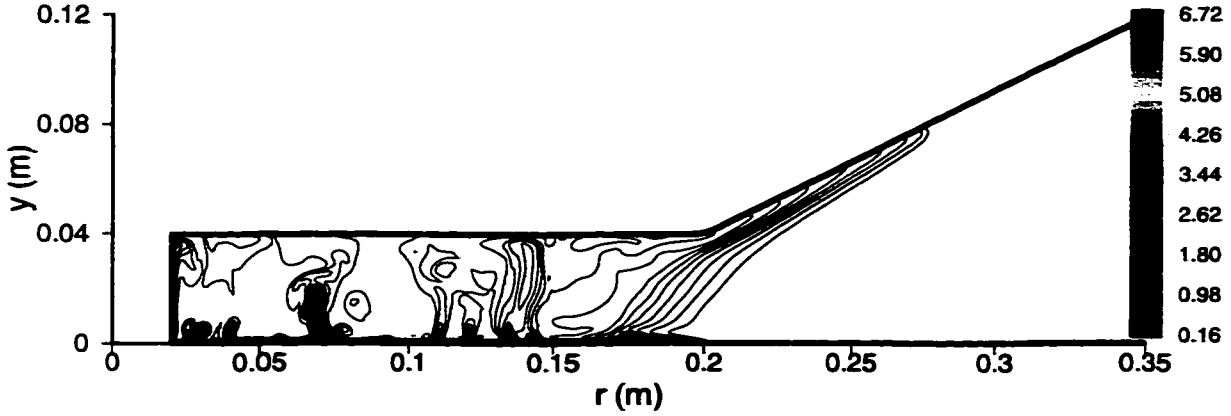

(a)

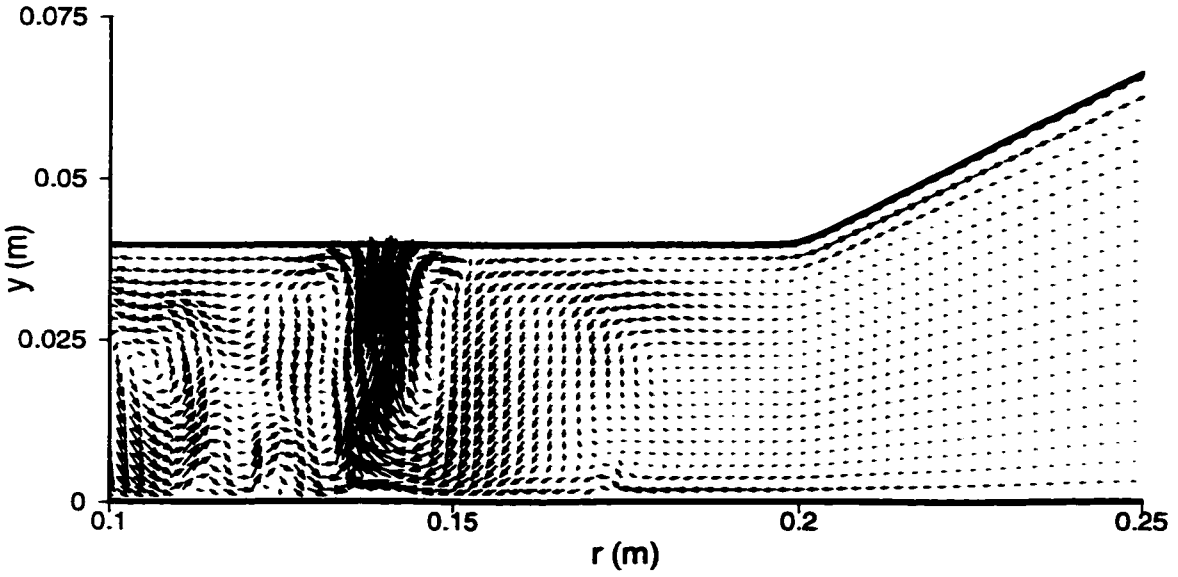

(b)

Figure 5.22: Side view of (a) temperature field (b) expanded velocity field at t=200s for $\Omega = 0.2$ rad/s, $B = 1.57 \times 10^{-6}$ m^2/s^3 (Case Run6).

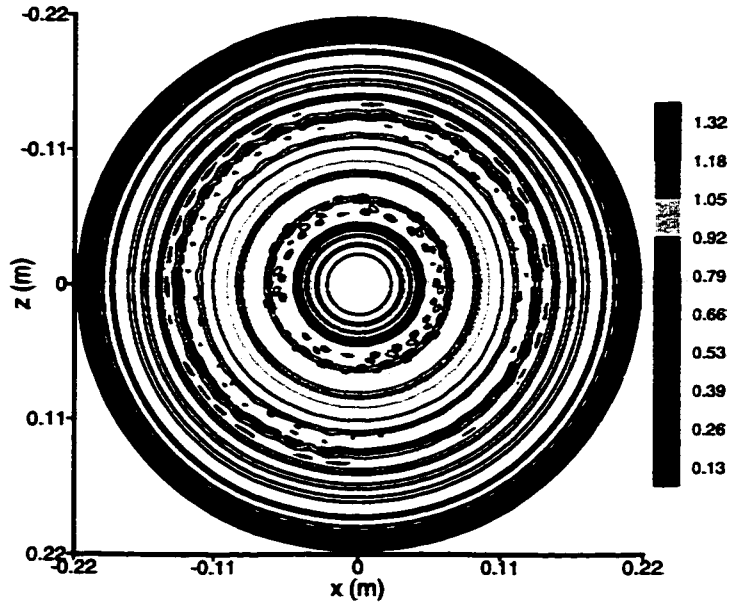

Figure 5.23: Top view of the temperature field at t=140s and y=20mm for $\Omega = 0.2$ rad/s, $B = 1.57 \times 10^{-6}$ m^2/s^3 (Case Run6). The rim of the heated disk is marked by the dashed line.

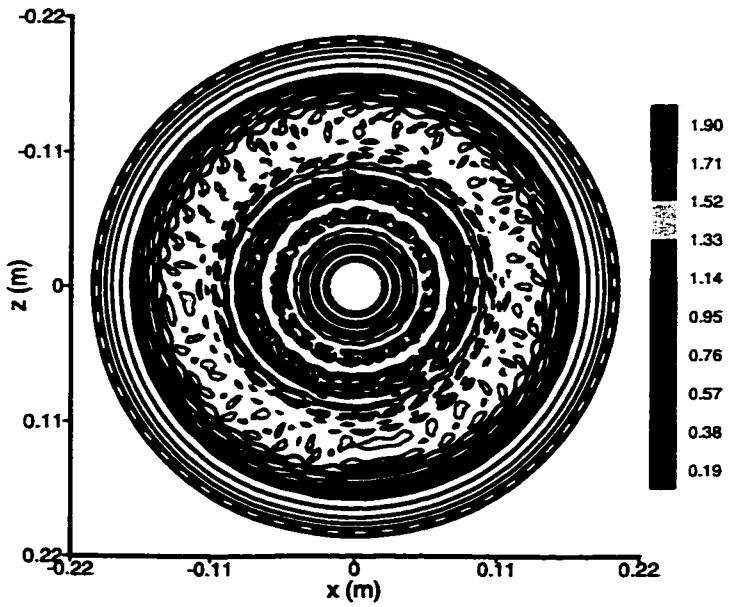

Figure 5.24: Top view of the temperature field at t=160s and y=20mm for $\Omega = 0.2$ rad/s, $B = 1.57 \times 10^{-6}$ m^2/s^3 (Case Run6). The rim of the heated disk is marked by the dashed line.

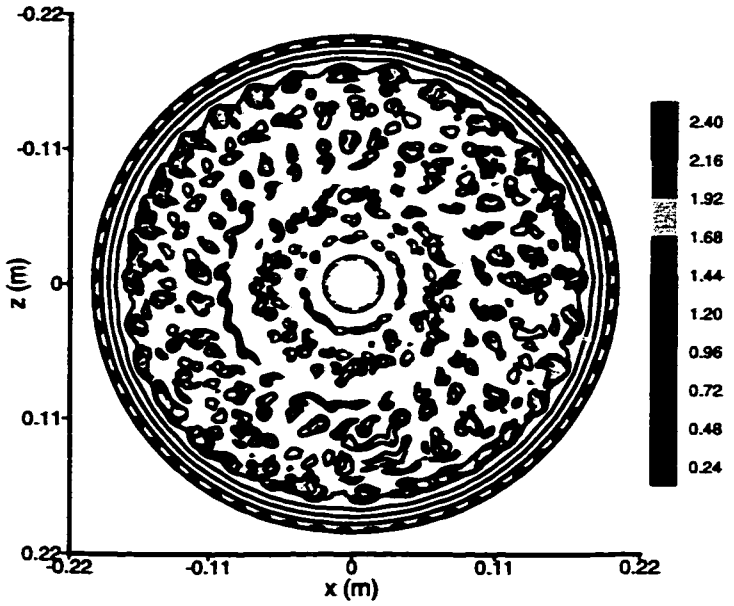

Figure 5.25: Top view of the temperature field at t=180s and y=20mm for $\Omega = 0.2$ rad/s, $B = 1.57 \times 10^{-6}$ m^2/s^3 (Case Run6). The rim of the heated disk is marked by the dashed line.

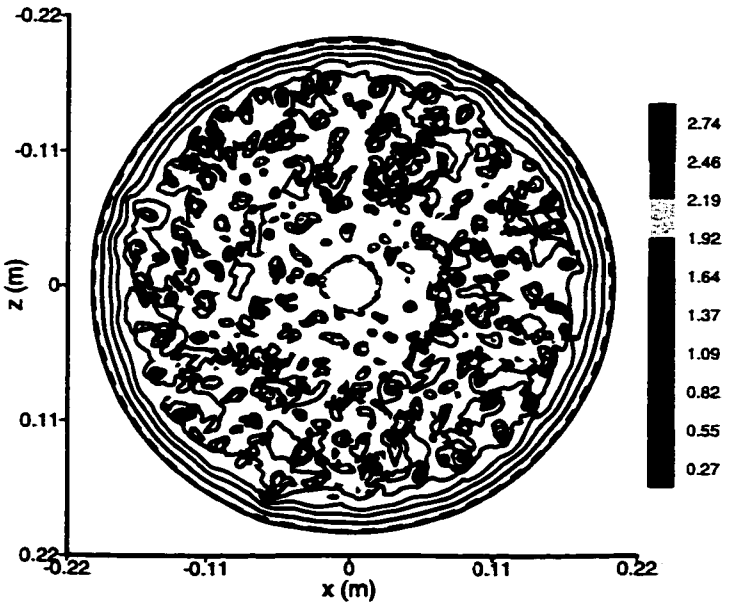

Figure 5.26: Top view of the temperature field at t=200s and y=20mm for $\Omega = 0.2$ rad/s, $B = 1.57 \times 10^{-6}$ m^2/s^3 (Case Run6). The rim of the heated disk is marked by the dashed line.

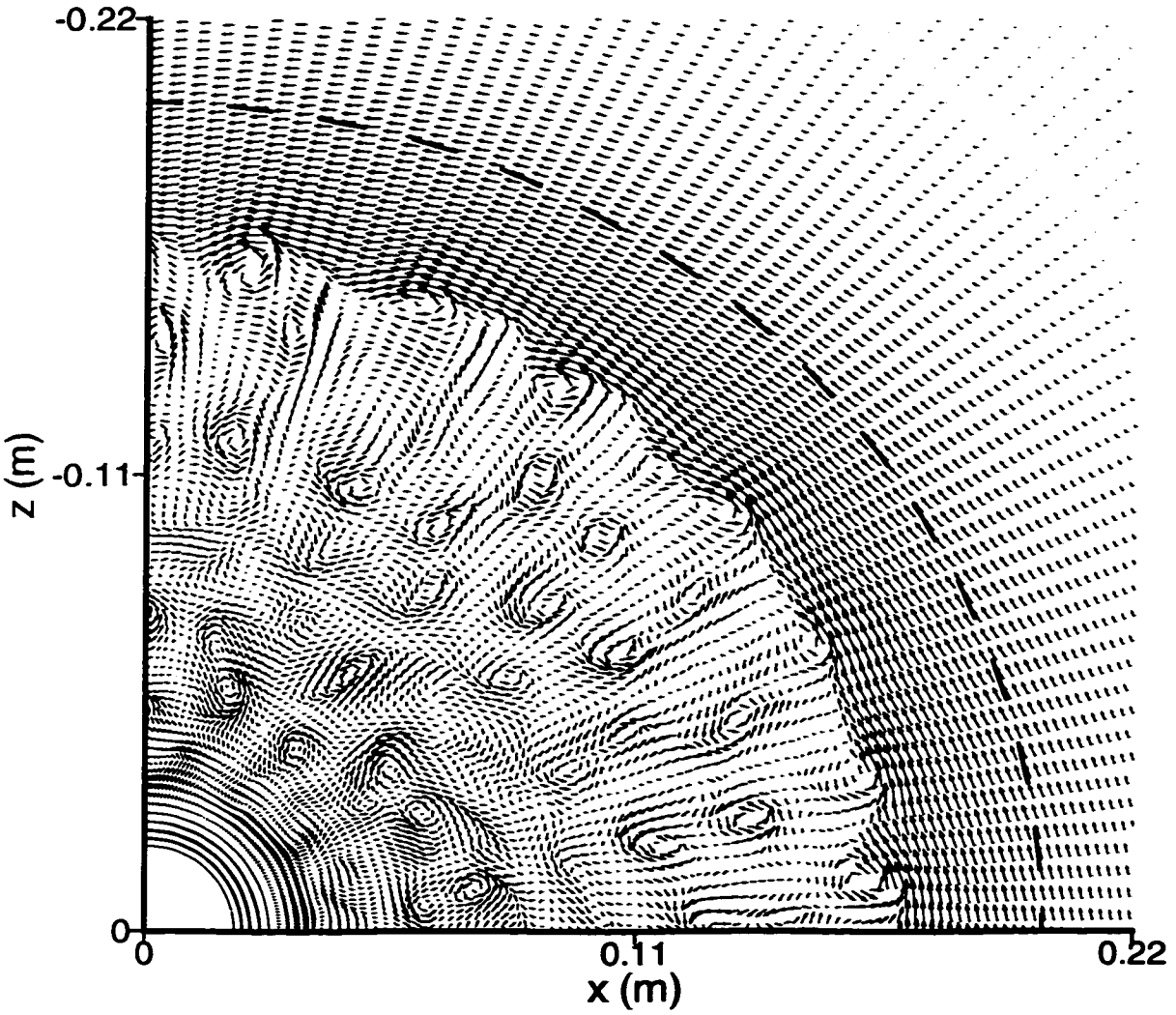

Figure 5.27: Top view of the velocity field at t=180s and y=5mm for $\Omega = 0.2$ rad/s, $B = 1.57 \times 10^{-6}$ m^2/s^3 (Case Run6). The rim of the heated disk is marked by the dashed line.

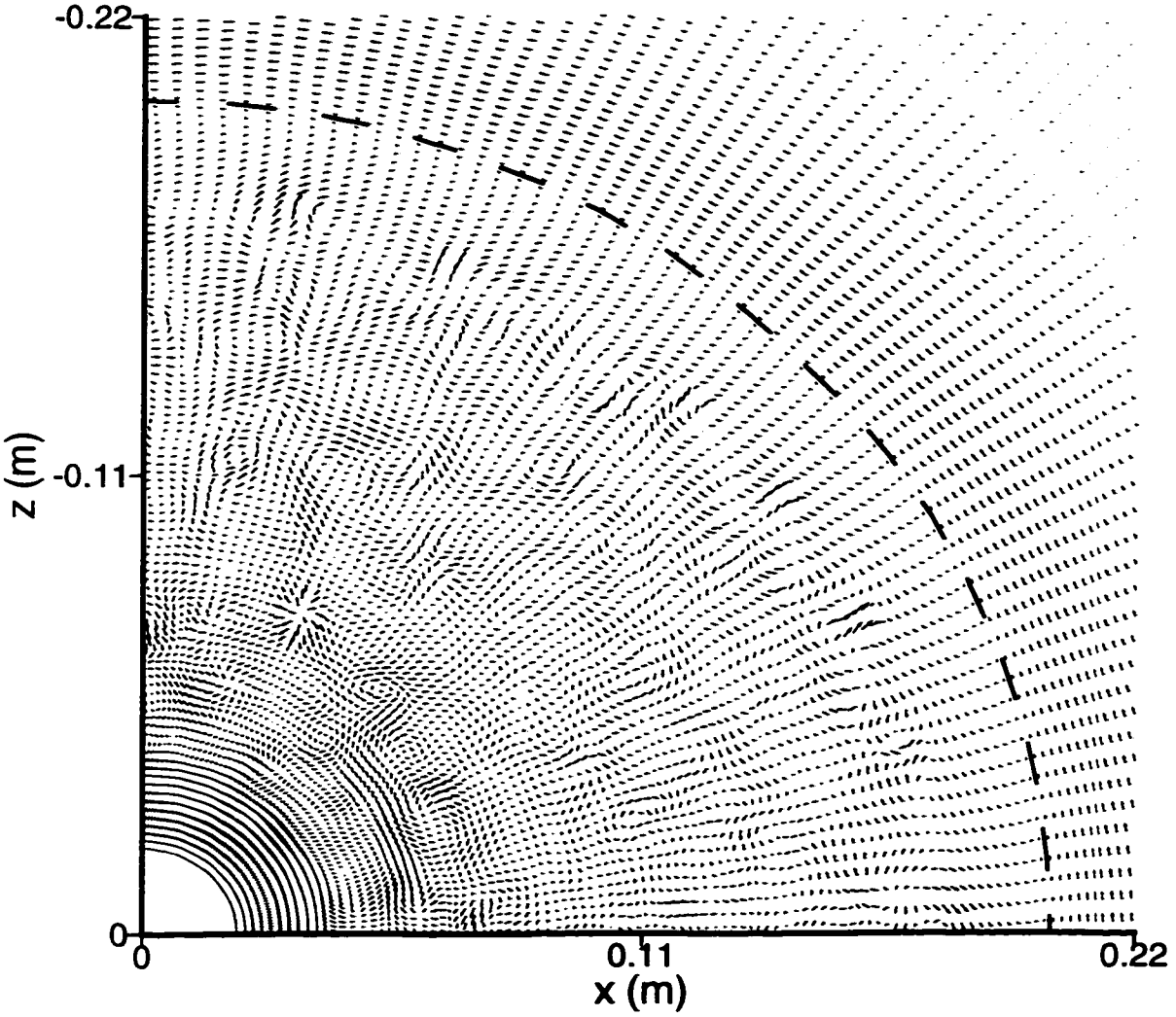

Figure 5.28: Top view of the velocity field at t=180s and y=20mm for Ω = 0.2 rad/s, $B = 1.57 \times 10^{-6}$ m^2/s^3 (Case Run6). The rim of the heated disk is marked by the dashed line.

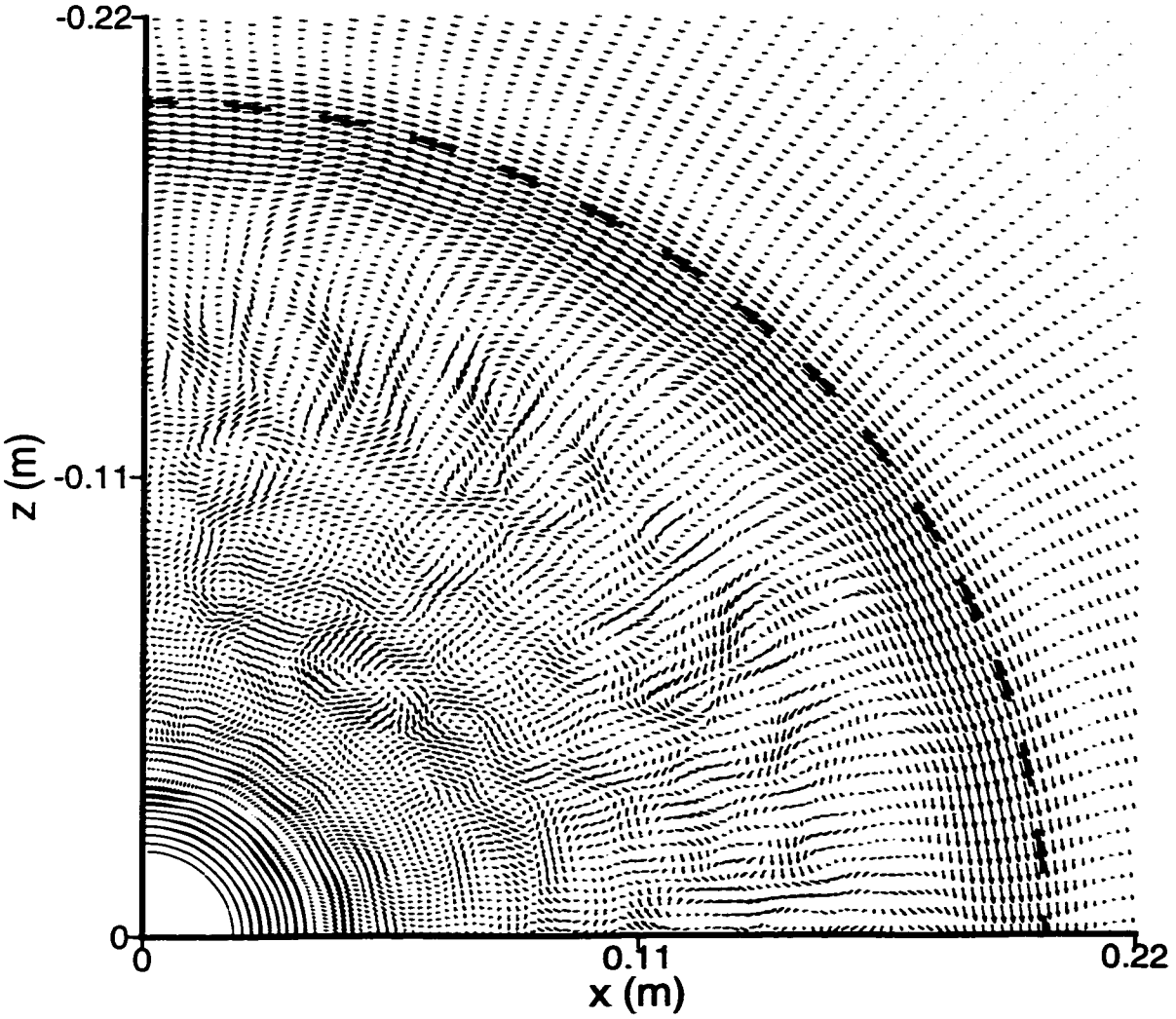

Figure 5.29: Top view of the velocity field at t=180s and y=35mm for $\Omega = 0.2$ rad/s, $B = 1.57 \times 10^{-6}$ m^2/s^3 (Case Run6). The rim of the heated disk is marked by the dashed line.

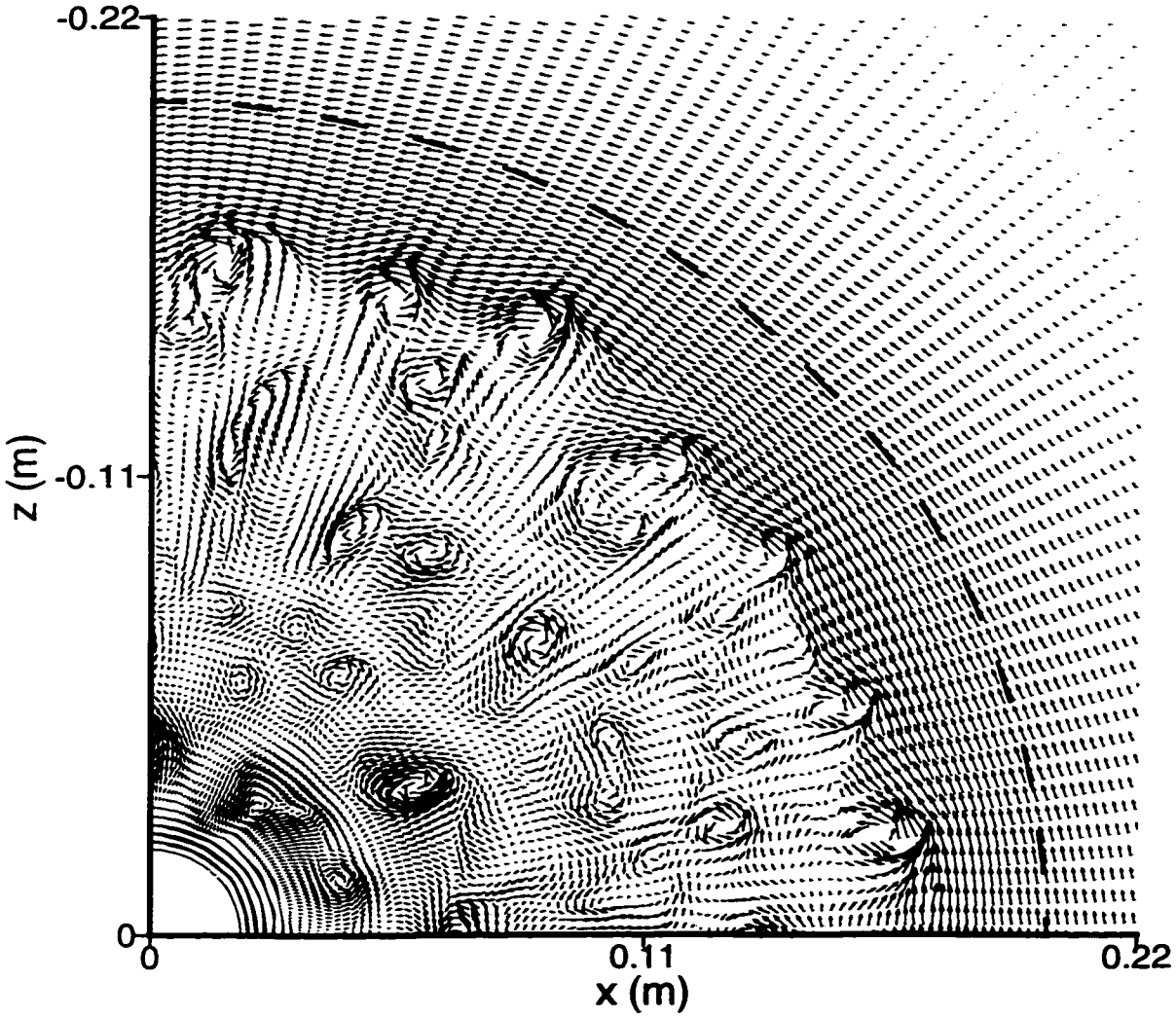

Figure 5.30: Top view of the velocity field at t=200s and y=5mm for $\Omega = 0.2$ rad/s, $B = 1.57 \times 10^{-6}$ m^2/s^3 (Case Run6). The rim of the heated disk is marked by the dashed line.

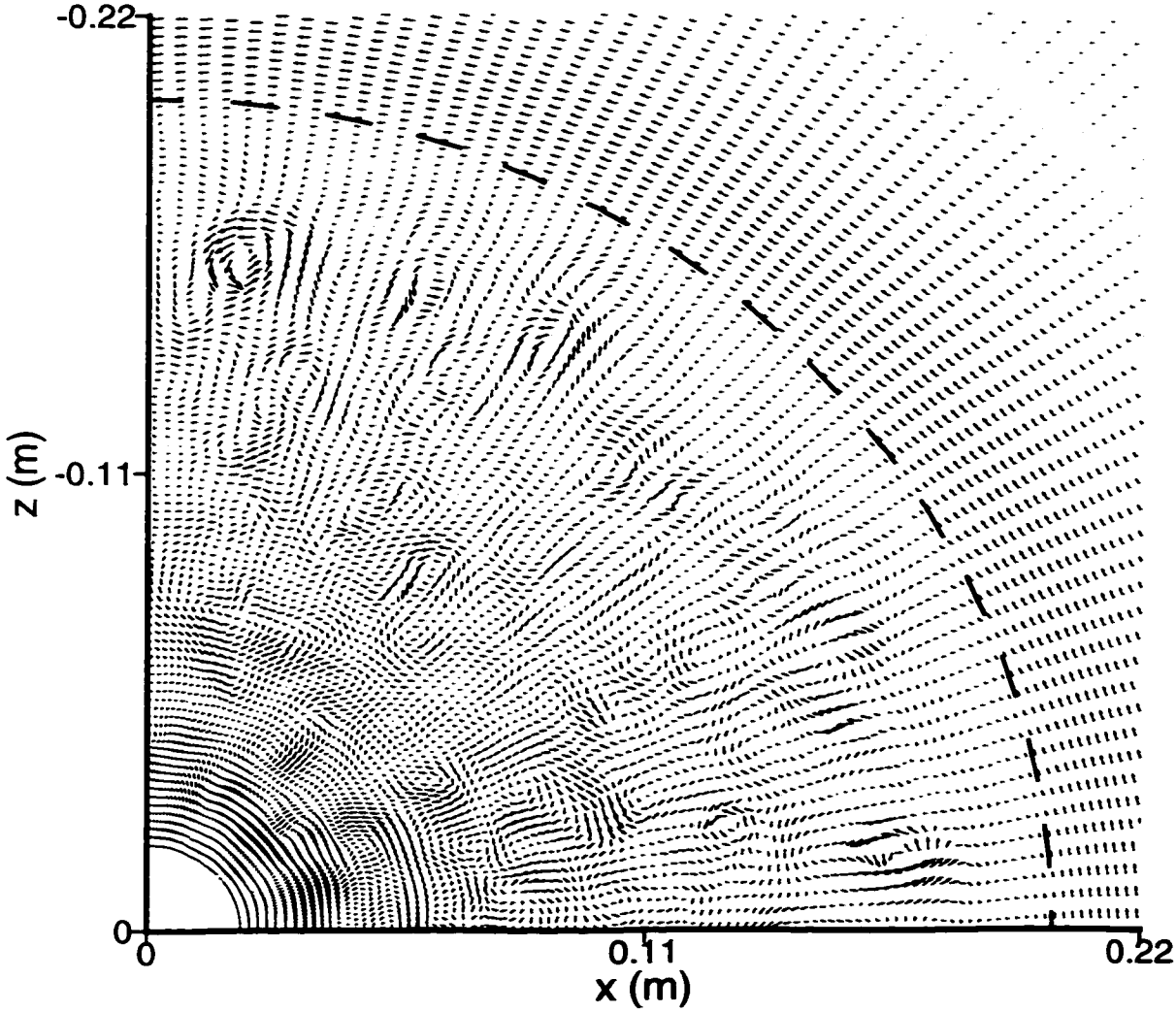

Figure 5.31: Top view of the velocity field at t=200s and y=20mm for $\Omega = 0.2$ rad/s, $B = 1.57 \times 10^{-6}$ m^2/s^3 (Case Run6). The rim of the heated disk is marked by the dashed line.

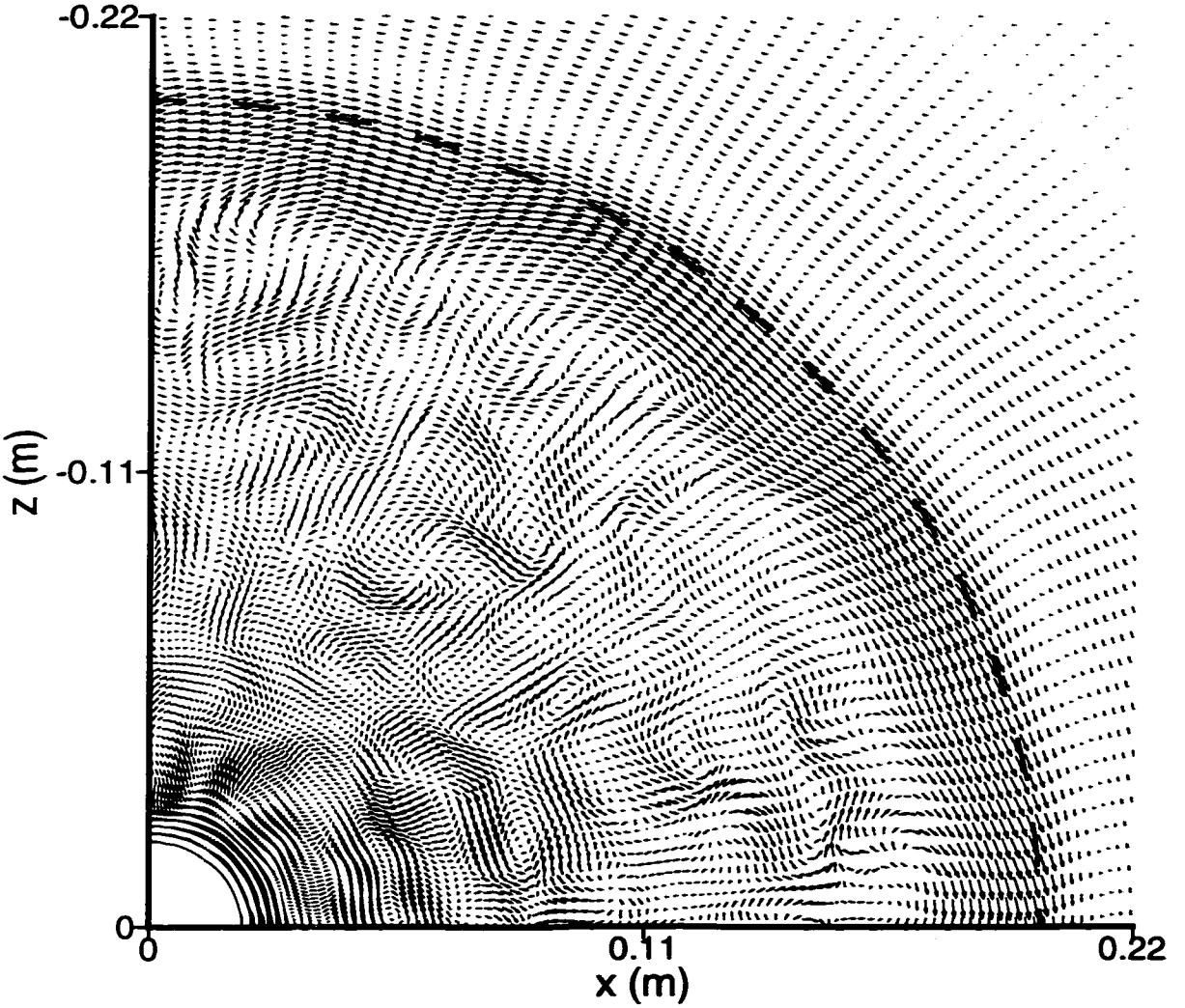

Figure 5.32: Top view of the velocity field at t=200s and y=35mm for $\Omega = 0.2$ rad/s, $B = 1.57 \times 10^{-6}$ m^2/s^3 (Case Run6). The rim of the heated disk is marked by the dashed line.

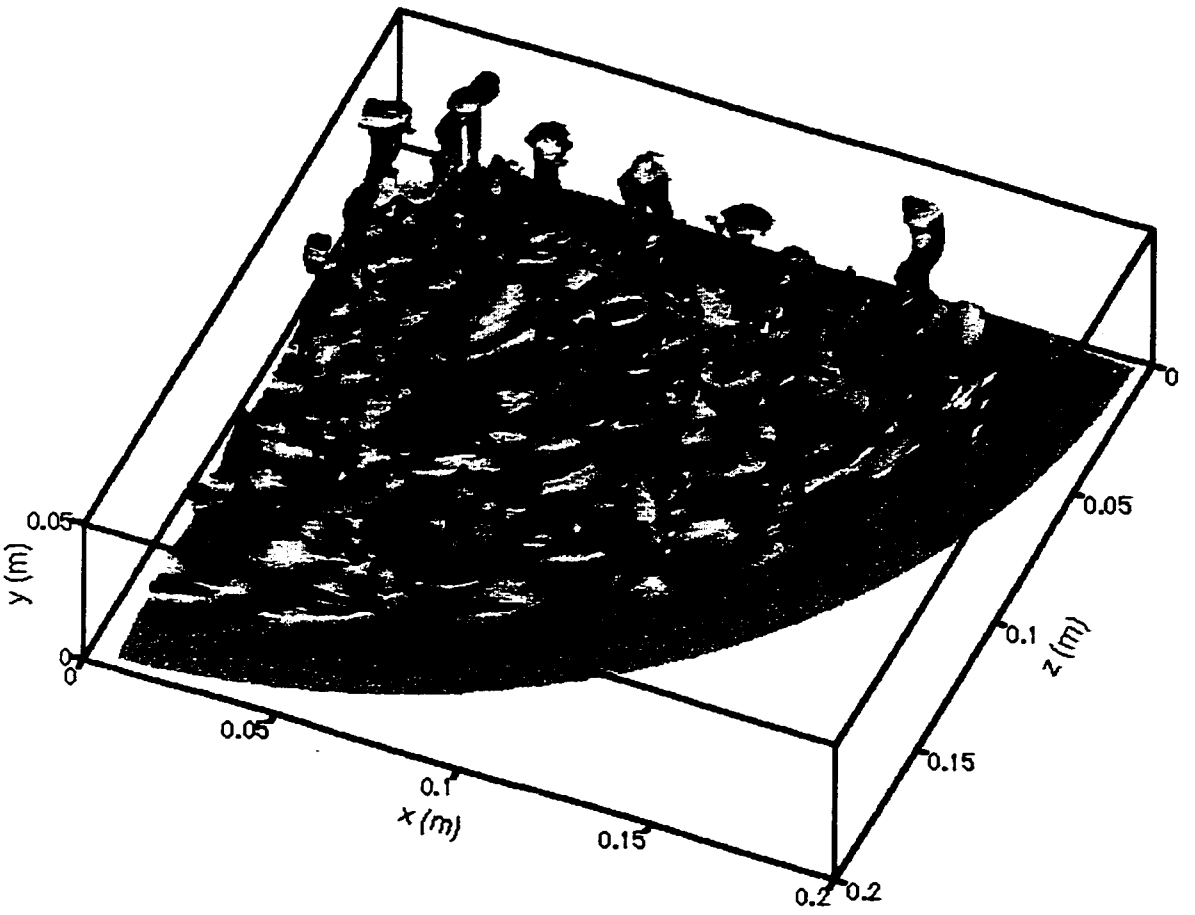

Figure 5.33: An Iso-thermal surface at t=200s for $\Omega = 0.2$ rad/s, $B = 1.57 \times 10^{-6}$ m^2/s^3 (Case Run6).

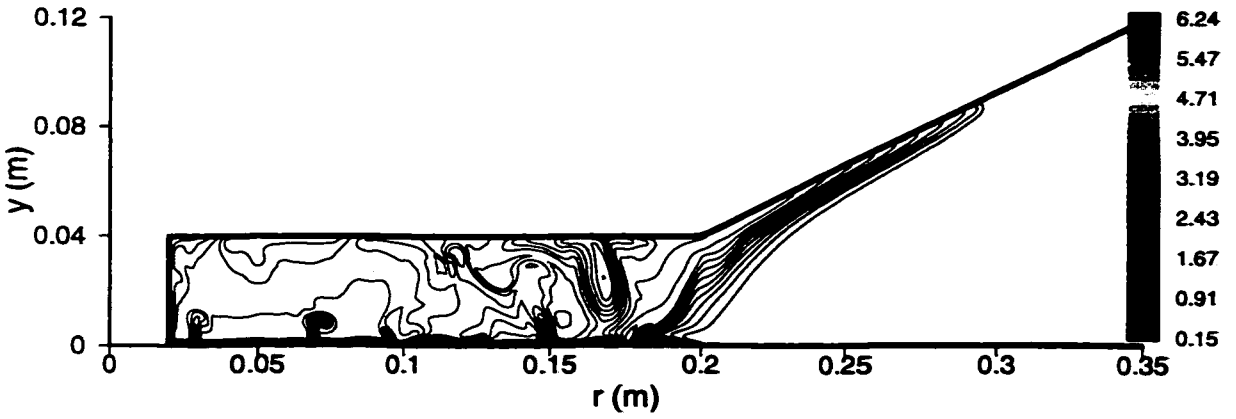

(a)

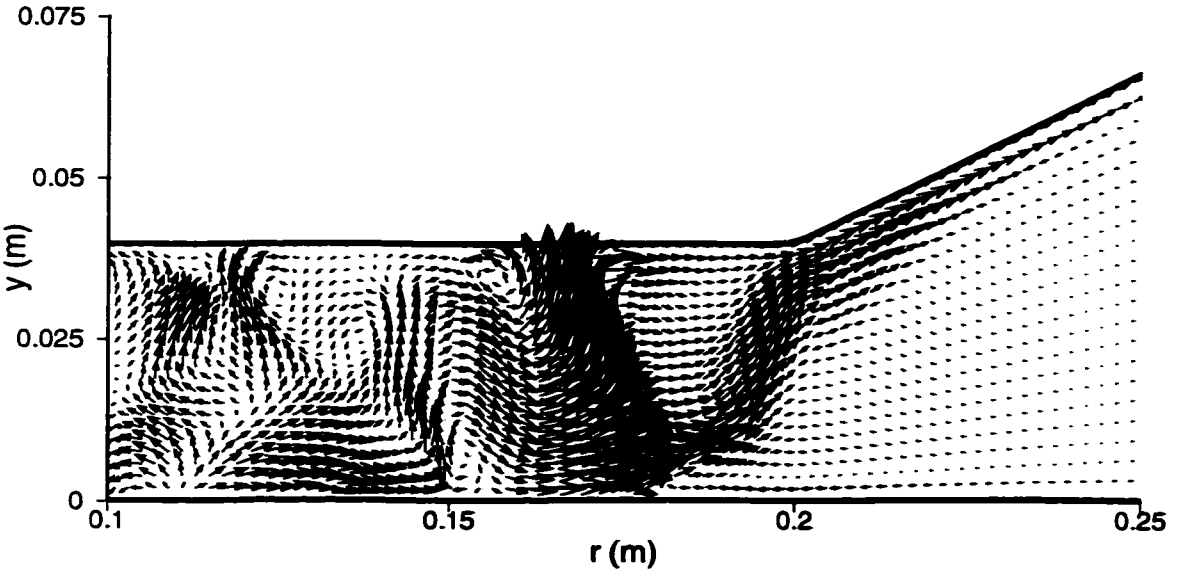

(b)

Figure 5.34: Side view of (a) temperature field (b) expanded velocity field at t=240s for $\Omega = 0.2$ rad/s, $B = 1.57 \times 10^{-6}$ m^2/s^3 (Case Run6).

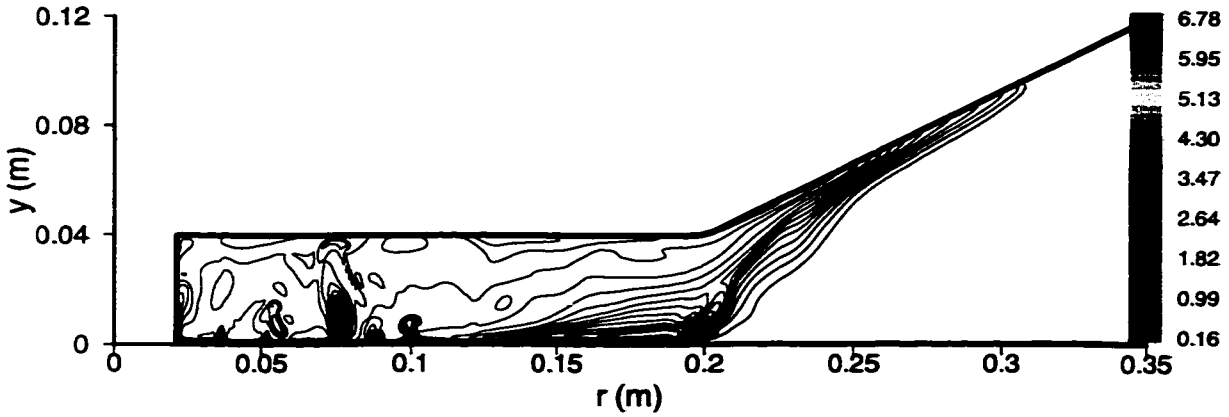

(a)

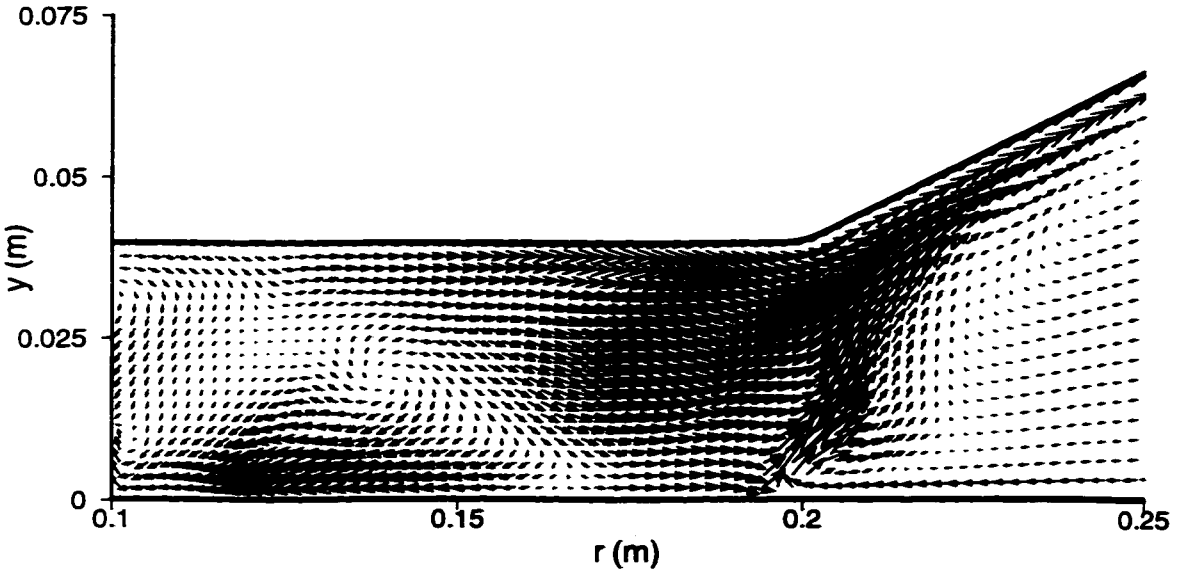

(b)

Figure 5.35: Side view of (a) temperature field (b) expanded velocity field at t=280s for $\Omega = 0.2$ rad/s, $B = 1.57 \times 10^{-6}$ m^2/s^3 (Case Run6).

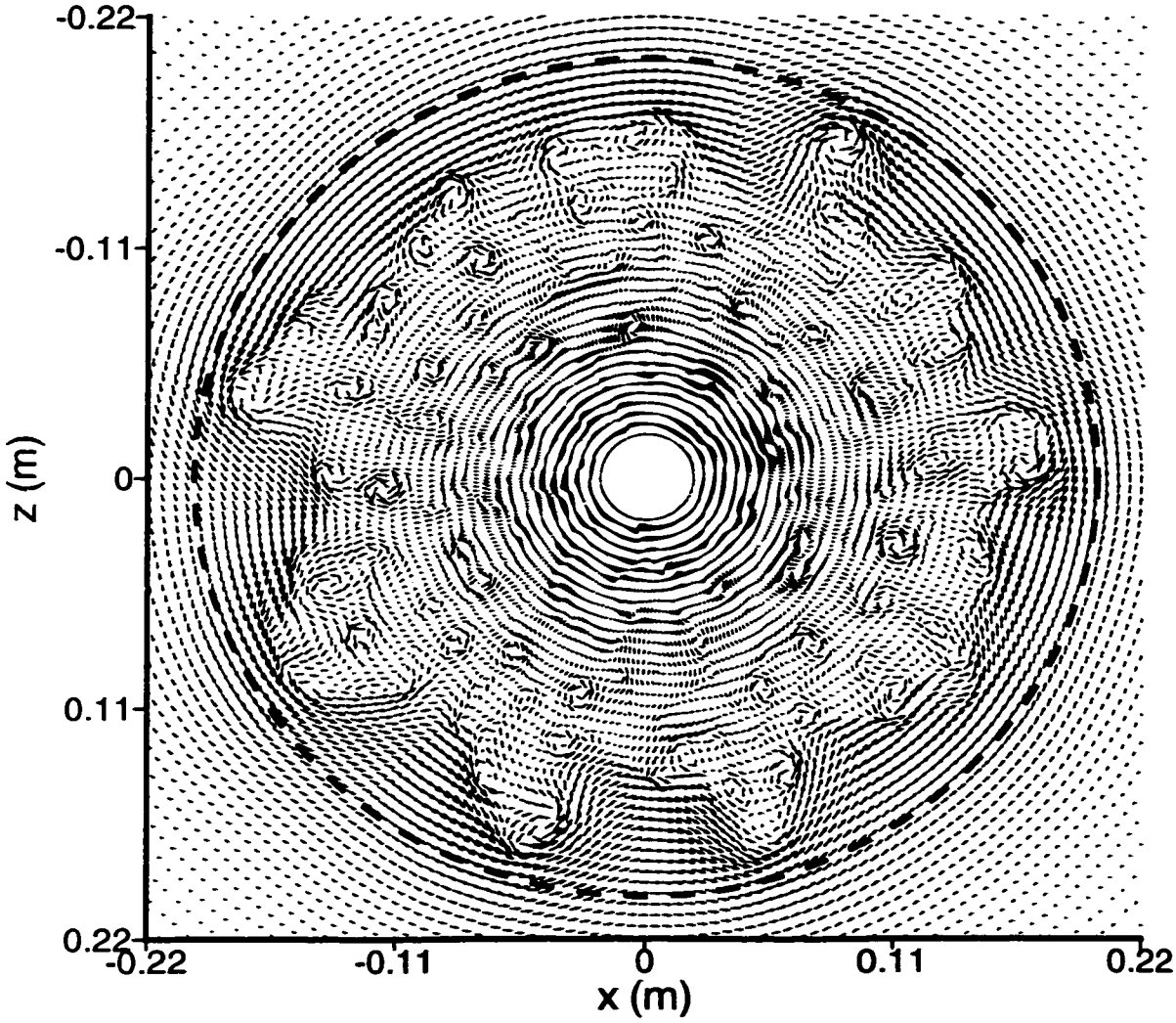

Figure 5.36: Top view of the velocity field at t=240s and y=5mm for $\Omega = 0.2$ rad/s, $B = 1.57 \times 10^{-6}$ m^2/s^3 (Case Run6). The rim of the heated disk is marked by the dashed line.

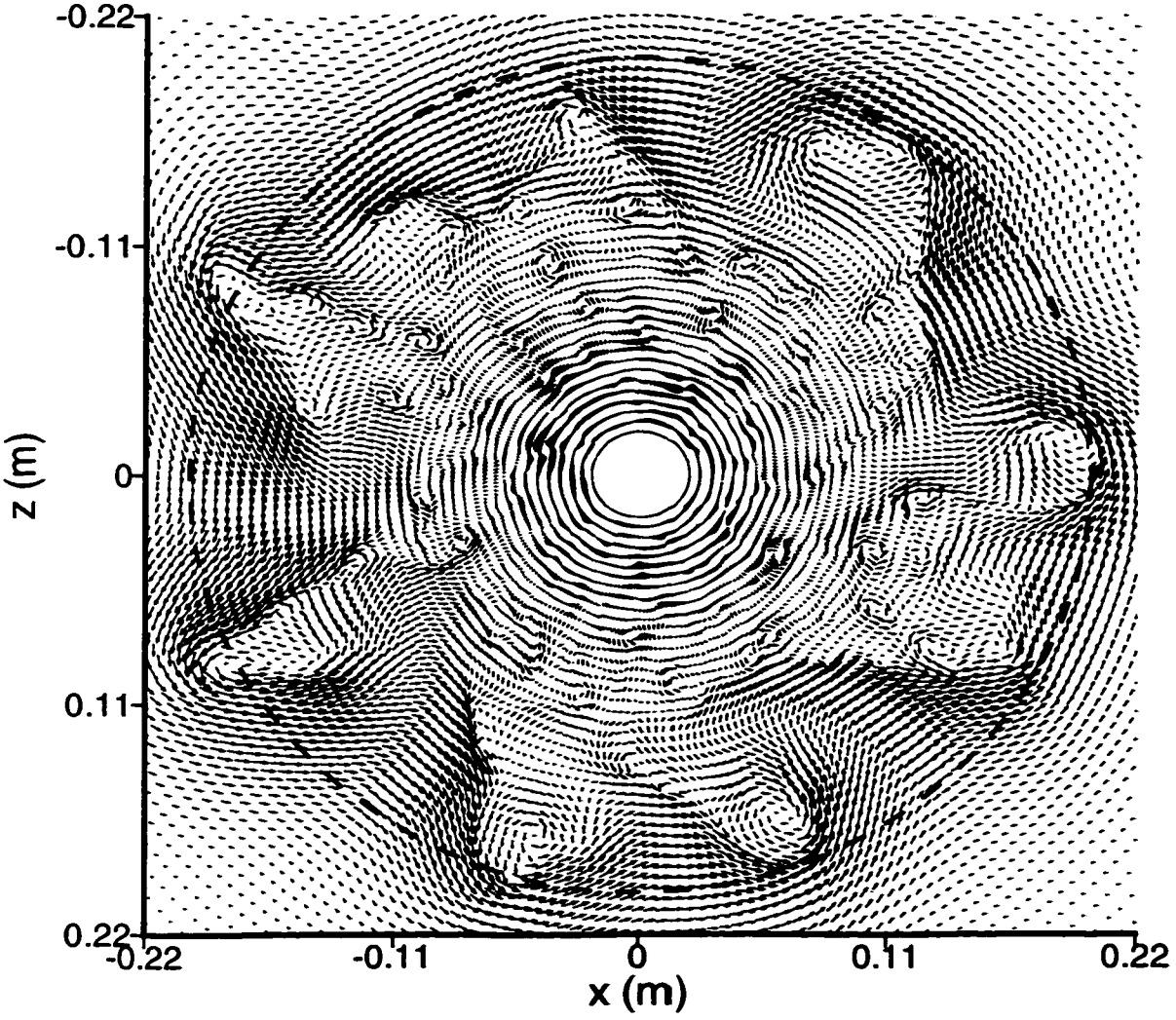

Figure 5.37: Top view of the velocity field at t=280s and y=5mm for $\Omega = 0.2$ rad/s, $B = 1.57 \times 10^{-6}$ m^2/s^3 (Case Run6). The rim of the heated disk is marked by the dashed line.

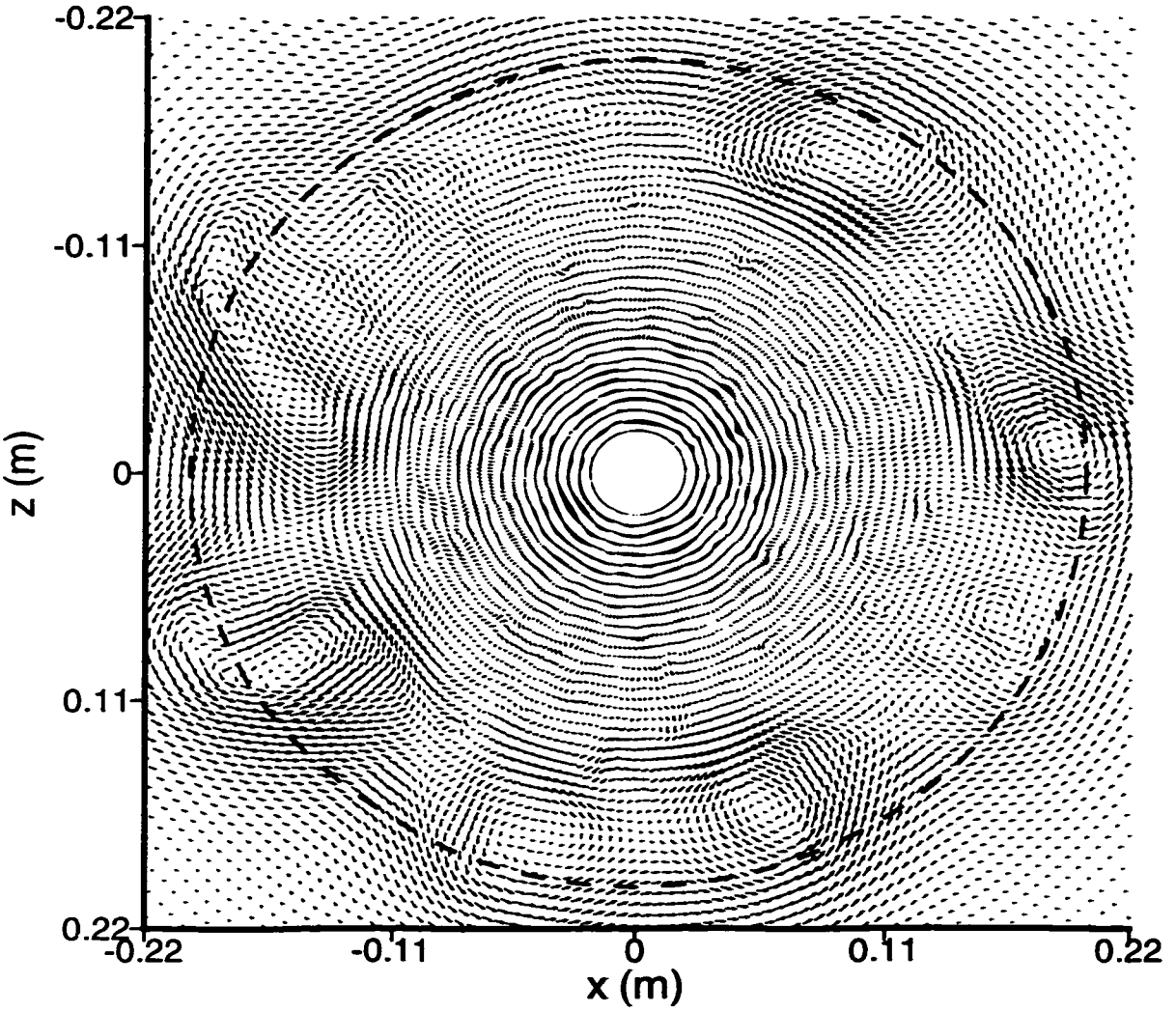

Figure 5.38: Top view of the velocity field at t=280s and y=20mm for $\Omega = 0.2$ rad/s, $B = 1.57 \times 10^{-6}$ m^2/s^3 (Case Run6). The rim of the heated disk is marked by the dashed line.

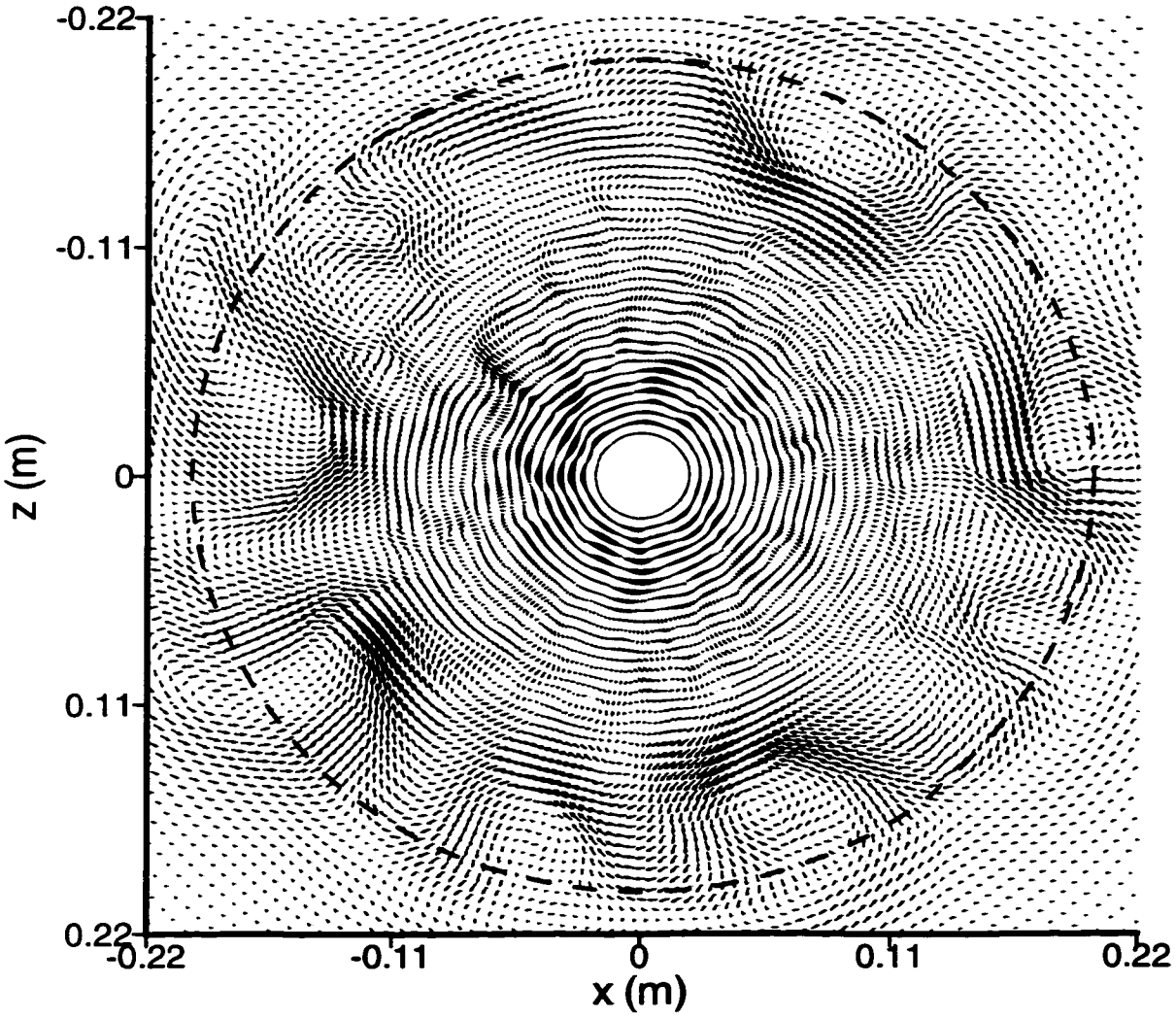

Figure 5.39: Top view of the velocity field at t=280s and y=35mm for $\Omega = 0.2$ rad/s, $B = 1.57 \times 10^{-6}$ m^2/s^3 (Case Run6). (Case Run6). The rim of the heated disk is marked by the dashed line.

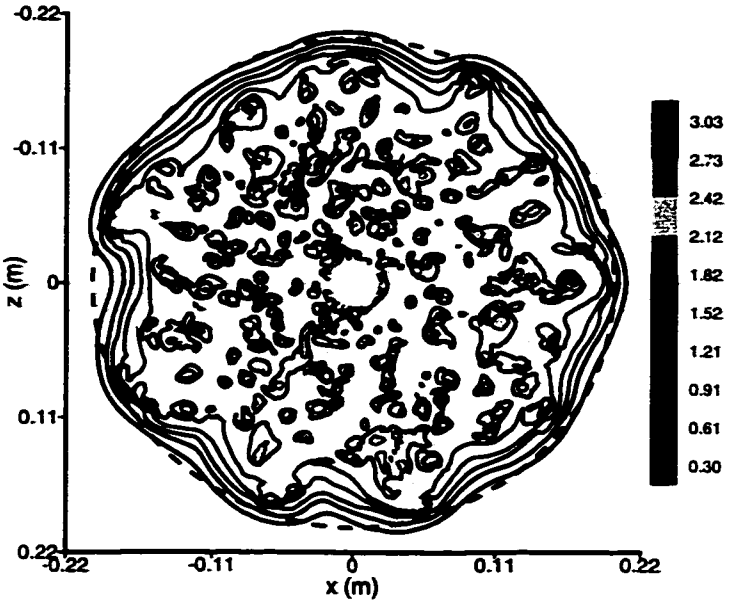

Figure 5.40: Top view of the temperature field at t=240s and y=20mm for $\Omega = 0.2$ rad/s, $B = 1.57 \times 10^{-6}$ m^2/s^3 (Case Run6). The rim of the heated disk is marked by the dashed line.

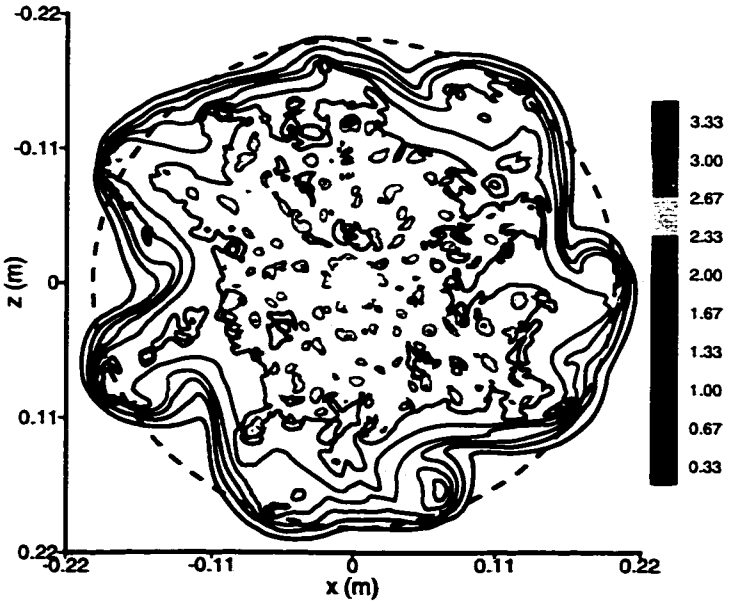

Figure 5.41: Top view of the temperature field at t=280s and y=20mm for $\Omega = 0.2$ rad/s, $B = 1.57 \times 10^{-6}$ m^2/s^3 (Case Run6). The rim of the heated disk is marked by the dashed line.

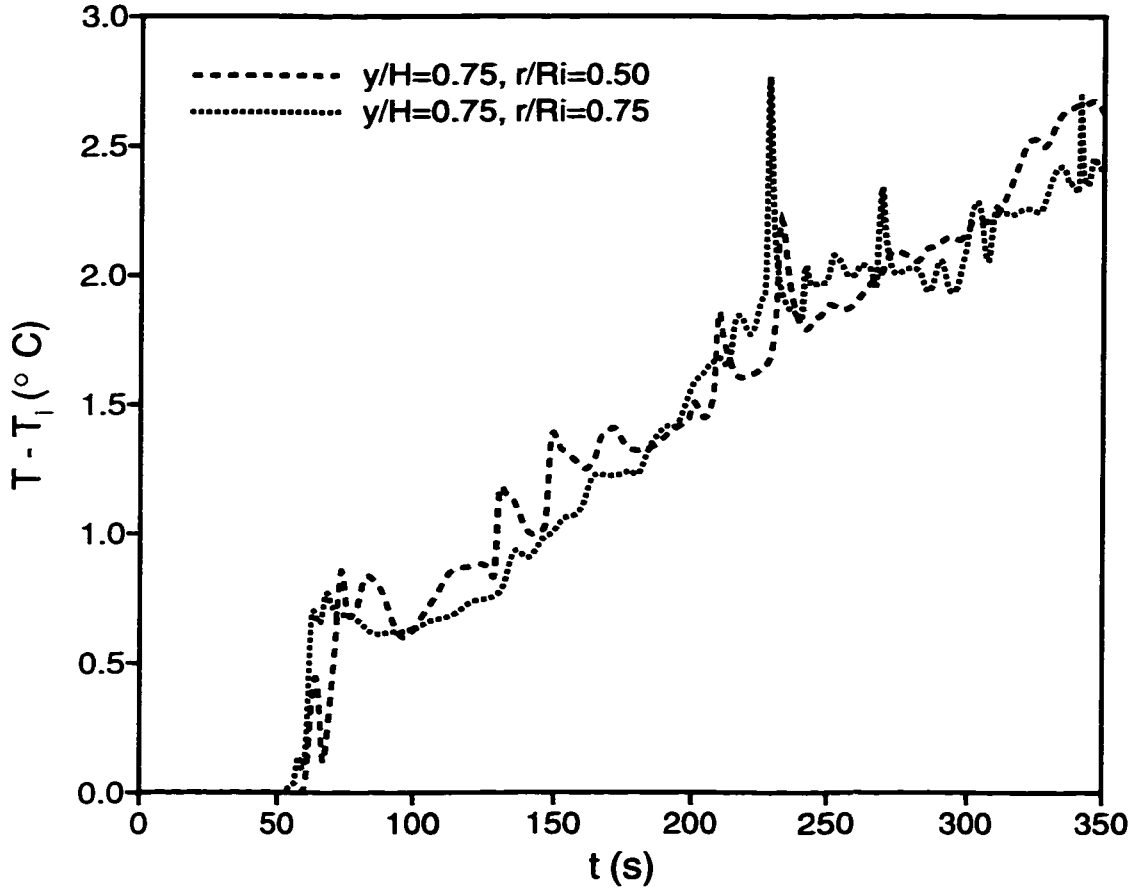

Figure 5.42: Temperature-time history for $\Omega = 0.2$ rad/s, $B = 1.57 \times 10^{-6}$ m^2/s^3 (Case Run6).

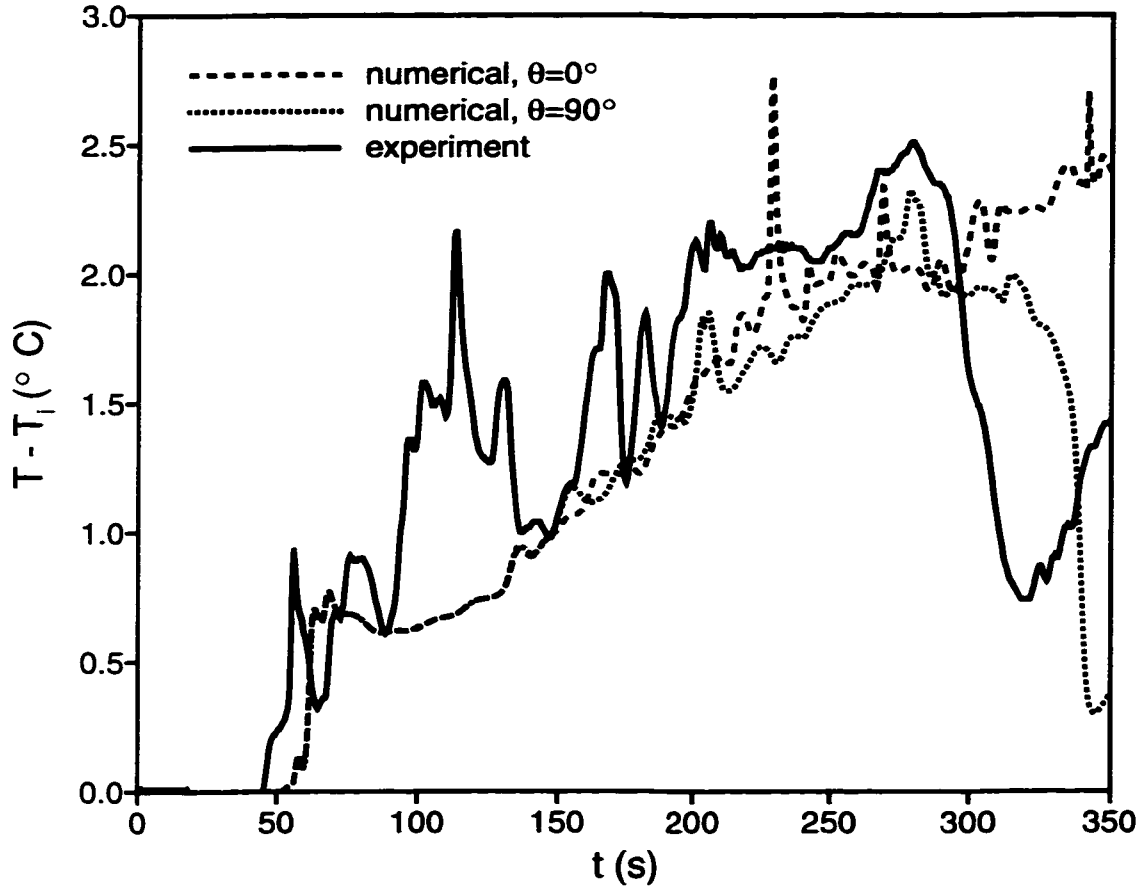

Figure 5.43: Temperature-time history at y/H=0.75 and r/R_i=0.75 for Ω = 0.2 rad/s, $B = 1.57 \times 10^{-6}$ m^2/s^3 (Case Run6).

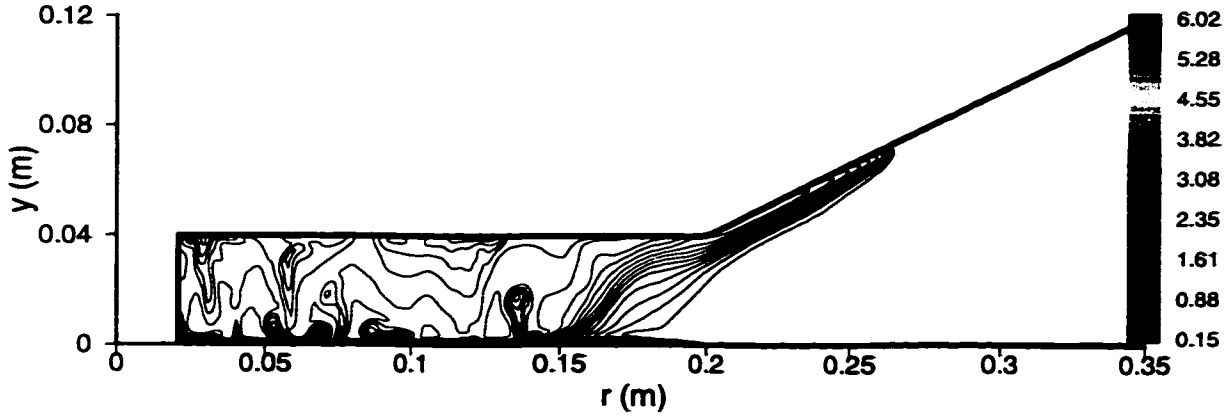

(a)

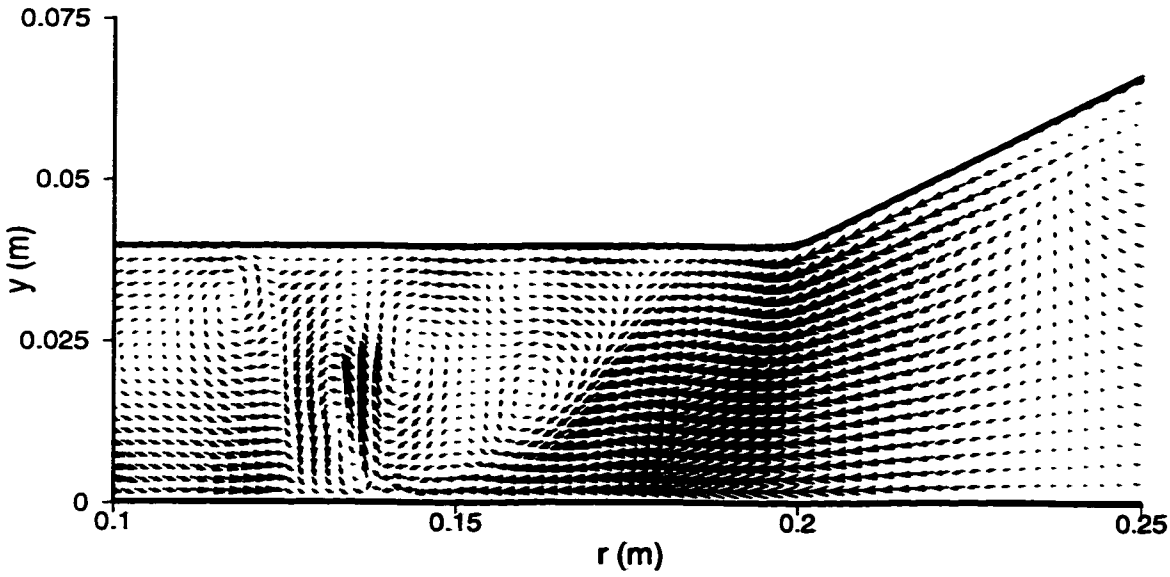

(b)

Figure 5.44: Side view of (a) temperature field (b) expanded velocity field at t=280s for $\Omega = 0.4$ rad/s, $B = 1.57 \times 10^{-6}$ m^2/s^3 (Case Run6).

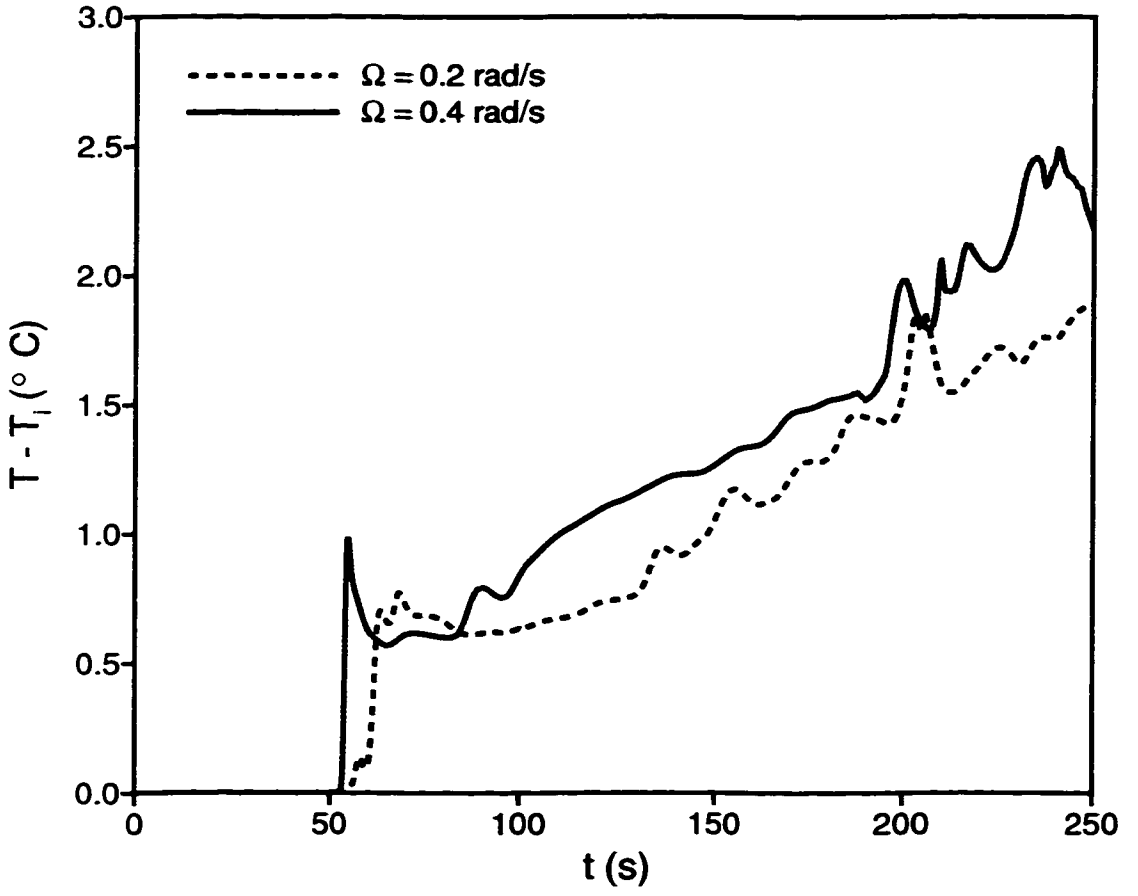

Figure 5.45: Temperature-time history at y/H=0.75 and r/R_i=0.75 for Case Run6 and Run8.

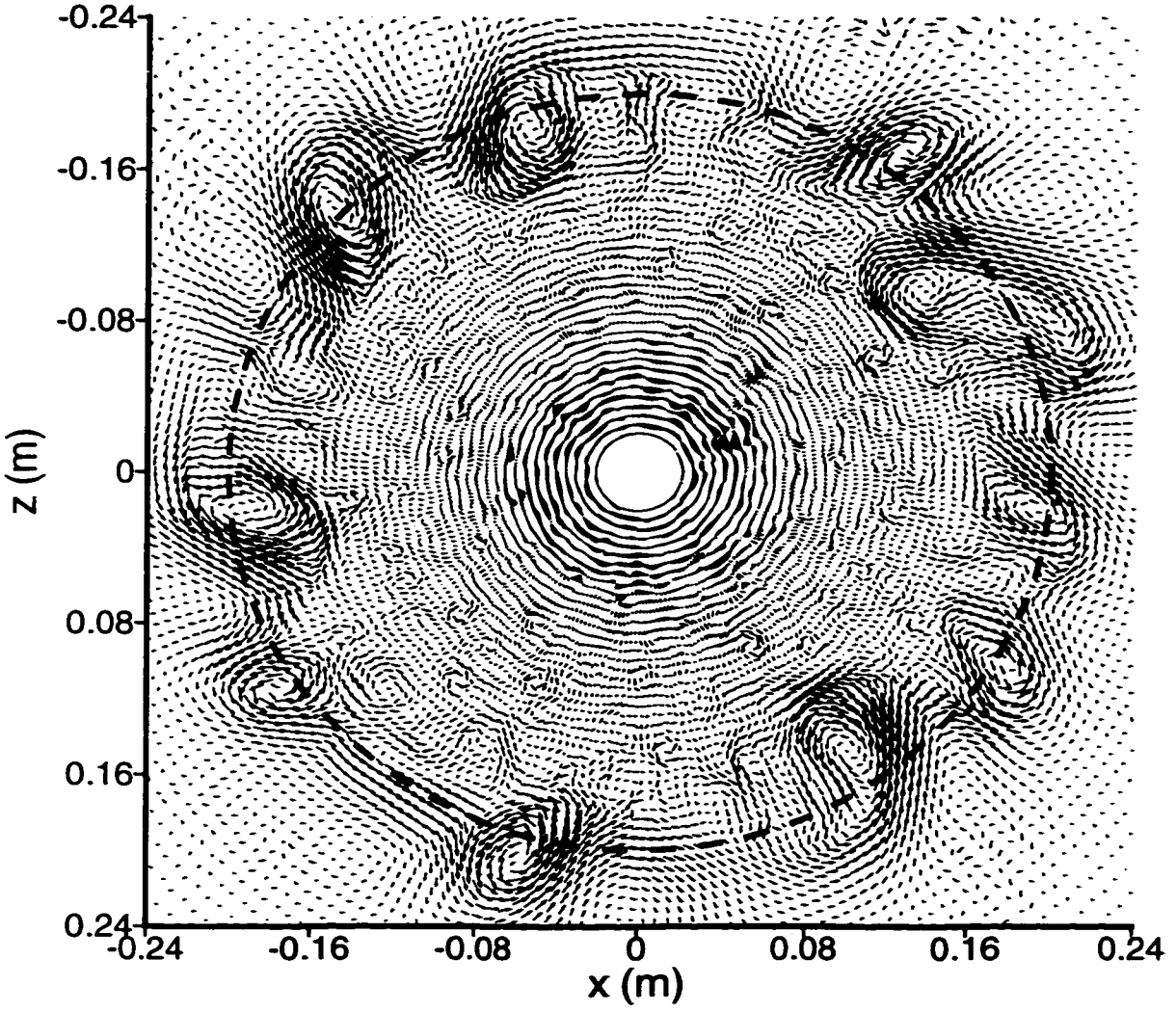

Figure 5.46: Top view of the velocity field at t=280s and y=5mm for Ω = 0.4 rad/s, $B = 1.57 \times 10^{-6}$ m^2/s^3 (Case Run8). The rim of the heated disk is marked by the dashed line.

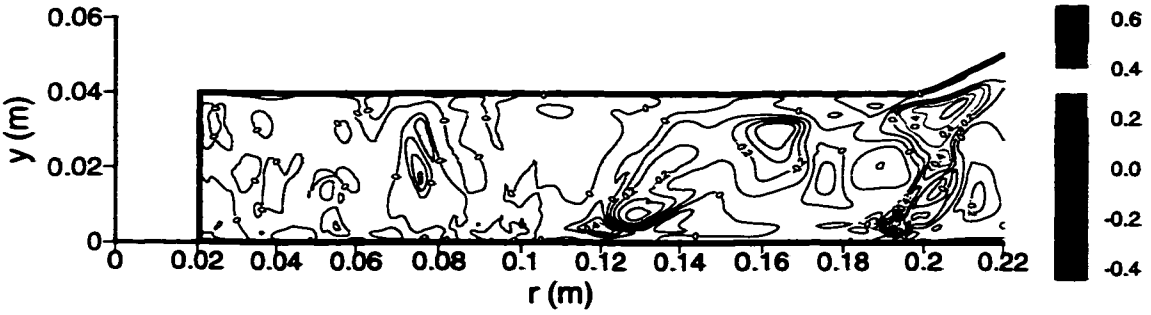

Figure 5.47: Side view of the ratio of SGS to viscous dissipation at t=280s for Ω = 0.2 rad/s, $B = 1.57 \times 10^{-6}$ m^2/s^3 (Case Run6).

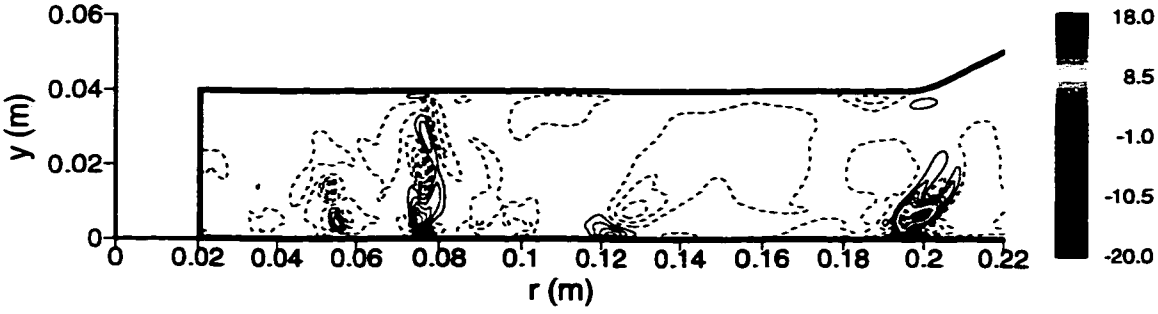

Figure 5.48: Side view of the SGS dissipation at t=280s for $\Omega = 0.2$ rad/s, $B = 1.57 \times 10^{-6}$ m^2/s^3 (Case Run6). Dashed lines represent negative values (forward scatter).

Chapter 6

Large-Eddy Simulation of Coastal Upwelling Flow

6.1 Introduction

The use of the term "upwelling" follows that of Sverdrup (1938), who points out that although upwelling is a widely used term in oceanography, a precise definition has not yet been given. In general, upwelling is the result of horizontal divergence in the surface layer, and usually the water comes from depths not exceeding a few hundreds meters. Upwelling occurs mostly from spring to summer near the eastern boundary of oceans (along the western coasts of continents) where prevailing winds carry the surface water away from the coast because of the Coriolis effect. Because upwelling brings cold and nutrient-rich deep water into the surface layer, it affects fishery productivity, ecology and climatology in the coastal regions. Since the importance of upwelling is widespread, so is the literature. A brief review of the analytical, numerical, experimental works and the field observations of coastal upwelling flows that relates to the present study can be found in Zang (1993).

Zang and Street (1995) were the first to carry out a large-eddy simulation (LES) of coastal upwelling flows which solved the full set of Navier-Stokes and scalar transport equations, and they compared their results with the experimental results of Narimousa and Maxworthy (1985 and 1987). Zang and Street made two approximations in their simulations: they employed a fluid viscosity that is 12.5 times larger than that of the water and they simulated upwelling flow in a section (one quadrant) of the tank used

in the corresponding laboratory study. Their simulation results confirm several flow structures observed in field observations and previous experiments and agree with some analytical criteria quantitatively. Since the viscosity used in Zang and Street's simulation is larger than that in the corresponding experiments, it is difficult to compare their simulation results to those measured data from the experiments which depend on viscosity. Zang and Street (1995) pointed out the need for simulations of high Reynolds number upwelling flows in a whole tank in order to yield a direct comparison with the experiments measurements.

It is the objective of the present study to carry out an LES of a full tank configuration using the actual viscosity of the working fluid and to make direct quantitative comparison with the measured data of the corresponding experiment. In the following sections of this chapter, the LES are carried out for two different upwelling laboratory experiments, one conducted at the University of Southern California and one at Stanford University. One of the important quantities in the upwelling flow, the disk friction velocity u_*, is discussed with regard to its experimental measurement, analytical determination and numerical calculation. The LES results are compared to the experiment measurements. The difference in the upwelling flow structures between the two experiments is also discussed.

6.2 Upwelling Experiments

A series of laboratory-scale experiments of shear-driven coastal upwelling was conducted by Narimousa and Maxworthy (hereafter referred to as NM) at the University of Southern California. In NM's experiments (1985 and 1987), a stably-stratified two-layer system with fluids of slightly different densities is brought to solid-body counter-clockwise rotation Ω inside a cylindrical tank with a conical bottom. The upper layer of working fluid is fresh water and the lower layer is salty water. At time t=0, the top lid begins to rotate in clockwise direction at a rotation rate $\Delta\Omega$

relative to the rotating tank to apply a stress to the top fluid surface. Upwelling flow is thus generated by the relative rotation of the top lid. Details of the experimental apparatus can be found in Narimousa and Maxworthy (1985). Similar experiments are being carried out at the Environmental Fluid Mechanics Laboratory (hereafter referred to as EFML) at Stanford University. Figure 6.1 is a schematic of the experimental apparatus. A summary of the geometric parameters of NM and EFML's experiment facilities is given in Table 6.1. In Table 6.1, H is the maximum depth of the tank, h_o is the initial depth of the upper layer, α is the slope angle of the sloping bottom, R_o is the outer radius, R_h is the inner radius, which is zero for NM's tank, and R_i is the distance between the center of the tank to the outer edge of the bottom of the tank. It can be seen from Table 6.1 that the experiment facilities at the two sites differ in the following respects: (i) unlike the NM cylindrical tank, an annular tank is used in the EFML experiment. (ii) the EFML tank is wider and taller than the NM tank.

6.3 Setup for the Numerical Simulations

Large-eddy simulations of NM's experiment have been carried out under exactly the same conditions as the experiment except that a small cylinder of radius R_h=0.045m was cut from the numerical domain to eliminate the coordinate singularity at the center. For the large-eddy simulations of EFML's experiment, the geometry of the flow domain is exactly the same as the configuration of EFML's laboratory test facility. In the simulations in this chapter, the subgrid dynamic mixed model (DMM) of Zang *et al.* (1993) was used.

6.3.1 Analytical Computation of the Grid Stretching and Mapping

For similar reasons to those given in Chapter 5, analytical stretching functions and analytical mapping functions are used in this simulation. The computational domain in the physical space (r, y, θ) can be mapped into a unit cube in the computational space $(\mathcal{R}, \mathcal{Y}, \Theta)$ by the following mapping functions:

$$\mathcal{R} = \frac{r - R_h}{R_t} \tag{6.1}$$

$$\mathcal{Y} = \frac{y - y_0}{H - y_0} \tag{6.2}$$

$$\Theta = \frac{\theta}{2\pi}, \tag{6.3}$$

where

$$R_t = R_o - R_h \tag{6.4}$$

$$R_b = R_i - R_h \tag{6.5}$$

$$y_0 = \frac{\tan\alpha}{2}\left[\frac{1}{A}\log\frac{\cosh A(r - R_i)}{\cosh AR_b} + (r - R_h)\right] \tag{6.6}$$

$$A = 0.4\text{mm}^{-1} \tag{6.7}$$

and

$$\mathcal{R} \in [0, 1] \tag{6.8}$$

$$\mathcal{Y} \in [0, 1] \tag{6.9}$$

$$\Theta \in [0, 1]. \tag{6.10}$$

The values of H, R_o, R_h, R_i and α are given in Table 6.1.

The grid points in the azimuthal direction of physical space (r, y, θ) are distributed uniformly due to the axisymmetric nature of the flow field. In order to resolve the

boundary layers at the solid walls and the Ekman layer at the top lid, non-uniform grids are used in the radial and vertical directions, with grid points clustered near the solid wall and stretched out away from the solid wall. The grid points in the computational space (ξ, η, ζ) are distributed uniformly with grid size $\Delta\xi = \Delta\eta = \Delta\zeta = 1$. The following stretching functions are used,

$$\begin{aligned}
\mathcal{R} &= \frac{d_\xi}{c_\xi}\frac{\xi}{N_\xi} \\
&+ \frac{1}{c_\xi}\left[\frac{1}{a_{\xi_1}}\log\frac{\cosh a_{\xi_1}(\xi/N_\xi - b_{\xi_1})}{\cosh a_{\xi_1} b_{\xi_1}} - \frac{1}{a_{\xi_2}}\log\frac{\cosh a_{\xi_2}(\xi/N_\xi - 1 + b_{\xi_2})}{\cosh a_{\xi_2}(1 - b_{\xi_2})}\right] \quad (6.11) \\
\mathcal{Y} &= \frac{d_\eta}{c_\eta}\frac{\eta}{N_\eta} \\
&+ \frac{1}{c_\eta}\left[\frac{1}{a_{\eta_1}}\log\frac{\cosh a_{\eta_1}(\eta/N_\eta - b_{\eta_1})}{\cosh a_{\eta_1} b_{\eta_1}} - \frac{1}{a_{\eta_2}}\log\frac{\cosh a_{\eta_2}(\eta/N_\eta - 1 + b_{\eta_2})}{\cosh a_{\eta_2}(1 - b_{\eta_2})}\right] \quad (6.12) \\
\Theta &= \zeta/N_\zeta, \quad (6.13)
\end{aligned}$$

where

$$\begin{aligned}
c_\xi &= d_\xi + \frac{1}{a_{\xi_1}}\log\frac{\cosh a_{\xi_1}(1 - b_{\xi_1})}{\cosh a_{\xi_1} b_{\xi_1}} - \frac{1}{a_{\xi_2}}\log\frac{\cosh a_{\xi_2} b_{\xi_2}}{\cosh a_{\xi_2}(1 - b_{\xi_2})} \quad (6.14) \\
c_\eta &= d_\eta + \frac{1}{a_{\eta_1}}\log\frac{\cosh a_{\eta_1}(1 - b_{\eta_1})}{\cosh a_{\eta_1} b_{\eta_1}} - \frac{1}{a_{\eta_2}}\log\frac{\cosh a_{\eta_2} b_{\eta_2}}{\cosh a_{\eta_2}(1 - b_{\eta_2})} \quad (6.15) \\
d_\eta &= e_\eta / \left\{ f_\eta - \frac{\tan\alpha}{2H}\left[\frac{1}{A}\log\frac{\cosh A(r - R_i)}{\cosh A R_b} + (r - R_h)\right]\right\}. \quad (6.16)
\end{aligned}$$

The values of the parameters used in the stretching function are

$$\begin{aligned}
a_{\xi_1} = a_{\xi_2} &= 12 \quad (6.17) \\
b_{\xi_1} = b_{\xi_2} &= 0.3 \quad (6.18) \\
d_\xi &= 0.25 \quad (6.19) \\
a_{\eta_1} = a_{\eta_2} &= 12 \quad (6.20) \\
b_{\eta_1} = b_{\eta_2} &= 0.3 \quad (6.21)
\end{aligned}$$

$$e_\eta = 0.16 \tag{6.22}$$

$$f_\eta = 0.8, \tag{6.23}$$

so that the stretching factor is less than 1.1 everywhere, which is consistent with the findings of Hodges (1997). Note that

$$\xi \in [0, N_\xi] \tag{6.24}$$

$$\eta \in [0, N_\eta] \tag{6.25}$$

$$\zeta \in [0, N_\zeta] \tag{6.26}$$

and N_ξ, N_η and N_ζ are the numbers of control volumes in the ξ-, η- and ζ-directions of the computational space.

In the physical space, the Cartesian coordinates (x, y, z) and cylindrical coordinates (r, y, θ) are related as follows (Figure 6.2):

$$x = r\cos\theta \tag{6.27}$$

$$y = y \tag{6.28}$$

$$z = r\sin\theta. \tag{6.29}$$

In summary, the relationship between the points in the physical space (x, y, z) and those in the computational space (ξ, η, ζ) are defined by Eqns. (6.11) to (6.13) and the following equations:

$$x = (R_h + R_t\mathcal{R})\cos(2\pi\Theta) \tag{6.30}$$

$$y = y_0 + (H - y_0)\mathcal{Y} \tag{6.31}$$

$$z = (R_h + R_t\mathcal{R})\sin(2\pi\Theta), \tag{6.32}$$

where

$$y_0 = \frac{\tan\alpha}{2}\left[\frac{1}{A}\log\frac{\cosh A(R_t\mathcal{R}-R_b)}{\cosh AR_b}+R_t\mathcal{R}\right]. \tag{6.33}$$

A section of the computational grid is illustrated in Figure 6.3.

6.3.2 Initial and Boundary Conditions

The working fluid, *i.e.,* the stably-stratified fluid, is initially in solid body rotation (Ω) with the tank. The initial density field, which is horizontally uniform and vertically separated by a narrow interface, approximates a "two-layer" stratified system with a lighter fluid on top of a heavier fluid. The density difference between the lower and upper layer is $\Delta\rho$. At time t=0, the top lid begins to rotate clockwise at a rate $\Delta\Omega$ relative to the rotating tank to apply a stress to the top fluid surface, and thus generates upwelling. The initial vertical density profile is approximated by a hyperbolic tangent function. Since there are no experimental data available on the thickness of the density interface, the interface thickness is chosen to be as small as possible and yet large enough to be resolved by the computational grid. A no-slip velocity boundary condition and no-flux scalar boundary condition are imposed at all solid walls.

6.4 Determination of the Disk Friction Velocity

Upwelling at a steady rate is caused by offshore Ekman transport. The amount of upwelling in a given region is proportional to changes in the Ekman flux across it, which depends on the wind stress applied at the ocean's surface. We define the disk friction velocity u_* to be the friction velocity applied to the surface of the fluid by the top disk. The disk friction velocity is directly related to the surface shear stress

τ_w at the disk as

$$u_* = \sqrt{\frac{\tau_w}{\rho}}. \tag{6.34}$$

Narimousa and Maxworthy (1985 and 1987) found in their experimental study that the upwelling flow field can be characterized by a single non-dimensional parameter

$$\theta_* = \frac{g' h_0}{u_* f \lambda_s}, \tag{6.35}$$

where $\Delta\rho$ is the density difference between the two layers, $g' = g\Delta\rho/\rho_0$ is the reduced gravity between the two layers, h_0 is the initial depth of the top layer, $f = 2\Omega$ is the Coriolis parameter, u_* is the disk friction velocity at the location of the upwelled front, and λ_s is the distance from the final stationary upwelled front to the outer edge of the tank. The parameter θ_* combines the effects of stratification, rotation and surface stress (or disk friction velocity), among which the surface stress is the most difficult to obtain in the experiment or in the simulation. Therefore, in order to quantitatively study upwelling flow, it is crucial to make accurate assessments of the shear stress τ_w (or disk velocity friction u_*) in the experiments and to produce accurate τ_w (or u_*) in the numerical simulations.

6.4.1 Experimental Estimation of the Disk Friction Velocity

While is is possible in an accurate and well-resolved simulation to determine u_* quite precisely, it is often virtually impossible to get a quantitative estimation of u_* in a physical experiment. Thus, no direct measurements of u_* were made by Narimousa and Maxworthy in their experimental studies of upwelling flows (1985 and 1987). Instead, they inferred the u_* for their upwelling experiment from an analysis of the experimental results of Kantha *et al.* (1977) and the experimental observation of Narimousa *et al.* (1986) for different flows.

The experimental apparatus of Kantha *et al.*'s experiment (1977) consists of a flat

bottom annular tank, which has inner and outer diameters of 106.7cm and 152.4cm, respectively, and is 28cm deep. The tank initially contains two homogeneous layers with a density difference $\Delta\rho$. The surface stress was applied by means of a rotating screen at the fluid surface. The shear stress τ_w applied at the fluid surface by the screen is then

$$\tau_w = \rho u_*^2 = (T_\theta - T_F)/AR, \tag{6.36}$$

where T_θ is the torque indicated by the deflection of the turntable, T_F is the frictional torque in the bearings, A is the surface area of the tank, R the mean radius and u_* is the disk friction velocity. By direct measurements of T_θ, T_F and U_s, they found that

$$u_* \approx 0.07 U_s, \tag{6.37}$$

where U_s is the speed of the screen. There are major differences between Kantha *et al.*'s experiment (1977) and Narimousa and Maxworthy's experiments (1985 and 1987). In Narimousa and Maxworthy's experiments, a solid top lid was used instead of a screen. Narimousa and Maxworthy's experimental apparatus is a cylindrical tank, not a thin annular tank, thus their τ_w (or u_*) is a function of radius. Therefore, it is not reasonable (as our simulations show) to assume τ_w (or u_*) to be independent of radius as in Kantha *et al.*'s experiment.

The experimental apparatus of Narimousa *et al.*'s experiment (1986) consists of a recirculating water channel with a straight test section and a pump section both 2m long. These two sections are joined by two semi-circular annuli of mean radii 0.45m. The width of the channel is 0.15m in the test section and in the semi-circular annuli. A two-layer fluid system with a free surface was produced initially. A disc pump was used to produce a turbulent shear flow in the top layer. They define a friction velocity of the pump u_*, which results from the pressure gradient force and the shear stress force accelerating the flow arising from the action of the pump. They found that the

mean mixed-layer velocity U is related to the friction velocity of the pump u_* as

$$U \approx 10.6u_*. \tag{6.38}$$

Narimousa and Maxworthy (1985) then conducted an experiment using the lowest tank rotation rate $\Omega = 0.622\text{rad/s}$ of their tank and made direct measurement of the top-layer mean velocity U, and found that U is related to the top plate (disk) velocity U_p as

$$U \approx 0.744U_p. \tag{6.39}$$

By combining Eqn. (6.38) and Eqn. (6.39), Narimousa and Maxworthy concluded that

$$u_* \approx 0.07U_p. \tag{6.40}$$

There is fundamental difference between Narimousa *et al.*'s experiment (1986) and Narimousa and Maxworthy's experiments (1985 and 1987). In Narimousa *et al.*'s experiment (1986), the friction velocity of the pump u_* is not caused by surface shear stress and thus has a different physical meaning than the disk friction velocity of Narimousa and Maxworthy's experiment (1985 and 1987).

Based on the experimental results of Kantha *et al.* (1977) and the experimental observation of Narimousa *et al.* (1986), Narimousa and Maxworthy (1985) directly relate disk friction velocity u_* with an independent variable, *i.e.*, the known disk velocity $U_p = r\Delta\Omega$, as

$$u_* \approx 0.07U_p = 0.07r\Delta\Omega. \tag{6.41}$$

6.4.2 Theoretical Discussion of the Disk Friction Velocity

We consider the motion of a homogeneous, incompressible fluid rotating with an angular velocity Ω. Two horizontal rigid walls, located at $y = 0$ and $y = -\infty$, are perpendicular to the axis of rotation. A horizontal uniform velocity U_w is specified at

the top wall and the bottom wall is kept stationary. The governing equations are :

$$\frac{\partial u}{\partial x}+\frac{\partial v}{\partial y}+\frac{\partial w}{\partial z} = 0 \tag{6.42}$$

$$\frac{\partial u}{\partial t}+u\frac{\partial u}{\partial x}+v\frac{\partial u}{\partial y}+w\frac{\partial u}{\partial z} = -\frac{1}{\rho}\frac{\partial p}{\partial x}+\nu\left(\frac{\partial^2 u}{\partial x^2}+\frac{\partial^2 u}{\partial y^2}+\frac{\partial^2 u}{\partial z^2}\right)+fw \tag{6.43}$$

$$\frac{\partial v}{\partial t}+u\frac{\partial v}{\partial x}+v\frac{\partial v}{\partial y}+w\frac{\partial v}{\partial z} = -\frac{1}{\rho}\frac{\partial p}{\partial y}+\nu\left(\frac{\partial^2 v}{\partial x^2}+\frac{\partial^2 v}{\partial y^2}+\frac{\partial^2 v}{\partial z^2}\right)-g \tag{6.44}$$

$$\frac{\partial w}{\partial t}+u\frac{\partial w}{\partial x}+v\frac{\partial w}{\partial y}+w\frac{\partial w}{\partial z} = -\frac{1}{\rho}\frac{\partial p}{\partial z}+\nu\left(\frac{\partial^2 w}{\partial x^2}+\frac{\partial^2 w}{\partial y^2}+\frac{\partial^2 w}{\partial z^2}\right)-fu, \tag{6.45}$$

where $f = 2\Omega$ is the Coriolis parameter. The boundary conditions are

$$u = U_w, \qquad v = w = 0 \qquad \text{at} \qquad y = 0 \tag{6.46}$$

$$u \to 0, \qquad v, w \to 0 \qquad \text{as} \qquad y \to -\infty. \tag{6.47}$$

The analytical solutions to the above governing equations and boundary conditions[1] are

$$u = U_w \exp\left(\sqrt{\frac{f}{2\nu}}y\right)\cos\left(\sqrt{\frac{f}{2\nu}}y\right) \tag{6.48}$$

$$v = 0 \tag{6.49}$$

$$w = U_w \exp\left(\sqrt{\frac{f}{2\nu}}y\right)\sin\left(\sqrt{\frac{f}{2\nu}}y\right). \tag{6.50}$$

Thus, the shear stress at the top wall ($y = 0$) is

$$\tau_w = \mu\frac{\mathrm{d}u}{\mathrm{d}y}|_{y=0} = \rho U_w\sqrt{\frac{\nu f}{2}}, \tag{6.51}$$

[1] Refer to Pedlosky 1987, page 186, for the solution procedure.

and the top wall friction velocity is

$$u_* = \sqrt{\frac{\tau_w}{\rho}} = \left(\frac{\nu U_w^2 f}{2}\right)^{1/4} = \left(\nu U_w^2 \Omega\right)^{1/4}. \tag{6.52}$$

When we use this analytical solution to evaluate the disk friction velocity u_* at the upwelled front of the upwelling flow, we use the disk velocity at the radial location of the upwelled front for the top wall velocity U_w of the analytical solution, *i.e.*, $U_w = r\Delta\Omega$. Thus, the analytical solution can only give an approximate estimation of the u_* value of the upwelling flow we are studying. The disk friction velocity at the upwelled front evaluated by the derived analytical solution is given by

$$u_* = \left[\nu(r\Delta\Omega)^2\Omega\right]^{1/4}. \tag{6.53}$$

6.4.3 Numerical Calculation of the Disk Friction Velocity

Since the surface shear stress τ_w (or disk friction velocity u_*) plays an important role in the prediction of the upwelling flow, it is essential to calculate it accurately in the numerical simulations. The primary length scale in the vertical direction is the thickness of the Ekman layer. The scaling relations for a laminar Ekman layer thickness δ_E^l (Greenspan 1968) and a turbulent Ekman layer thickness δ_E^t (Caldwell *et al.* 1972) are

$$\delta_E^l \sim \sqrt{\frac{\nu}{f}} \tag{6.54}$$

$$\delta_E^t \sim \frac{u_*}{f}, \tag{6.55}$$

where ν is the kinematic viscosity and f is the Coriolis parameter. A grid resolution study was performed to decide whether there are enough grid points inside the top and the bottom Ekman layers. Two numerical simulations (see Table 6.1 and discussion about it later) of NM's experiment (Cases NM1 and NM2), with 128 and 160 grid

points in the vertical direction, respectively, are carried out and the results are given in Figure 6.4. Figure 6.4 shows that the two u_* curves lay on each other indicating that there are sufficient grid points inside the Ekman layers. Thus, 128 grid points in the vertical direction will be used in the simulation runs. The azimuthally-averaged u_* at different times are plotted against radius r in Figure 6.5. Figure 6.5 shows that u_*, which is always a function of r, first decreases with time, then stops changing with time between t=200s ($t/t_s = 0.91$) and t=250s ($t/t_s = 1.14$). A curve fitting of the u_* vs. radius r at t=250s (Figure 6.6) for the Case NM1 gives

$$u_* = 0.0145r + 0.0025. \tag{6.56}$$

The units for r and u_* used in the above equation are m and m/s, respectively. For this simulation case (Case NM1), the top lid rotation rate $\Delta\Omega = 0.185$rad/s. Thus, the relation between u_* and $U_p = r\Delta\Omega$ is

$$u_* = 0.078U_p + 0.025 = 0.078r\Delta\Omega + 0.0025, \tag{6.57}$$

which is different from the formula obtained from experimental estimation [Eqn. 6.41].

6.4.4 Conclusions

In summary, at the stationary upwelled front $r = 0.33$m of Case NM1, the u_* value from the experimental estimation [Eqn. (6.41)], the analytical analysis [Eqn. (6.53)] and the numerical calculation [Eqn. (6.57)] are $u_*^{\text{exp}} = 0.0043$m/s, $u_*^{\text{ana}} = 0.0096$m/s and $u_*^{\text{num}} = 0.0073$m/s, respectively. As noted above, no direct measurements were made toward u_* in NM's upwelling experiments. Instead, NM inferred the u_* for their upwelling experiments from an analysis of previous experiments using different experimental apparatus. There are considerable differences between the NM's and the previous experiments, thus the experimental estimation [Eqn. (6.41)] may not

give an accurate assessment of the u_* value of the upwelling flow we are studying. The analytical analysis performed above is based on a uniform fluid velocity, while the fluid velocity is a function of radius in the upwelling flow. Thus, the analytical solution can only give an approximate estimation of the u_* value of the upwelling flow. The grid resolution study above shows that the current simulation is well resolved and thus the u_* value can be determined precisely.

6.5 Simulations Conducted and Relevant Parameters

Two sets and a total of four cases of large-eddy simulations were carried out in this work. The first set of simulations (Cases NM1 and NM2) simulate Case (a) of Narimousa, Maxworthy and Spedding's experiments (1991). The only difference between the Case NM1 and NM2 is the grid resolution. The second set of simulations (Cases EFML1 and EFML2) simulate EFML's on-going experiments. The only difference between the Case EFML1 and EFML2 is also the grid resolution. A summary of the grid resolutions and physical parameters for the four cases of the simulation runs is given in Table 6.2. The number of grid points for each case shown in Table 6.2 is for interior points. Two fictitious points outside the physical domain are added in each dimension in the simulations to facilitate implementing boundary conditions. The reference time scale t_s used this study is the spin-up time scale defined by Linden and van Heijst (1984) as

$$t_s = (h_o/\Delta\Omega)[(\Omega + \Delta\Omega)/\nu]^{1/2}. \tag{6.58}$$

The non-dimensional parameters for the two different upwelling experiments are given in Table 6.3. θ_* is the non-dimensional parameter defined in Eqn. (6.35), which can be used to characterize the upwelling flow field (Narimousa and Maxworthy 1987). The Rossby number ϵ evaluates the ratio of the convective acceleration to the Coriolis

acceleration. In the definition of ϵ, $U_p = R_o\Delta\Omega$ is the maximum disk velocity, and $L_R = R_o - R_h$ is a horizontal length scale. The Ekman number E gives the ratio of the frictional force to the Coriolis acceleration. $\hat{R}$ is the geometric mean of the radii of the two layers

$$\hat{R} = \sqrt{\overline{R}_1\overline{R}_2}, \tag{6.59}$$

and the deformation radius for each layer is defined as

$$\overline{R}_i = \sqrt{g'\overline{h}_i}/f, \tag{6.60}$$

where $\overline{h_i}$ is the averaged initial depth of each layer and $g' = g(\rho_2 - \rho_1)/\rho_1$. The values of $\hat{R}$ are much smaller than L_R for both experiments, which indicates that the effect of the inner wall of the annulus on the rotation-dominated flow structures near the outer wall is small.

6.6 LES of Narimousa and Maxworthy's Experiment

6.6.1 Grid Resolution

A grid resolution study in the vertical direction was conducted in simulation Cases NM1 and NM2 in Section 6.4.3 to determine whether there are enough grid points inside the top Ekman layer. One hundred and twenty-eight grid points in the vertical direction are thus used in the production run (Case NM1); 192 grid points are used in the radial direction to ensure that there are five grid points inside the inner and outer wall boundary layers. About 20 azimuthal frontal waves are observed by the Narimousa *et al.* (1991). Three hundred and twenty grid points have been used in the azimuthal direction to resolve the twenty waves.

6.6.2 Qualitative Description

At time t=0s, the top disk is set to rotate clockwise relative to the system at disk rotation rate $\Delta\Omega$ after the two-layer fluid system is brought to counter-clockwise solid-body rotation at tank rotation rate Ω. A stress is then applied to the top surface of the upper-layer of fluid by the differentially rotating disk. The fluid below the top disk which moves with the disk is driven radially inward by the Coriolis force and forms the top Ekman layer. The resulting Ekman flux causes the density interface to rise near the outer wall and descend near the inner wall. As this process continues, the density interface intersects the top disk and a surface front is formed. The time scale when the front appears at the top surface is called the front-surfacing time t_f. Yoshida (1955) proposed a analytical criterion for t_f as

$$t_f = \rho h_0 \hat{R} f / \tau_s, \tag{6.61}$$

where ρ is the fluid density, h_0 is the initial depth of the upper layer, f is the Coriolis parameter, τ_s is the surface stress and $\hat{R}$ is the geometric mean of the radii of the two layers defined in Eqn. (6.59). For Case NM1, the front-surfacing time t_f is 39s by Yoshida's analytical criterion. The density field at t=40s (t/t_s=0.18) from LES is shown in Figure 6.7. We can see from Figure 6.7 that the density interface reaches the top disk and a axisymmetric surface front forms near the outer edge of the tank at t=40s (t/t_s=0.18), which is in agreement with the analytical prediction. Zang and Street (1995) denotes the surface density front as the "primary front". Even before the density interface reaches the top surface, mixed layer fluid is carried radially inward by the Ekman transport. Thus, a thin layer of the mixed fluid, which is slightly heavier than the upper-layer fluid develops under the top disk. Zang and Street (1995) denote this layer as the "top inversion layer". At the tip of the top inversion layer, another weak secondary front is developed.

The primary front migrates away from the outer wall after its formation and allows

the lower-layer fluid to contact the top disk in a narrow strip of width λ around the outer edge of the tank, as shown in Figure 6.8. From Figure 6.8, which gives the density field from LES at t=80s (t/t_s=0.36), one can see that the top inversion layer extends further towards the center of the tank. In the process of the migration of the surface front, the Coriolis force tends to increase the distance from the outer edge of the tank to the front λ, while the radial pressure gradient caused by the front deformation opposes the Coriolis force, and tends to stop the front. Eventually, geostrophic balance is reached and the front becomes stationary, so that λ reaches its steady-state value λ_s at approximately t=220s (t/t_s=1.0).

A sequence of side views of the density field from t=40s (t/t_s=0.18) to 300s (t/t_s=1.36) is shown in Figures 6.9 to 6.12. They show that the top inversion layer becomes thicker and a mixing zone can be seen developing with time near the outer edge of the tank, which is consistent with the observation of Mooers *et al.* (1976). Those figures also show that a Rayleigh-Taylor type of instability takes place in the top inversion layer due to the unstable stratification, the heavier mixed fluid in the top inversion layer begins to sink to the lower level and thus deepens the top inversion layer.

Before the front becomes stationary, at some time when $\lambda < \lambda_s$, the front becomes unstable to small perturbations and small amplitude azimuthal frontal waves appear at the axisymmetric front. The developed instabilities are believed to be baroclinic instabilities (Narimousa *et al.* 1991). The potential energy contained in the density field is the source of kinetic energy for the baroclinic instabilities. A more detailed discussion about the instability mechanism in the upwelling flow is given in Section 6.8 of this chapter. At t=80s (t/t_s=0.36), such small amplitude frontal waves are already seen at the axisymmetric front (Figure 6.8). When the waves first appear at the front, they have their smallest wavelength. As time proceeds, neighboring waves combine to create waves of larger size. The process continues until the waves reach their maximum (saturated) size λ_w. When the waves first appear at the front, they

have their lowest azimuthal drift velocity in the direction of the applied stress. As the neighboring waves combine to create waves of larger size, the drift velocity of the waves also increases. The waves reach their maximum drift velocity u_w when the waves reach their saturated size λ_w.

Figures 6.13 to 6.15 show the the top view density field and velocity field [2] development from t=100s (t/t_s=0.46) to 200s (t/t_s=0.91). Due to the existence of the frontal wave drift velocity, the velocity vectors are plotted in a reference frame traveling with the maximum drift velocity u_θ in order to reveal the vortex-like structure of the frontal waves. At t=100s (t/t_s=0.46), Figure 6.13 shows a nearly axisymmetric wave pattern. Figures 6.13 and 6.14 show that smaller frontal waves at t=100s (t/t_s=0.46) grow into larger waves at t=200s (t/t_s=0.91). By t=200s (t/t_s=0.91), the previous axisymmetric bands of the mixed fluid at the unstable top inversion layer break into isolated patches (Figure 6.14) and the heavier fluid sinks back to the lower level (Figure 6.11). A close look at the density and velocity fields of four different locations (points A, B, C and D) on Figure 6.14a reveals the rich flow structures in the upwelling flow (Figures 6.15a, b, c and d). The corresponding vertical vorticity and velocity fields for the same four locations (Figures 6.16a, b, c and d) show that a meandering, jet-like wave motion is produced around the outer edge of the upwelled front, with cyclones to the offshore side (at a wave trough) and anticycloclones to the inshore side (at a wave crest). In other words, the frontal waves appear in the form of cyclone/anticyclone pairs when the axisymmetric front becomes unstable. These wave troughs propagate in the direction of the applied surface stress and eventually detach from the wave troughs. Figure 6.16a shows that a cyclone is about to pinch off at location C. Meanwhile, a cyclone just pinches off at location D (Figure 6.16b). At locations A and B (Figures 6.16c and d), the pinched-off cyclone interacts with its neighboring frontal anticyclone and leads to generation of an outward meandering jet

[2]The velocity vectors are plotted at every second point in the radial direction, at every second point in the azimuthal direction.

transferring a filament of heavier fluid towards the center of the tank (Figures 6.15c and d). The flow structures observed here closely resemble those observed in one of the NM's experiment (1987) with similar parameters (Figure 6.17). Figure 6.18 shows the density and velocity fields at t=220s (t/t_s=1.0) with the updated locations of the four points marked at t=200s (t/t_s=0.91). The pinched-off eddies at locations A and D continue to grow in size. From t=200s (t/t_s=0.91) to 300s (t/t_s=1.36) (Figures 6.14 and 6.19), the size of the frontal waves remain about the same, suggesting that the frontal waves reach their saturated size during this time period.

6.6.3 Quantitative Comparisons with Experiment

Because the large-eddy simulation is carried out under the same conditions as NM's experiments, a direct comparison between the simulation results and the experiment measurements can be made. Twenty saturated frontal waves are reported by NM (1991). Figure 6.20 is a streak photograph of the flow field (top view) from NM's experiment. About seventeen saturated frontal waves are observed in the LES result (Figures 6.14a and 6.19a). The saturated wavelength λ_w is related to the number of saturated waves N_w by $\lambda_w = 2\pi(R_o - \lambda_s)/N_w$. The discrepancy in the number of saturated waves lies in the fact that it is difficult to count the number of waves accurately from the highly irregular flow structures obtained, no matter in the experiment or numerical simulation (Figures 6.19 and 6.20). The distance from the front to the outer edge of the tank when the density front becomes stationary is the stationary-front width λ_s. Its LES value is compared here to the measurements of NM (1987). In NM's experiment, small neutrally buoyant particles were placed in the interface between the two layers and their motion recorded by streak photograph. Figure 6.21 is a streak photograph of the flow field (top view) at t=320s (t/t_s=1.45) for Case NM1. The radius of the tank is R_o=0.45m and a direct measurement on the photo gives a λ_s value of 0.13m. Figure 6.22 shows the side view of an *azimuthally-averaged*

density field at t=320s (t/t_s=1.45) from the LES. A λ_s value of 0.12m is obtained from Figure 6.22. The uncertainty in the comparison of λ_s lies in the fact that there is no experimental data available on the thickness of the density interface and the specific vertical location where the small buoyant particles were placed initially is unknown. In the LES, the density interface expands some distance (Figure 6.22), but the location of the density plane with the average density value of the mixed layer is chosen. The maximum drift velocity given by NM (1987) is

$$u_w = 0.37U_p, \tag{6.62}$$

where $U_p = r\Delta\Omega$ is the disk velocity. At the stationary front $\lambda_s = 0.11$m, u_w is 0.023 m/s from the experiment. The computed wave drift speed from the LES result is about 0.027m/s. In NM's experiment, they measured the speed of the waves by measuring their distance from a fixed point on the tank from photographs taken from the experiments. In the LES, similar method is used except that the instantaneous flow field plots are used to replace the photographs. The above comparisons are summarized in Table 6.4. The differences for λ_s, N_w and u_w between the LES-computed and the experimentally-measured values are -8%, 18% and -15% of the LES values, respectively.

6.7 LES of EFML's Experiment

6.7.1 Grid Resolution

A grid resolution study in the vertical direction was conducted in simulation Cases EFML1 and EFML2 to determine whether there are enough grid points inside the top Ekman layer. Figure 6.23 shows that the two u_* vs. r curves, obtained by using different number of vertical grid points, are identical, indicating that there are sufficient grid points inside the Ekman layers. Thus, 128 grid points in the vertical

direction are used in the production run (Case EFML1); 256 grid points are used in the radial direction to ensure that there are five grid points inside each of the inner and outer wall boundary layers. Less than 20 azimuthal frontal waves have been observed in the on-going experiment conducted at EFML. Three hundred and twenty grid points have been used in the azimuthal direction to resolve these waves.

6.7.2 Simulation Results

The on-going experiment at EFML has not produced production data sets yet; thus only a qualitative description of the time evolution and structure of the upwelling flow will be provided. Tables 6.2 and 6.3 summarize the physical and the non-dimensional parameters used for the two different upwelling cases. Since the EFML's tank is much bigger than NM's tank, it is structurally unsafe to rotate as fast as NM's tank. Thus, the main difference lies in the tank rotation rate. From Table 6.3, one can see that the θ_* value for Case EFML1 (θ_*=5.8) is more than four times bigger than that of Case NM1 (θ_*=1.4), which is mainly due to the slow rotation of both the tank and the disk. Narimousa and Maxworthy (1985 and 1987) found in their experimental study that the upwelling flow field can be characterized by the non-dimensional parameter θ_*; accordingly, flow field features different from those observed in Case NM1 are expected.

As in Case NM1, at t=0s, the top disk exerts a stress to the fluid surface as it rotates opposite to the tank's rotation. The applied surface stress produces an along-shore shear flow and an offshore Ekman flux in the top layer. The resulting Ekman flux causes the density interface to descend near the inner wall and to rise near the outer wall. At t=50s (t/t_s=0.2), the density interface just intersects the top disk and forms an axisymmetric density front (Figure 6.24). The front-surfacing time t_f predicted by Yoshida's analytical criterion [Eqn. (6.61)] is 56s. Driven by the Coriolis force, the front migrates further away from the outer wall. In this process,

the upwelling front becomes unstable to small perturbations and baroclinic instability develops. By t=100s (t/t_s=0.4), a narrow strip of lower-layer fluid has appeared at the surface around the outer edge of the tank, and small amplitude baroclinic frontal waves have also appeared at the axisymmetric front (Figure 6.25). As time proceeds, the frontal waves continue to grow in size (Figures 6.26 to 6.28) [3] and develop into large amplitude baroclinic waves. Due to the existence of the frontal wave drift velocity, the velocity vectors are plotted in a reference frame traveling with the maximum drift velocity u_θ in order to reveal the vortex-like structure of the frontal waves. The wave structure consists of cyclone/anticyclone pairs (Figure 6.29) as observed in Case NM1. At a later time t=300s (t/t_s=1.2), the flow structures (Figure 6.30) remain similar to those observed before (Figure 6.28) and still no pinch-off process occurs (Figure 6.31). When the horizontal pressure gradient caused by the front deformation balances the Coriolis force and the front becomes stationary at a distance λ_s from the outer edge of the tank. The disk friction velocity u_* at different times are plotted against radius r in Figure 6.32. Figure 6.32 shows that u_* first decreases with time and is approaching to a constant value at each radial location at approximately t=250s (t/t_s=1.0), suggesting that the upwelling front is just becoming stationary.

The time evolution process of simulation Case EFML1 is similar to that of simulation Case NM1. However, a close examination of the flow structure reveals the following differences between the two simulation cases. The amount of upwelling in a given region is proportional to changes in the Ekman flux across it, which depends on the shear stress applied at the fluid surface. As a result, the top inversion layer is much thinner in Case EFML1 (Figures 6.33 to 6.36) than that of Case NM1 (Figures 6.9 to 6.12). The top inversion layer is so thin that the sinking of the mixed fluid in

[3]The velocity vectors are plotted at every third point in the radial direction, at every second point in the azimuthal direction.

the top inversion layer due to unstable stratification in Case EFML1 is not as obvious as that of Case NM1. A mixing zone can be seen developing with time near the outer edge of the tank, as in Case NM1. Compared to Case NM1 (Figure 6.18), the frontal instabilities in Case EFML1 are less intense (Figure 6.28) at the same non-dimensional time $t/t_s = 1$. This finding is consistent with the observation of NM's experiments (1987). NM (1987) reported that the frontal instabilities are much more intense and the upwelling front itself display strong unsteadiness and cyclonic eddies containing the lower-layer fluid pinches off from the front at low θ_* values ($\theta_* \leq 6$). At large values of θ_* ($\theta_* > 6$), the frontal waves are large, and they tend to remain at the front and consequently no pinch-off process is observed. Unlike Case NM1, the frontal waves remain at the front and no pinch-offs are observed (Figure 6.31) by t=300s ($t/t_s = 1.2$) for Case EFML1 (θ_*=5.8). Likewise, no pinch-offs were found in the EFML physical experment either under the same conditions. While in Case NM1 (θ_*=1.4), pinched-off eddies and jet-like motions are already observed (Figure 6.16) at t=200s ($t/t_s = 0.91$). This finding agrees with the observations of both the NM's experiments (1987) and the EFML experiments.

6.8 Instability Mechanism

In order to better understand the upwelling flow, it is important to identify the instability mechanisms in the flow. When the experimentally measured values of the saturated wavelength λ_w obtained by Narimousa *et al.* (1991) are compared with those obtained in previous studies of baroclinic turbulence (Phillips 1954; Griffiths and Linden 1982, Chia, Griffiths and Linden 1982; and Killworth, Paldor and Stern 1984), good agreement is achieved. Narimousa *et al.* (1991), thus, believes that the frontal waves first appear at the front due to baroclinic instabilities. The potential energy contained in the density field is the source of kinetic energy for the baroclinic instabilities. After the eddies are pinched off from the front, their scale increases

and such eddies could be equivalent-barotropic type (McWilliams 1984). However, Griffiths and Linden (1981) showed that at values $h_0/H_{avg} \geq 0.25$ (H_{avg} is the average total depth of the water), which is the case in NM's experiments, the generated instabilities are of baroclinic type. Tadepalli (1997) showed that the primary instability of the upwelling flow in NM's experiment is of mixed barotropic-baroclinic type based on a linear instability analysis of two-layer, inviscid, shallow water equations. A formal stability analysis, which should include the effects of rotation, stratification, three-dimensional shear and possibly viscosity, is still needed in the future.

6.9 Summary

Large-eddy simulations of two different full tank configurations using the actual viscosity of the working fluid were carried out. Different approaches to assess an important quantity, namely, the disk friction velocity u_*, in the upwelling flow are discussed. The simulation results are compared to experimentally measured data and good agreement is obtained. The three-dimensional LES results are able to reveal the complex upwelling structures in detail. The main findings are:

- A single non-dimensional parameter θ_* can be used to characterize the upwelling flow field. At low θ_* values, the frontal instabilities are much more intense and the upwelling front itself displays strong unsteadiness and cyclonic eddies containing the lower-layer fluid pinch off from the front.
- The primary front is unstable to azimuthal perturbations and develops large amplitude baroclinic waves.
- The frontal wave structure consists of cyclone/anticyclone pairs, associated with jet-like motion.
- A Rayleigh-Taylor type of instability takes place in the top inversion layer due to the unstable stratification, the heavier mixed fluid in the top inversion layer

sinks back to the lower level. Consequently, the secondary front breaks into isolated patches.

- A mixing zone can be seen to develop with time near the outer edge of the tank.

The effects of bottom topography and coastal perturbations should be studied in the future. A formal stability analysis, which should include the effects of rotation, stratification, three-dimensional shear and possibly viscosity, is also needed.

Table 6.1: Geometric parameters of upwelling simulations

Case	H (m)	h_o (m)	$\alpha(°)$	R_o (m)	R_h (m)	R_i (m)
NM	0.15	0.026	15	0.45	0.0	0.055
EFML	0.1905	0.03048	15	0.9144	0.2286	0.3302

Table 6.2: Grid resolutions and physical parameters of upwelling simulations

Case	Grid $N_r \times N_y \times N_\theta$	Ω rad/s	$\Delta\Omega$ rad/s	$\Delta\rho/\rho$ kg/m^3	ν m^2/s	t_s s
NM1	192 × 128 × 320	2.27	0.185	0.018	10^{-6}	220
NM2	192 × 160 × 320	2.27	0.185	0.018	10^{-6}	220
EFML1	256 × 128 × 320	0.628	0.105	0.015	10^{-6}	250
EFML2	256 × 160 × 320	0.628	0.105	0.015	10^{-6}	250

Table 6.3: Non-dimensional parameters of two different upwelling simulations

Case	$\theta* = g'h_0/u_*f\lambda_s$	$\epsilon = U_p/fL_R$	$E = \nu/fH^2$	$\hat{R}/L_R$
NM1	1.4	0.045	9.8×10^{-6}	0.047
EFML1	5.8	0.11	2.2×10^{-5}	0.099

Table 6.4: Comparisons of LES-computed and experimentally-measured values

Case	λ_s (m)	N_w	u_w (m/s)
LES	0.13	17	0.027
NM	0.12	20	0.023

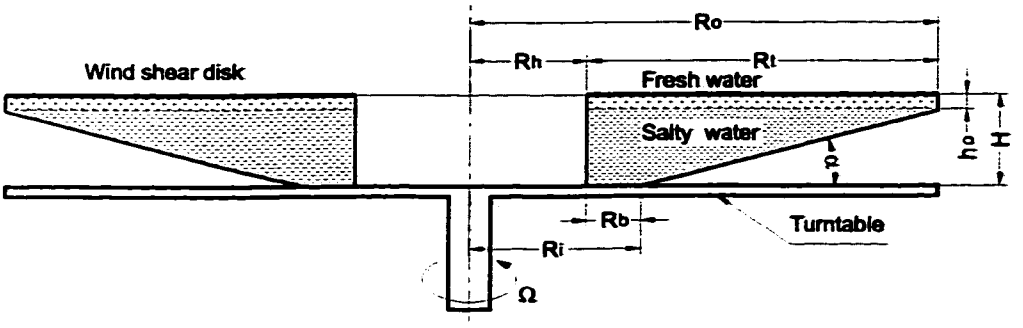

Figure 6.1: A schematic of the cross-section of the experimental apparatus.

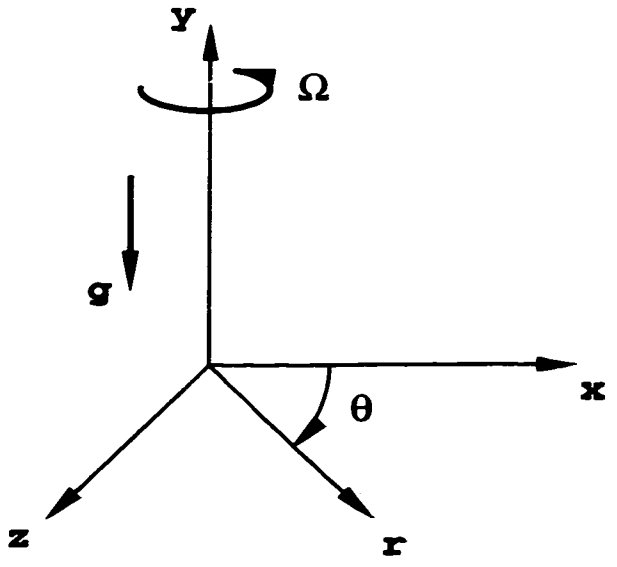

Figure 6.2: Coordinate diagram.

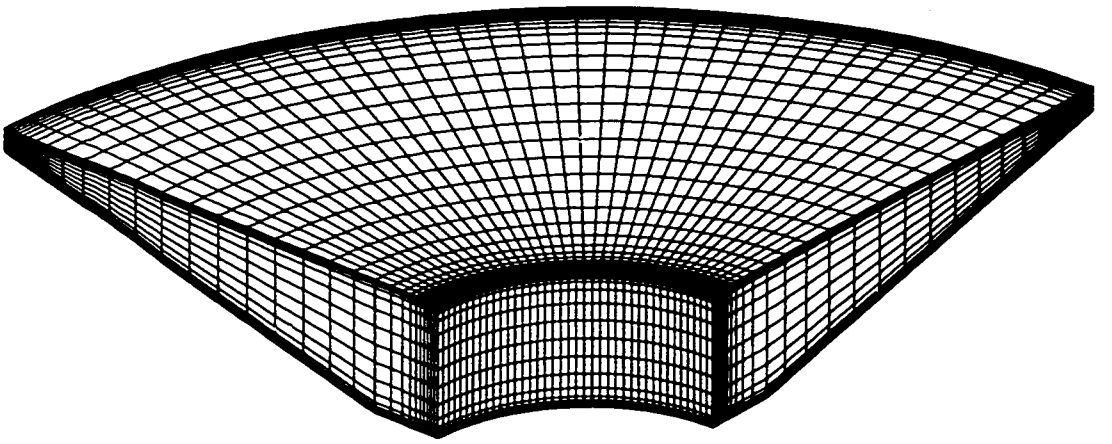

Figure 6.3: An illustration of a section of the computational grid.

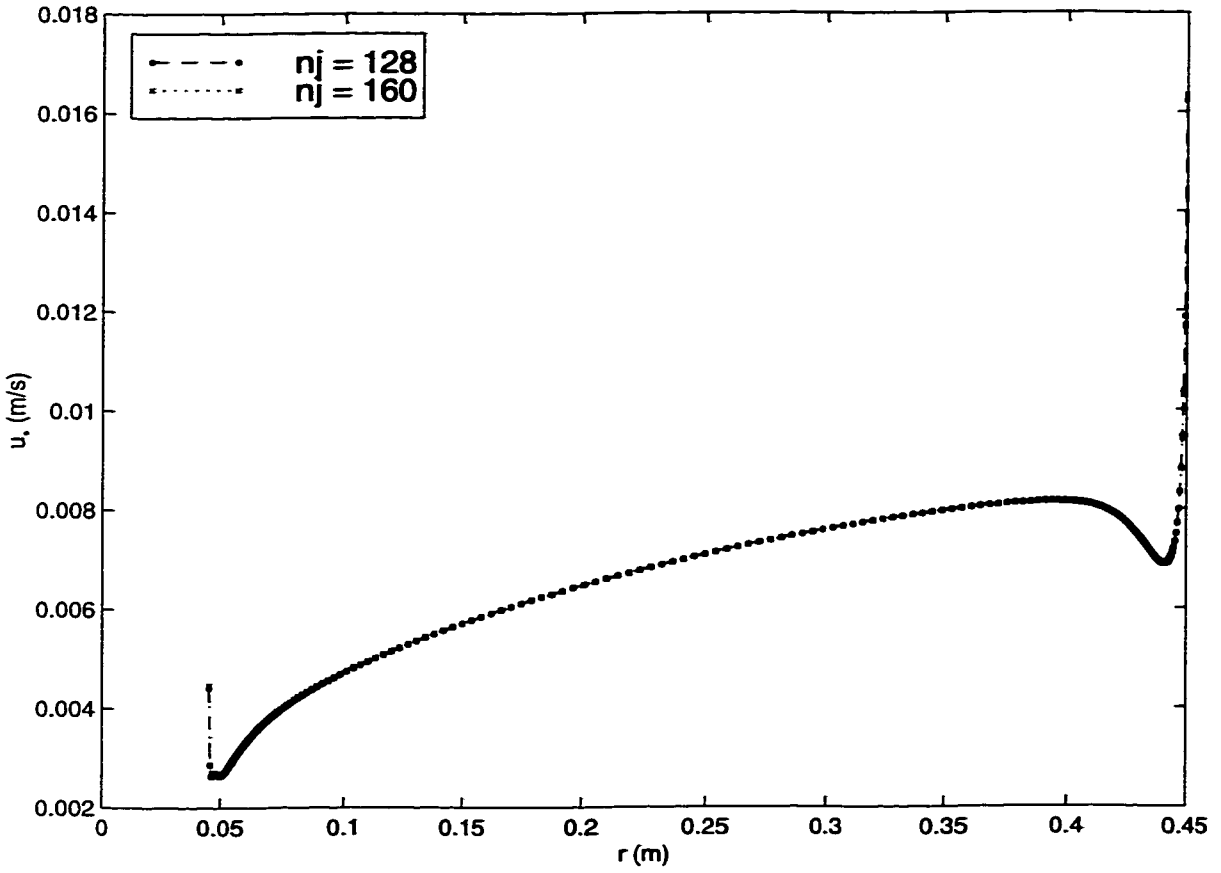

Figure 6.4: Disk friction velocity u_* vs. radius r at t=25s for different numbers of vertical grid points.

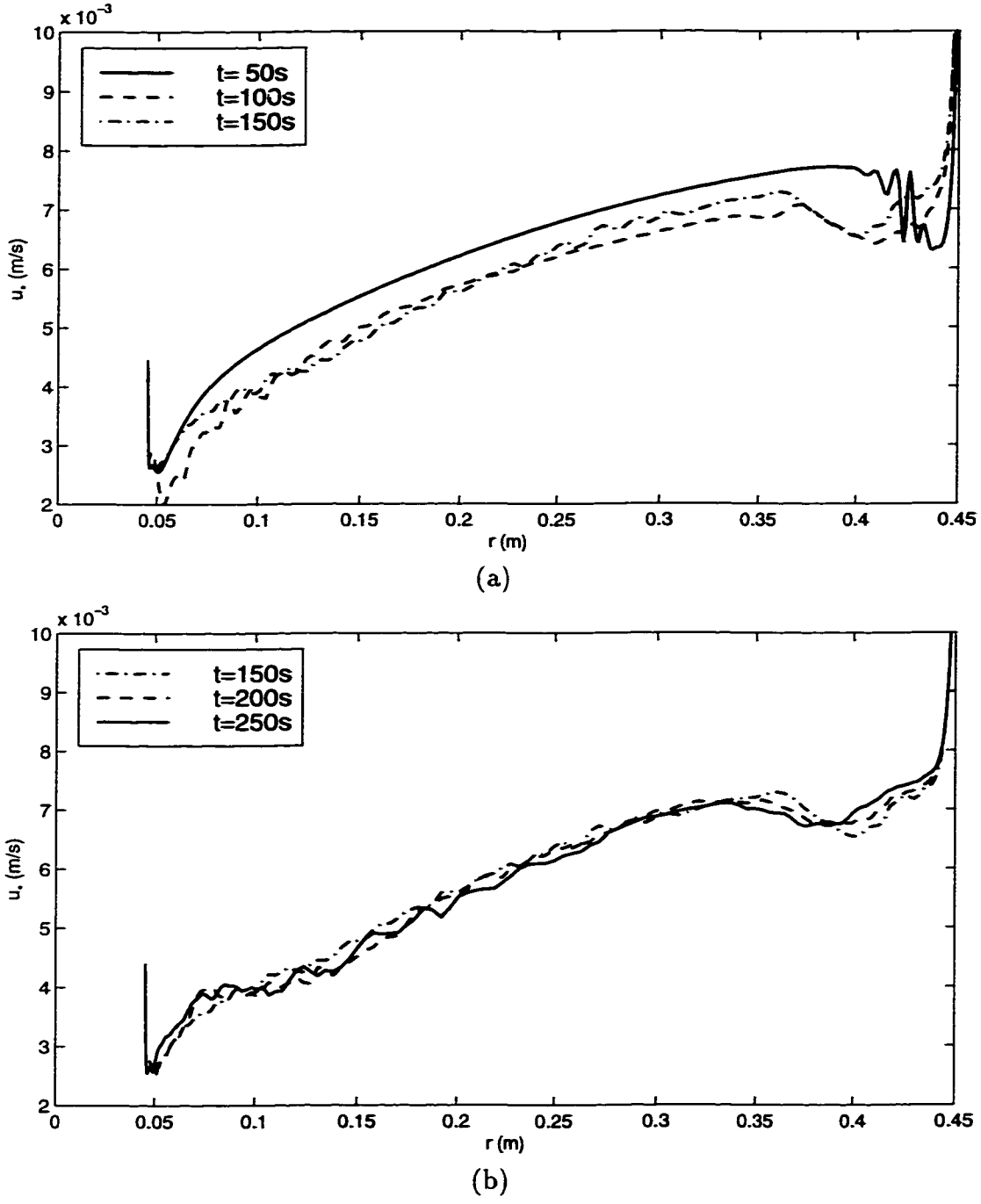

Figure 6.5: Disk friction velocity u_* vs. radius r at different times (NM1).

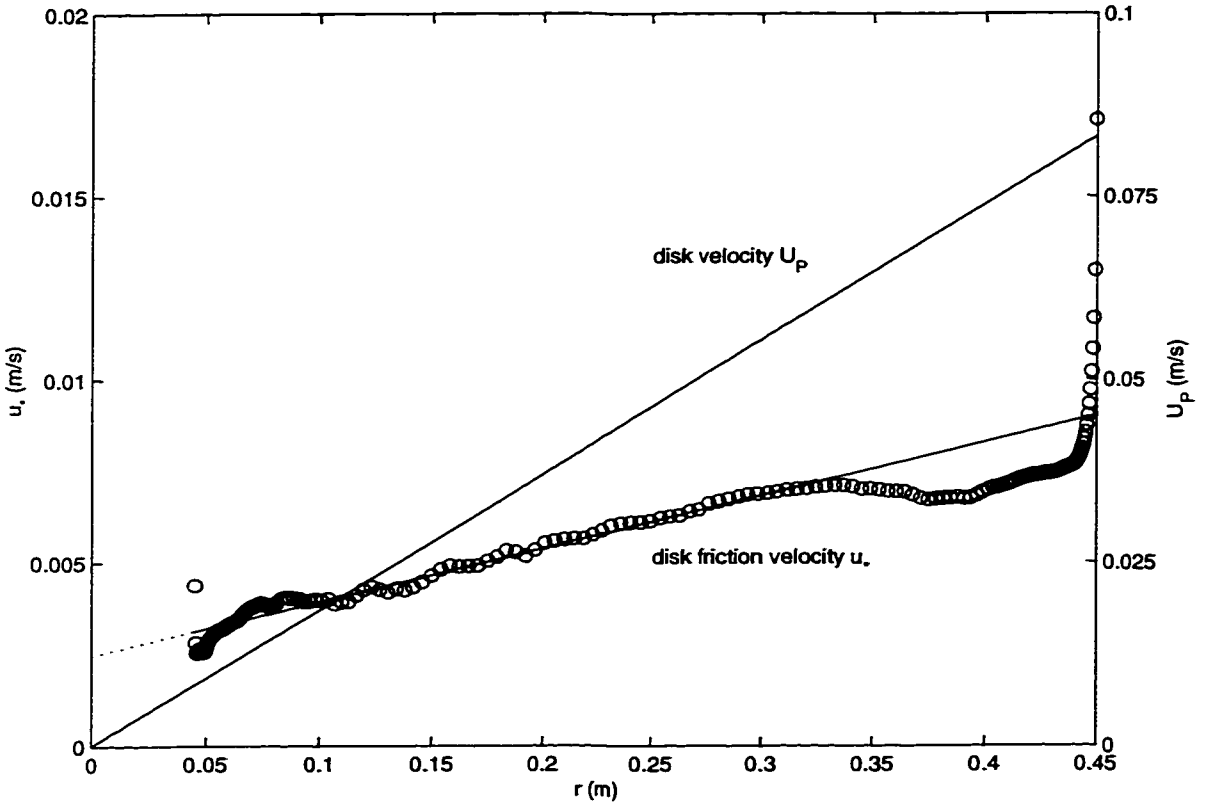

Figure 6.6: Curve fitting of disk friction velocity u_* vs. radius r at $t = 250$s (NM1).

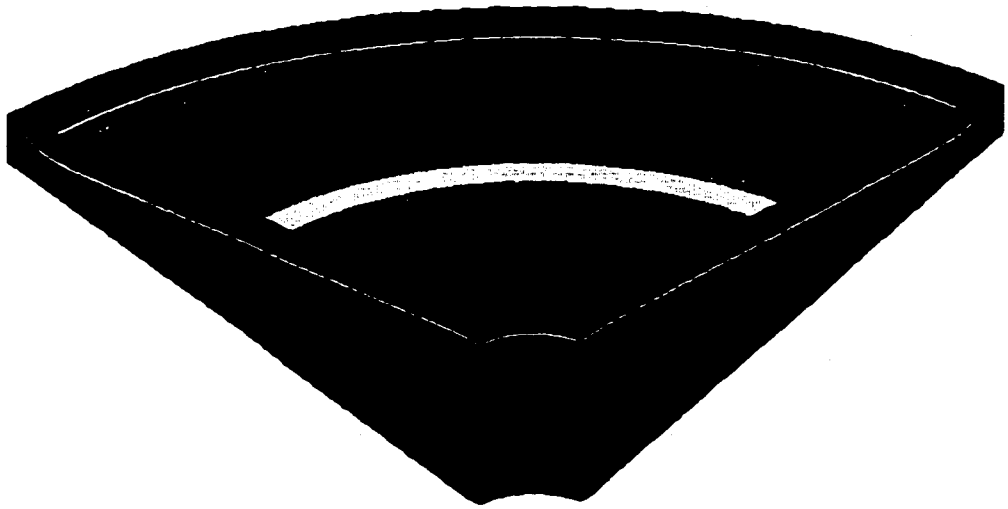

Figure 6.7: A section of the density field at t/t_s=0.18 (Case NM1).

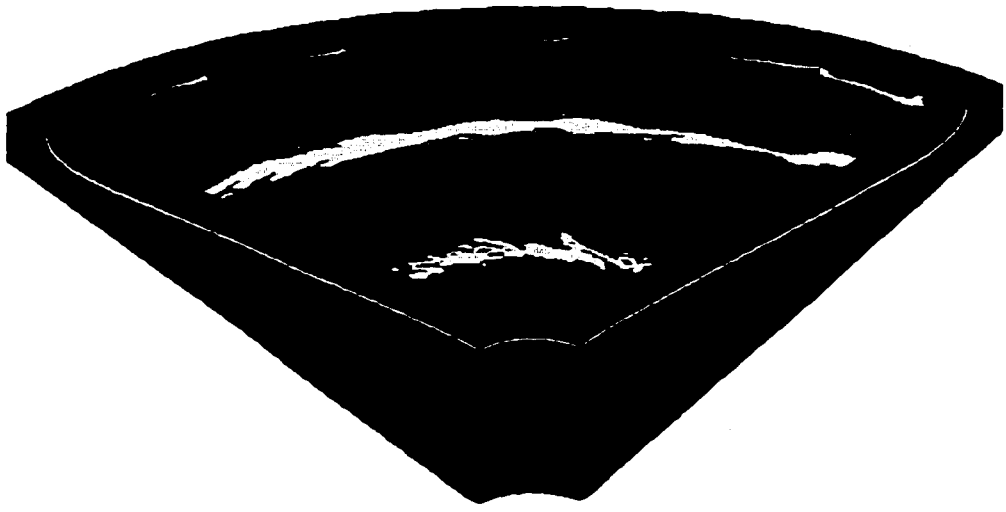

Figure 6.8: A section of the density field at t/t_s=0.36 (Case NM1).

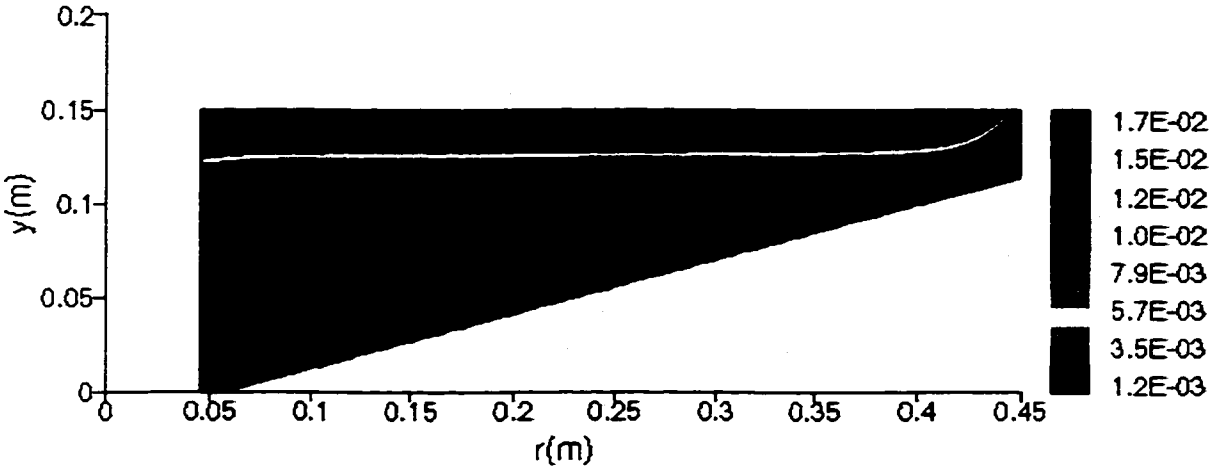

Figure 6.9: Side view of the density field at t/t_s=0.18 (Case NM1).

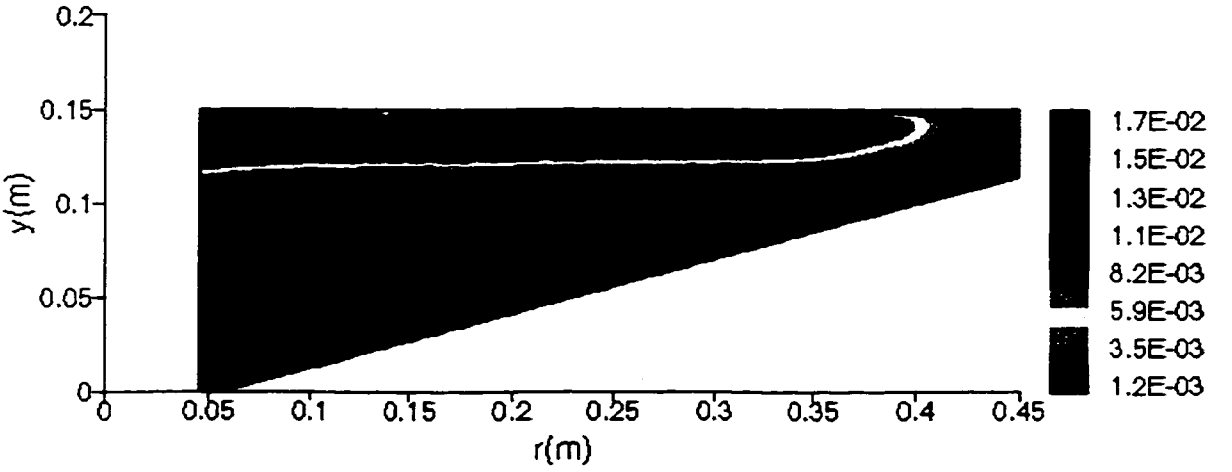

Figure 6.10: Side view of the density field at t/t_s=0.46 (Case NM1).

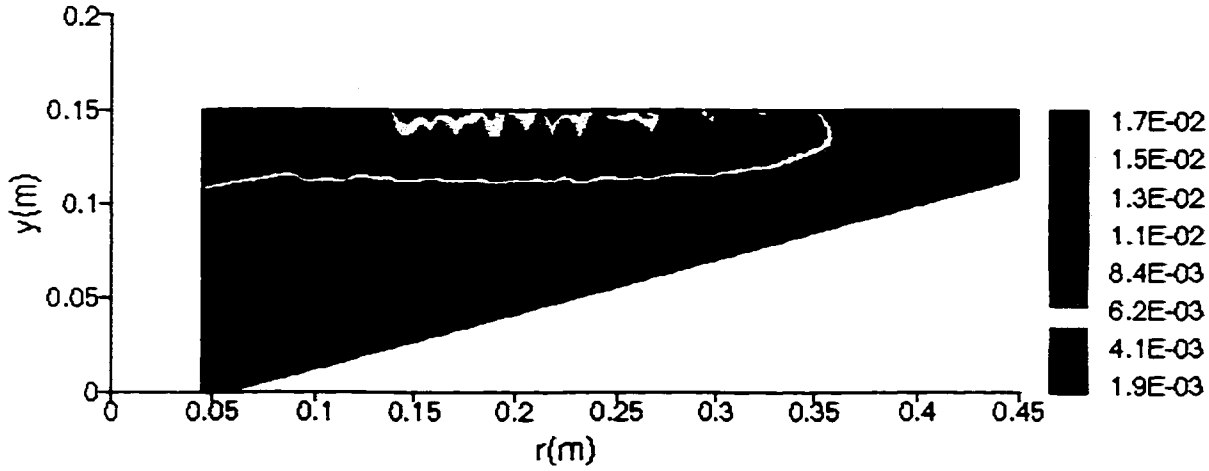

Figure 6.11: Side view of the density field at t/t_s=0.91 (Case NM1).

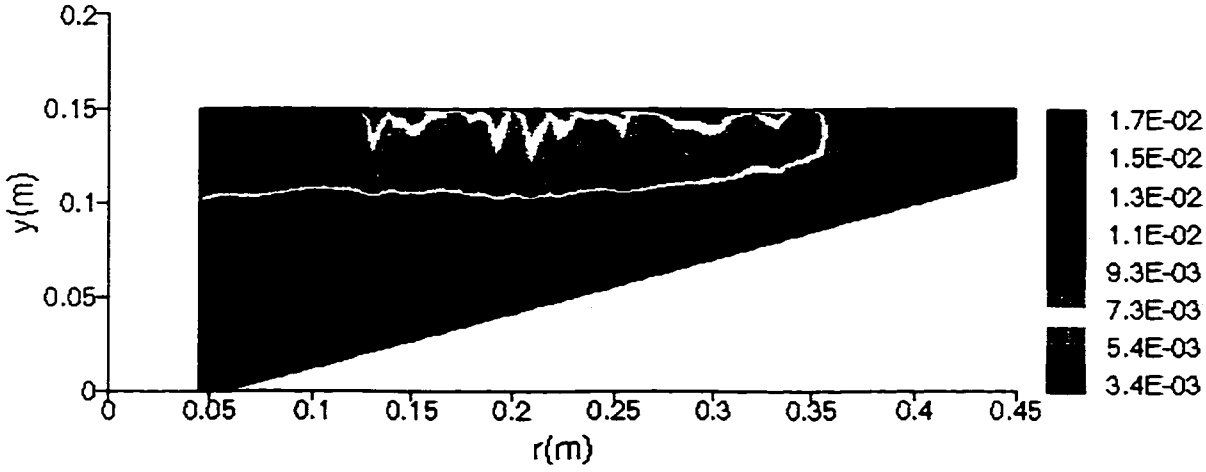

Figure 6.12: Side view of the density field at t/t_s=1.36 (Case NM1).

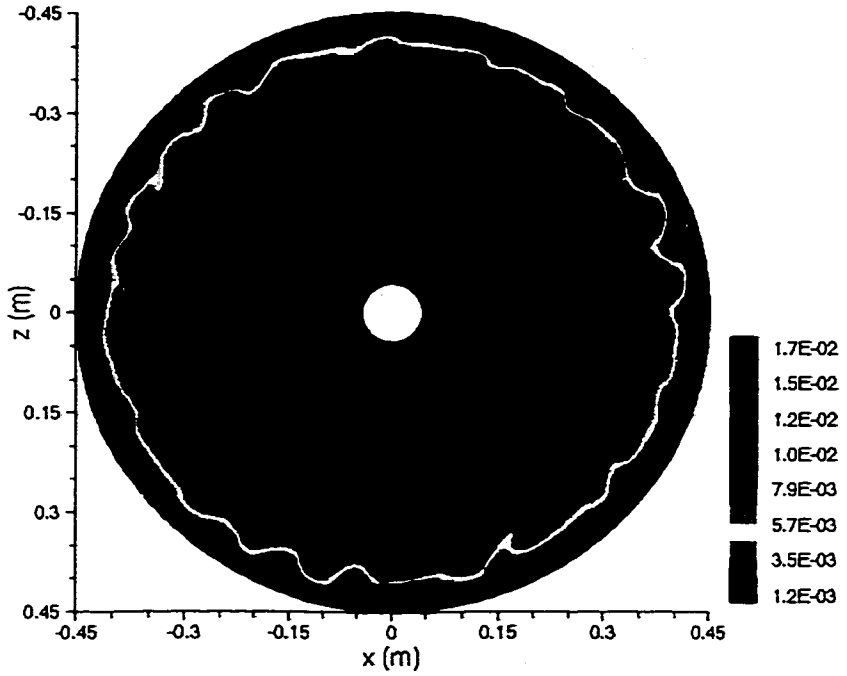

(a)

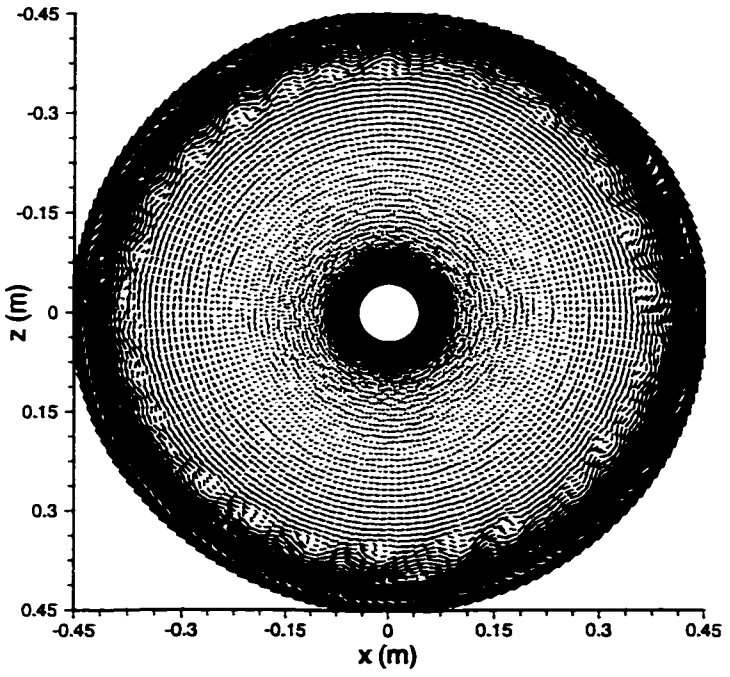

(b)

Figure 6.13: Top view of (a) density field (b) velocity field at y/H=0.9 and t/t_s=0.46 for Case NM1.

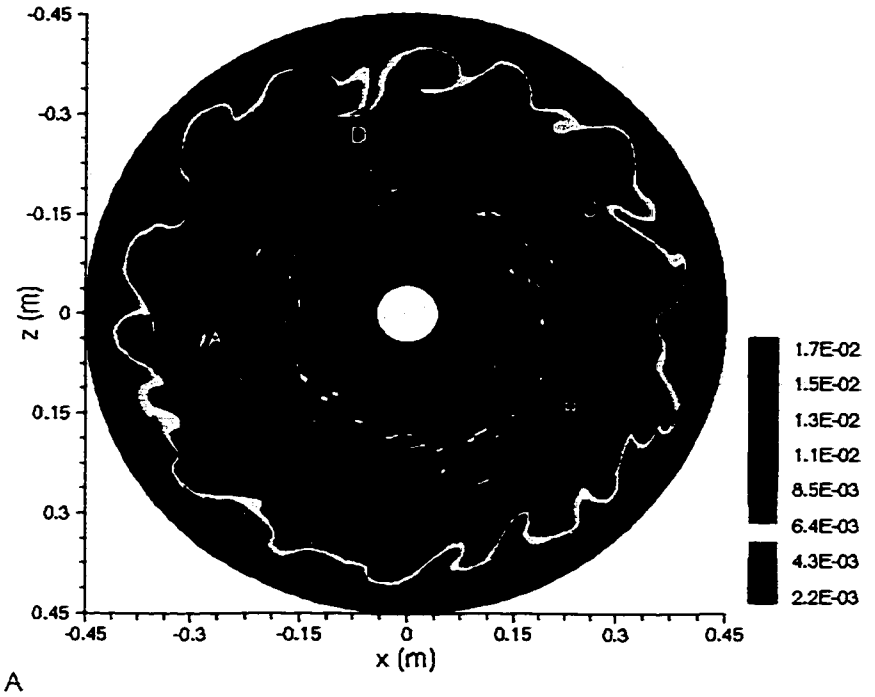

A

(a)

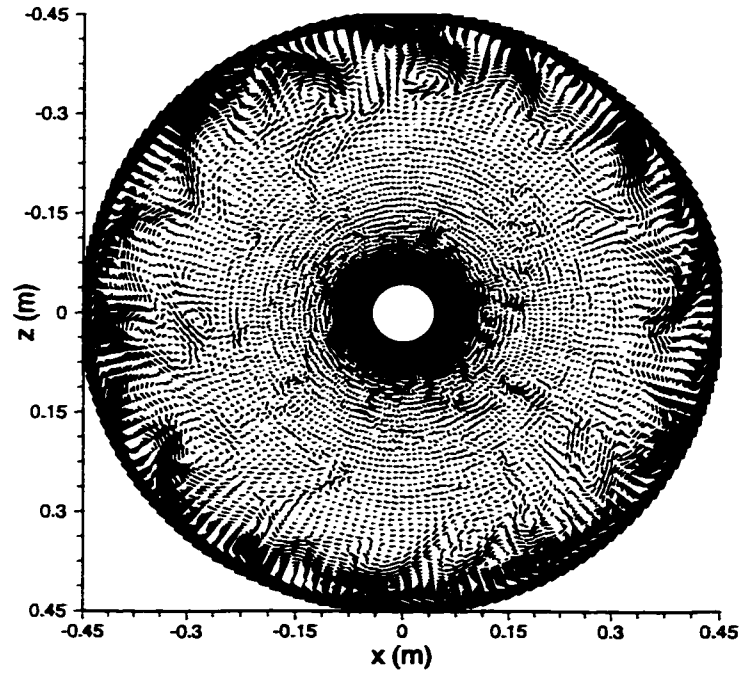

(b)

Figure 6.14: Top view of (a) density field (b) velocity field at y/H=0.9 and t/t_s=0.91 for Case NM1.

(a) density and velocity fields around point C

Figure 6.15: Expanded top view of the density and the velocity fields at four different locations at y/H=0.9 and t/t_s=0.91 for Case NM1.

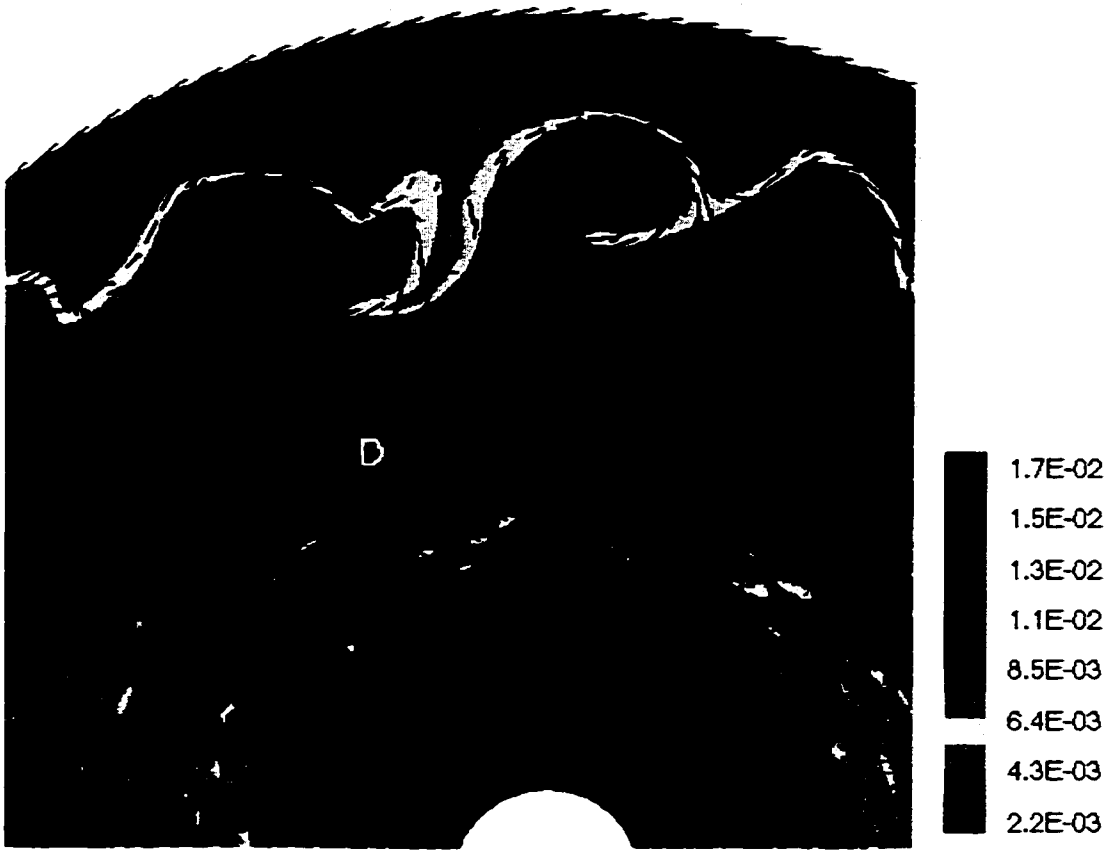

Figure 6.15 (continued) (b) density and velocity fields around point D

Figure 6.15 (continued) (c) density and velocity fields around point A

Figure 6.15 (continued) (d) density and velocity fields around point B

(a) vertical vorticity and velocity fields around point C

Figure 6.16: Expanded top view of the vertical vorticity and the velocity fields at four different locations at y/H=0.9 and t/t_s=0.91 for Case NM1.

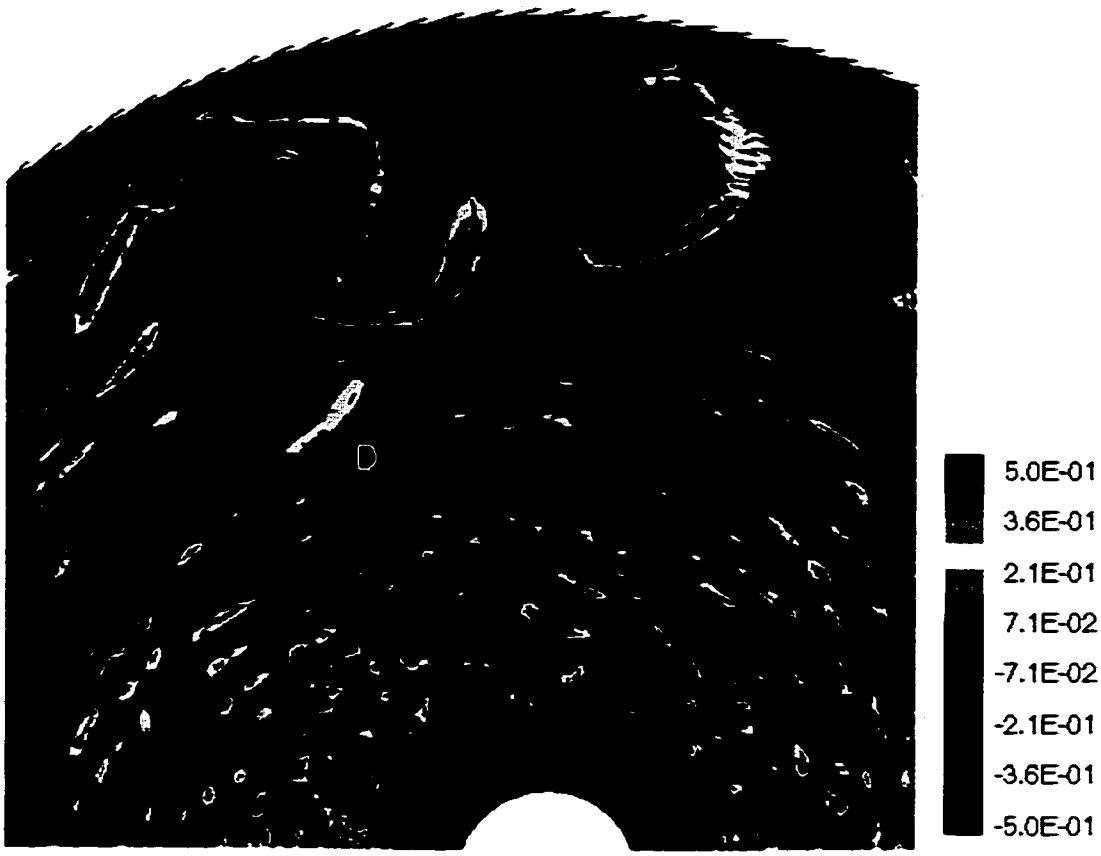

Figure 6.16 (continued) (b) vertical vorticity and velocity fields around point D

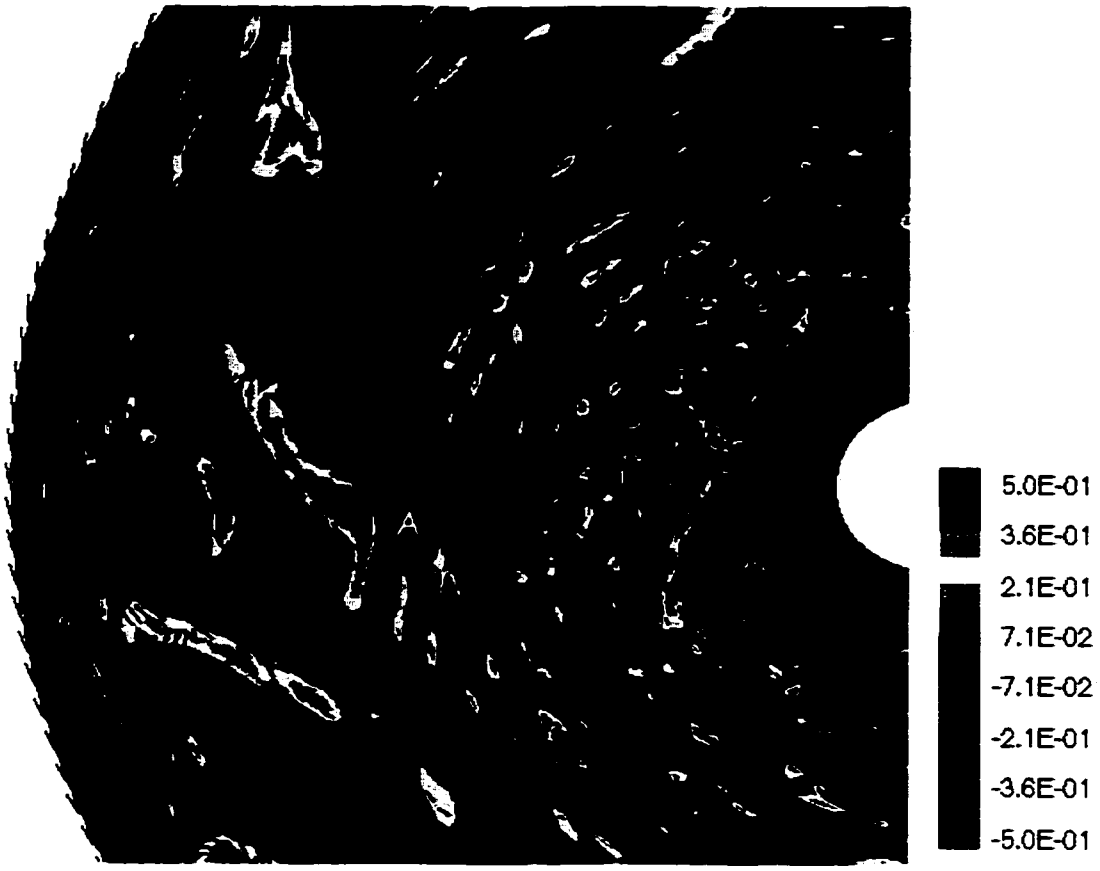

Figure 6.16 (continued) (c) vertical vorticity and velocity fields around point A

Figure 6.16 (continued) (d) vertical vorticity and velocity fields around point B

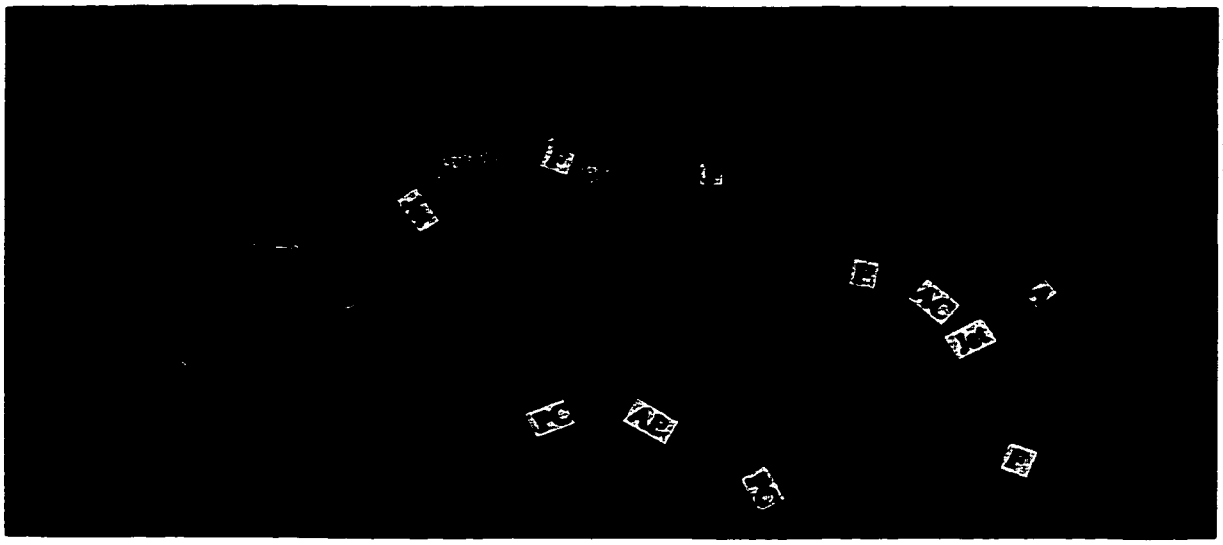

Figure 6.17: A combined dye and streak photograph with parameter values of $\Omega = 2.47\text{rad/s}$, $\Delta\Omega = 0.18\text{rad/s}$, h_o=0.026m, $\Delta\rho/\rho$=0.026 [Figure 12(b) of Narimousa and Maxworthy (1987)]. PC, AE are for pinched-off cyclones and anticyclonic eddies, respectively. The frontal waves are indicated by F.

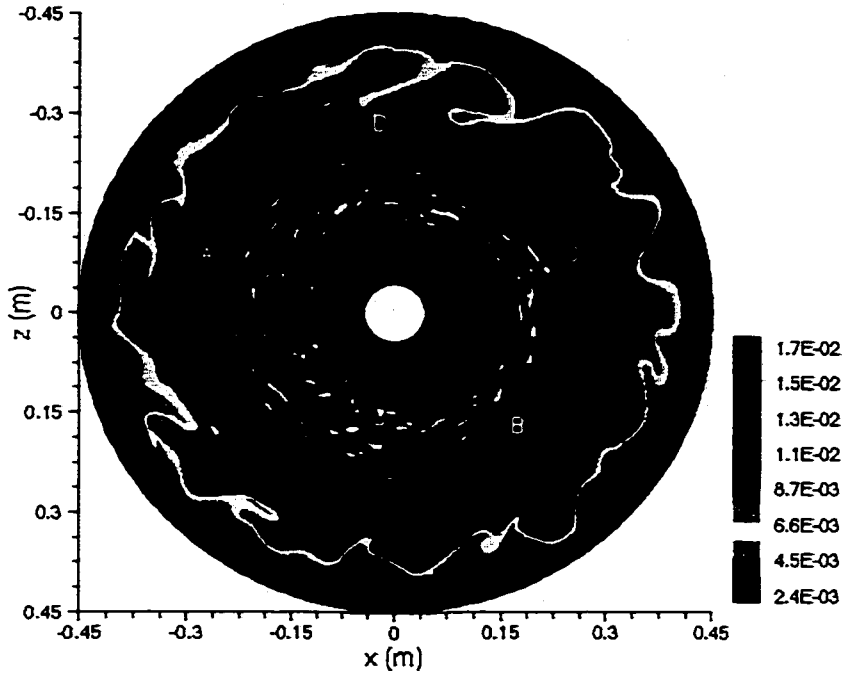

(a)

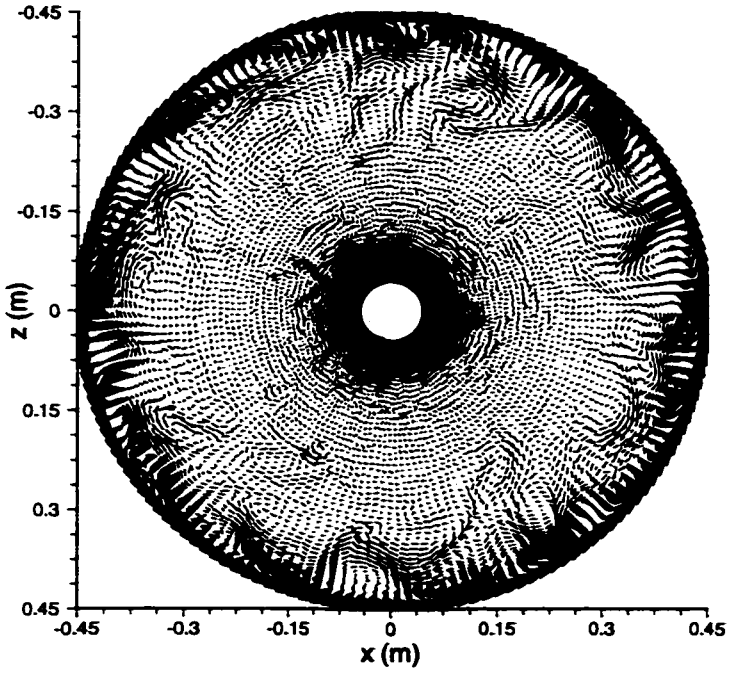

(b)

Figure 6.18: Top view of (a) density field (b) velocity field at y/H=0.9 and t/t_s=1.0 for Case NM1.

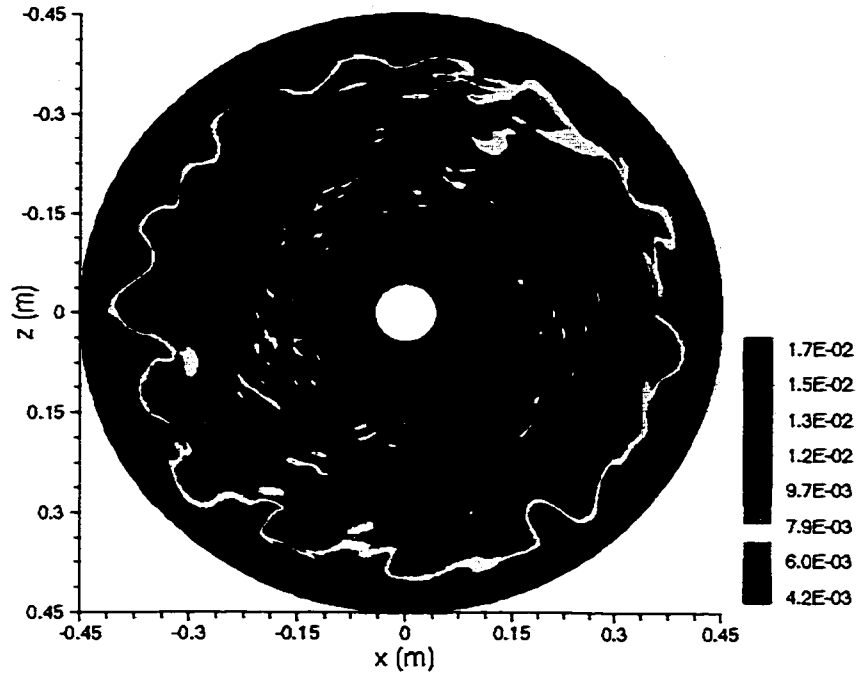

(a)

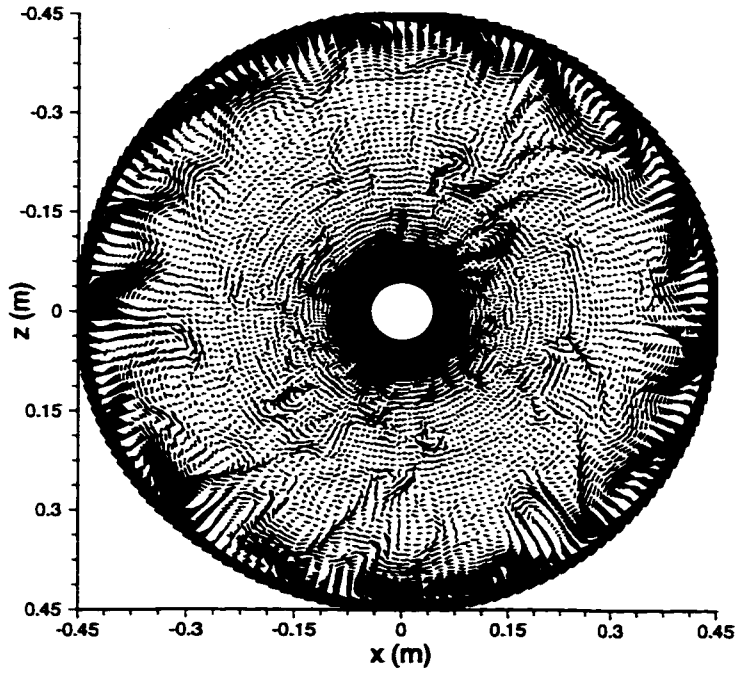

(b)

Figure 6.19: Top view of (a) density field (b) velocity field at y/H=0.9 and t/t_s=1.36 for Case NM1.

Figure 6.20: A streak photograph of the flow field (top view) for Case NM1 [Figure 1(c) of Narimousa *et al.* (1991)].

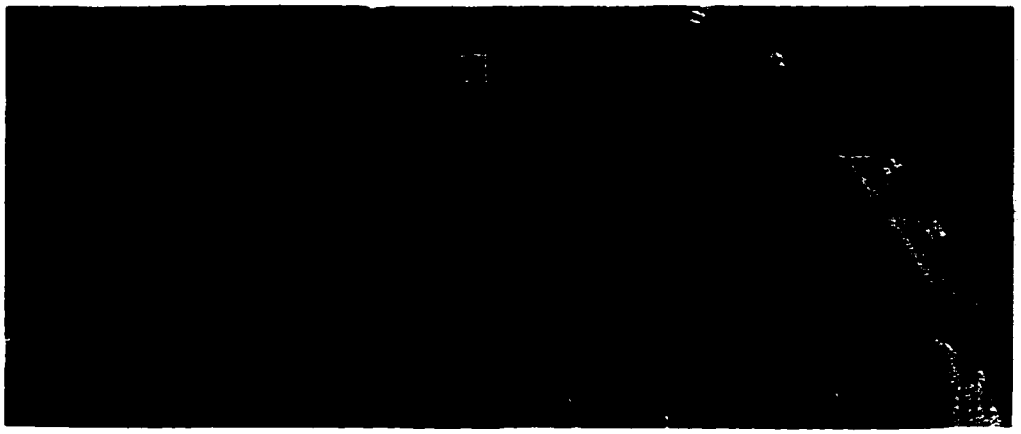

Figure 6.21: A streak photograph of the flow field (top view) at t/t_s=1.45 [Figure 2(c) of Narimousa and Maxworthy (1987)].

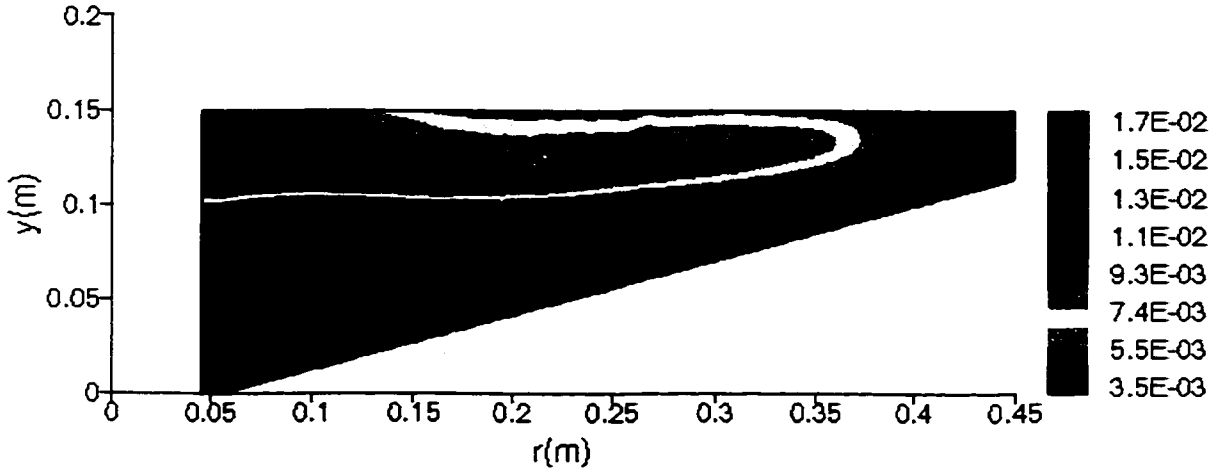

Figure 6.22: Side view of an azimuthally-averaged density field at t/t_s=1.45 (Case NM1).

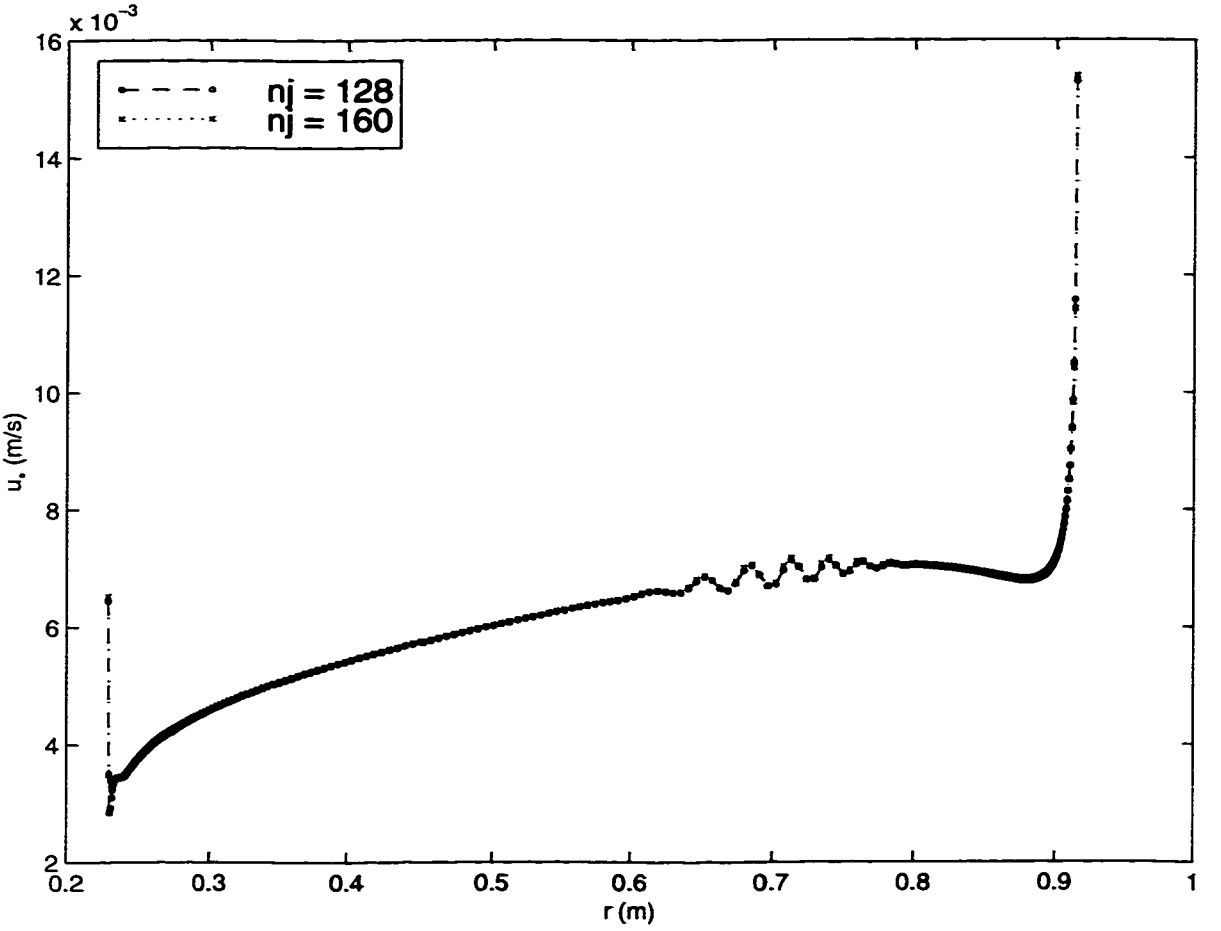

Figure 6.23: Disk friction velocity u_* vs. radius r at t=20s for different numbers of vertical grid points.

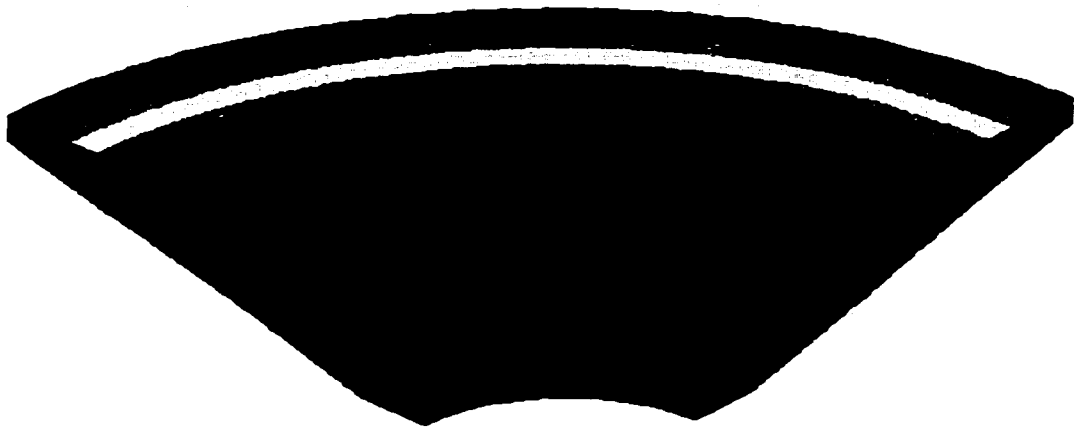

Figure 6.24: A section of the density field at t/t_s=0.2 (Case EFML1).

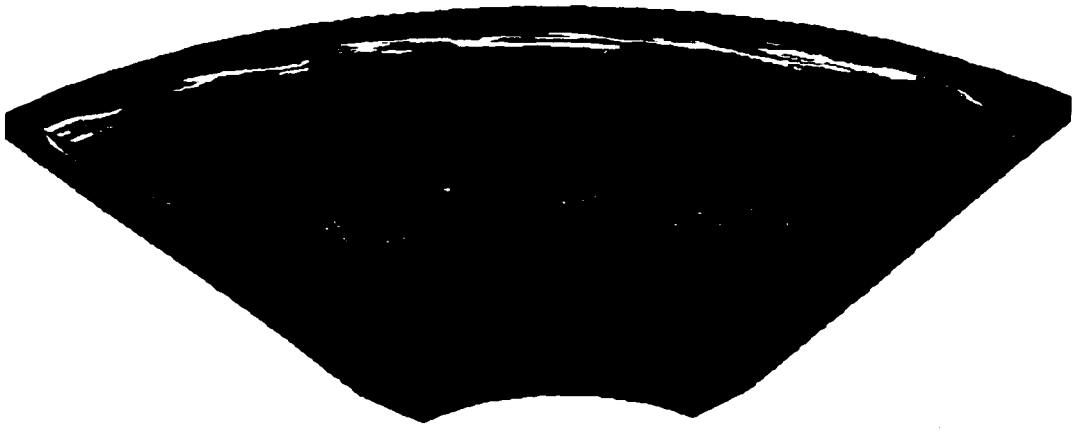

Figure 6.25: A section of the density field at t/t_s=0.4 (Case EFML1).

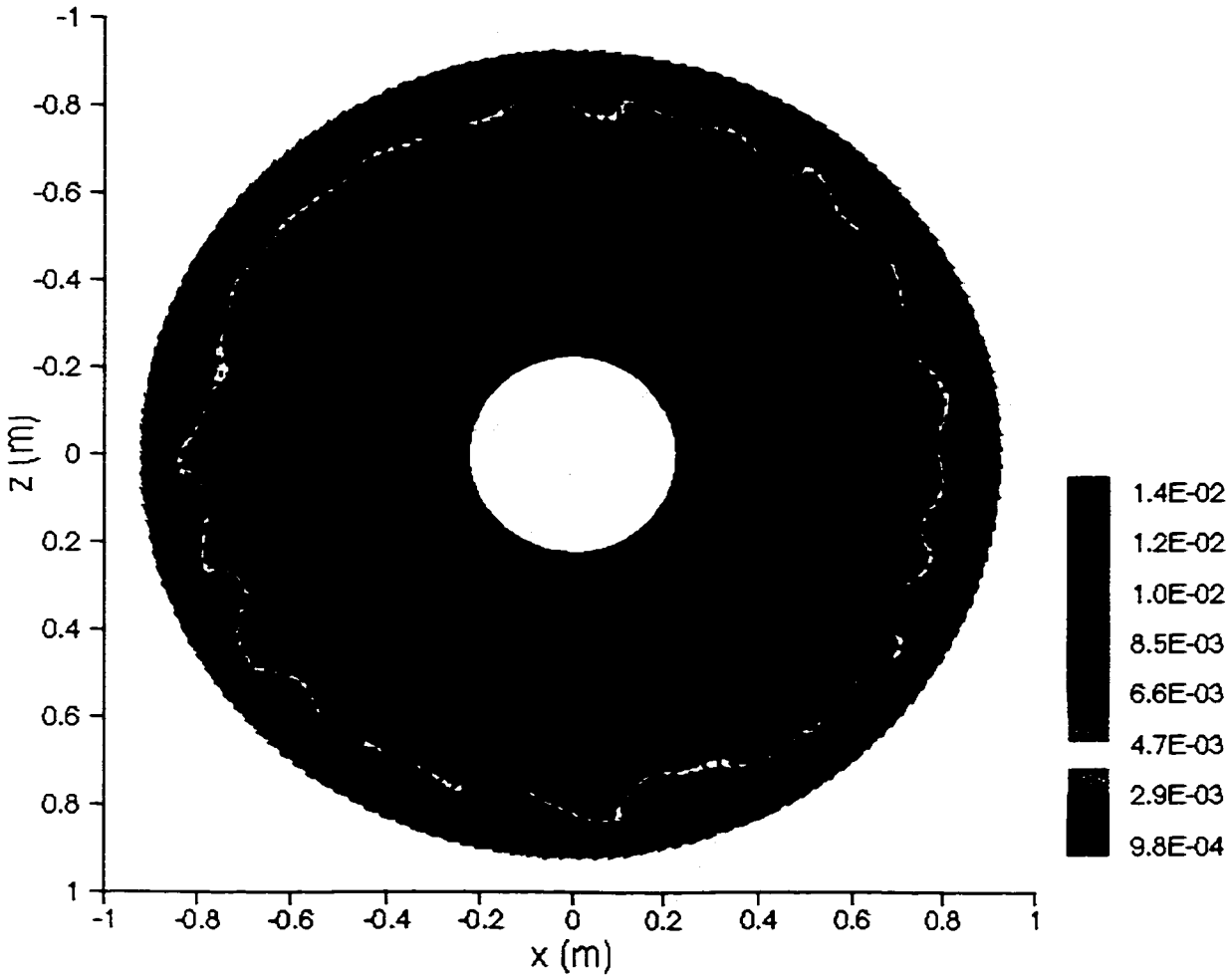

Figure 6.26: Top view of the density and the velocity fields at y/H=0.95 and t/t_s=0.6 (Case EFML1).

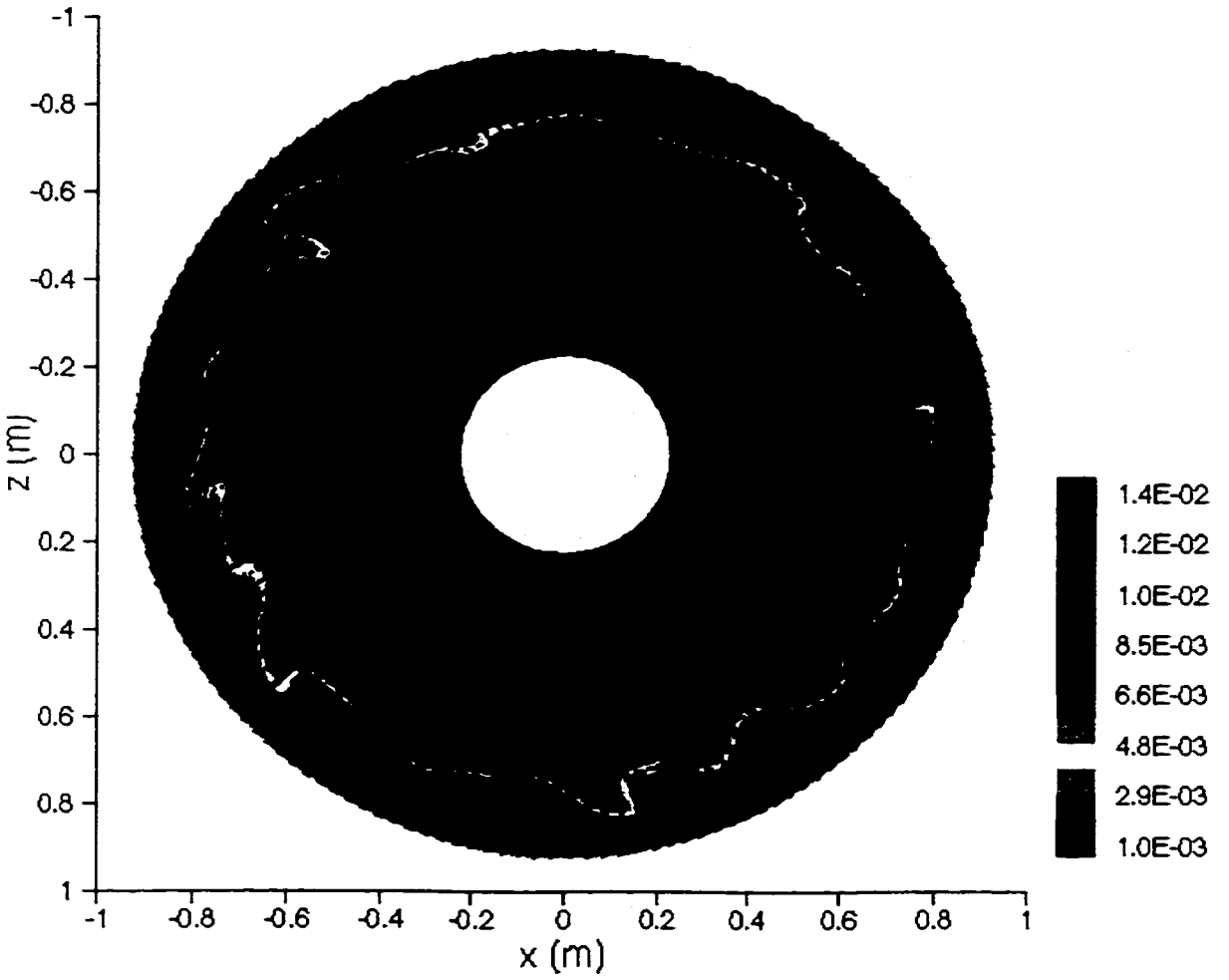

Figure 6.27: Top view of the density and the velocity fields at y/H=0.95 and t/t_s=0.8 (Case EFML1).

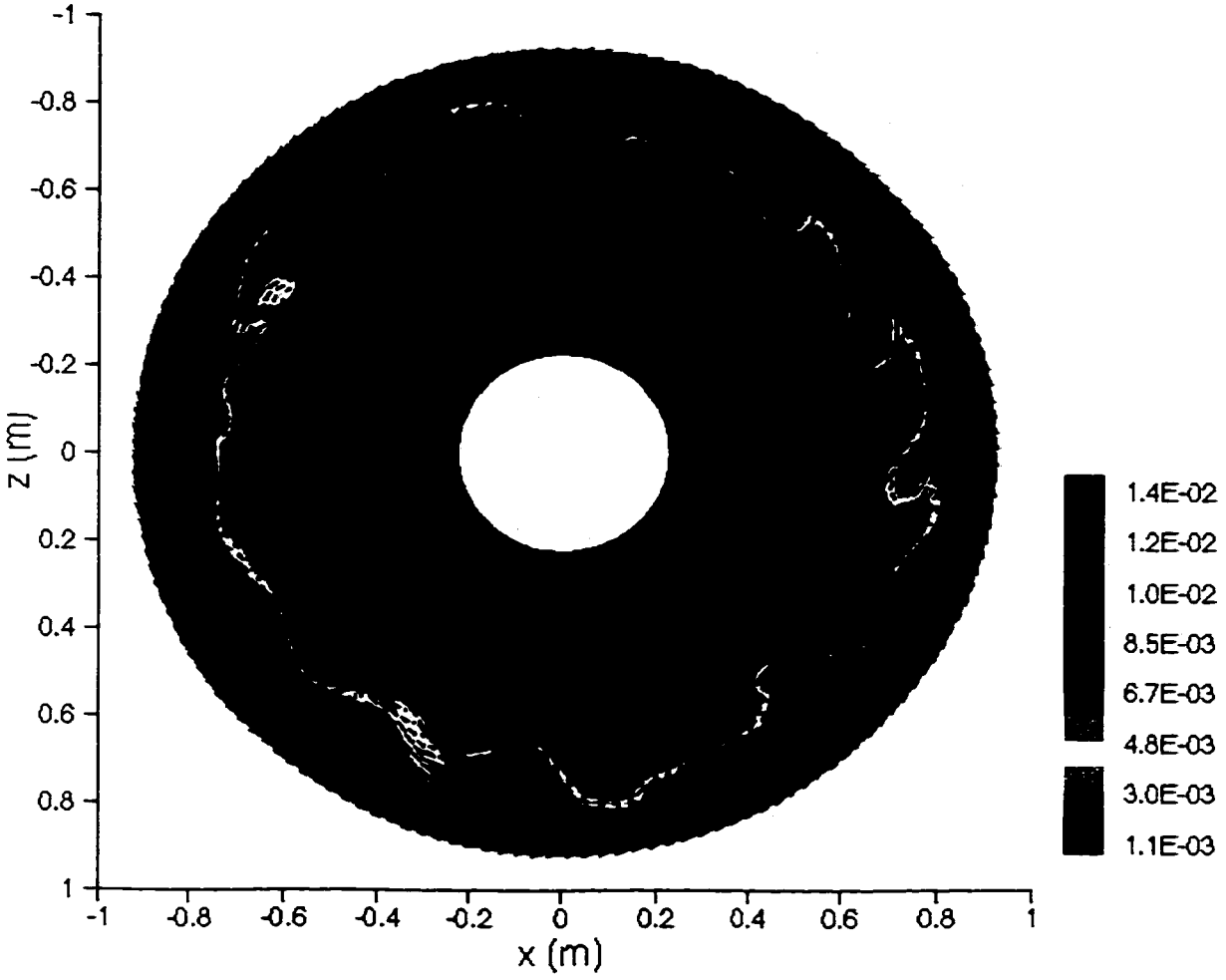

Figure 6.28: Top view of the density and the velocity fields at y/H=0.95 and t/t_s=1.0 (Case EFML1).

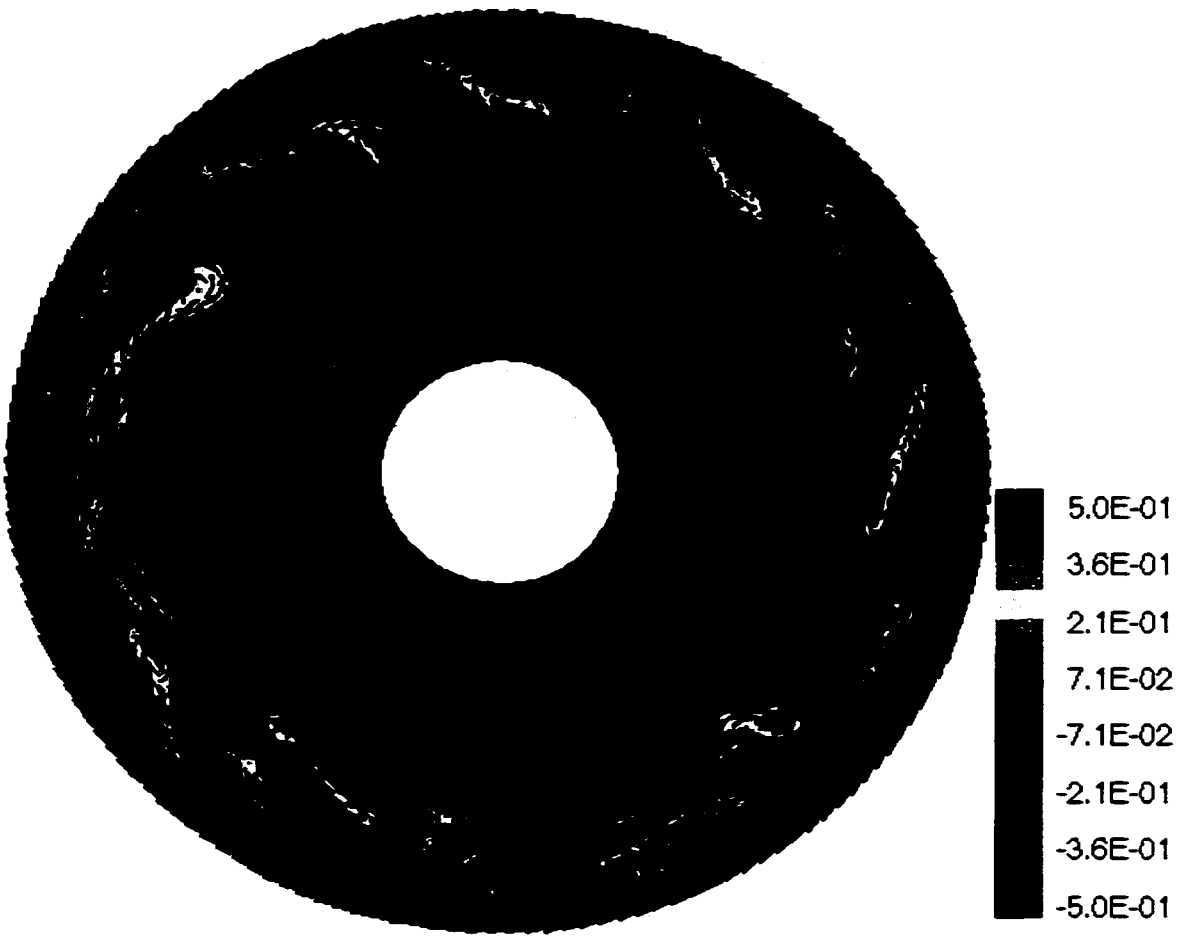

Figure 6.29: Top view of the vertical vorticity and the velocity fields at y/H=0.95 and t/t_s=1.0 (Case EFML1).

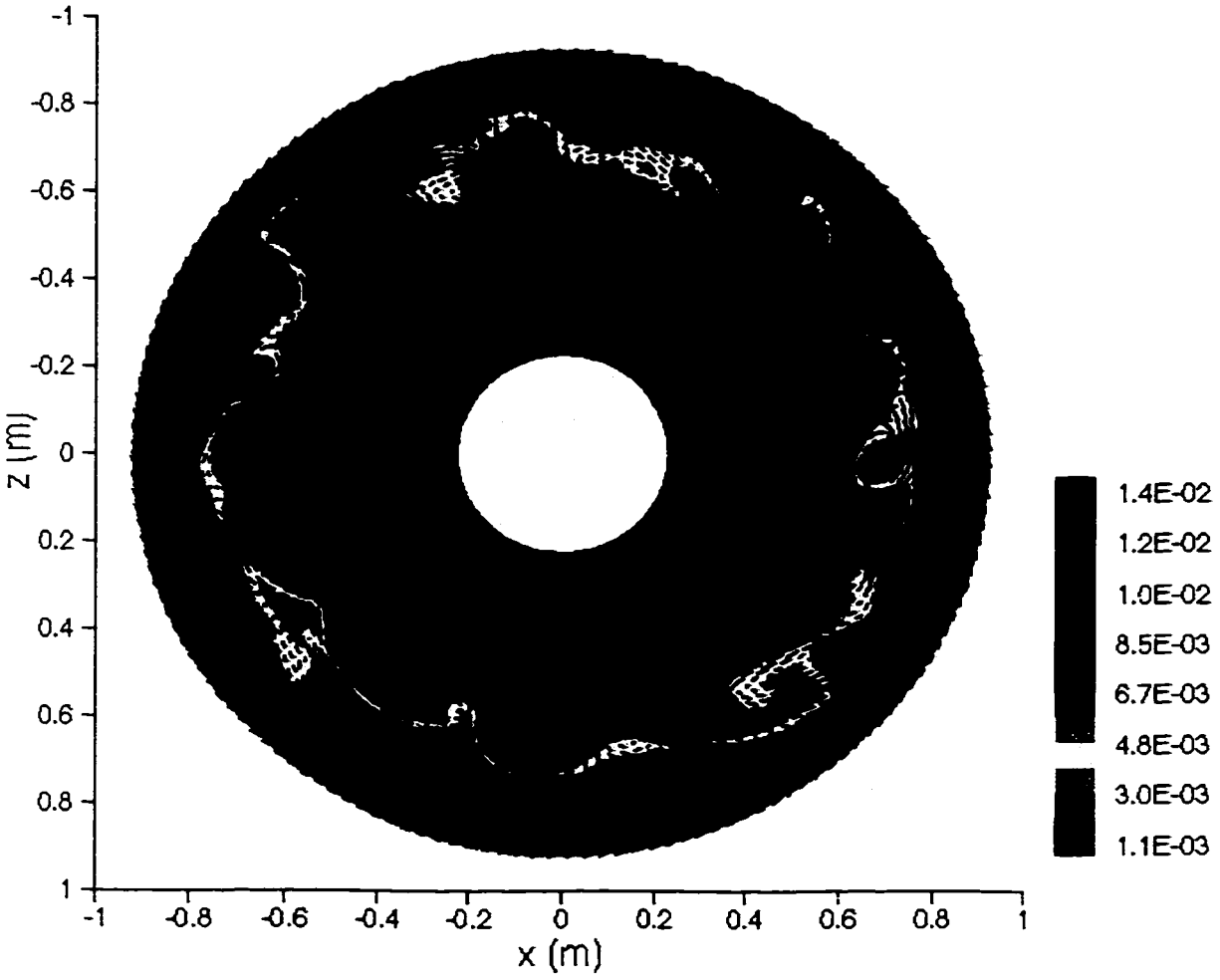

Figure 6.30: Top view of the density and the velocity fields at y/H=0.95 and t/t_s=1.2 (Case EFML1).

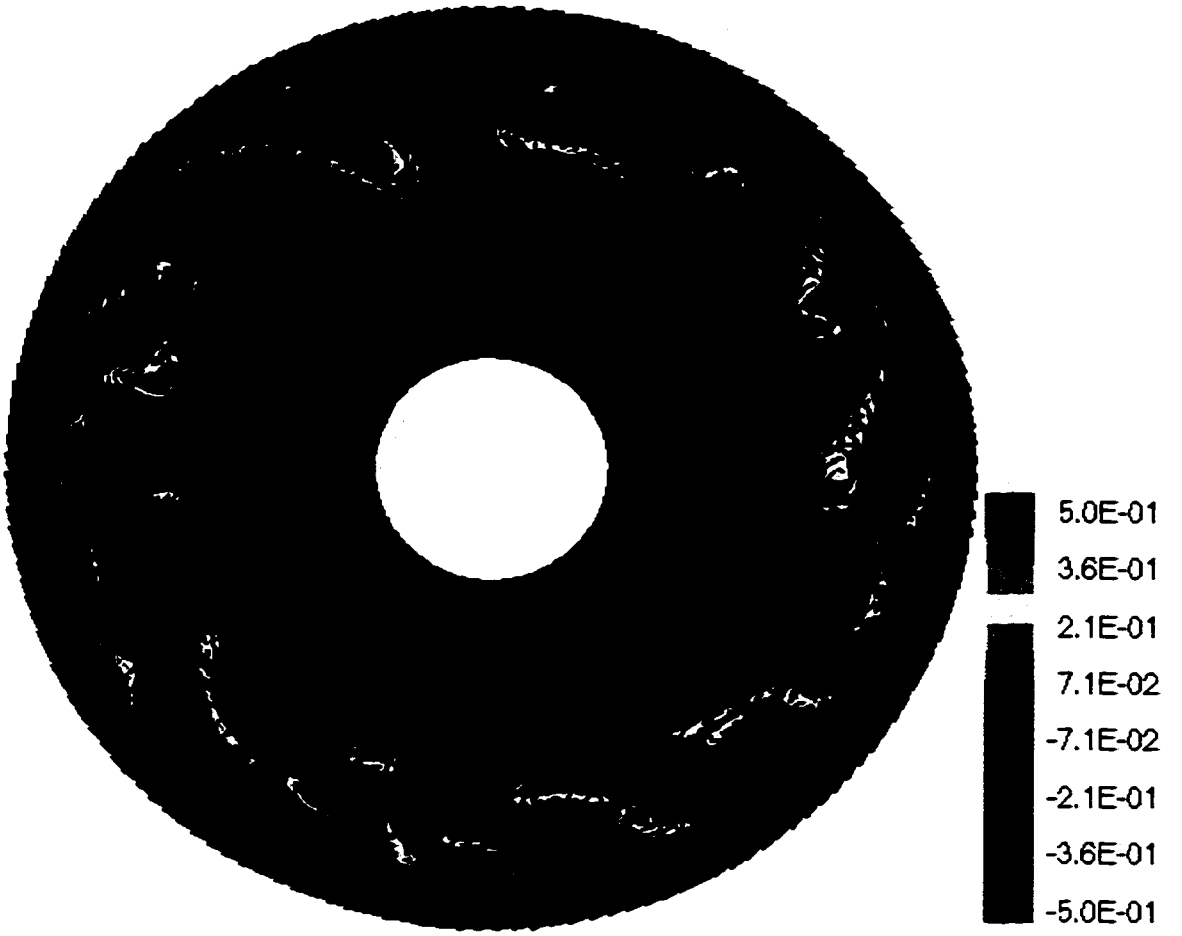

Figure 6.31: Top view of the vertical vorticity and the velocity fields at y/H=0.95 and t/t_s=1.2 (Case EFML1).

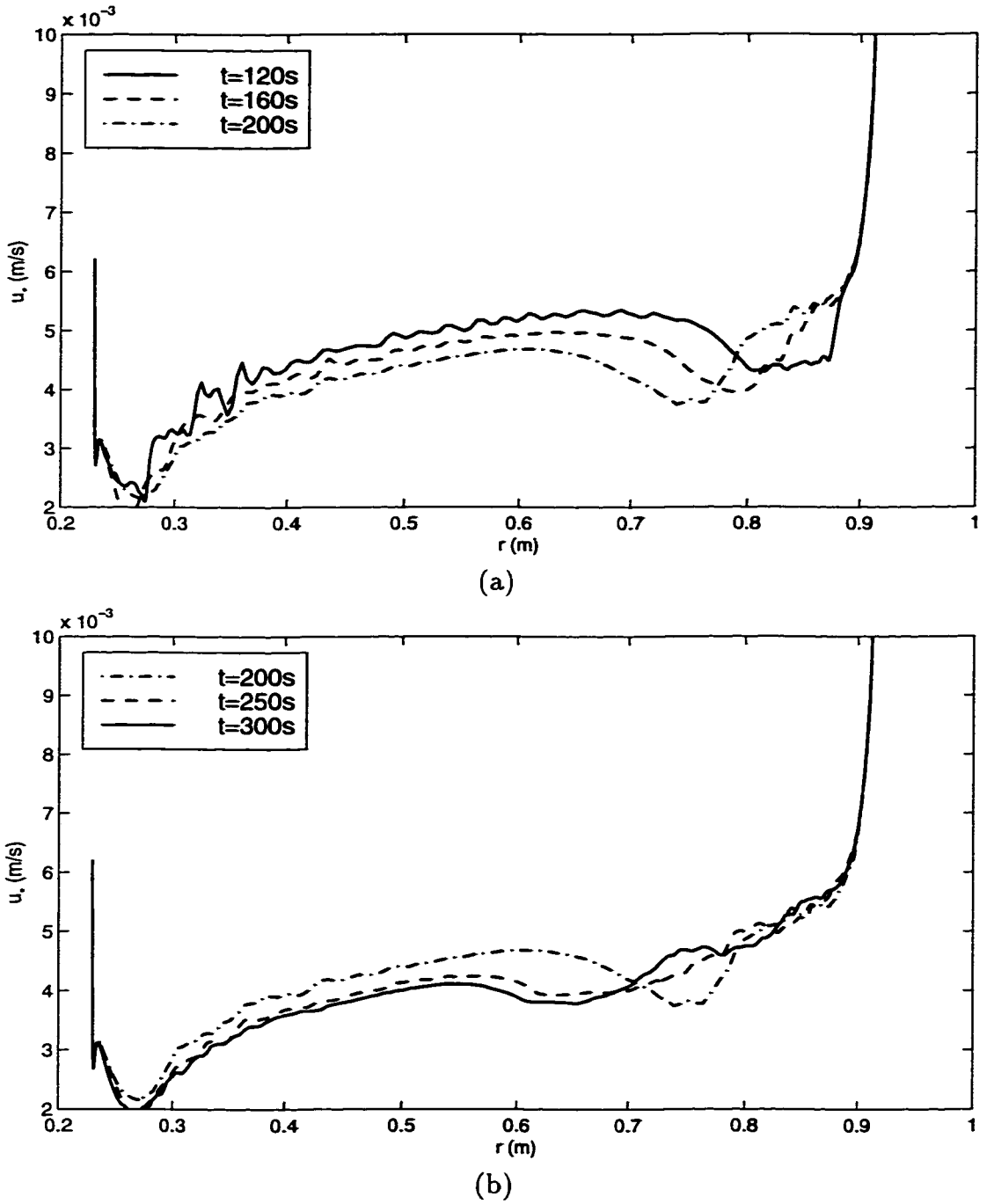

Figure 6.32: Disk friction velocity u_* vs. radius r at different times (Case EFML1).

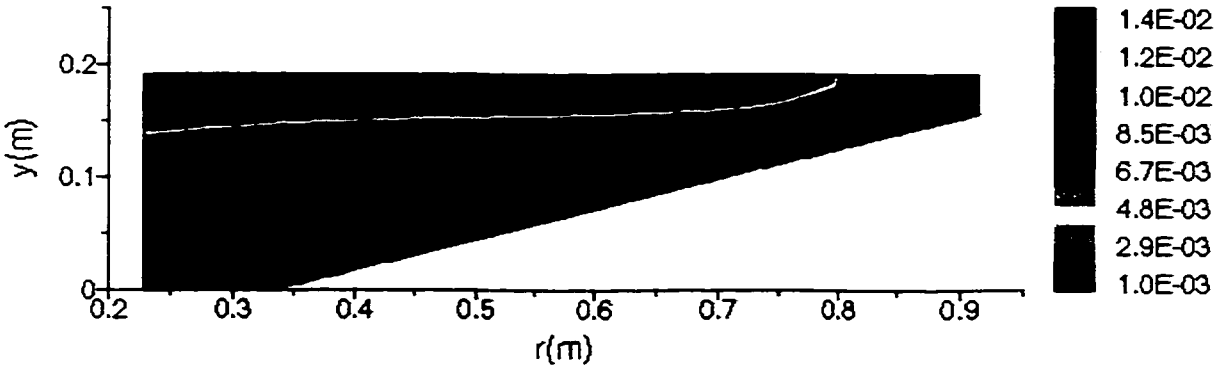

Figure 6.33: Side view of the density field at t/t_s=0.6 (Case EFML1).

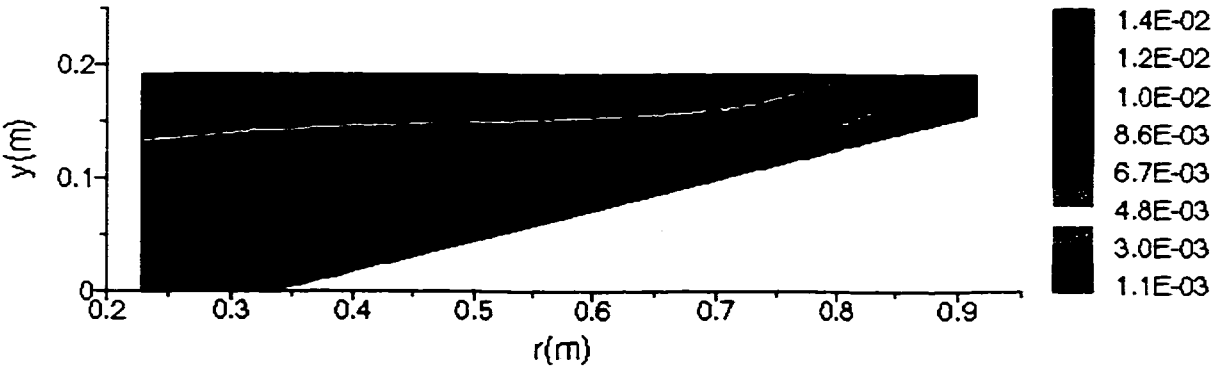

Figure 6.34: Side view of the density field at t/t_s=0.8 (Case EFML1).

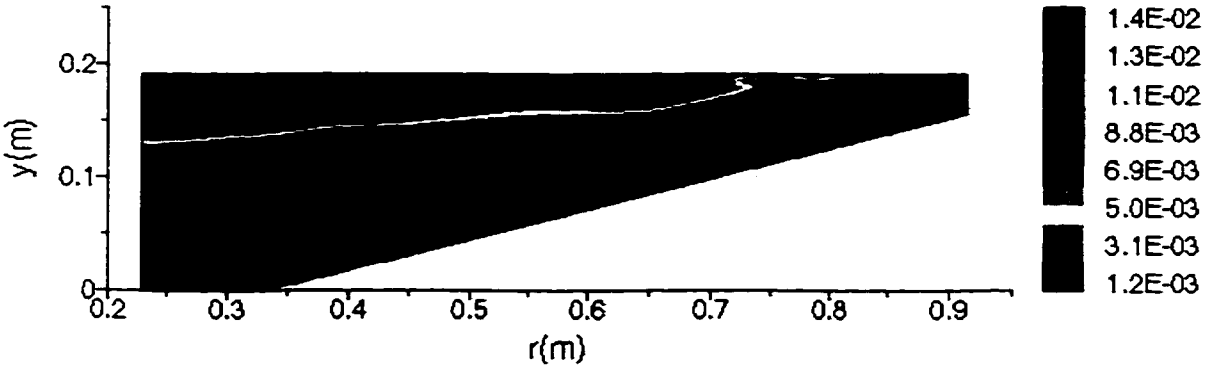

Figure 6.35: Side view of the density field at t/t_s=1.0 (Case EFML1).

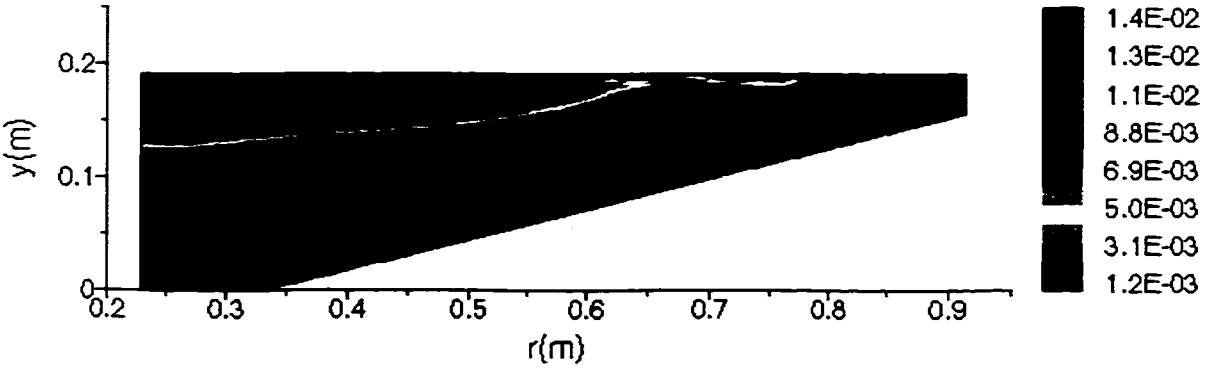

Figure 6.36: Side view of the density field at t/t_s=1.2 (Case EFML1).

Chapter 7

Data Assimilation by Nudging of the Upwelling Flow

7.1 Introduction

The name "data assimilation" originated in meteorology about thirty years ago. Data assimilation is a process that combines a numerical model simulation with one or more measured data sets in real time to improve the forecast. A review of data assimilation in meteorology and oceanography can be found in Ghil and Malanotte-Rizzoli (1991).

Nudging is one of the assimilation methods. The nudging scheme was first introduced in meteorology by Anthes and colleagues (Anthes 1974; Hoke and Anthes 1976). Prompted by the new availability of global synoptic data sets provided by satellite, the nudging scheme was later introduced for oceanographic data assimilation by Verron and Holland (1989) and by Holland and Malanotte-Rizzoli (1989). The altimetric data set can provide information about the sea surface elevation. Ocean acoustic tomography is the technique that is capable of providing synoptic mapping of the interior of a water body. The combination of altimetry and tomography is often presented as the definitive answer to detailed measurement of the ocean. Experiments such as (SYNOP) project, sponsored by the Office of Naval Research, provide data sets collected in limited regions that can be used for local data assimilation. The Optimum Thermal Interpolation Scheme (OTIS) developed at the U.S. Navy Fleet Numerical Oceanography Center provides a global data set for global data assimilation. Nudging not only has been used in localized, surface data sets but also has been

tested by assimilating of the three-dimensional interior temperature and salinity field. For more recent and realistic assimilations, see Malanotte-Rizzoli and Young (1995).

Unlike previous nudging experiments, in which only simplified equations were employed, we will perform time intermittent nudging to upwelling flow results obtained by solving three-dimensional Navier-Stokes equations. This chapter is organized as follows. In Section 7.2, the general nudging scheme is introduced. Section 7.3 discusses the data sets used in the nudging scheme. In Section 7.4, the application of nudging scheme to the specific upwelling flow is presented. Seven nudging experiments were carried out to study the dependence of the assimilation results upon the time-scale and the nudging coefficient in the nudging term and to evaluate the effectiveness of nudging the velocity field (u, v, w) and/or the density field ρ'.

7.2 Nudging Scheme

The governing equations are the three-dimensional Navier-Stokes equations and the scalar transport equation described in Chapter 2. A complete description of the model, including its implementation, solution procedures can also be found in Chapter 2. After moving all the terms except the time-derivative term in the governing equations to their corresponding Right-Hand Sides (RHS), the governing equations can be written schematically as

$$\frac{\partial f}{\partial t} = \text{RHS}, \tag{7.1}$$

where variable f represents u, v, w or ρ' and RHS contains all the terms except the unsteady term of the governing equations. Following the original formulation by Anthes (1974), the equation for nudging can be written in a general form as

$$\frac{\partial f}{\partial t} = \text{RHS} - \sum_{n=1}^{N} G(\delta t, \delta r_n)(f - f_n^{\text{obs}}), \tag{7.2}$$

where f_n^{obs}, n=1,...,N, are the measurements of f at N observational stations, G is a function of space and time, δt is the time separation between the observation times t^{obs} and the model evaluation time t, and δr_n is the distance between the model grid point (x, y, z) and the observational point $(x_n^{\text{obs}}, y_n^{\text{obs}}, z_n^{\text{obs}})$. The equation for nudging is then integrated forward in time. During the integration period, Eqn. (7.2) is modified at each time step by a correction based on N observed data. For effective assimilation, data needs to be available at time intervals that are shorter than the time scale over which the model loses memory of the initial state. As pointed by Anthes (1974), there is no general form of G that will apply to all dynamic models, nor even to the same model under different synoptic conditions. For example, the decay of G with distance separation should be larger in a region of strong gradient, such as baroclinic zone, than in a quiet, barotropic zone. The decay of G with time separation in a highly transient regime should be much larger than during a more steady regime.

The convergence of the assimilation experiment towards the observations is quantified by monitoring the time evolution of the global root-mean-square (r.m.s.) difference between the model-predicated variable f and the corresponding independent observations f^{obs} as:

$$\epsilon_{\text{rms}} = \sqrt{\frac{1}{N}\sum_{n=1}^{N}(f - f^{\text{obs}})^2}, \tag{7.3}$$

where N is the total number of grid points.

7.3 Data Sets

In data assimilation, observed data has to be inserted into a numerical model as it is integrated forward in time. Therefore, two sets of data, one from real measurements and the other generated by the numerical model are needed. The numerical

simulation of upwelling flow corresponding to Narimousa and Maxyworthy's experiment (Narimousa and Maxyworthy 1987) were performed on a fine computational grid of 192(radial)×128(vertical)×320(azimuthal). The physical parameters relevant to the upwelling flow and an illustration of the computational grid can be found in Chapter 6. The simulation results are in good agreement with the corresponding experimental data. Since the previous lab experiment did not provide the data for three-dimensional velocity and density fields, the high resolution simulation data will be used to represent the measured data in the absence of the real measured data from experiment. The fine resolution simulation run will be called hereafter the "control run" and the data obtained from the control run will be used as the observation data. Although the fine-grid computation produces accurate results, it also led to high computation cost. We will reduce the computational grid size from 192×128×320 to 96×128×160. Nudging is then performed to assimilate the observed data into the coarse grid numerical forecast to produce a new improved forecast. The new forecast results will be compared to the control run results.

7.4 Application of Nudging Scheme

In this section, three-dimensional global data sets of the three velocity field (u, v, w) and/or the density field ρ' are assimilated intermittently at every model grid point. Following Malanotte-Rizzoli and Young (1995), the function G in Eqn. (7.2) takes the form:

$$G(x, y, z, t) = R_0 r_1(x, y, z) r_2(t), \tag{7.4}$$

where R_0 is an inverse time constant. The spatial structure $r_1(x, y, z)$ takes the form

$$r_1(x, y, z) = e^{-\delta r_n^2 / L^2}, \tag{7.5}$$

where $\delta r_n = [(x-x_n^{obs})^2+(y-y_n^{obs})^2+(z-z_n^{obs})^2]^{1/2}$ is the distance between the model grid point and the observation point; thus the point information is smoothed around the measurement point by a Gaussian function. L is a length-scale, usually prescribed to be of the order of the Rossby deformation radius of the region. Regarding the time dependence of the data, there are usually two types of applications, *i.e.,* forecast and hind-cast. In a forecast experiment, there is no future data available. However, in a hind-cast experiment, there are a whole time series of data to work with. The hind-cast type of application has been used in the present implementation. Thus we choose the following time dependence for the data insertion:

$$r_2(t) = \tanh\left[a(\frac{t-t^{obs}+\Delta t}{\Delta t})\right] \qquad t^{obs}-\Delta t \le t \le t^{obs}, \tag{7.6}$$

where Δt is the time interval over which nudging is performed, a is a dimensionless constant and $\Delta t/a$ is a decay time-scale for the nudging. The observation fields begin to influence the numerical model evolution before the moment that the observation data are taken, and the inserted observation data is felt most strongly at the observation time t^{obs}. When the nudging is repeated for every Δt seconds, the time t^{obs} is reset each time new observation data become available.

As the data sets are provided at every model grid point in this work, the spatial error function r_1 [Eqn. (7.5)] is unity and drops out of the function of errors G [Eqn. (7.4)]. The equation for nudging becomes:

$$\frac{\partial f}{\partial t} = \mathrm{RHS} - R_0 \tanh\left(\frac{t-t^{obs}+\Delta t}{\Delta t/a}\right)(f-f_n^{obs}) \qquad \text{for} \qquad t^{obs}-\Delta t \le t \le t^{obs}. \tag{7.7}$$

Implementation of Eqn. (7.7) is particularly straight-forward. The simplicity of nudging as a data assimilation scheme has made it very popular in a broad range of oceanographic and meteorological applications. However, in order to perform nudging effectively, the proper length-scale L, the time-scale $\Delta t/a$ and the nudging coefficient

R_0 should be decided by case study for each specific flow.

The observation data are inserted into the numerical model every Δt =2.5 seconds at every model grid. The time step for the numerical simulation is 0.005 second. At each nudging period, the equation for nudging is integrated from $t^{obs} - \Delta t$ to t^{obs}. Each nudging experiment lasts 10 seconds. The assimilation starts from initial time t = 80s, when the density front has migrated from the outer wall and the baroclinic frontal waves have just begun to develop (Figure 7.1). The simulation results of the control run at t = 85s and t = 90s (Figures 7.2 and 7.3) show that the baroclinic frontal waves grow in amplitude with time. For comparison, the results of the coarse grid simulation run without nudging at corresponding times (t = 85s and t = 90s) are shown in Figures 7.4 and 7.5. It is obvious that the coarse grid simulation without nudging cannot resolve the evolution of the baroclinic frontal waves with time and the top view density fields are completely different from the control run results.

A number of assimilation experiments have been performed in this chapter and they are summarized in Table 7.1. First, the effects of changing the time scale $\Delta t/a$ are studied in experiments Exp1 to Exp3 and the effect of changing nudging coefficient R_0 are studied in experiments Exp1, Exp4 and Exp5 while both the velocity fields (u, v, w) and the density field ρ' are nudged. Then the efficacy of nudging only the velocity fields (u, v, w) or the density field ρ' is compared to nudging both of them.

7.4.1 Effect of Changing Time Scale

The time scale $\Delta t/a$ defines how fast the data are assimilated toward to the observation data. Three assimilation experiments (Exp1 to Exp3) with different $\Delta t/a$ values, *i.e.*, Δt = 2.5s and a = 12, 3 and 1 are performed. The nudging coefficient value $R_0 = 2s^{-1}$, which strongly relaxes the model evolution toward the observation, is chosen. The density field and the time evolution of the normalized r.m.s. differences between the control run results and the simulation results of the three experiments

are presented in Figures 7.6 to 7.8. All the r.m.s. difference curves presented in this chapter are normalized by their initial values at each nudging period, thus giving a value of 1 at the beginning of each nudging period. One may notice that the vertical velocity v field converges better than the other two velocity fields in the first nudging period. This is because that the assimilation run has the same number of vertical grid points as the control run and thus the vertical velocity field has a better initial value than the other two velocity fields at the first nudging period.

Figures 7.6b, 7.7b and 7.8b show that the time scale $\Delta t/a$ directly affects the convergence rate of the normalized r.m.s. differences. The r.m.s. difference converges slower with an increasing $\Delta t/a$ value (or a decreasing a value). Figures 7.6b and 7.7b show that the normalized density r.m.s. difference eventually reaches the same asymptotic value for $a = 12$ and $a = 3$ cases at a decreasing convergence rate, while the normalized density r.m.s. difference for $a = 1$ case reaches a slightly higher value at the slowest rate (Figures 7.8b). Therefore, the top view density fields of cases $a = 12$ and $a = 3$ (Figures 7.6a and 7.7a) are identical and the top view density field for $a = 1$ case (Figure 7.8a) is slightly different from the other two cases. The density fields of all the three cases resemble the control run density field. For the $a = 12$ and $a = 3$ cases, each normalized r.m.s. difference of the velocity component reaches its distinct asymptotic value quickly. However, the normalized r.m.s. difference for the velocity component for $a = 1$ case converges too slowly so that the velocity field evolves differently than the fast converging cases (*i.e.*, cases $a = 12$ and 3) and each of the normalized velocity r.m.s. differences reaches an asymptotic value that is about 40% higher than its corresponding normalized r.m.s. difference of the other two cases, indicating that the evolved velocity field at $t = 90$s for $a = 1$ case is different for $a = 12$ and $a = 3$ cases.

7.4.2 Effect of Changing Nudging Coefficient

The nudging coefficient R_0 decides the intensity of the nudging. Holland and Malanotte-Rizzoli (1989) carried out a sensitivity study by changing the value of R_0. They found that the nudging term is very weak and the data assimilation process is ineffective for small R_0 values, while too large R_0 values "shock" the model dynamics with the excitation of undesirable internal gravity waves. These two extreme behaviors should be avoided in the process of choosing an R_0 value. The nudging coefficient value $R_0 = 2s^{-1}$ was used in the time scale study. Two more assimilation experiments (Exp4 and Exp5) with different R_0 values, *i.e.*, $R_0 = 4s^{-1}$ and $1s^{-1}$ are carried out. The time scale $\Delta t/a$ is fixed at 2.5/12s.

The results of assimilation experiments with $R_0 = 2s^{-1}$ and $4s^{-1}$, *i.e.*, with increasing nudging strength, are shown in Figures 7.6 and 7.9. The top view of the density field at $t = 90$s for each of the two experiments (Figures 7.6a and 7.9a) are almost identical to the control run results at the same time (Figure 7.3). The time evolution of the normalized r.m.s. differences between the control run results and the simulation results for the corresponding experiments (Figures 7.6b and 7.9b) show that simulation data converges better toward the observation data with increasing R_0 values. For the assimilation experiment with $R_0 = 1s^{-1}$, Figure 7.10a shows that the density field has already departed from the control run results (Figure 7.2) by $t = 85$s, even though the nudged density field is improved compared to the simulation run density field without nudging (Figure 7.4). The time evolution of the normalized r.m.s. differences (Figure 7.10b) for the same experiment shows that the r.m.s. differences already converge to higher values (about 40% and 95% higher than $R_0 = 2s^{-1}$ and $4s^{-1}$ cases, respectively) by the end of the second nudging period, indicating that the assimilation results are diverging from the observation data. Therefore, one can reach the conclusion that the nudging with $R_0 = 1s^{-1}$ is too "gentle" and fails to keep the evolution of the baroclinic waves close to the control run for the present upwelling

flow case. Even though a large R_0 value can drive the flow field toward the control run results, as pointed out by Malanotte-Rizzoli and Young (1995), a very strong nudging intensity over-constrains the model and the effect is similar to a replacement of the numerical field by the observation data.

7.4.3 Nudging Velocity Field or Density Field

The experiments of nudging both the velocity field (u, v, w) and the density field ρ' have been performed. We now proceed to study the effects of nudging the velocity field (Exp6) or the density field (Exp7) alone. A strong nudging coefficient $R_0 = 4s^{-1}$ and a small time scale $\Delta t/a = 2.5/12$ are chosen. The assimilation experiment result of nudging velocity field (u, v, w) alone is shown in Figure 7.11. Examination of the normalized r.m.s. difference between the control run results and the simulation results indicates that the normalized r.m.s. difference of the density field decreases only about 30% in the first nudging period, decreases only about 10% in the second nudging period and then has an increasing trend. The nudged velocity components u and w converge well to the observation data. However, the vertical velocity component v converges poorly to the observation data because the poorly converged density field affects the vertical velocity via the buoyancy term. The top view density field shown in Figure 7.11a reveals that the density field is completely different from the control run density field (Figure 7.2) by $t = 85$s. The result suggests that a globally converged velocity field cannot lead to the expected time evolution of the density field near the baroclinic wavy front without the guidance of the "correct" information of the observation density field.

The assimilation experiment result of nudging the density field ρ' alone is shown in Figure 7.12. Without nudging the velocity field, the simulated velocity field quickly departs from the control run result as indicated by the increasing normalized r.m.s. differences between the control run results and the simulation results (Figure 7.12b).

The normalized r.m.s. difference of the vertical velocity component v diverges slower than the normalized r.m.s. differences of the other two components simply because that the vertical velocity field is directly affected by the nudged density field via the buoyancy term. Even though the simulated velocity field is totally different from the observation velocity field, the assimilation result for the density field still converges to the control run result with the strong density nudging, which is confirmed by the converged normalized density r.m.s. difference and the good agreement between the top view density field (Figure 7.12a) and the control run density field at the same time (Figure 7.2). The above results suggest that both the velocity and the density field information are needed in the nudging in order to obtain the correct time evolution of both the the velocity and the density field for the present study in which only a rather coarse computation grid has been employed.

7.5 Summary

A number of time intermittent, three-dimensional nudging experiments are performed on the velocity field (u, v, w) and/or the density field ρ'. An extensive study of the effect the time scale $\Delta t/a$ and the nudging coefficient R_0 used in the nudging term was carried out. The effectiveness of nudging the velocity field (u, v, w) and/or the density field ρ' are evaluated in this chapter. The following conclusions can be reached:

- The effect of changing time scale $\Delta t/a$

  The time scale $\Delta t/a$ defines how fast the data are assimilated toward to the observation data. It directly affects the convergence rate of the flow field r.m.s. differences.

- The effect of changing nudging coefficient R_0

  The nudging coefficient R_0 decides the intensity of the nudging. Too weak R_0 will fail to keep the time evolution of the flow field to the observation field. Too

strong R_0 will over-constrain the model up to the limit of acting effectively as a mechanism for replacement of the numerical field with assimilated data.

- Nudging velocity (u, v, w) and/or density ρ' fields

  Both the velocity and the density field information are needed in the nudging experiment in order to obtain the correct time evolution of both the velocity and the density field for the present study in which a rather coarse computation grid has been employed.

Although only a limited number of nudging experiments have been performed in this work, the results are encouraging and demonstrate that the hind-cast type of nudging is applicable to laboratory-scale upwelling flows we studied in Chapter 6 with appropriate selection of nudging parameters. Further work is needed to test the forecast-type of nudging and nudging with only localized, partial data sets. The forecast-type of assimilation experiments have been performed successfully by Haines *et al.* (1993). After the experimental data being made available in the EFML studies, forecast-type nudging of the same upwelling flow should be performed on a fine enough grid resolution (lower than our control run grid resolution but much higher than our assimilation run grid resolution) so that the flow field can evolve properly with the correction of the observation data most strongly at the beginning of each nudging. Due to the limitation of efficient communication between the nearest neighboring processors required by the parallel computer and the parallel algorithm we are using, nudging only partial data sets is more suitable to be tested on a serial computer instead of a parallel computer.

Table 7.1: A summary of the assimilation experiments performed.

Experiment	Assimilated data	time scale $\Delta t/a$ (s)	Nudging Coeff. R_0 (s^{-1})
Exp1	u, v, w and ρ'	2.5/12	2.0
Exp2	u, v, w and ρ'	2.5/3	2.0
Exp3	u, v, w and ρ'	2.5/1	2.0
Exp4	u, v, w and ρ'	2.5/12	4.0
Exp5	u, v, w and ρ'	2.5/12	1.0
Exp6	u, v, w	2.5/12	4.0
Exp7	ρ'	2.5/12	4.0

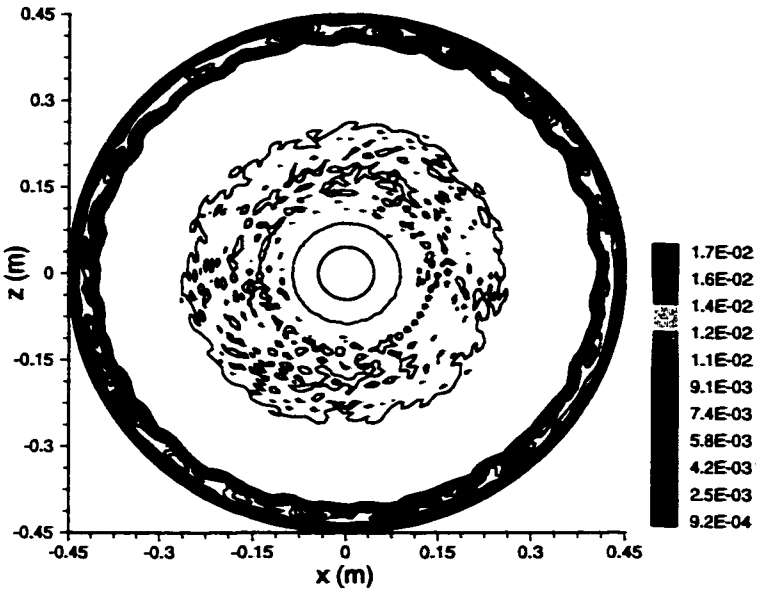

(a) Top view (y/H=0.93)

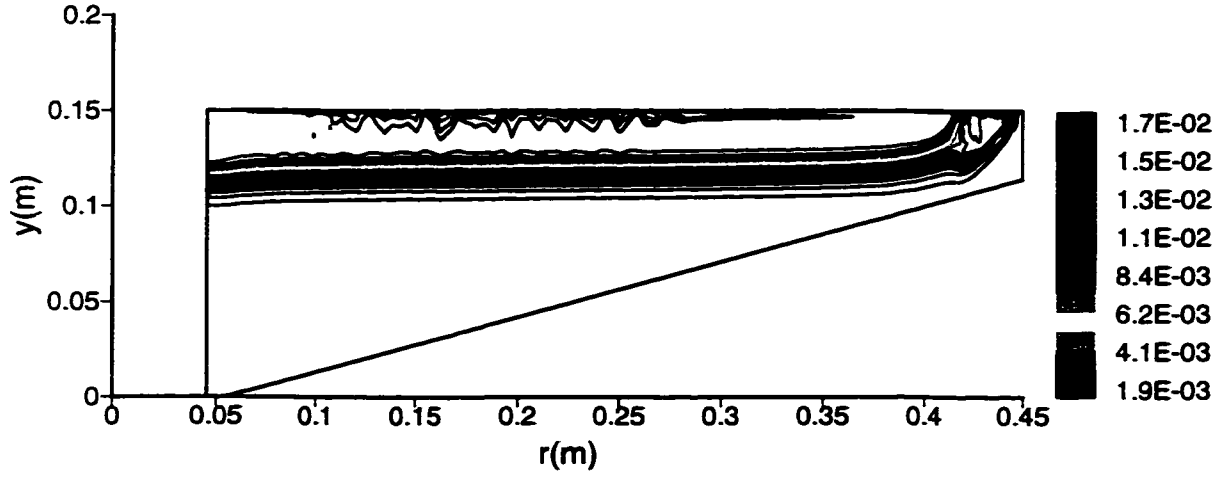

(b) Side View

Figure 7.1: The density field at the the beginning of the assimilation experiments (t=80s).

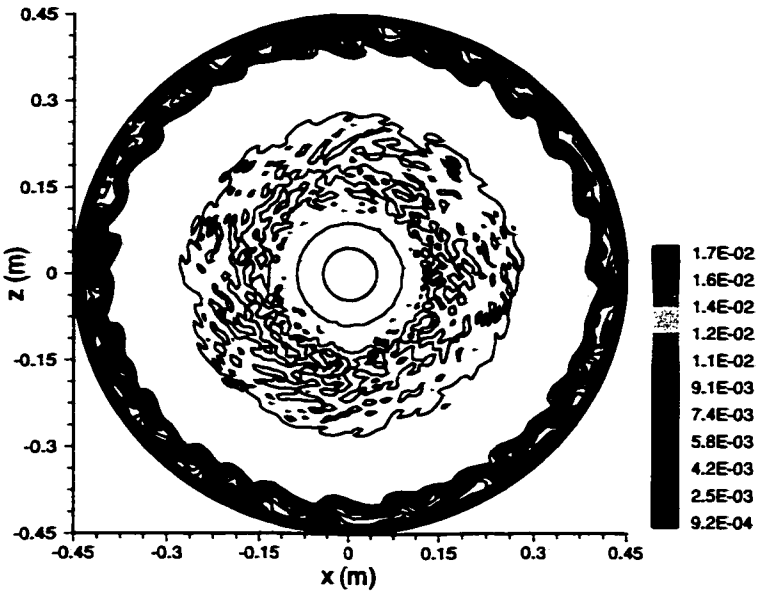

Figure 7.2: Top view of the density field at y/H=0.93 and t=85s for the control run.

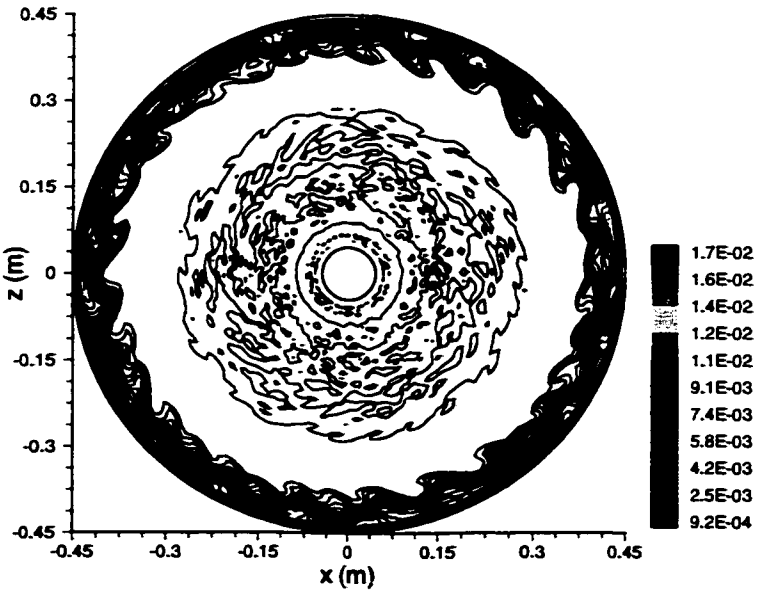

Figure 7.3: Top view of the density field at y/H=0.93 and t=90s for the control run.

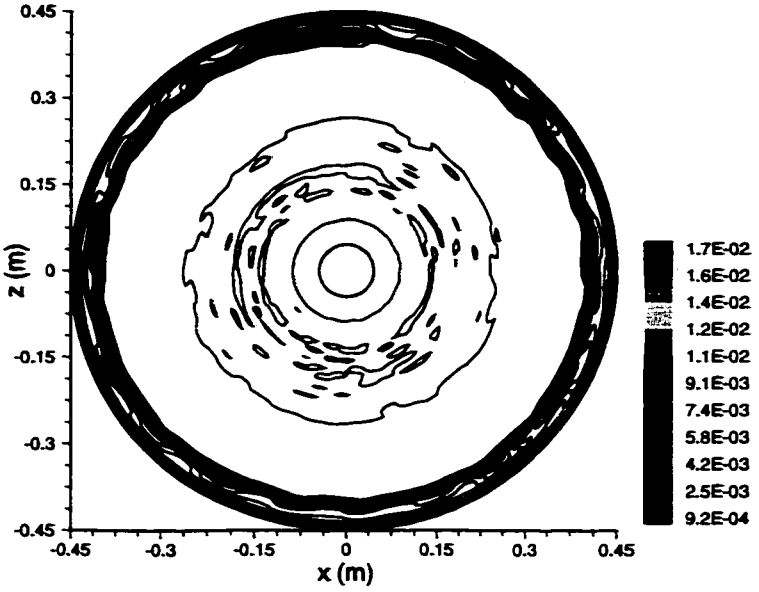

Figure 7.4: Top view of the density field at y/H=0.93 and t=85s for the simulation run without nudging.

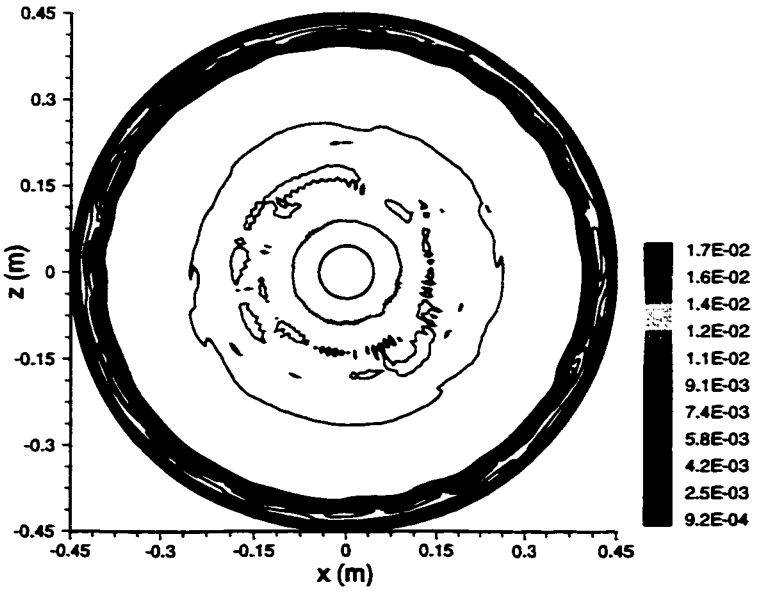

Figure 7.5: Top view of the density field at y/H=0.93 and t=90s for the simulation run without nudging.

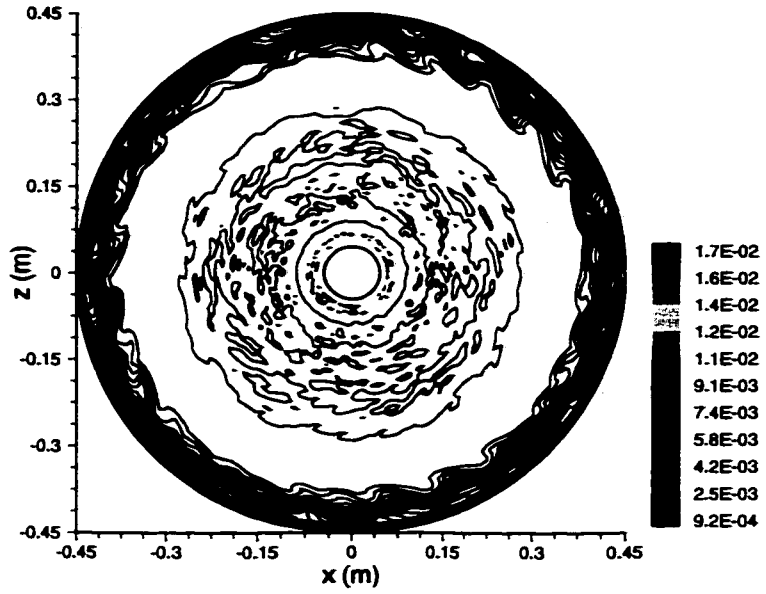

(a) Top view of the density field

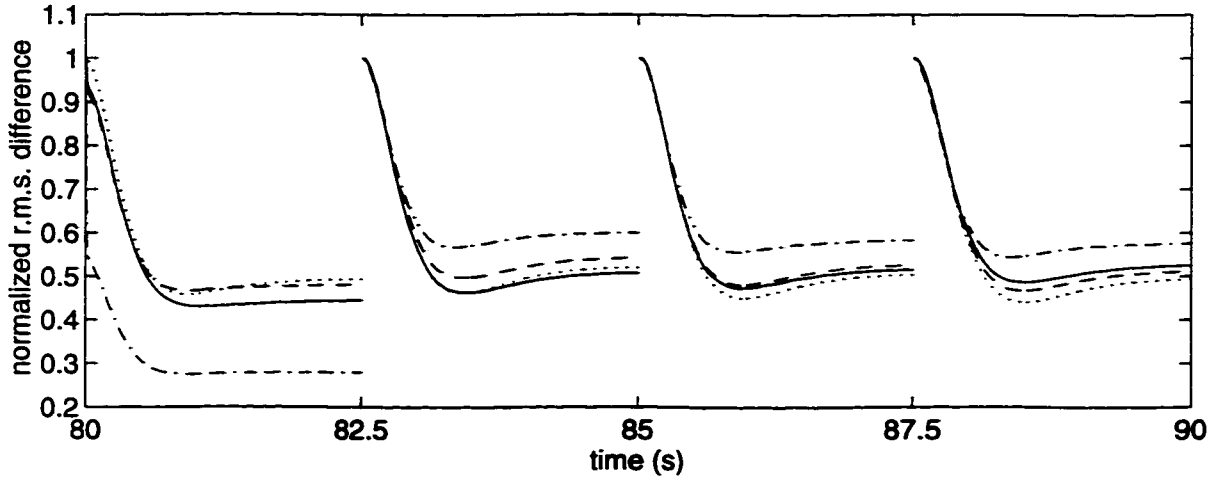

(b) The convergence history of the normalized r.m.s. difference between the control run result and the simulation result

Figure 7.6: The simulation run with (u, v, w) and ρ' nudging ($\Delta t/a = 2.5/12s$ and $R_0 = 2s^{-1}$) at y/H=0.93 and t=90s. The solid line is for u, the dash-dot line for v, the dashed line for w and the dotted line for ρ'.

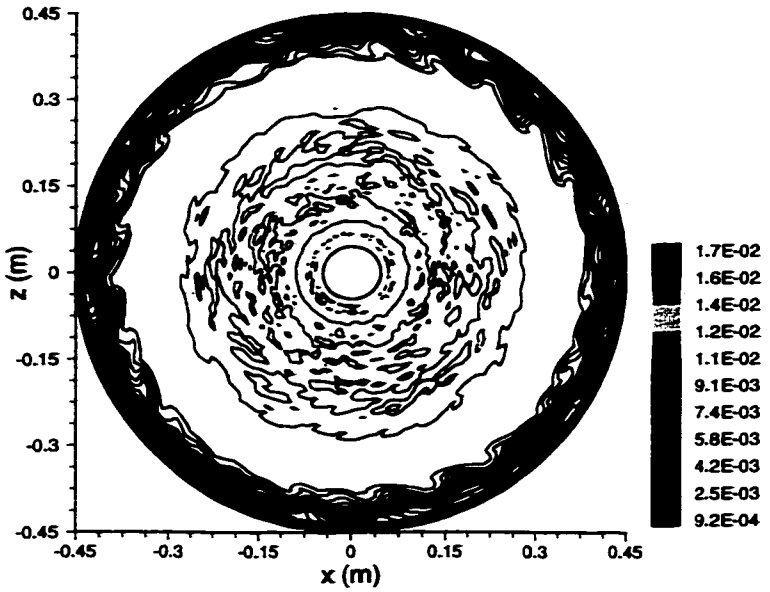

(a) Top view of the density field

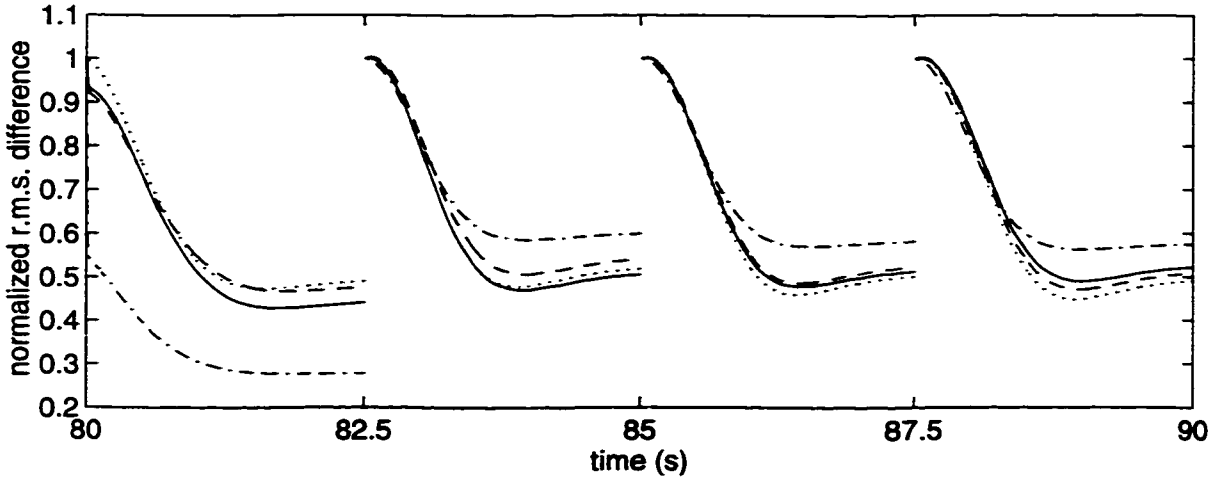

(b) The convergence history of the normalized r.m.s. difference between the control run result and the simulation result

Figure 7.7: The simulation run with (u, v, w) and ρ' nudging ($\Delta t/a = 2.5/3s$ and $R_0 = 2s^{-1}$) at y/H=0.93 and t=90s. The solid line is for u, the dash-dot line for v, the dashed line for w and the dotted line for ρ'.

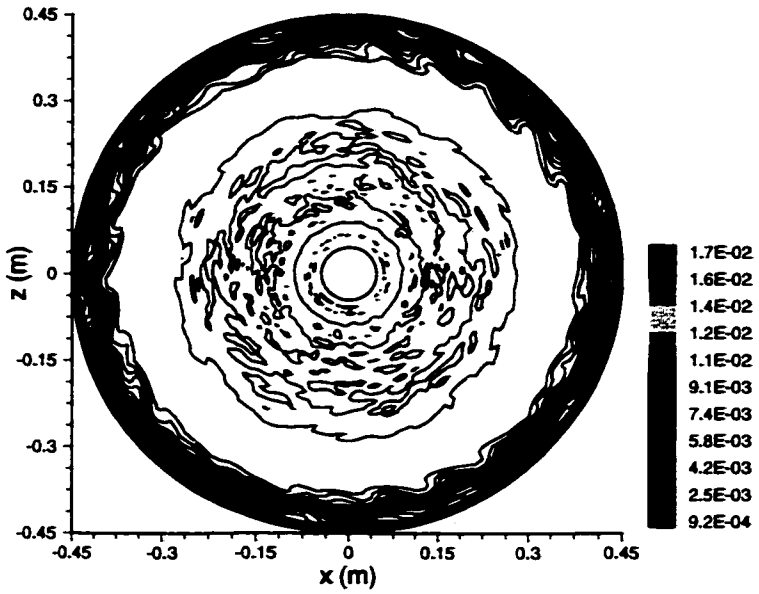

(a) Top view of the density field

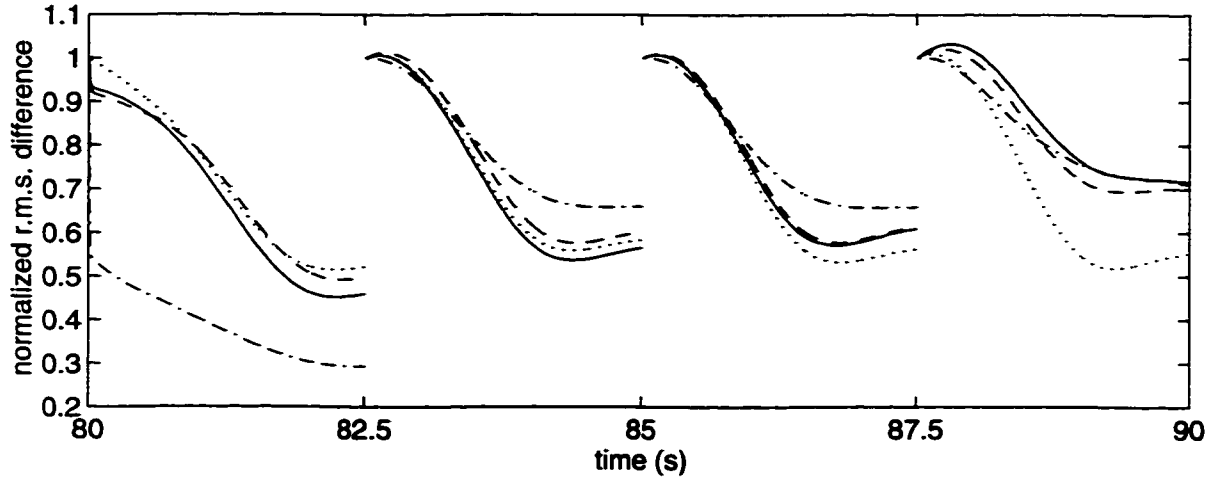

(b) The convergence history of the normalized r.m.s. difference between the control run result and the simulation result

Figure 7.8: The simulation run with (u, v, w) and ρ' nudging ($\Delta t/a = 2.5/1s$ and $R_0 = 2s^{-1}$) at y/H=0.93 and t=90s. The solid line is for u, the dash-dot line for v, the dashed line for w and the dotted line for ρ'.

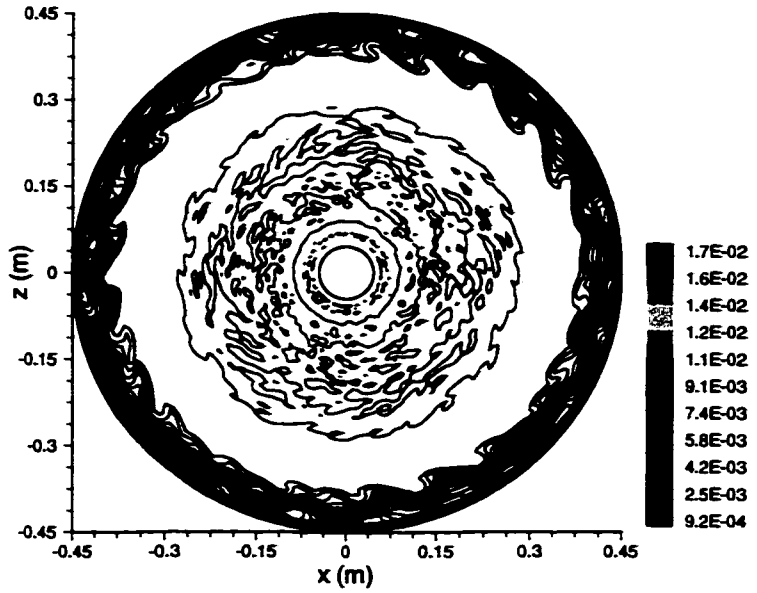

(a) Top view of the density field

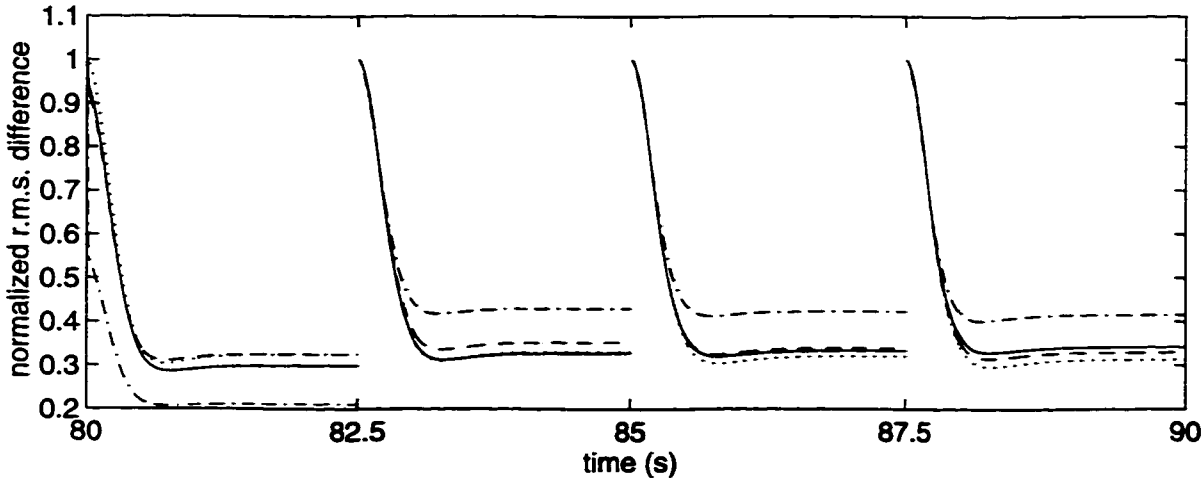

(b) The convergence history of the normalized r.m.s. difference between the control run result and the simulation result

Figure 7.9: The simulation run with (u, v, w) and ρ' nudging ($\Delta t/a = 2.5/12s$ and $R_0 = 4s^{-1}$) at y/H=0.93 and t=85s. The solid line is for u, the dash-dot line for v, the dashed line for w and the dotted line for ρ'.

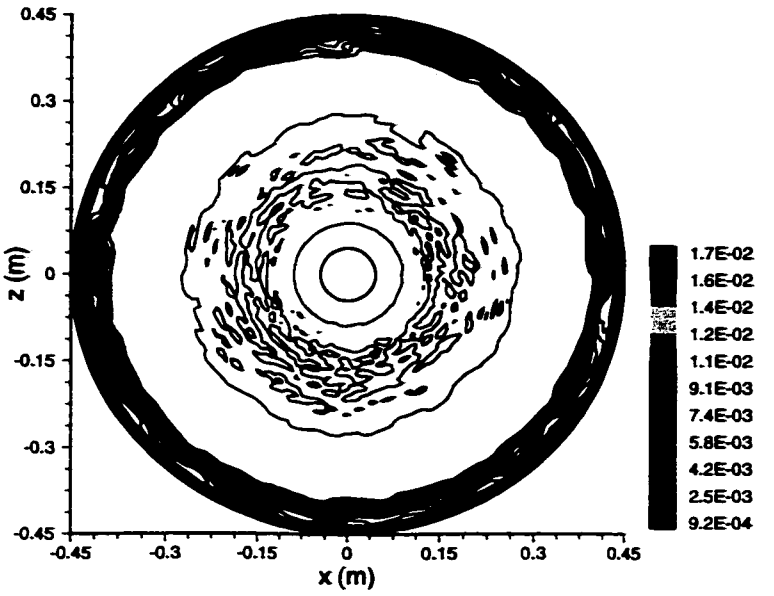

(a) Top view of the density field

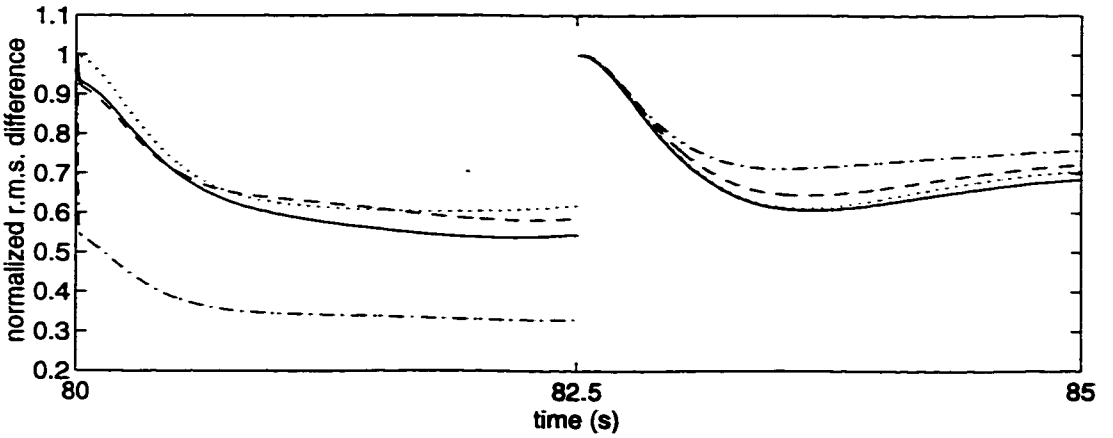

(b) The convergence history of the normalized r.m.s. difference between the control run result and the simulation result

Figure 7.10: The simulation run with (u, v, w) and ρ' nudging ($\Delta t/a = 2.5/12s$ and $R_0 = 1s^{-1}$) at y/H=0.93 and t=85s. The solid line is for u, the dash-dot line for v, the dashed line for w and the dotted line for ρ'.

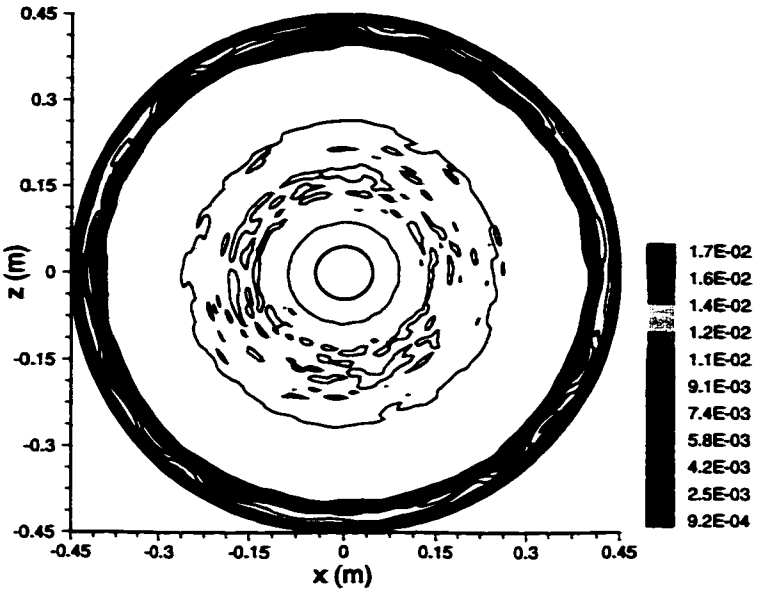

(a) Top view of the density field

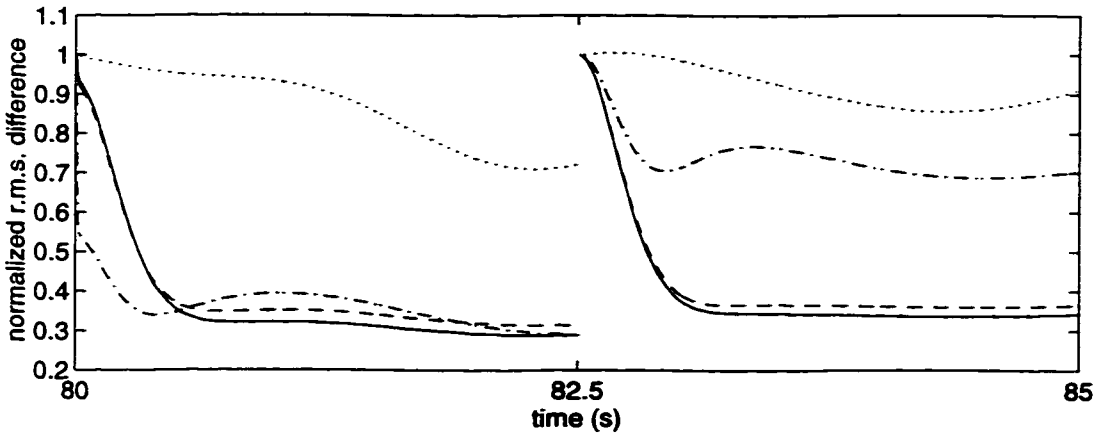

(b) The convergence history of the normalized r.m.s. difference between the control run result and the simulation result

Figure 7.11: The simulation run with (u, v, w) nudging ($\Delta t/a = 2.5/12s$ and $R_0 = 4s^{-1}$) at y/H=0.93 and t=85s. The solid line is for u, the dash-dot line for v, the dashed line for w and the dotted line for ρ'.

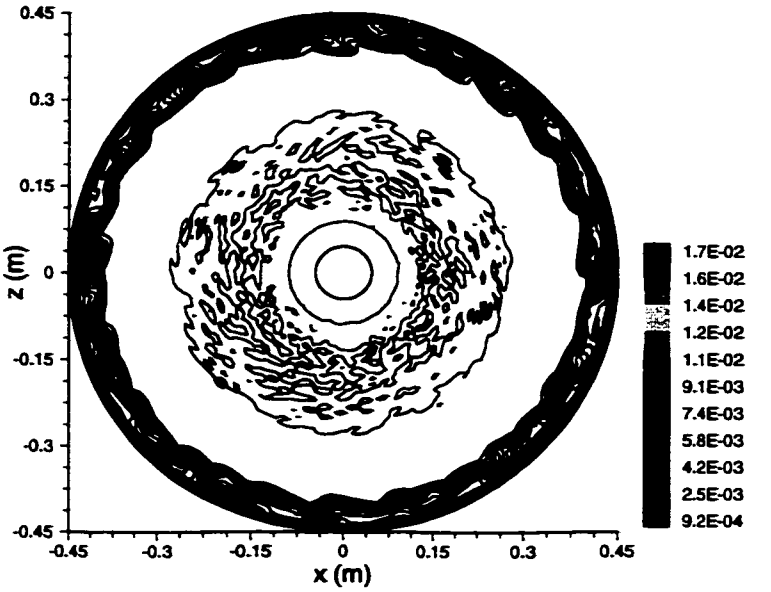

(a) Top view of the density field

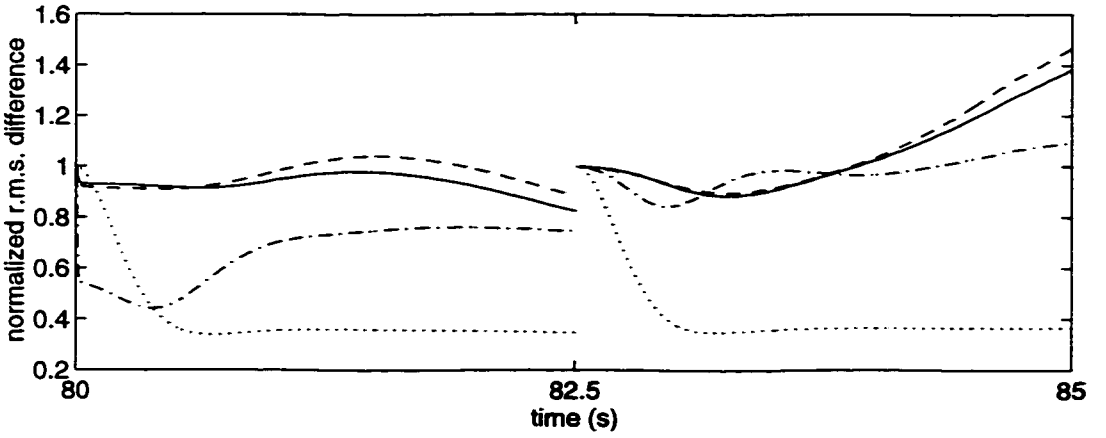

(b) The convergence history of the normalized r.m.s. difference between the control run result and the simulation result

Figure 7.12: The simulation run with ρ' nudging ($\Delta t/a = 2.5/12s$ and $R_0 = 4s^{-1}$) at y/H=0.93 and t=85s. The solid line is for u, the dash-dot line for v, the dashed line for w and the dotted line for ρ'.

Chapter 8

Numerical Investigation of Rotating Stratified Flows

8.1 Introduction

Atmospheric and oceanic flows may be thought of as turbulent motions under the constraints of geometry, stratification and rotation. The motions at large scales tend to be horizontal due to the combined effects of large diameter-to-height aspect ratio and the existence of stable stratification. The combined effects of these constraints are to produce approximately two-dimensional turbulent flows at very high Reynolds numbers. The most striking feature of two-dimensional flows at high Reynolds numbers is the "inverse cascade" of energy to large scales. Energy is observed to accumulate in large scales and coherent structures emerge from a random initial field, which is demonstrated by the numerical calculations of McWilliams (1984), Legras, Santangelo and Benzi (1988), Dritschel (1993) and others. The accumulation of energy in these structures results from the inability of vortex lines to be stretched or twisted in a two-dimensional flow. This scenario is very attractive as a model for geophysical flows, which are known to contain very energetic structures in atmospheric highs and lows and mesoscale oceanic eddies.

In a series of laboratory experiments, Boubnov, Dalziel and Linden (1994) and Linden, Boubnov and Dalziel (1995) have investigated the dynamics of the inverse energy cascade in stratified flows. Their experiments consist of forcing a stably-stratified fluid in a square tank with an array of sources and sinks around the perimeter

of the tank. These sources and sinks induce horizontal motion in a single horizontal plane; thus their experiments are capable of producing horizontal eddies directly without there first being a decay of three-dimensional motion. The laboratory system has the capability of studying flows with direct application to the atmosphere and oceans under controlled conditions, and enables accurate measurements of the flow to be made, so that underlying dynamics can be investigated.

In their on-going experiments, Hacker and Linden at Cambridge University have modified the experiment apparatus of Linden, Boubnov and Dalziel (1995) slightly to accommodate the present numerical study. The forcing consists now of an array of eight source-sink pairs, located in a horizontal plane at the mid-depth around the inner perimeter of an annular tank containing stably-stratified fluid. The objective of the present numerical study is to carry out numerical simulations under the same conditions as those of Hacker and Linden's experiments and to compare the simulation results with the quantitative data obtained from the experiments. The objectives of the combined study are to examine a number of fundamental questions about the dynamics of the turbulent, rotating and stratified flows, *e.g.,* the effects of the rotation rate, stratification and forcing strength, *etc.* on the flow dynamics. However, so far only the rotation effects on a flow field resulting from weak forcing have been investigated numerically. Data from the physical experiments have not been made available yet. Accordingly, this chapter reports on numerical experiments and the insights drawn from them which are being used in the experimental design and planning.

8.2 Experiment of Hacker and Linden

The on-going experiments of Hacker and Linden are conducted in an annular tank whose inner radius R_i=75mm, outer radius R_o=275mm and depth H=100mm. A schematic of the experimental apparatus is shown in Figure 8.1. The tank is filled with

linearly stratified salt solution. The whole apparatus is mounted on a rotating table and spun with constant angular velocity about a vertical axis of rotation. Around the inner perimeter of the tank, a set of eight source-sink pairs is located symmetrically at mid-depth in a horizontal plane, as shown in Figure 8.1. The orifices of the sources and sinks have a diameter $d = 4$mm and are oriented along radial lines from the center of the tank. Equal flow rates Q are provided for each source and sink. The forcing arrangement is set up so that no net impulse or angular momentum is imparted to the fluid in the tank. The idea is that fluid is removed at a given level and then re-injected at the same neutral density level.

8.3 Setup for the Numerical Simulations

Numerical simulations of Hacker and Linden's experiment have been carried out under exactly the same conditions as the experiment except that a top lid, which rotates with the tank, is added to the the simulations to simplify the top boundary condition. This approximation is acceptable since the free-surface curvature in the experiments due to rotation is small, *i.e.*, the maximum deviation of the free surface from the initial flat surface is less than 1mm, within the range of the tank rotation rate $0 \leq \Omega \leq 1$ rad/s in this study.

8.3.1 Analytical Computation of the Grid Stretching and Mapping

For similar reasons to those given in Chapter 5, analytical stretching functions and analytical mapping functions are used in this simulation. The computational domain in the physical space (r, y, θ) can be mapped into a unit cube in the computational

space $(\mathcal{R}, \mathcal{Y}, \Theta)$ by the following mapping functions:

$$\mathcal{R} = \frac{r - R_i}{R_b} \tag{8.1}$$

$$\mathcal{Y} = \frac{y}{H} \tag{8.2}$$

$$\Theta = \frac{\theta}{2\pi}, \tag{8.3}$$

where

$$R_b = R_o - R_i \tag{8.4}$$

$$R_i = 75\text{mm} \tag{8.5}$$

$$R_o = 275\text{mm} \tag{8.6}$$

$$H = 100\text{mm} \tag{8.7}$$

and

$$\mathcal{R} \in [0, 1] \tag{8.8}$$

$$\mathcal{Y} \in [0, 1] \tag{8.9}$$

$$\Theta \in [0, 1]. \tag{8.10}$$

The grid points in the azimuthal direction of physical space (r, y, θ) are distributed uniformly due to the axisymmetric nature of the flow field. In order to resolve the small scale flow structures around the sources and sinks, non-uniform grids are used in the radial direction, with grid points clustered near the inner wall and then stretching out radially; and non-uniform grids are used in the vertical direction with grid points clustered near the mid-depth and then stretching out vertically. A section of the computational grid is illustrated in Figure 8.2. The grid points in the computational space (ξ, η, ζ) are distributed uniformly with grid size $\Delta\xi = \Delta\eta = \Delta\zeta = 1$. The

following stretching functions are used,

$$\mathcal{R} = \left[\xi/N_\xi + \frac{c_r}{a_r}\log\frac{\cosh a_r(\xi/N_\xi - b_r)}{\cosh a_r b_r}\right] / \left[1 + \frac{c_r}{a_r}\log\frac{\cosh a_r(1-b_r)}{\cosh a_r b_r}\right] \quad (8.11)$$

$$\mathcal{Y} = \left[\eta/N_\eta - \frac{c_y}{a_y}\log\frac{\cosh a_y(\eta/N_\eta - b_y)}{\cosh a_y b_y} + \frac{c_y}{a_y}\log\frac{\cosh a_y(\eta/N_\eta - 1 + b_y)}{\cosh a_y(1-b_y)}\right] / \left[1 - \frac{2c_y}{a_y}\log\frac{\cosh a_y(1-b_y)}{\cosh a_y b_y}\right] \quad (8.12)$$

$$\Theta = \zeta/N_\zeta, \quad (8.13)$$

where

$$\xi \in [0, N_\xi] \quad (8.14)$$

$$\eta \in [0, N_\eta] \quad (8.15)$$

$$\zeta \in [0, N_\zeta] \quad (8.16)$$

and N_ξ, N_η and N_ζ are the numbers of control volumes in the ξ-, η- and ζ-directions of the computational space. The values of the parameters used in the stretching function are

$$a_r = 3 \quad (8.17)$$

$$b_r = 0 \quad (8.18)$$

$$c_r = 5 \quad (8.19)$$

$$a_y = 9 \quad (8.20)$$

$$b_y = 0.15 \quad (8.21)$$

$$c_y = 1/3.5, \quad (8.22)$$

so that the stretching factor is less than 1.1 everywhere, which is consistent with the recommendation of Hodges (1997) regarding the maximum stretching factor.

In the physical space, the Cartesian coordinates (x, y, z) and cylindrical coordinates (r, y, θ) are related as follows (Figure 8.3):

$$x = r\cos\theta \tag{8.23}$$

$$y = y \tag{8.24}$$

$$z = r\sin\theta. \tag{8.25}$$

In summary, the relationship between the points in the physical space (x, y, z) and those in the computational space (ξ, η, ζ) are defined by Eqns. (8.11) to (8.13) and the following equations:

$$x = (R_i + R_b\mathcal{R})\cos(2\pi\Theta) \tag{8.26}$$

$$y = H\mathcal{Y} \tag{8.27}$$

$$z = (R_i + R_b\mathcal{R})\sin(2\pi\Theta). \tag{8.28}$$

8.3.2 Initial and Boundary Conditions

The linearly stratified working fluid is initially in solid body rotation Ω with the tank. The buoyancy frequency of the fluid N is defined as

$$N = \sqrt{-\frac{g}{\rho_0}\frac{\mathrm{d}\rho}{\mathrm{d}y}}, \tag{8.29}$$

where $\rho(y)$ is the density, ρ_0 is a reference density, y is the vertical Cartesian coordinate and g is the gravitational acceleration constant. The initial buoyancy frequency N for the linearly stratified fluid is $2\mathrm{s}^{-1}$. Thus, the initial vertical density distribution is

$$\rho(y) = \rho(0) - \int_0^y \frac{\rho_0}{g}N^2 dy. \tag{8.30}$$

Beginning at time $t = 0$s, fluid is sucked from the sinks and re-injected into the tank through the sources with a mean velocity $V = 30$mm/s at the same (neutral density) level. The mean velocity V of jets from the sources is related to the flow rate of a source/sink Q through $V = 4Q/\pi d^2$, where d is the diameter of the sources and sinks. A no-slip velocity boundary condition and no-flux scalar boundary condition are imposed at all solid walls.

8.3.3 The Inlet/Outlet Forced Velocity Profile

The round orifices of the sources and sinks are located at the inner tank wall. The position of the orifice center is specified by its cylindrical coordinate (R_i, θ_s, y_s), where R_i is the inner radius of the tank. The radius of the orifice is $R_s = d/2$. The cylindrical coordinate of the center of each computational cell on the inner tank wall is (R_i, θ_k, y_j). An illustration of the coordinates of the orifice center and the centers of the computational cells on the inner tank wall is shown in Figure 8.4. The inlet/outlet forced velocity profile is assumed to be a paraboloid. Thus, the inlet/outlet velocity, which is in the radial direction, has the following form

$$u_{jk} = C\left(1 - \frac{(y_j - y_s)^2 + [R_i(\theta_k - \theta_s)]^2}{R_s^2}\right) \quad \text{for} \quad (y_j - y_s)^2 + [R_i(\theta_k - \theta_s)]^2 < R_s^2. \tag{8.31}$$

The constant C in the above equation is determined by

$$Q = \sum_N u_{jk} A_{jk}. \tag{8.32}$$

where N is the number of computational cells that are within the orifice, A_{jk} is the area of each computational cell that is within the orifice and Q is the known flow rate of the sources and sinks.

8.4 Simulation Results

Three simulation runs were carried out covering three different rotation rates. A summary of the grid resolutions and parameters for the three cases (Cases Run1 to Run3) of the simulation runs is given in Table 8.1. The number of grid points was selected to adequately resolve the expected flow based on our experience with the grid resolution studies for the simulations described in Chapters 5 and 6. The number of grid points for each case shown in Table 8.1 is for interior points. Two fictitious points outside the physical domain are added in each dimension in the simulations to facilitate implementing boundary conditions.

For a given fluid and geometric arrangement of sources and sinks, there are four parameters governing the behaviors of the flow. They are the mean velocity V of the fluid through the source orifices, the diameter of the orifices d, the initial buoyancy frequency N and the Coriolis parameter $f = 2\Omega$. These parameters may be expressed in terms of three non-dimensional external parameters: the forcing parameter $F_d = V/dN$, the Reynolds number $Re_d = Vd/\nu$, where ν is the kinematic viscosity of the fluid, and the ratio f/N of the Coriolis and buoyancy frequencies. It should be emphasized that F_d and Re_d, based on the external variables that control the flow, are not the internal Froude and Reynolds numbers of the flow.

The forcing parameter F_d characterizes the relative strength of the forcing to the stratification. F_d is also a measure of the internal Froude number of the jet flow from the sources. $F_d = V/Nd$ can be interpreted as the ratio of a vertical wave frequency $\omega = V/d$ to the buoyancy frequency N, *i.e.*, $F_d = \omega/N$. When $F_d > 1$ for the jet flow, *i.e.*, when $\omega > N$, no internal wave motions are generated by the jet disturbances since the dispersion relation (page 238 of Kundu, 1990) requires that $F_d = \omega/N = \cos\theta \leq 1$. The Reynolds number Re_d is a measure of the Reynolds number of the jet flow from the sources. The low values of Re_d in the present study indicate that little or no turbulence is injected into the flow. For the present numerical study, flows at different

rotation rates but at the same low Reynolds number $Re_d = 120$ and the same low value of forcing parameter $F_d = 3.75$ are studied. Boubnov *et al.* (1994) show that the character of the flow changes according to the value of F_d. Thus, when F_d <10, the forcing is weak and the flow is characterized by approximately horizontal flow motion, while when F_d >10, vertical mixing occurs and the flow motion eventually becomes three-dimensional.

8.4.1 Velocity Field

For the non-rotating case (Case Run1), the jet flow from the source penetrates towards the outer tank wall as time progresses. After the arrival of the jet flow at the outer wall, the flow is stalled by the wall and splits equally into two parts. Thus, two recirculating regions are formed at each side of the jet flow, as shown in Figure 8.5. The side views of the velocity field (Figures 8.6a and b) on the centerlines of the source and sink show that the flow motion is primarily horizontal. The velocity vectors in the above figures are plotted at every second point in the radial direction, at every point in the azimuthal direction and at every point in the vertical direction.

The expanded top view of the velocity field and the side views of the velocity field at the centerlines of the source and sink for $\Omega = 0.5$ rad/s (Case Run2) at $t = 60$s are shown in Figures 8.7, 8.8 a and b, respectively. The corresponding velocity fields at the same time but at a higher rotation rate $\Omega = 1.0$ rad/s (Case Run3) are shown in Figures 8.9, 8.10 a and b. The velocity vectors in Figures 8.7 to 8.10 are plotted at every third point in the radial direction, at every second point in the azimuthal direction and at every point in the vertical direction. There are number of similarities in the observed flow patterns. First, eight vortices are formed linked to the eight source flows. Second, these vortices are all anticyclones as a result of the Coriolis force pushing the jet from the source to the right. There are also some differences in the observed flow patterns. Figures 8.7 and 8.9 show that the vortices are smaller at

higher rotation rates. It is clearly shown in the side views of velocity field (Figures 8.8a and 8.10a) that the jet flow penetrates further at the lower rotation rate, while the jet flow spreads more widely at the higher rotation rate. Those figures also show that the flow motion is primarily horizontal with very small vertical velocities, which is consistent with the observation of Linden, Boubnov and Dalziel (1995).

The time-evolution of the flows in the horizontal plane at the mid-depth is given in Figure 8.11. The root-mean-square (rms) horizontal velocities (u and w) averaged over the horizontal flow domain are plotted against time for three different values of Ω. There is almost no difference between the two velocity components indicating that the horizontal flow is isotropic. Figure 8.11 shows that the flow accelerates quickly over the first twenty seconds, and then continues to accelerate at a much reduced rate, reaching an asymptotic value at later times.

The Rossby deformation radius corresponding to the lowest baroclinic mode is defined as $R_D = NH/f$, where N is the buoyancy frequency, H the height of the tank and f the Coriolis parameter. For Cases Run2 and Run3, R_D values are 200mm and 100mm, respectively. The size of the vortices in Cases Run2 and Run3 depends on the rotation rate. At t =60s, size of the vortices in each case is much smaller than the corresponding R_D value (see Figures 8.8a and 8.10a). Since the Rossby deformation radii for the rotating flow cases in the present study are comparable or smaller than the flow domain $R_o - R_i = 200$mm, the rotation effects are important. When R_D is comparable to or smaller than the flow domain, the inverse energy cascade is altered by baroclinic instability. Instead of a large-scale circulation, small-scale eddies, whose sizes are consistent with R_D, were found in the interior of the flow along with the eddies around the forcing boundary by Linden, Boubnov and Dalziel (1995). The current simulations for the rotating cases need to be run longer in order to explore the development of the baroclinic instability.

8.4.2 Vorticity Field

The vorticity imparted to the flow field by the forcing is determined by the velocity profile of the source across the orifice. Figures 8.12 to 8.14 show the vertical and azimuthal components of the vorticity for the three simulation cases studied. For the non-rotating case (Figure 8.12) at $t = 150$s, the vorticity is confined to two zones, one containing positive and the other negative vorticity. The total vorticity contained in these two zones is of equal magnitude so that the circulation around a contour enclosing all the flows from a jet is zero. For the two rotating cases at $t = 60s$, Figures 8.13a and 8.14a show that the negative (anticyclonic) vertical vorticity zone gets turned back on itself to be concentrated into an anticyclone under the effect of the Coriolis force. At the same time, the positive (cyclonic) vertical vorticity zone is stretched around the outside of the anticyclone to form a thinner cyclonic zone. One may notice that there is a small negative vorticity region inside the positive vertical vorticity zone near the left part of the jet inlet for $\Omega = 0.5$rad/s case and a bigger negative vorticity region inside the positive vertical vorticity zone near the left part of the jet inlet for $\Omega = 1.0$rad/s case. A close-up look at the velocity and the vertical vorticity fields (Figures 8.15 and 8.16) reveals that this is caused by the combined effects of the Coriolis force and the viscosity. The dominant effect of the Coriolis force turns the jet to the right, while the dominant effect of the viscosity causes the fluid on the left side of the jet to spread. In the middle of the two regions the fluid velocity is smaller than the adjacent fluid velocity, which leads to the formation of the negative vorticity region inside the positive vertical vorticity zone near the left part of the jet inlet . The azimuthal vorticity on the centerline of a source for the two rotating cases (Figures 8.13b and 8.14b) show a pair of vorticities with opposite sign near the inner tank wall resulting from the inlet source velocity profile. There is another pair of vorticities with opposite sign on the left of the first pair resulting from the wake of the jet flow from the source. At a later time ($t = 100s$) for the

rotating case $\Omega = 0.5$rad/s, Figure 8.17 shows that the vorticity fields still have the similar features as those at $t = 60$s (Figure 8.13) except that the vorticities spread further in both the radial and the vertical directions.

8.5 Summary

This chapter describes a numerical investigation of the response of a rotating stratified fluid to continuous forcing produced by an array of sources and sinks arranged symmetrically around the inner boundary of the fluid domain. Simulations of three different rotation rates at low values of the source forcing parameter are carried out and the effects of the rotation rate are evaluated. The outflow from a source is affected directly by the Coriolis force. The size of the anticyclones formed as a result of Coriolis force pushing the jet decreases with the increasing rotation rate. The strength of the anticyclones increases with the increasing rotation rate. The horizontal penetration of the jet flow decreases with the increasing rotation rate, while the spreading width of the jet flow increases with the increasing rotation rate. As a result of these observations, one can conclude that the increase in the rotation rate produces mainly quantitative changes to the early development stage of the flow. The motion is found to be primarily horizontal and there is no significant vertical mixing at the low value of the forcing parameter $F_d = 3.75$. This finding is consistent with the observation of Linden, Boubnov and Dalziel (1995).

When Rossby deformation radius R_D is comparable or smaller than the flow domain, baroclinic instability is expected to develop. Small-scale eddies, whose sizes are consistent with R_D, are found in the interior of the flow along with the eddies around the forcing boundary by Linden, Boubnov and Dalziel (1995). The current simulations for the rotating cases need to be run longer in order to explore the development of the baroclinic instability.

At high injection velocities, the jets from the sources are turbulent and cause vertical mixing, as reported by Boubnov, Dalziel and Linden (1994) and Linden, Boubnov and Dalziel (1995). An extensive study of flows with higher values of forcing parameter F_d is needed in the future to study the three-dimensional turbulence generated by strong forcing and the relevant vertical mixing process. The information on the effects of the different rotation rates on the flows with higher values of F_d is also much needed.

Table 8.1: Grid resolutions and parameters of rotating and stratified flow simulations

Case	Grid $N_r \times N_y \times N_\theta$	f rad/s	V mm/s	N s^{-1}	f/N	F_d	Re_d
Run1	128 × 96 × 320	0.0	30	2	0.0	3.75	120
Run2	192 × 96 × 384	1.0	30	2	0.5	3.75	120
Run3	192 × 96 × 384	2.0	30	2	1.0	3.75	120

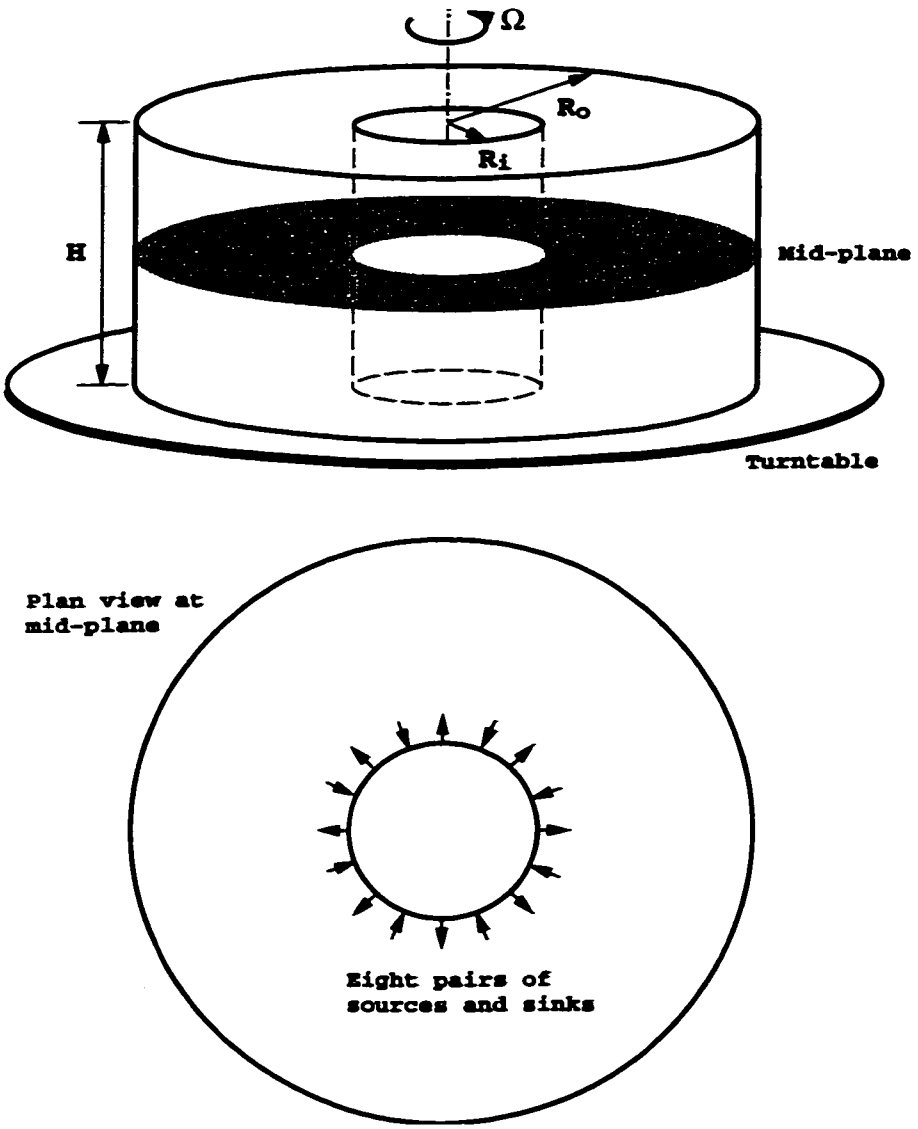

Figure 8.1: A schematic of the experimental apparatus.

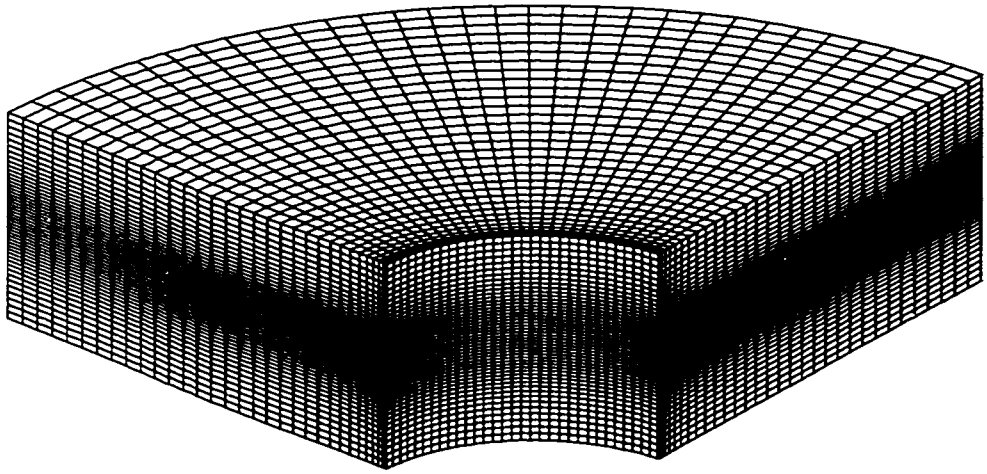

Figure 8.2: An illustration of a section of the computational grid.

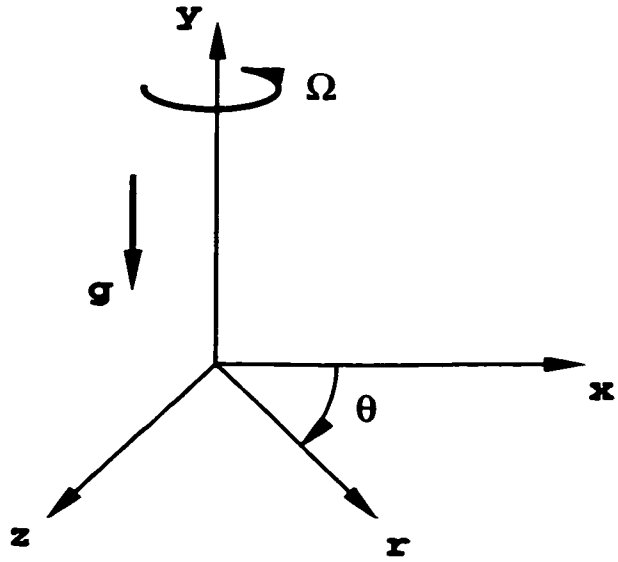

Figure 8.3: Coordinate diagram.

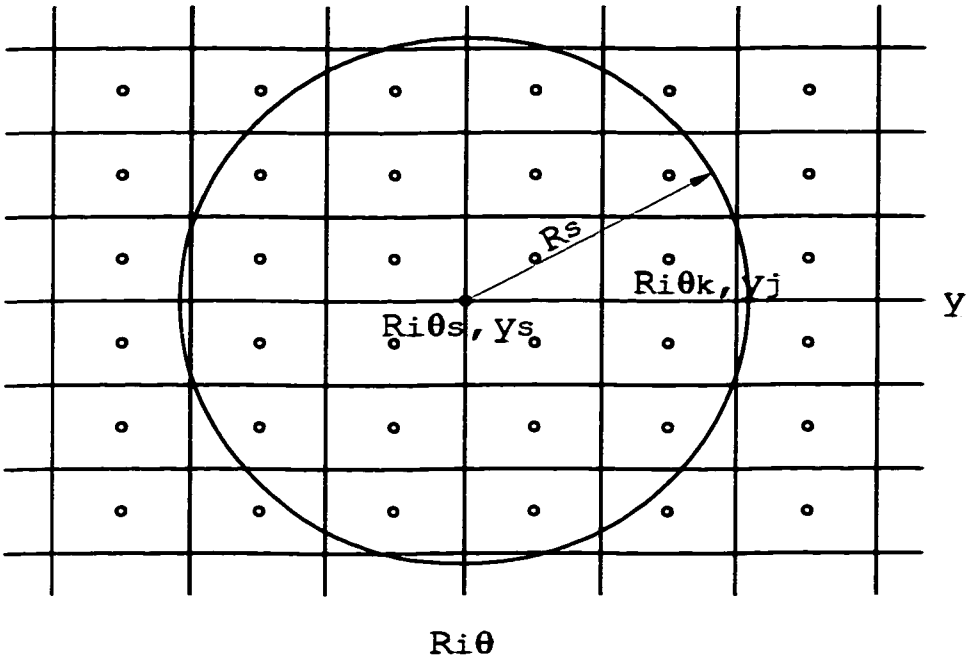

Figure 8.4: An illustration of the coordinates of the orifice and the computational cells on the wall.

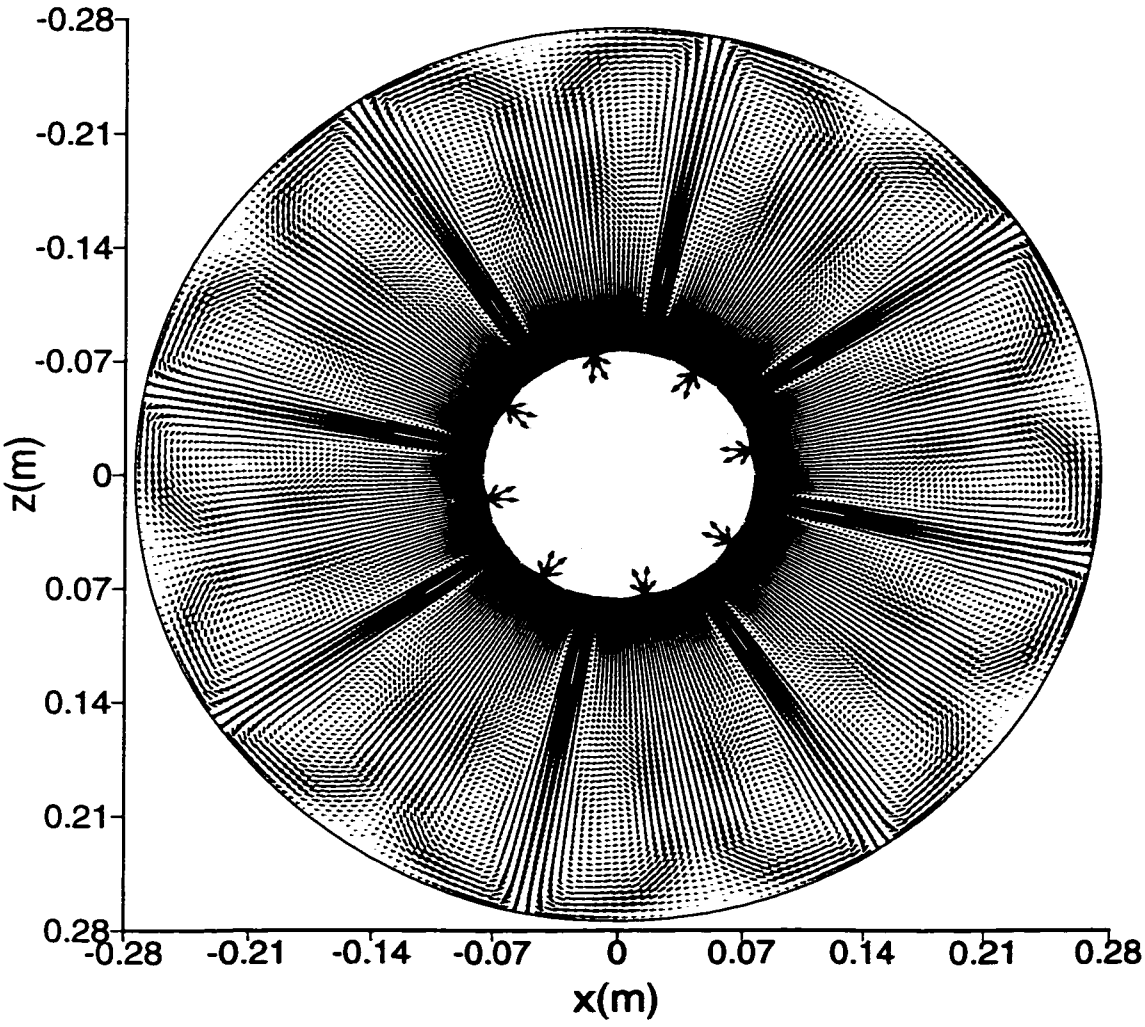

Figure 8.5: Top view of the velocity field for Ω=0 at y/H=0.5 and t=150s (Case Run1).

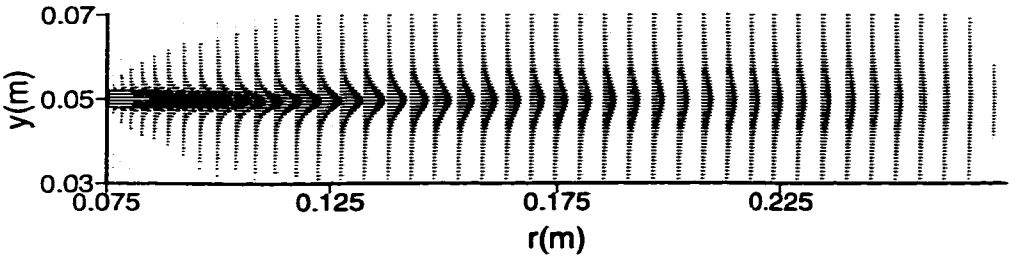

(a) side view on the centerline of the source

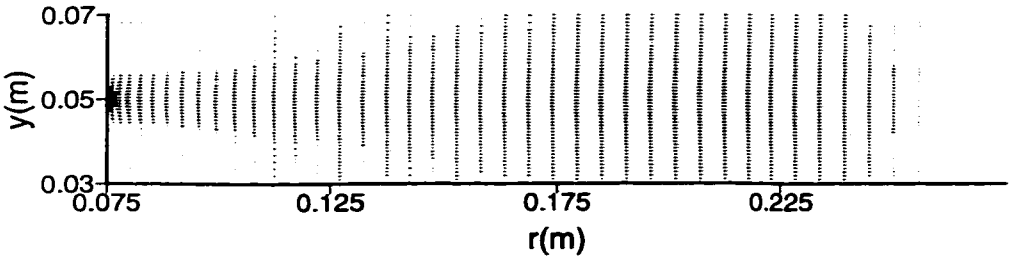

(b) side view on the centerline of the sink

Figure 8.6: Expanded side view of the velocity field for $\Omega = 0$ at t=150s (Case Run1).

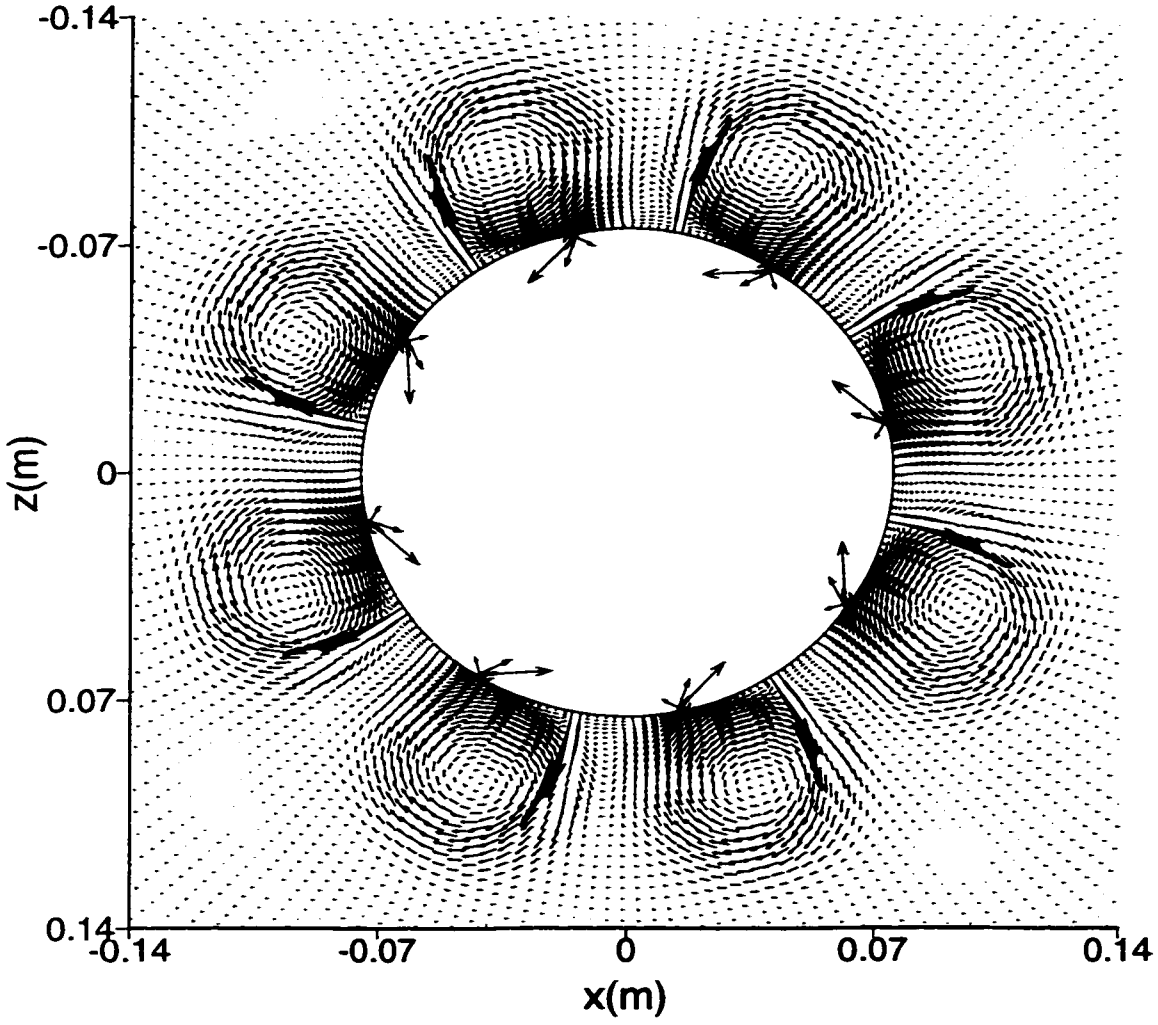

Figure 8.7: Expanded top view of the central section of the velocity field for $\Omega = 0.5$rad/s at y/H=0.5 and t=60s (Case Run2).

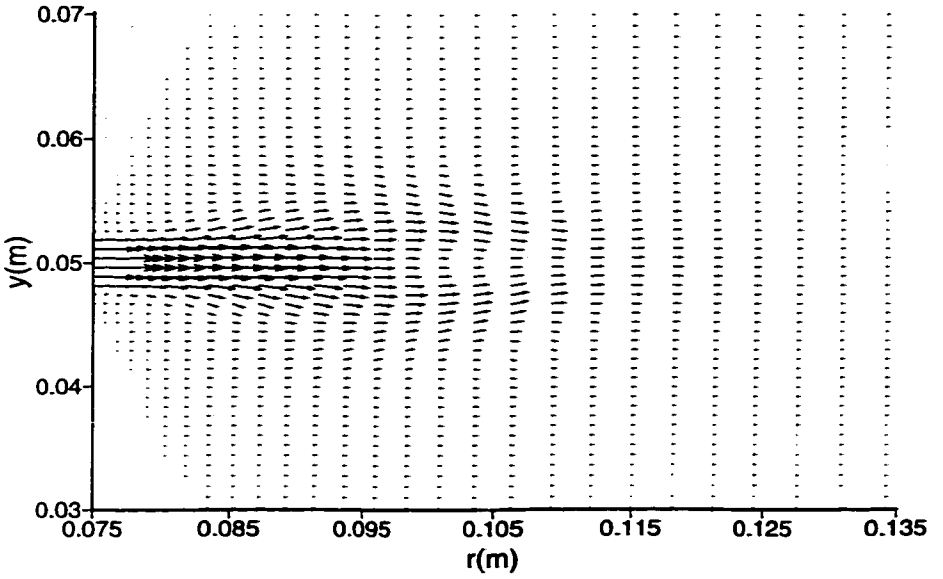

(a) side view on the centerline of the source

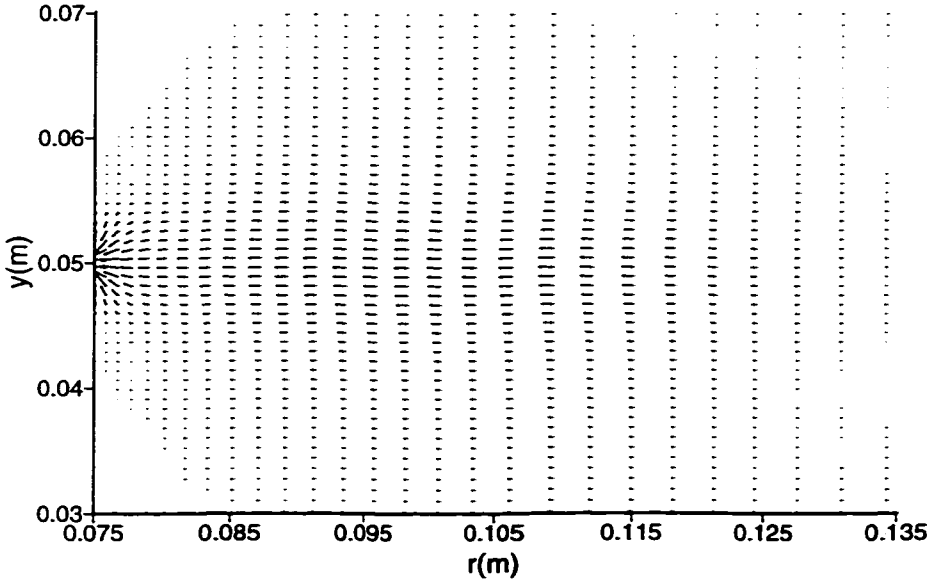

(b) side view on the centerline of the sink

Figure 8.8: Expanded side view of the velocity field for Ω = 0.5rad/s at t=60s (Case Run2).

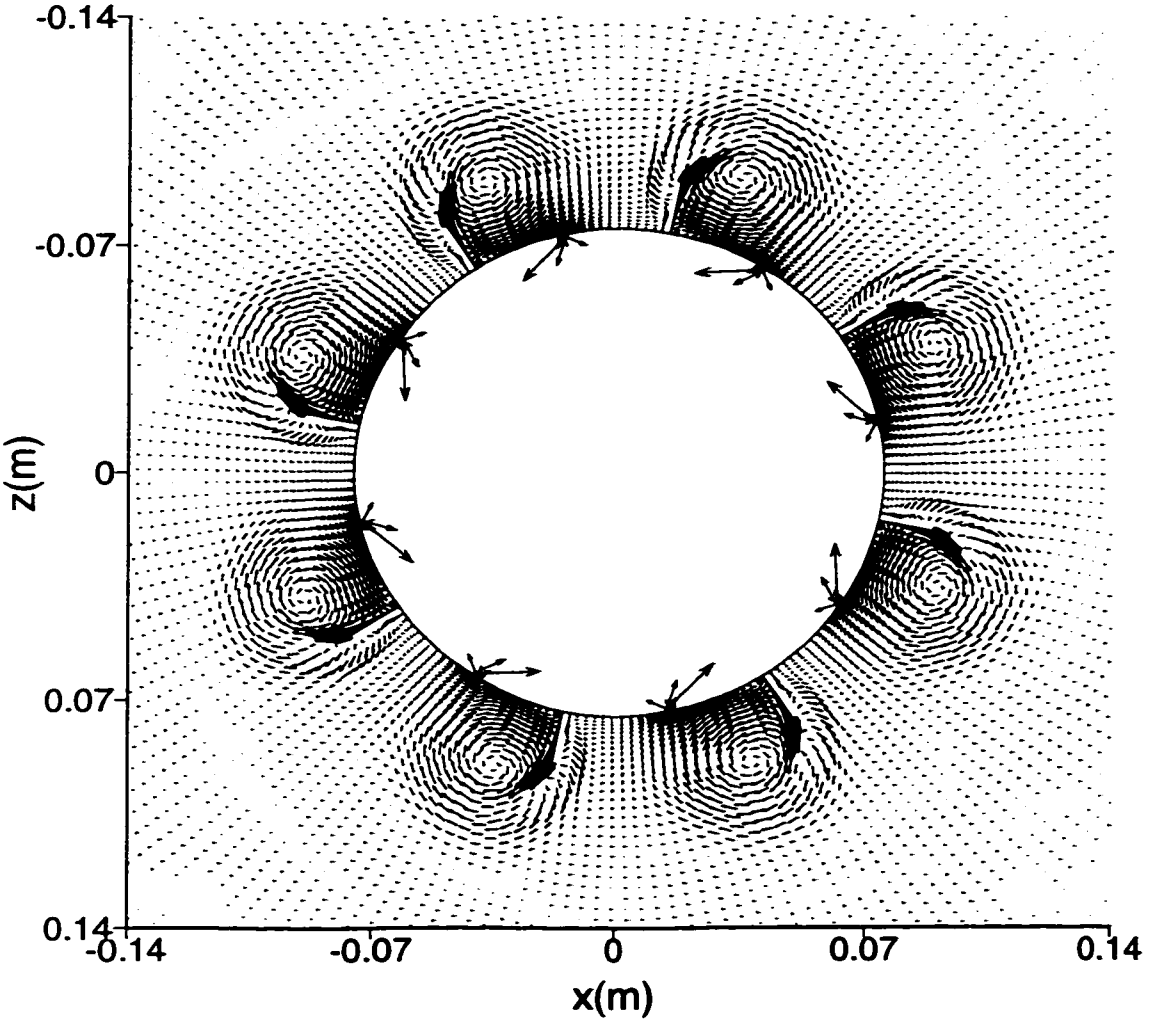

Figure 8.9: Expanded top view of the central section of the velocity field for $\Omega = 1.0$rad/s at y/H=0.5 and t=60s (Case Run3).

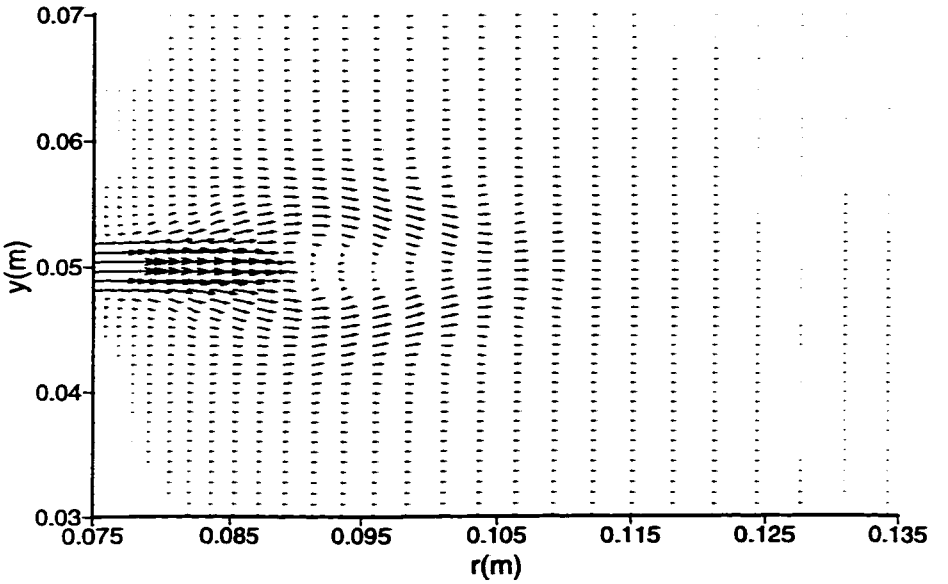

(a) side view on the centerline of the source

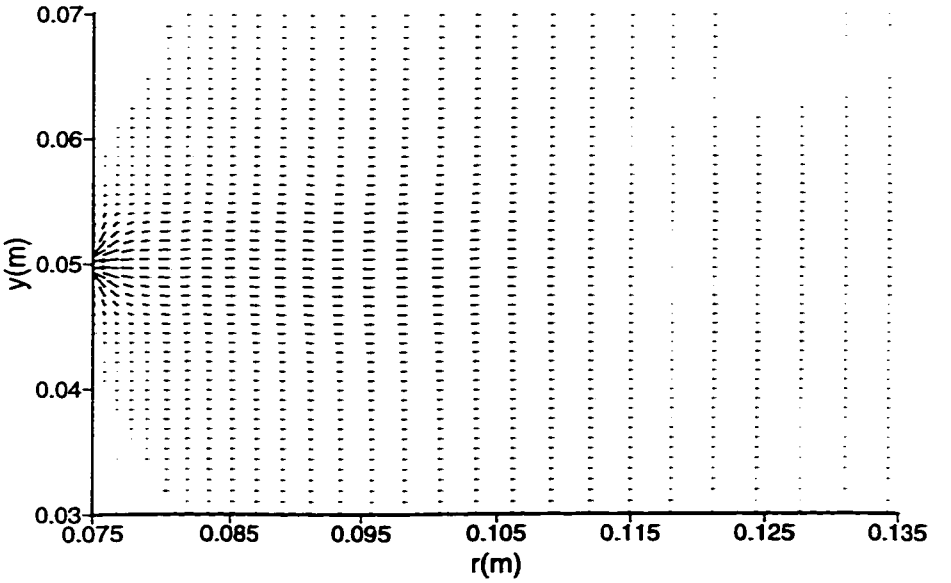

(b) side view on the centerline of the sink

Figure 8.10: Expanded side view of the velocity field for Ω = 1.0rad/s at t=60s (Case Run3).

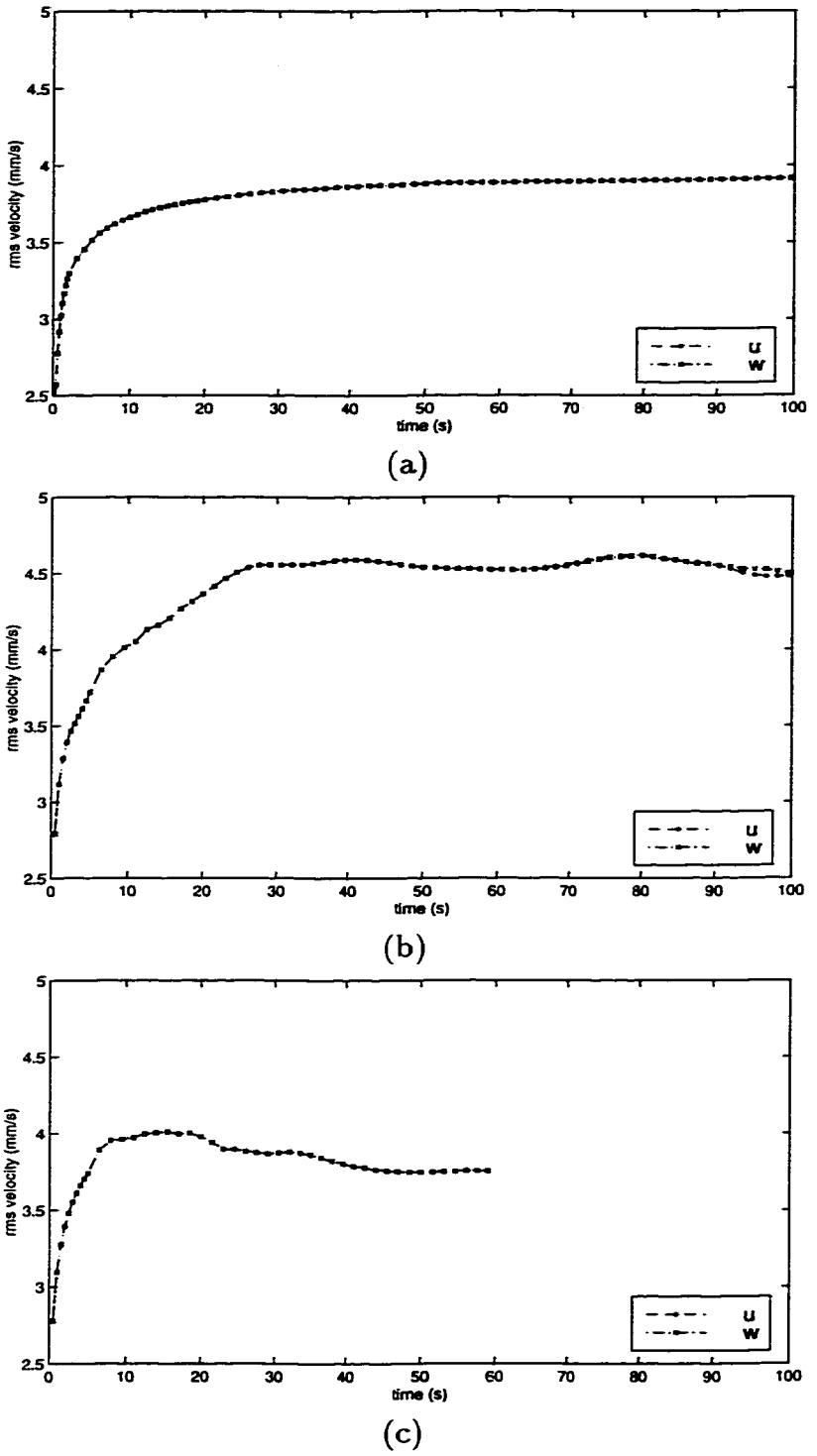

Figure 8.11: Root-mean-square horizontal velocities plotted against time for (a) $\Omega = 0$ (Case Run1), (b) $\Omega = 0.5$rad/s (Case Run2) and (c) $\Omega = 1.0$rad/s (Case Run3).

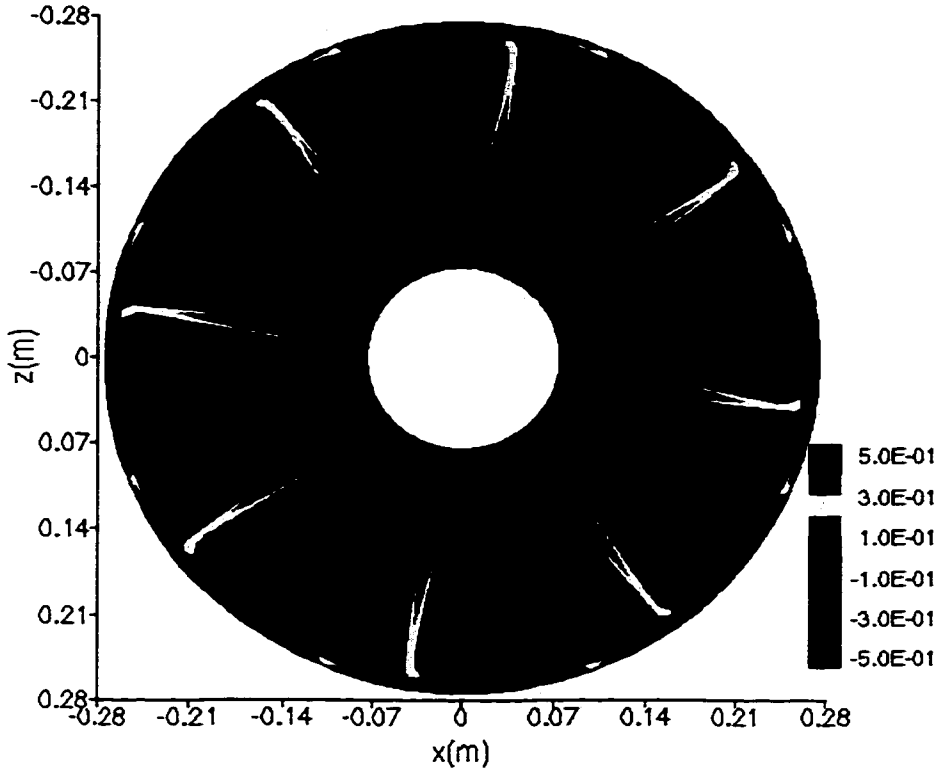

(a) top view

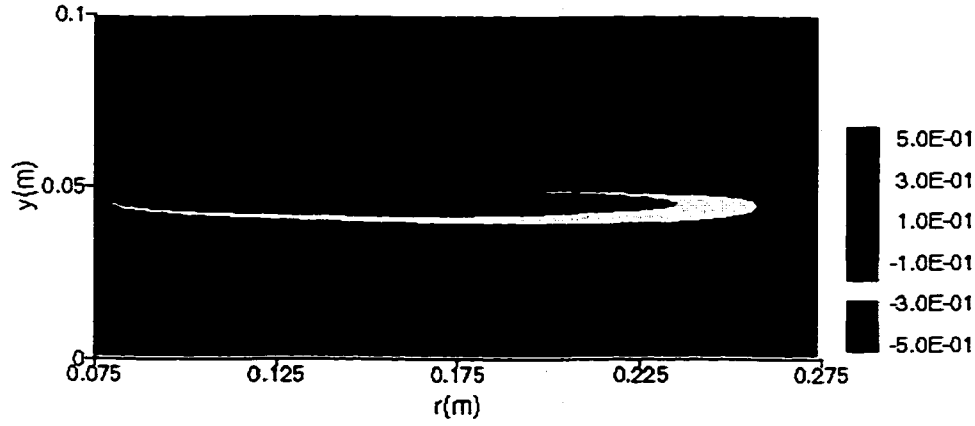

(b) side view on the centerline of the source

Figure 8.12: (a) vertical vorticity field and (b) azimuthal vorticity field for $\Omega = 0$ at y/H=0.5 and t=150s (Case Run1).

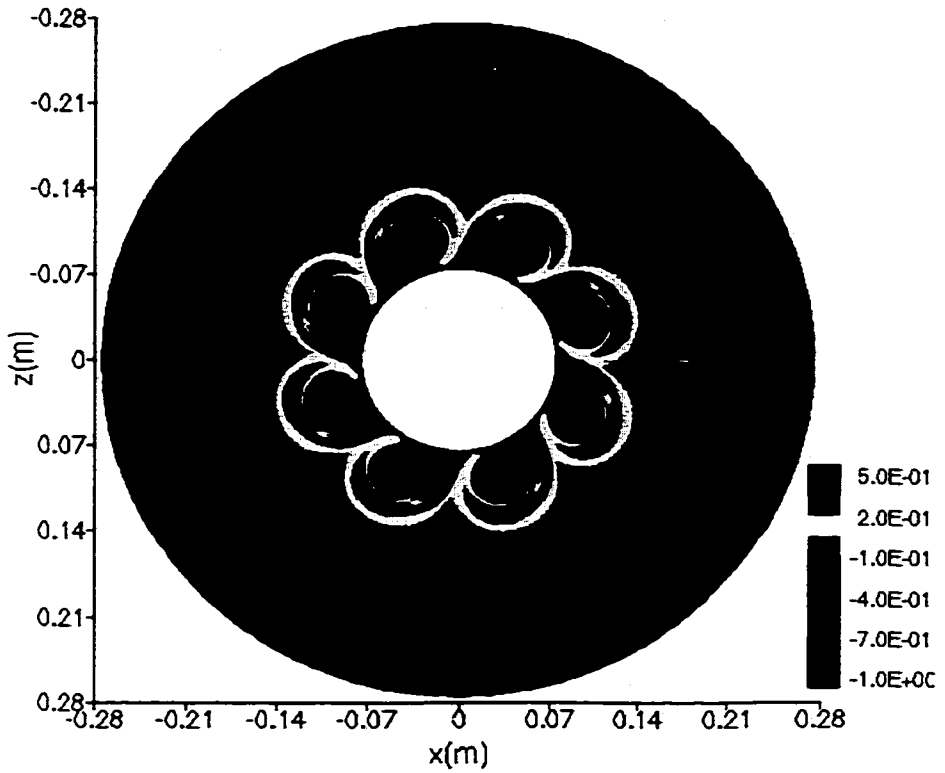

(a) top view

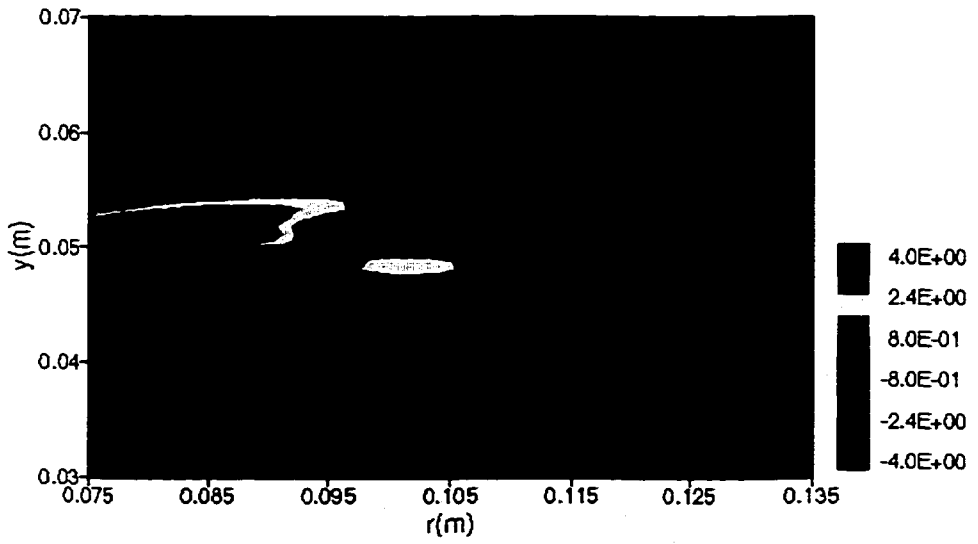

(b) expanded side view on the centerline of the source

Figure 8.13: (a) vertical vorticity field and (b) azimuthal vorticity field for $\Omega = 0.5$rad/s at y/H=0.5 and t=60s (Case Run2).

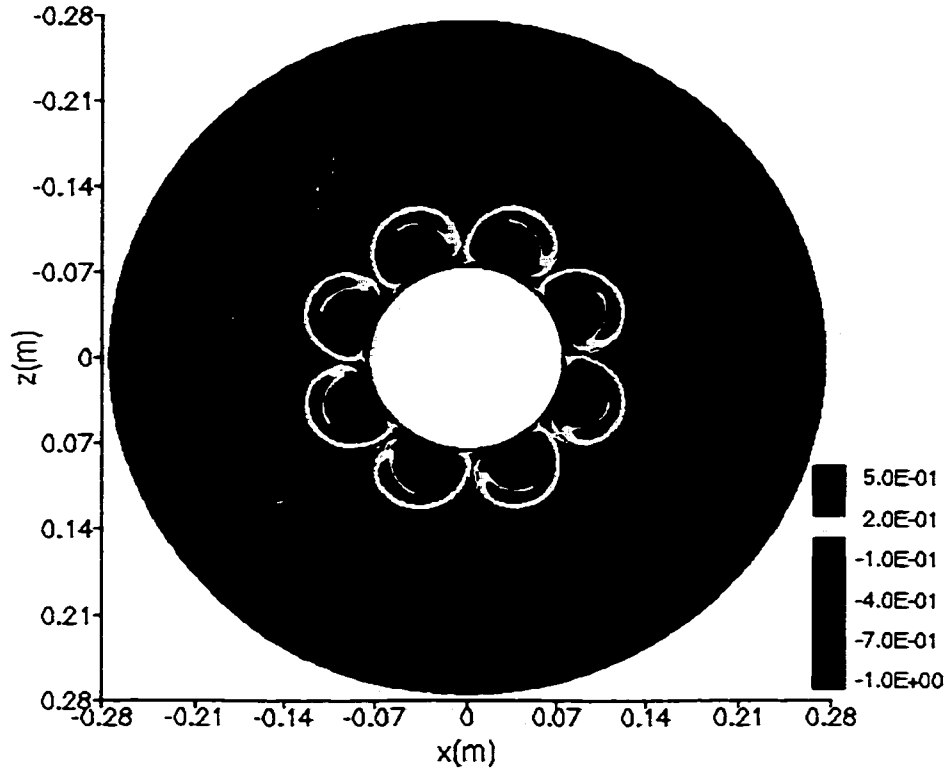

(a) top view

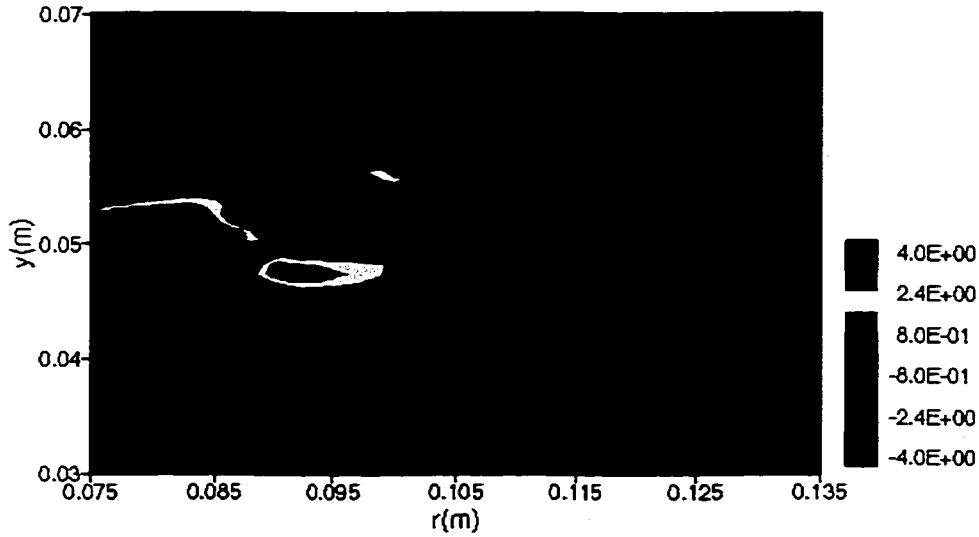

(b) expanded side view on the centerline of the source

Figure 8.14: (a) vertical vorticity field and (b) azimuthal vorticity field for $\Omega = 1.0$rad/s at y/H=0.5 and t=60s (Case Run3).

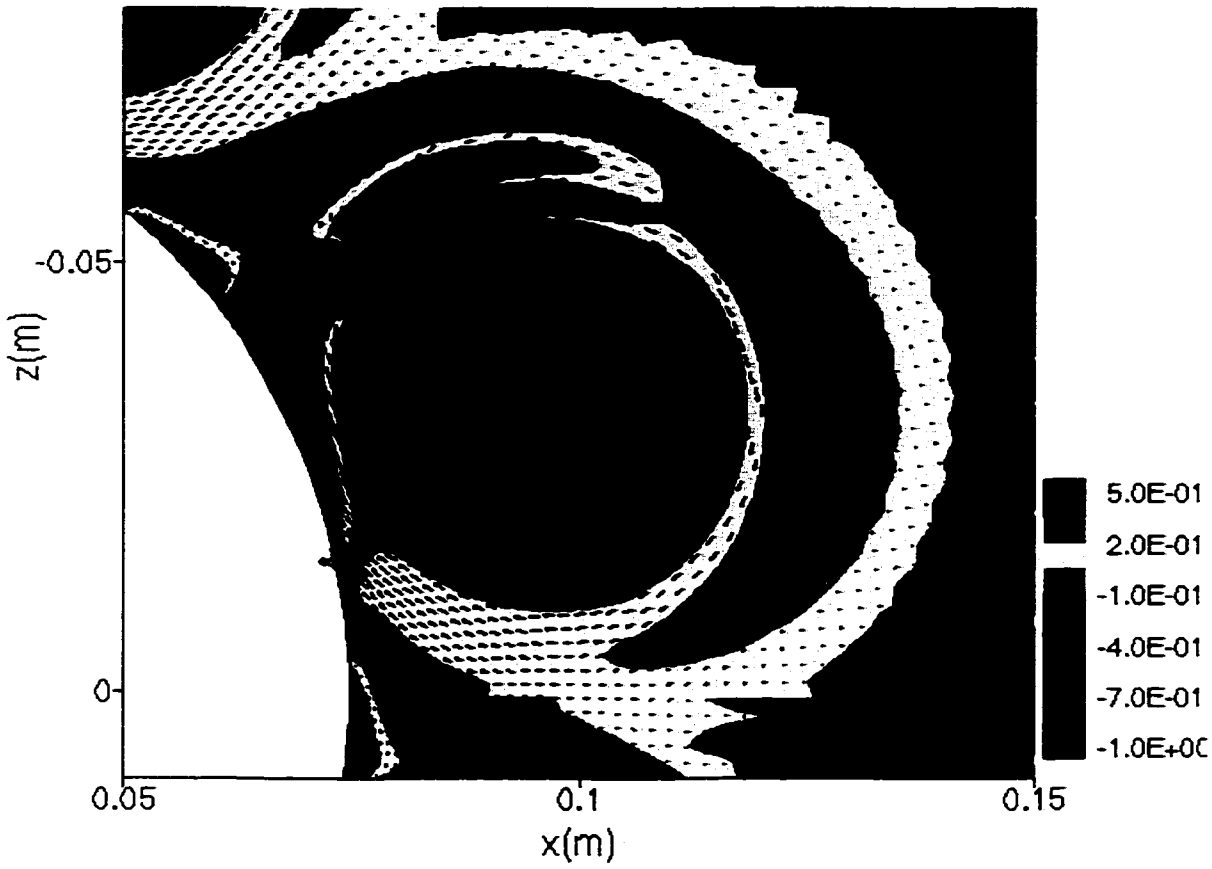

Figure 8.15: Expanded top view of the velocity and the vertical vorticity fields for Ω = 0.5rad/s at y/H=0.5 and t=60s (Case Run2).

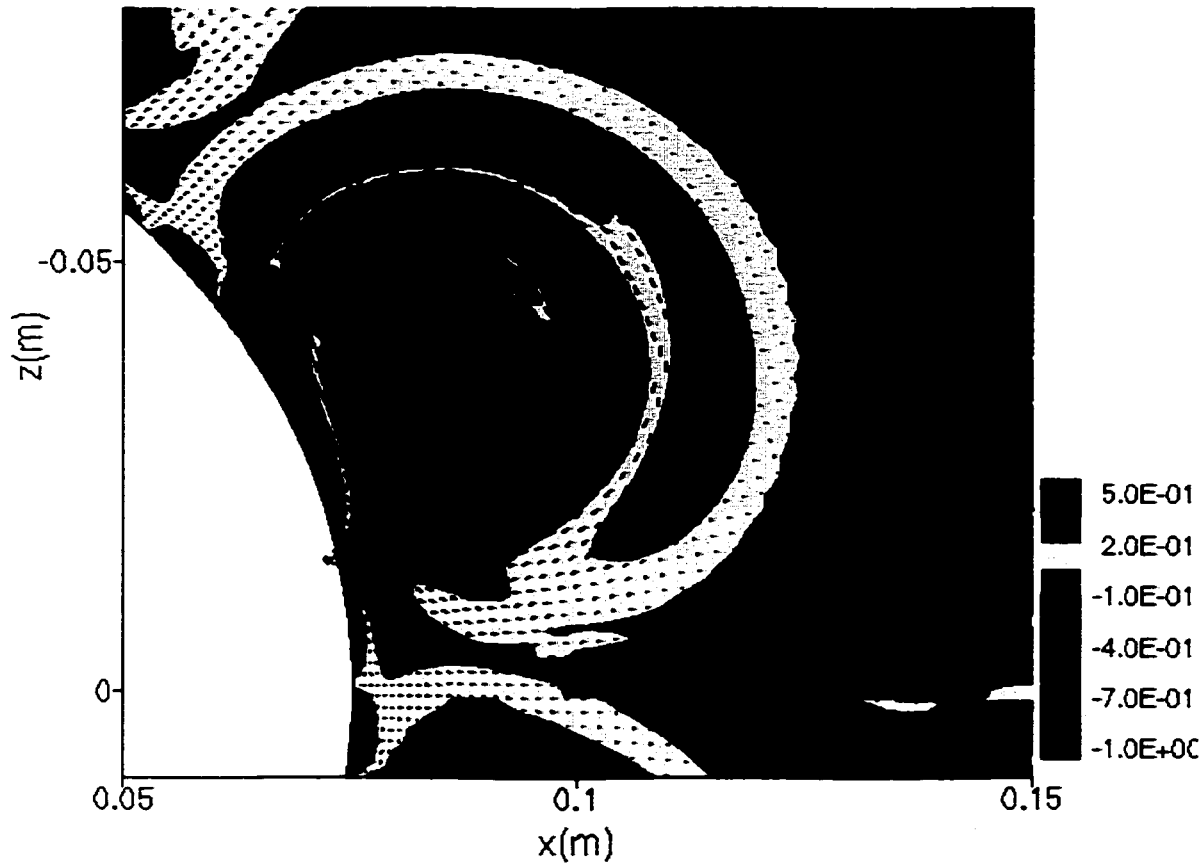

Figure 8.16: Expanded top view of the velocity and the vertical vorticity fields for Ω = 1.0rad/s at y/H=0.5 and t=60s (Case Run3).

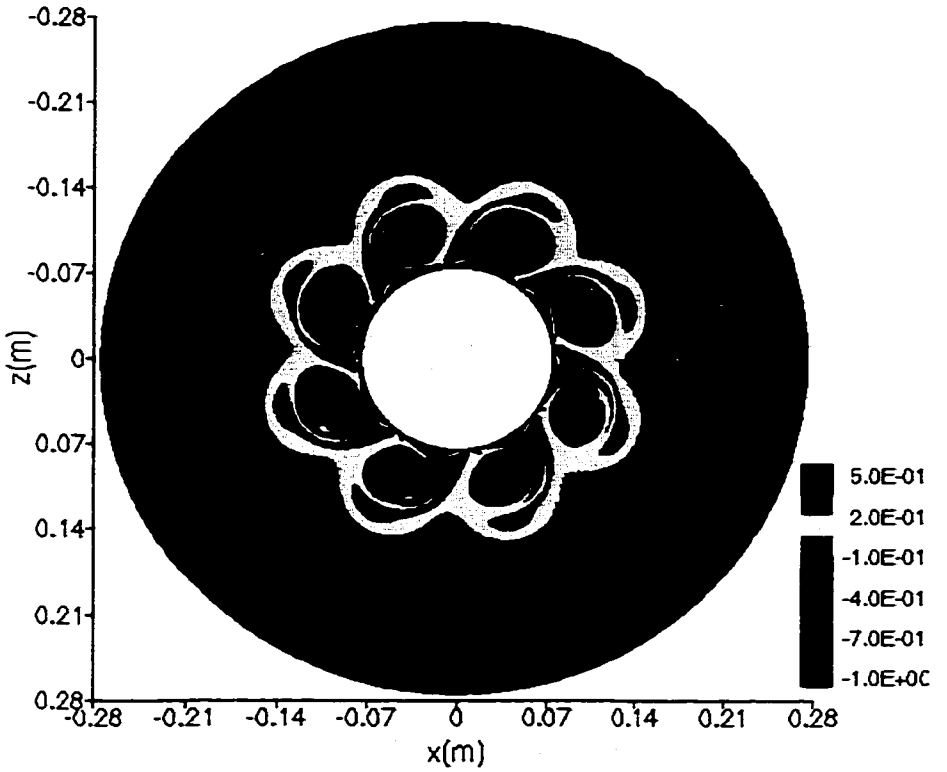

(a) expanded top view

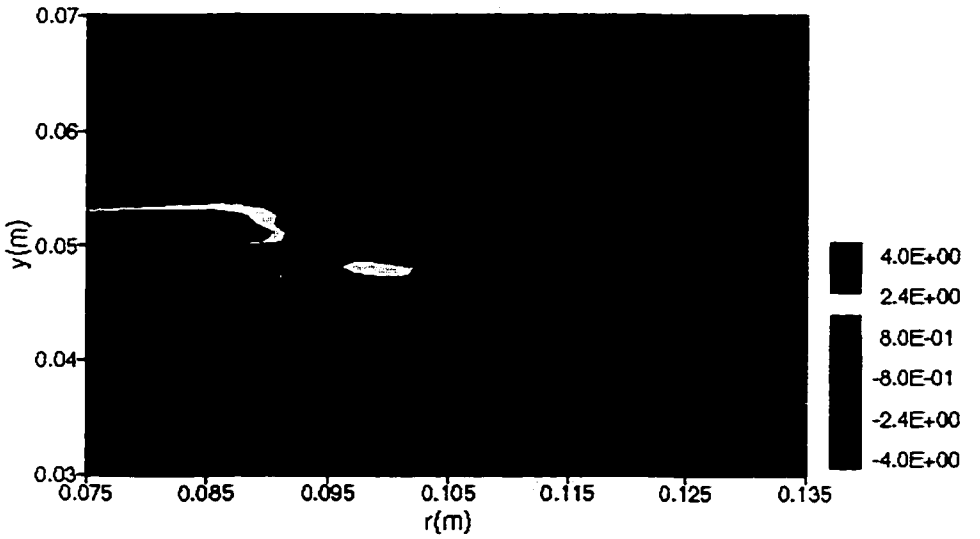

(b) expanded side view on the centerline of the source

Figure 8.17: (a) vertical vorticity field and (b) azimuthal vorticity field for $\Omega = 0.5$rad/s at y/H=0.5 and t=100s (Case Run2).

Chapter 9

Conclusions and Recommendations

The objectives of this study were (1) to implement a high-performance numerical code for three-dimensional, unsteady, incompressible flow governed by the Navier-Stokes equations and (2) to carry out large-eddy simulations of several laboratory-scale realizations of geophysical flows in complex geometries. The code was implemented on a distributed memory massively parallel computer, *viz.*, the IBM SP2.

9.1 Conclusions

Parallel Code

A simulation code for the three-dimensional, unsteady, turbulent, variable density, and rotation-influenced motions of an incompressible fluid was developed on the IBM SP2 using the message passing interface (MPI). Three different dynamic subgrid-scale turbulence models were implemented in the code. The use of MPI enables good portability of the code among a broad class of parallel computers. The present code, which was originally developed on the IBM SP2, was directly ported to the SGI Origin2000 without making any changes to the code. The code was optimized and a code performance of 38 MFlops per node on a 28-node job was achieved, which was the reported peak rate on NASA's IBM SP2 (Bergeron 1998). The code is being used by NASA for benchmark testing.

Turbulent Rotating Convective Flows

Large-eddy simulations were carried out under the same conditions as the experiments of Jacobs and Ivey (1988) to simulate laboratory-scale turbulent rotating

convective flows. An extensive grid resolution study was conducted and led to the use of up to twelve million grid points in the simulation. The simulation results provided a step-by-step precise description of the development of a turbulent rotating convective flow. The simulation results also were in reasonable agreement with the experimental data of Jacobs and Ivey (1998). With the fine-grid resolution results, the Rayleigh-Bénard instability in the form of circular concentric convective rolls was recognized in the initiation process of the convection, which was not observed in Jacobs and Ivey's experiment due to the visualization technique used. New insights were gained into the evolution process of the convection and baroclinic wave formation through the use of the detailed three-dimensional simulation results.

Coastal Upwelling Flows

Large-eddy simulations of the motions in an annular tank of rotating, stratified fluid were carried out using the actual viscosity of the working fluid to simulate the upwelling experiments conducted by Narimousa and Maxworthy (1985 and 1987) and the on-going experiments at the Environmental Fluid Mechanics Laboratory at Stanford University. To our knowledge, this is the first large-eddy simulation of upwelling flows to solve the full set of Navier-Stokes using the actual fluid viscosity and achieving the resolution obtained here, with up to ten million grid points. Different approaches to make an assessment of an important quantity, namely, the disk friction velocity u_*, in the upwelling flow are discussed. While it is possible in an accurate and well-resolved simulation to determine u_* quite precisely, it is often virtually impossible to get a quantitative estimation of u_* in a physical experiment. The simulation results of this study are compared to experimentally measured data and good agreement is achieved. Baroclinic waves, meanders and pinched-off eddies near the upwelled-surface front in the form of jets and cyclone/anticyclone pairs, as reported by Narimousa and Maxworthy (1987), were observed in the simulation results.

Data Assimilation

A data assimilation algorithm, *i.e.*, the nudging method, has been incorporated

into the code. Hindcast data assimilation was successfully performed for the laboratory-scale coastal upwelling flow. A reduced resolution simulation was nudged by data from a very accurate simulation to demonstrate that the concept is applicable to laboratory-scale flows with appropriate selection of parameters.

Rotating Stratified Flows

Numerical simulations of flows induced by source-sink pairs in a rotating stratified fluid were performed under the same conditions as those in the on-going experiment of Hacker and Linden. Simulations of three different rotation rates at low values of the source-sink forcing parameter, *i.e.,* the internal Froude number of the source, are carried out and the effects of the rotation rate were evaluated. It is found that the size of the formed vortices decreases, while the expansion rate of the jet increases with increasing rotation rate. The insight drawn from the numerical experiments in this study are being used in the experimental design and planning.

9.2 Recommendations for Future Study

The present study has led to improved understanding of three interesting, but rather different geophysical flows, namely, turbulent rotating convective flow, coastal upwelling flow and source-sink induced flow in a rotating stratified fluid. Based on the insight gained in this study, some recommendations for future study are given below:

- Since baroclinic instability and other instabilities are identified in all the three rotating, stratified flows, a formal stability analysis, which should include the effects of rotation, stratification, three-dimensional shear and possibly viscosity, is needed.

- Turbulence remains the grand challenge problem in fluid mechanics. The key to the success of large-eddy simulations is to accurately represent subgrid-scale stress term. The concept of the dynamic model is very promising in achieving

this goal. However, for geophysical flows, more physics, such as the effect of rotating and stratification, may need to be incorporated into the subgrid-scale model.

- In the rotating convective flow, the density anomaly is thought to depend on the ratio R/H of the radius of the heated disk to the distance between the tank bottom and the shelf. However, it is difficult to create an aspect ratio R/H larger than 5-8 in the existing rotating convective flow laboratory setup. Thus, it would be desirable to explore the case for R/H $>$ 10 numerically and to determine the dependence of the density anomaly on the ratio R/H. The effect of changing the bottom slope on the size of the baroclinic eddies could also be investigated by numerical simulations.

- In order to study upwelling flow that is close to the real flow condition, the effects of bottom topography and coastline perturbation need to be examined.

- Hindcast data assimilation performed in this study has demonstrated that the concept is applicable to laboratory-scale flows. After the experimental data become available in either the EFML or the Hacker and Linden studies, forecast data assimilation should be performed.

- In source-sink induced flow in a rotating stratified fluid, further numerical investigation of flows with higher values of the forcing parameter is needed in the future to study the three-dimensional turbulence generated by strong forcing and the relevant vertical mixing processes.

Appendix A

SGS Dissipation for Coastal Upwelling Cases

In this appendix, we display the ratios of the SGS "dissipation" to viscous dissipation for the two upwelling cases studied in Chapter 6 to develop a visual and qualitative picture of what is happening. The resolved kinetic energy is defined as

$$\frac{\overline{q}^2}{2} = \frac{\overline{u}_i \overline{u}_i}{2}. \tag{A.1}$$

The transport equation for $\overline{q}^2/2$ can be derived by multiplying the momentum equation [Eqn. (2.41)] by $\overline{u}_i$. Thus, we have

$$\begin{aligned} \frac{\partial}{\partial t}\left(\frac{1}{2}\overline{q}^2\right) + \frac{\partial}{\partial x_j}\left(\overline{u}_j \frac{\overline{q}^2}{2}\right) &= -\frac{\partial}{\partial x_j}\left[\overline{p}\,\overline{u}_j - \overline{u}_i \tau_{ij} - \nu \frac{\partial}{\partial x_j}\left(\frac{\overline{q}^2}{2}\right)\right] - g(\overline{\rho}_* - \rho_b)\overline{u}_2 \\ &\quad - \nu \frac{\partial \overline{u}_i}{\partial x_j}\frac{\partial \overline{u}_i}{\partial x_j} + \tau_{ij}\overline{S}_{ij}, \end{aligned} \tag{A.2}$$

where $\overline{S}_{ij}$ is the resolved strain-rate tensor. The last two terms on the right hand side of Eqn. (A.2) represent the viscous dissipation (ϵ_v) and SGS dissipation (ϵ_{sgs}) terms (see Section 5.4.7). When ϵ_{sgs} is negative, energy is transferred from the resolved scales to the sub-grid scales, this is denoted as "forward scatter". On the contrary, when ϵ_{sgs} is positive, energy is fed into the resolved scales from the sub-grid scales, which is called "backscatter".

The ratios of SGS to viscous dissipation at $t = 220$s (t/t_s=1) for Case NM1 and at $t = 250$s (t/t_s=1) for Case EFML1 are shown in Figures A.1 and A.2. The two figures

show the two flows at equivalent real times because the non-dimensional time $t/t_s = 1$ in both figures. The reference time scale t_s is defined in Chapter 6 and its value for each case is given in Table 6.2. The flow patterns are complex and, hence, the ratios of SGS to viscous dissipation are also. While we do not attempt to interpret these plots quantitatively, one can observe that (i) sizeable areas of backscatter (positive ratio) at these instants in both flow configurations and (ii) considerable difference between the two flows at equivalent real time t/t_s=1. It appears that the SGS model is playing a useful, but not large role here; and that is as it should be.

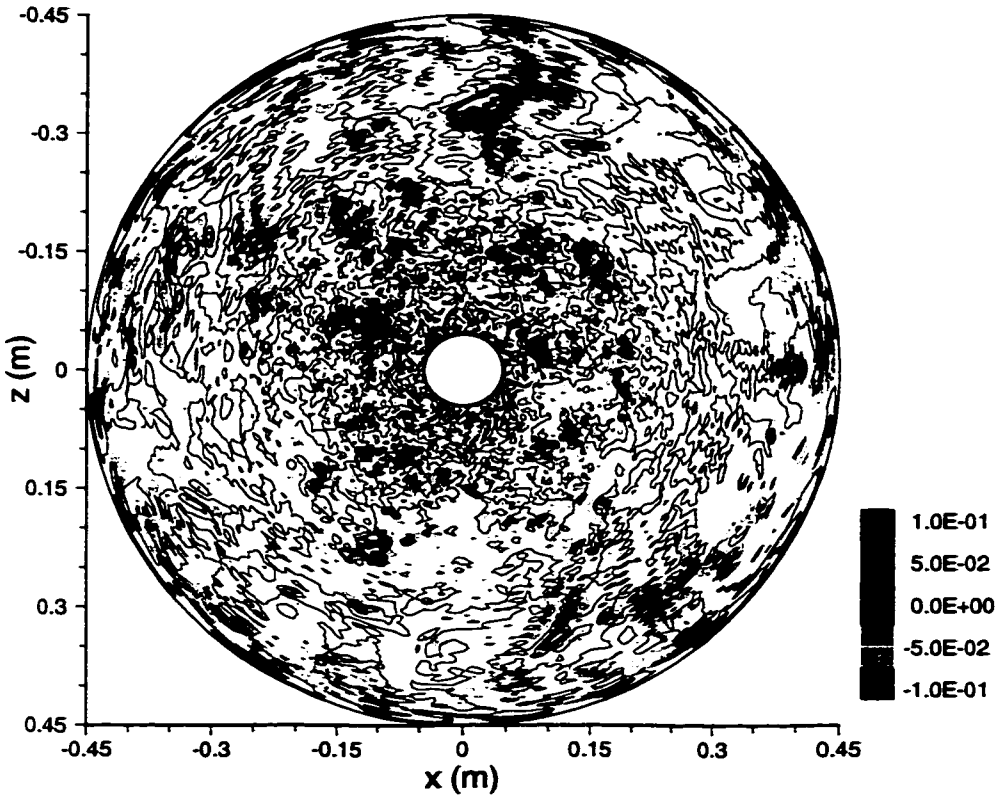

(a) top view at y/H=0.9

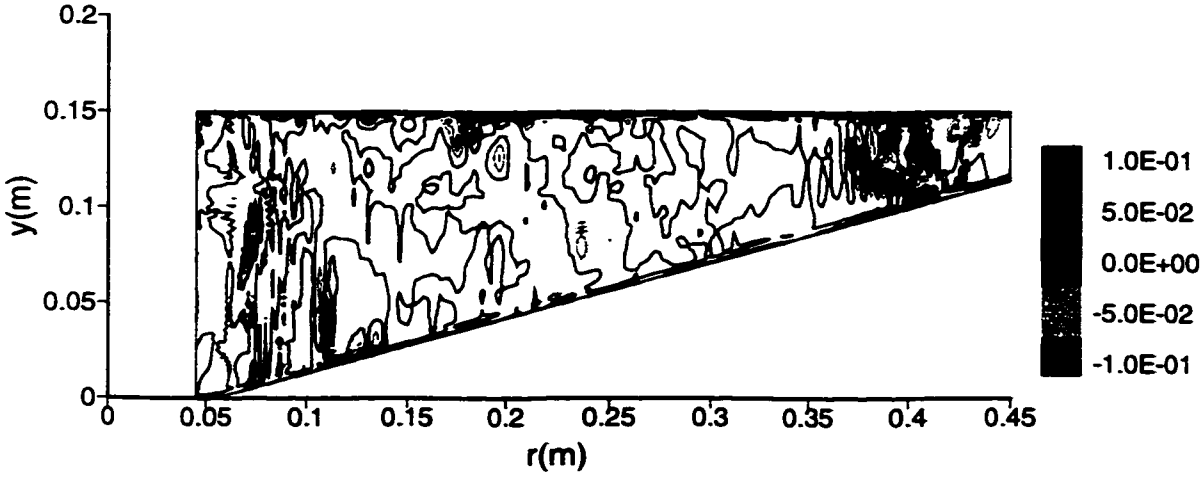

(a) side View

Figure A.1: The ratio of SGS to viscous dissipation at t/t_s=1 (Case NM1).

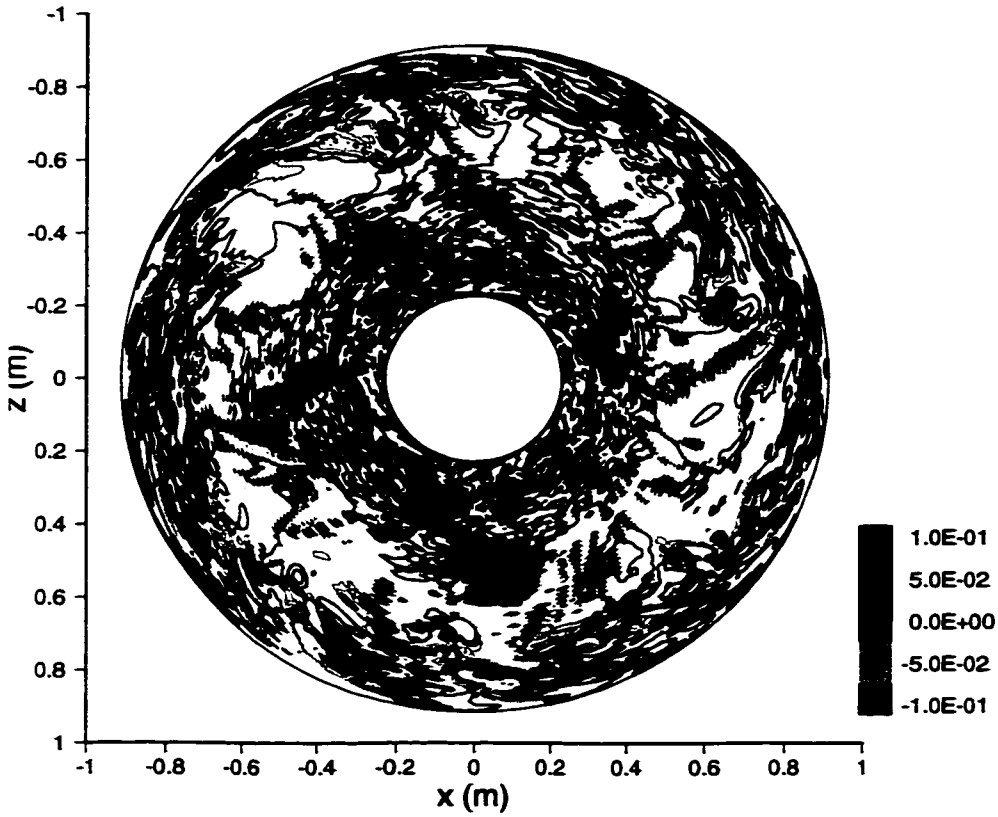

(a) top view at y/H=0.95

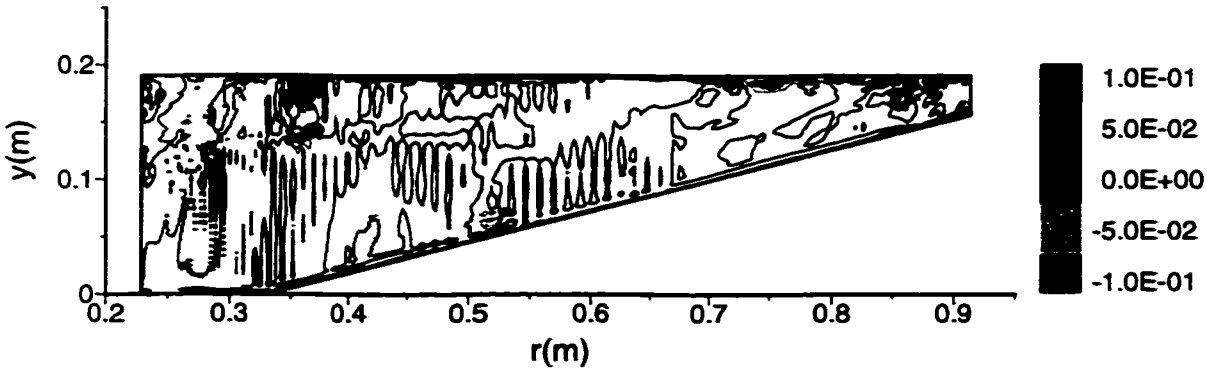

(a) side View

Figure A.2: The ratio of SGS to viscous dissipation at t/t_s=1 (Case EFML1).

Bibliography

[1] R.A. Anthes. Data assimilation and initialization of hurricane prediction models. *Journal of the Atmospheric sciences*, 31: 702–719, 1974.

[2] J. Bardina, J.H. Ferziger, and W.C. Reynolds. Improved turbulence models based on large eddy simulation of homogeneous, incompressible, turbulent flows. Technical Report TF-19, Thermoscience Division, Department of Mechanical Engineering, Stanford University, 1983.

[3] R.M. Beam and R.F. Warming. An implicit finite-difference algorithm for hyperbolic systems in conservation-law form. *Journal of Computational Physics*, 22: 87–110, 1976.

[4] R. Bergeron. Measurement of a scientific workload using the IBM hardware performance monitor. In *Proceedings of the Supercomputing'98 Conference*, Orlando, Florida, 1998.

[5] B.M. Boubnov, S.B. Dalziel, and P.F. Linden. Source-sink turbulence in a stratified fluid. *Journal of Fluid Mechanics*, 261: 273–303, 1994.

[6] B.M. Boubnov and G.S. Golitsyn. Experimental study of convective structures in rotating fluids. *Journal of Fluid Mechanics*, 167: 503–531, 1986.

[7] B.M. Boubnov and G.S. Golitsyn. Temperature and velocity field regimes of convective motions in a rotating plane fluid layer. *Journal of Fluid Mechanics*, 219: 215–239, 1990.

[8] A. Brandt. Multi-level adaptive solutions to boundary-value problems. *Mathematics of Computation*, 31(138): 333–390, 1975.

[9] A. Brandt. *Multigrid Solvers on Parallel Computers.* Academic Press, New York, 1981.

[10] D. Brickman. Heat flux partitioning in open-ocean convection. *Journal of Physical Oceanography*, 25: 2609–2623, 1995.

[11] F.H. Buse and K.E. Heikes. Convection in a rotating layer: A simple case of turbulence. *Science*, 208: 173–175, 1980.

[12] W. Cabot. Large-eddy simulation of passive and buoyant scalars with dynamic subgrid-scale models. Annual research brief, Center for Turbulence Research, Stanford University/NASA-Ames, 1991.

[13] D.R. Caldwell, C.W. Van Atta, and K.N. Helland. A laboratory study of the turbulent Ekman layer. *Geophysical Fluid dynamics*, 3: 125–160, 1972.

[14] S. Chandrasekhar. *Hydrodynamic and Hydromagnetic Stability.* Dover, Clarendon, 1961.

[15] D.C. Chapman and G. Gawarkiewicz. Shallow convection and buoyancy equilibration in an idealized coastal polynya. *Journal of Physical Oceanography*, 27(4): 555–566, 1997.

[16] F.R. Chia, R.W. Griffiths, and P.F. Linden. Laboratory experiments on fronts. Part II. The formation of cyclonic eddies at upwelling fronts. *Geophysical and Astrophysical Fluid Dynamics*, 19: 189–206, 1982.

[17] A.J. Chorin. A numerical method for solving incompressible viscous flow problems. *Journal of Computational Physics*, 2: 12–26, 1967.

[18] M. Coates and G.N. Ivey. Instability of a convectively driven mixed layer in a rotating fluid. In *The 5th Australia Heat Mass Transfer Conference*, Sydney, Australia, 1993.

[19] M. Coates and G.N. Ivey. On convective turbulence and the influence of rotation. *Dynamics of Atmospheres and Oceans*, 25: 217–232, 1997.

[20] M. Coates, G.N. Ivey, and J.R. Taylor. Unsteady, turbulent convection into a rotating, linearly stratified fluid: Modeling deep ocean convection. *Journal of Physical Oceanography*, 25: 3032–3050, 1995.

[21] Thinking Machine Corporation. *CM Fortran Programming Guide.* Cambridge, Massachusetts, 1991.

[22] D.G. Dritschel. Vortex properties of two-dimensional turbulence. *Physics of Fluids A*, 5(4): 984–997, 1993.

[23] H.J.S. Fernando, D.L. Boyer, and R.-R. Chen. Turbulent thermal convection in rotating stratified fluids. *Dynamics of Atmospheres and Oceans*, 13: 95–121, 1989.

[24] H.J.S. Fernando, R.-R. Chen, and D.L. Boyer. Effects of rotation on convective turbulence. *Journal of Fluid Mechanics*, 228: 513–547, 1991.

[25] G. Gawarkiewicz and D.C. Chapman. A numerical study of dense water formation and transport on a shallow, sloping continental shelf. *Journal of Geophysical Research*, 100(C3): 4489–4507, 1995.

[26] M. Germano. A proposal for a redefinition of the turbulent stresses in the filtered Navier-Stokes equations. *Physics of Fluids*, 29: 2323–2324, 1986.

[27] M. Germano, U. Piomelli, P. Moin, and W.H. Cabot. A dynamic subgrid-scale eddy viscosity model. *Physics of Fluids A*, 238: 1760–1765, 1991.

[28] M. Ghil and P. Malanotte-Rizzoli. Data assimilation in meteorology and oceanography. *Advances in Geophysics*, 33: 141–266, 1991.

[29] G.S. Golitsyn. Structure of convection at fast rotation. *Doklady Akademii Nauk SSSR*, 261: 317–320, 1981.

[30] H.P. Greenspan. *The Theory of Rotating Fluids.* Cambridge University Press, London, 1968.

[31] R.W. Griffiths and P.F. Linden. The stability of buoyancy driven coastal currents. *Dynamics of Atmospheres and Oceans*, 5: 281–306, 1981.

[32] R.W. Griffiths and P.F. Linden. Laboratory experiments on fronts. Part I. Density driven boundary currents. *Geophysical and Astrophysical Fluid Dynamics*, 19: 159–187, 1982.

[33] W. Gropp, E. Lusk, and A. Skjellum. *Using MPI: Portable Parallel Programming with the Message-Passing Interface.* The MIT Press, Cambridge, Massachusetts, 1994.

[34] L.A. Hageman and D.M. Young. *Applied Iterative Methods.* Wiley, New York, 1981.

[35] K. Haines, P. Malanotte-Rizzoli, R.E. Young, and W.R. Holland. A comparison of two methods for the assimilation of a altimeter data into a shallow-water model. *Dynamics of Atmospheres and Oceans*, 17: 89–133, 1993.

[36] D.H. Hathaway and R.C.J. Somerville. Three-dimensional simulations of convection in layers with tilted rotation vectors. *Journal of Fluid Mechanics*, 126: 75–89, 1983.

[37] R.G. Hindman. Generalized coordinate forms of governing fluid equations and associated geometrically induced errors. *AIAA Journal*, 10: 65–68, 1982.

[38] B.R. Hodges. *Numerical Simulation of Nonlinear Free-Surface Waves on a Turbulent Open-Channel Flow.* PhD thesis, Stanford University, 1997.

[39] J.E. Hoke and R.A. Anthes. The initialization of numerical models by a dynamic initialization technique. *Monthly Weather Review*, 104: 1551–1556, 1976.

[40] W.R. Holland and P. Malanotte-Rizzoli. Assimilation of altimeter data into an ocean circulation model: Space versus time resolution studies. *Journal of Physical Oceanography*, 19: 1507–1534, 1989.

[41] P. Jacobs and G.N. Ivey. The influence of rotation on shelf convection. *Journal of Fluid Mechanics*, 369: 23–48, 1998.

[42] H. Jones and J. Marshall. Convection with rotation in a natural ocean: A study of open-ocean convection. *Journal of Physical Oceanography*, 23: 1009–1039, 1993.

[43] L.H. Kantha, O.M Phillips, and R.S. Azad. On turbulent entrainment at a stable density interface. *Journal of Fluid Mechanics*, 79: 753–768, 1977.

[44] P.D. Killworth, N. Paldor, and M. Stern. Wave propagation and growth on a surface front in a two-layer geostrophic current. *Journal of Marine Research*, 42: 761–785, 1984.

[45] J. Kim and P. Moin. Application of a fractional-step method to incompressible Navier-Stokes equations. *Journal of Computational Physics*, 59: 308–323, 1985.

[46] E.L. Koschmieder. On convection on a uniformly heated plane. *Beiträgo zar Physik Atmosphäre*, 39: 1–11, 1966.

[47] E.L. Koschmieder. *Bénard Cells and Taylor Vortices.* Cambridge University Press, 1993.

[48] J.R. Koseff and R.L. Street. Visualization studies of a shear driven three-dimensional recirculation flow. *Journal of Fluids Engineering*, 106: 21–29, 1984.

[49] P.K. Kundu. *Fluid Mechanics.* Academic Press Inc., 1990.

[50] B. Legras, P. Santangelo, and R. Benzi. High resolution numerical experiments for forced two-dimensional turbulence. *Europhysics Letters*, 5: 37–42, 1988.

[51] B.P. Leonard. A stable and accurate convective modeling procedure based on quadratic upstream interpolation. *Computer Methods in Applied Mechanics and Engineering*, 19: 59–98, 1979.

[52] B.P. Leonard. Third order multi-dimensional Euler/Navier-Stokes solver. *AIAA/ASME/SIAM/APS First National Fluid Dynamics Congress*, pages 226–231, 1988.

[53] D.K. Lilly. A proposed modification of the germano subgrid scale closure method. *Physics of Fluids A*, 4: 633–635, 1992.

[54] P.F. Linden, B.M. Boubnov, and S.B. Dalziel. Source-sink turbulence in a rotating stratified fluid. *Journal of Fluid Mechanics*, 298: 81–112, 1995.

[55] P.F. Linden and G.J.F. van Heijst. Two-layer spin-up and frontogenesis. *Journal of Fluid Mechanics*, 143: 69–94, 1984.

[56] G. Madec, M. Chartier, P. Delecluse, and M. Crepon. A three-dimensional numerical model of deep water formation in the northwestern Mediterranean Sea. *Journal of Physical Oceanography*, 21: 1349–1371, 1991.

[57] P. Malanotte-Rizzoli and R.E. Young. Assimilation of global versus local data sets into a regional model of Gulf Stream system. *Journal of Geophysical Research*, 100(C12): 24773–24796, 1995.

[58] T. Maxworthy and S. Narimousa. Unsteady, turbulent convection into a homogeneous, rotating fluid, with oceanographic applications. *Journal of Physical Oceanography*, 24: 865–887, 1994.

[59] J.C. McWilliams. The emergence of isolated coherent vortices in turbulent flow. *Journal of Fluid Mechanics*, 146: 21–43, 1984.

[60] M. Metcalf. *Fortran 90 Explained.* Clarendon Press, New York, 1991.

[61] P. Moin, K. Squires, W. Cabot, and S. Lee. A dynamic subgrid-scale model for compressible turbulence and scalar transport. *Physics of Fluids A*, 3: 2746–2757, 1991.

[62] C.N.K. Mooers, C.A. Collins, and R.L. Smith. The dynamics structure of the frontal zone in the coastal upwelling region of Oregon. *Journal of Physical Oceanography*, 6: 3–21, 1976.

[63] N.H. Naik, V.K. Naik, and M. Nicoules. Parallelization of a class of implicit finite difference schemes in computational fluid dynamics. *International Journal of High Speed Computing*, 5: 1–50, 1993.

[64] Y. Nakagawa and P. Frenzen. A theoretical and experimental study of cellular convection in rotating fluids. *Tellus*, 7(I): 1–21, 1955.

[65] S. Narimousa. Dynamics of mesoscale vortices generated by turbulent convection at large aspect ratios. *Journal of Geophysical Research*, 102(C3): 5615–5624, 1997.

[66] S. Narimousa, R.R. Long, and S.A. Kitaigorodskii. Entrainment due to turbulent shear flow at the interface of a stably stratified fluid. *Tellus*, 38A: 76–87, 1986.

[67] S. Narimousa and T. Maxworthy. Two-layer model of shear-driven coastal upwelling in the presence of bottom topography. *Journal of Fluid Mechanics*, 159: 503–531, 1985.

[68] S. Narimousa and T. Maxworthy. Coastal upwelling on a slopping bottom: the formation of plumes, jets and pinched-off cyclones. *Journal of Fluid Mechanics*, 176: 169–190, 1987.

[69] S. Narimousa, T. Maxworthy, and G.R. Spedding. Experiments on the structure and dynamics of forced, quasi-two-dimensional turbulence. *Journal of Fluid Mechanics*, 223: 113–133, 1991.

[70] J. Pedlosky. *Geophysical Fluid Dynamics.* Springer-Verlag, New York, 2nd edition, 1987.

[71] C.Y. Perng. *Adaptive-Multigrid Computations for Incompressible Flows, Including Geometry, Temperature, and Salinity Effects.* PhD thesis, Stanford University, 1990.

[72] C.Y. Perng and R.L. Street. 3-D unsteady flow Simulation: Alternative strategies for a volume-average calculation. *International Journal for Numerical Methods in Fluids*, 9: 341–362, 1989.

[73] N.A. Phillips. Energy transformations and meridional circulations associated with simple baroclinic waves in a two-level, quasi-geostrophic model. *Tellus*, 6: 273–286, 1954.

[74] U. Piomelli. Large-eddy simulation: achievements and challenges. *Progress in Aerospace Sciences*, 35(4): 335–362, 1999.

[75] A.K. Prasad. *Effect of Variable Geometry on Momentum and Heat Transfer in a Lid-Driven Cavity Flow.* PhD thesis, Stanford University, 1989.

[76] A.K. Prasad and J.R. Koseff. Reynolds number and end-wall effects on a lid-driven cavity flow. *Physics of Fluids A*, 1(2): 208–218, 1989.

[77] S. Raasch and D. Etling. Numerical simulation of rotating turbulent thermal convection. *Beiträgo zar Physik Atmosphäre*, 64(3): 185–199, 1991.

[78] D.A. Reed, L.M. Adams, and M.L. Patrick. Stencils and problem partitionings: their influence on the performance of multiple processor systems. *IEEE Transactions on Computers*, C-36: 845–858, 1987.

[79] M. Rosenfeld, D. Kwak, and M. Vinokur. A fractional step solution method for the unsteady incompressible Navier-Stokes equations in generalized coordinate systems. *Journal of Computational Physics*, 94: 102–137, 1991.

[80] H.T. Rossby. A study of Bénard convection with and without rotation. *Journal of Fluid Mechanics*, 36: 309–337, 1969.

[81] M.V. Salvetti and S. Banerjee. A priori tests of a new dynamic subgrid-scale model for finite-difference large-eddy simulations. *Physics of Fluids A*, 7(11): 2831–2847, 1995.

[82] M.V. Salvetti, Y. Zang, R.L. Street, and S. Banerjee. Large eddy simulation of free-surface decaying turbulence with dynamic mixed subgrid-scale models. *Physics of Fluids A*, 9(8): 2405–2419, 1997.

[83] J. Sander, D. Wolf-Gladrow, and D. Olbers. Numerical studies of open ocean deep convection. *Journal of Geophysical Research*, 100(C10): 20579–20600, 1995.

[84] P.M. Saunders. The instability of a baroclinic vortex. *Journal of Physical Oceanography*, 3(1): 61–65, 1973.

[85] J. Smagorinsky. General circulation experiments with the primitive equations. I. The basic experiment. *Monthly Weather Review*, 99: 99–164, 1963.

[86] R.C.J. Somerville and F.B. Lipps. A numerical study in three space dimensions of Bénard convection in a rotating fluid. *Journal of the Atmospheric Sciences*, 30: 590–596, 1973.

[87] H.S. Stone. Parallel tridiagonal equation solvers. *ACM Transactions on Mathematical Software*, 1(4): 289–307, 1975.

[88] H.U. Sverdrup. On the processes of upwelling. *Journal of Marine Research*, 1: 155–164, 1938.

[89] S. Tadepalli. *Numerical Simulation and Prediction of Upwelling Flow.* PhD thesis, Stanford University, 1997.

[90] J. Verron and W.R. Holland. Impacts des données d'altimètrie satellitaire sur les simulations numériques des circulations générales océaniques aux latitudes moyennes. *Annales Geophysicae*, 7: 31–46, 1989.

[91] K. Yoshida. Coastal upwelling off the California coast. *Records of Oceanographic Works in Japan*, 2(2): 1–13, 1955.

[92] Y. Zang. *On the Development of Tools for the Simulation of Geophysical Flows.* PhD thesis, Stanford University, 1993.

[93] Y. Zang and R.L. Street. Numerical simulation of coastal upwelling and interfacial instability of a rotating and stratified fluid. *Journal of Fluid Mechanics*, 305: 47–75, 1995.

[94] Y. Zang, R.L. Street, and J.R. Koseff. A dynamic mixed subgrid-scale model and its application to turbulent recirculating flows. *Physics of Fluid A*, 5(12): 3186–3196, 1993.